

1 LEVERAGING MULTI-MESSENGER ASTROPHYSICS FOR DARK MATTER SEARCHES

By

Daniel Nicholas Salazar-Gallegos

A DISSERTATION

Submitted to  
Michigan State University  
in partial fulfillment of the requirements  
for the degree of

Physics—Doctor of Philosophy  
Computational Mathematics in Science and Engineering—Dual Major

Today

**ABSTRACT**

3 I did Dark Matter with HAWC and IceCube. I also used Graph Neural Networks

<sup>4</sup> Copyright by

<sup>5</sup> DANIEL NICHOLAS SALAZAR-GALLEGOS

<sup>6</sup> Today

## ACKNOWLEDGMENTS

8 I love my friends. Thanks to everyone that helped me figure this out. Amazing thanks to the people  
9 at LANL who supported me. Eames, etc Dinner Parties Jenny and her child Kaydince Kirsten, Pat,  
10 Andrea Family. You're so far but so critical to my formation. Unconditional love. Roommate

## TABLE OF CONTENTS

12	LIST OF TABLES . . . . .	vii
13	LIST OF FIGURES . . . . .	ix
14	LIST OF ABBREVIATIONS . . . . .	xx
15	CHAPTER 1 INTRODUCTION . . . . .	1
16	CHAPTER 2 DARK MATTER IN THE COSMOS . . . . .	2
17	2.1 Introduction . . . . .	2
18	2.2 Dark Matter Basics . . . . .	3
19	2.3 Evidence for Dark Matter . . . . .	4
20	2.4 Searching for Dark Matter: Particle DM . . . . .	11
21	2.5 Sources for Indirect Dark Matter Searches . . . . .	16
22	2.6 Multi-Messenger Dark Matter . . . . .	18
23	CHAPTER 3 HIGH ALTITUDE WATER CHERENKOV (HAWC) OBSERVATORY . . . . .	21
24	3.1 The Detector . . . . .	21
25	3.2 Event Reconstruction . . . . .	26
26	3.3 Background Estimation: Direct Integration . . . . .	34
27	CHAPTER 4 ICECUBE NEUTRINO OBSERVATORY . . . . .	36
28	4.1 The Detector . . . . .	36
29	4.2 Events Reconstruction and Data Acquisition . . . . .	36
30	4.3 Northern Test Site . . . . .	36
31	CHAPTER 5 GLORY DUCK: MULTI-WAVELENGTH SEARCH FOR DARK MATTER ANNIHILATION TOWARDS DWARF SPHEROIDAL GALAXIES . . . . .	37
32	5.1 Introduction . . . . .	37
33	5.2 Dataset and Background . . . . .	39
34	5.3 Analysis . . . . .	41
35	5.4 Likelihood Methods . . . . .	45
36	5.5 HAWC Results . . . . .	52
37	5.6 Glory Duck Combined Results . . . . .	54
38	5.7 HAWC Systematics . . . . .	59
39	5.8 $J$ -factor distributions . . . . .	61
40	5.9 Discussion and Conclusions . . . . .	67
43	CHAPTER 6 MULTITHREADING HAWC ANALYSES FOR DARK MATTER SEARCHES . . . . .	71
44	6.1 Introduction . . . . .	71
45	6.2 Dataset and Background . . . . .	71
46	6.3 Analysis . . . . .	73

48	6.4	Likelihood Methods . . . . .	77
49	6.5	Computational Methods: Multithreading . . . . .	77
50	6.6	Analysis Results . . . . .	83
51	6.7	Systematics . . . . .	88
52	6.8	Conclusion and Discussion . . . . .	88
53	<b>CHAPTER 7</b>	<b>HEAVY DARK MATTER ANNIHILATION SEARCH WITH ICE-CUBE'S NORTH SKY TRACK DATA</b>	90
54	7.1	Introduction . . . . .	90
55	7.2	Dataset and Background . . . . .	90
56	7.3	Analysis . . . . .	92
57	7.4	Likelihood Methods . . . . .	101
58	7.5	Background Simulation . . . . .	101
59	7.6	Signal Recovery . . . . .	119
60	7.7	Systematics . . . . .	122
61	7.8	Conclusions . . . . .	125
63	<b>CHAPTER 8</b>	<b>NU DUCK: CONCLUSIONS AND FUTURE DIRECTIONS</b>	127
64	8.1	Conclusions . . . . .	127
65	8.2	Future Directions: Multi-Messenger Dark Matter Search . . . . .	128
66	<b>APPENDIX A</b>	<b>MULTI-EXPERIMENT SUPPLEMENTARY FIGURES</b>	130
67	<b>APPENDIX B</b>	<b>MULTITHREADING DARK MATTER ANALYSES SUPPLEMENTARY MATERIAL</b>	131
68	B.1	Remaining Spectral Models . . . . .	131
69	B.2	<code>mpu_analysis.py</code> . . . . .	132
70	B.3	Comparison with Glory Duck . . . . .	141
72	<b>APPENDIX C</b>	<b>ICECUBE HEAVY DARK MATTER ANALYSIS SUPPLEMENTARY MATERIAL</b>	144
73	C.1	Docker Image for Oscillating Neutrino Spectra . . . . .	144
74	C.2	Spline Fitting Statuses . . . . .	147
75	C.3	Neutrino Composite Spectra . . . . .	148
76	C.4	Segue 1 And Ursa Major II Signal Recovery . . . . .	149
77	C.5	$n_s$ Sensitivities . . . . .	155
79	<b>BIBLIOGRAPHY</b>		157

## LIST OF TABLES

<p>81    Table 3.1    Definitions of <math>f_{\text{hit}}</math> energy estimator bins. Bins are defined by the fraction of 82    available PMTs that are triggered during an air shower event. The angular 83    resolution, <math>\Theta_{68}</math>, is the bin containing 68% of events [34]. . . . .</p> <p>84    Table 5.1    Summary of the relevant properties of the dSphs used in the present work. 85    Column 1 lists the dSphs. Columns 2 and 3 present their heliocentric distance 86    and galactic coordinates, respectively. Columns 4 and 5 report the <math>J</math>-factors of 87    each source given from the <math>\mathcal{GS}</math> and <math>\mathcal{B}</math> independent studies and their estimated 88    <math>\pm 1\sigma</math> uncertainties. The values <math>\log_{10} J</math> (<math>\mathcal{GS}</math> set) [59] correspond to the mean 89    <math>J</math>-factor values for a source extension truncated at the outermost observed star. 90    The values <math>\log_{10} J</math> (<math>\mathcal{B}</math> set) [63] are provided for a source extension at the tidal 91    radius of each dSph. <b>Bolded sources are within HAWC's field of view and</b> 92    <b>provided to the Glory Duck analysis.</b> . . . . .</p> <p>93    Table 5.2    Summary of dSph observations by each experiment used in this work. A 94    ‘-’ indicates the experiment did not observe the dSph for this study. For 95    Fermi-LAT, the exposure at 1 GeV is given. For HAWC, <math> \Delta\theta </math> is the absolute 96    difference between the source declination and HAWC latitude. HAWC is more 97    sensitive to sources with smaller <math> \Delta\theta </math>. For IACTs, we show the zenith angle 98    range, the total exposure, the energy range, the angular radius <math>\theta</math> of the signal or 99    ON region, the ratio of exposures between the background-control (OFF) and 100    signal (ON) regions (<math>\tau</math>), and the significance of gamma-ray excess in standard 101    deviations, <math>\sigma</math>. . . . .</p> <p>102    Table 6.1    Summary of the relevant properties of the dSphs used in the present work. 103    Column 1 lists the dSphs. Columns 2 and 3 present their heliocentric distance 104    and galactic coordinates, respectively. Column 4 reports the <math>J</math>-factors of each 105    source given from the <math>\mathcal{LS}</math> studies and estimated <math>\pm 1\sigma</math> uncertainties. The 106    values <math>\log_{10} J</math> (<math>\mathcal{LS}</math> set) [80] correspond to the mean <math>J</math>-factor values for a 107    source extension truncated at <math>0.5^\circ</math>. . . . .</p> <p>108    Table 6.2    Timing summaries for analyses for serial and multithreaded processes. <math>M</math> 109    tasks is the number of functional-parallel tasks ran for the computation. <math>T_{p,c}</math> 110    is a single run time in hours:minutes:seconds for runs utilizing <math>p</math> nodes and 111    <math>c</math> threads. Runs are run interactively on the same computer to maximize 112    consistency. Empty entries are indicated with ‘-’. (·) entries are estimated 113    entries extrapolated from data earlier in the column. . . . .</p> <p>114    Table 6.3    Speed up summaries for analyses for serial and multithreaded processes. <math>M</math> 115    tasks is the number of functional-parallel tasks ran for the computation. <math>S_{p,c}</math> 116    is a single speedup comparison for runs utilizing <math>p</math> nodes and <math>c</math> threads. [·] 117    are the estimated speedups calculated from Tab. 6.2, Eq. (6.7), and Eq. (6.4). 118    Empty entries are indicated with ‘-’. . . . .</p>	<p>30</p> <p>46</p> <p>47</p> <p>77</p> <p>81</p> <p>83</p>
-----------------------------------------------------------------------------------------------------------------------------------------------------------------------------------------------------------------------------------------------------------------------------------------------------------------------------------------------------------------------------------------------------------------------------------------------------------------------------------------------------------------------------------------------------------------------------------------------------------------------------------------------------------------------------------------------------------------------------------------------------------------------------------------------------------------------------------------------------------------------------------------------------------------------------------------------------------------------------------------------------------------------------------------------------------------------------------------------------------------------------------------------------------------------------------------------------------------------------------------------------------------------------------------------------------------------------------------------------------------------------------------------------------------------------------------------------------------------------------------------------------------------------------------------------------------------------------------------------------------------------------------------------------------------------------------------------------------------------------------------------------------------------------------------------------------------------------------------------------------------------------------------------------------------------------------------------------------------------------------------------------------------------------------------------------------------------------------------------------------------------------------------------------------------------------------------------------------------------------------------------------------------------------------------------------------------------------------------------------------------------------------------------------------------------------------------------------------------------------------------------------------------------------------------------------------------------------------------------------------------------------------------------------------------------------------------------------------------------------------------------------------------------------------------------------------------------------------------------------------------------------------------------------------------------------------------------------------------------------------------------------------------------------------------------------------------------------------------------------------------------------------------------------------------------------------------------------------------------------------------------------------------------------------------------------------------------------------------------------------------------------------------------------------------------------------------------------------------------------------------------------------------------------------------------------------------------------------------------------------------------------------------------------------------------------------------------------------------------------------------------------------------------------------------------------------------------------------------------------------------------------------------------------------------------------------	-------------------------------------------------------------

119	Table 7.1	Spline err tolerances used for input in particle physics component to Eq. (5.1).		
120		Column 1 is the DM annihilation channel being fit. Columns 2, 3, and 4		
121		are the tolerances for "GOOD" (pass), "OK" requires inspection, and "FAIL"		
122		(tune and refit) respectively. Column 5 has the X ranges over which the error		
123		is evaluated. MAX/MIN $[ \cdot, \cdot ]$ takes the maximum or minimum of the two		
124		enclosed values. . . . .		98
125	Proof I know how to include			

## LIST OF FIGURES

127	Figure 2.1	Rotation curve fit to NGC 6503 from [7]. Dashed line is the contribution 128 from visible matter. Dotted curves are from gas. Dash-dot curves are from 129 dark matter (DM). Solid line is the composite contribution from all matter 130 and DM sources. Data are indicated with bold dots with error bars. Data 131 agree strongly with a matter + DM composite prediction. . . . .	5
132	Figure 2.2	Light from distant galaxy is bent in unique ways depending on the distribution 133 of mass between the galaxy and Earth. Yellow dashed lines indicate where 134 the light would have gone if the matter were not present [8]. . . . .	7
135	Figure 2.3	(left) Optical image of galactic cluster 1E0657-558. (right) X-ray image of the 136 cluster with redder meaning hotter and higher baryon density. (both) Green 137 contours are reconstruction of gravity contours from weak lensing. White 138 rings are the best fit mass maxima at 68.3%, 95.5%, and 99.7% confidence. 139 The matter maxima of the clusters are clearly separated from x-ray maxima. [9]	8
140	Figure 2.4	Plank CMB sky. Sky map features small variations in temperature in primor- 141 dial light. These anisotropies are used to make inferences about the universe's 142 energy budget and developmental history. [10] . . . . .	9
143	Figure 2.5	Observed Cosmic Microwave Background power spectrum as a function of 144 multipole moment from Plank [10]. Blue line is best fit model from $\Lambda$ CDM. 145 Red points and lines are data and error, respectively. . . . .	10
146	Figure 2.6	Predicted power spectra of CMB for different $\Omega_m h^2$ values for fixed baryon 147 density from [11]. (left) Low $\Omega_m h^2$ increases the prominence of first and 148 second peaks. (middle) $\Omega_m h^2$ is most similar to the observed power spectrum. 149 The second and third peaks are similar in height. (right) $\Omega_m h^2$ is large which 150 suppresses the first peak and raises the prominence of the third peak. . . . .	10
151	Figure 2.7	The Standard Model (SM) of particle physics. Figure taken from <a href="http://www.quantumdiaries.org/2014/03/14/the-standard-model-a-beautiful-but-flawed-theory/">http://www.quantumdiaries.org/2014/03/14/the-standard-model-a-beautiful-but-flawed-theory/</a> . . . . .	12
154	Figure 2.8	Simplified Feynman diagram demonstrating with different ways DM can 155 interact with SM particles. The 'X's refer to the DM particles whereas the 156 SM refer to fundamental particles in the SM. The large circle in the center 157 indicates the vertex of interaction and is purposely left vague. The colored 158 arrows refer to different directions of time as well as their respective labels. 159 The arrows indicate the initial and final state of the DM -SM interaction in time.	13

160	Figure 2.9 A single jet event in ATLAS detector from 2017 [16]. Jet momentum was 161 observed to be 1.9 TeV. Missing transverse momentum was observed to be 162 1.9 TeV compared to the initial transverse momentum of the event was 0. 163 Implied MET is traced by a red dashed line in event display. . . . .	14
164	Figure 2.10 More detailed pseudo-Feynman diagram of particle cascade from dark matter 165 annihilation into 2 quarks. The quarks hadronize and down to stable particles 166 like $\gamma$ or the anti-proton ( $p^-$ ). Diagram pulled from ICRC 2021 presentation 167 on DM annihilation search [17]. . . . .	15
168	Figure 2.11 Dark Matter (DM) decay spectrum for $b\bar{b}$ initial state and $\gamma$ final state. Redder 169 spectra are for larger DM masses. Bluer spectra are light DM masses. $x$ is a 170 unitless factor defined as the ratio of the mass of DM, $m_\chi$ , and the final state 171 particle energy $E_\gamma$ . Figure from [19]. . . . .	17
172	Figure 2.12 Different dark matter density profiles compared. Some models produce ex- 173 ceptionally large densities at small r [20]. . . . .	18
174	Figure 2.13 The Milky Way Galaxy in photons ( $\gamma$ ) and neutrinos ( $\nu$ ) [22]. The Galactic 175 center is at $l=0^\circ$ and is the brightest region in all panels. (top) An Optical 176 color image of the Milky Way galaxy seen from Earth. Clouds of gas and dust 177 obscure some light from stars. (2nd down) Integrated flux of $\gamma$ -rays observed 178 by the Fermi-LAT telescope [23]. (middle) Expected neutrino emission 179 that corresponds with Fermi-LAT observations. (2nd up) Expected neutrino 180 emission profile after considering detector systematics of IceCube. (bottom) 181 Observed neutrino emission from region of the galactic plane. Substantial 182 neutrino emission was detected. . . . .	19
183	Figure 2.14 Dark Matter annihilation spectra for different final state particle and standard 184 model annihilation channels [24]. Photons (red), $e^\pm$ (green), $\bar{p}$ (blue), $\nu$ (black). . . . .	20
185	Figure 3.1 Photo of the HAWC detector that I took on May 17, 2023. Main array is 186 centered in the photo and comprised of the larger tanks. Outriggers are the 187 smaller tanks around the main array. . . . .	21
188	Figure 3.2 A particle physics illustration of high energy particle showers. Left shower is 189 an electromagnetic shower from a high energy gamma-ray. Most particles in 190 the shower will be a combination of photons and charged leptons, in this case 191 electrons (e). Right figure shows a cosmic ray particle shower. The cosmic 192 ray will produce many more types of particles including pions ( $\pi$ ), neutrinos, 193 and charged leptons. Figure pulled from [26]. . . . .	22
194	Figure 3.3 The WCDs. Left image features several WCDs looking from within the main 195 array of HAWC. Right image shows a schematic of a WCD pulled from [25]. . . . .	23

196	Figure 3.4	Overview of HAWC control and data electronics. The LoToT and HiToT threshold signals are discussed in Section 3.1.2. Figure from [27] . . . . .	24
198	Figure 3.5	Schematic of data flow in HAWC data acquisition and online processing system. Pulled from [29]. . . . .	25
200	Figure 3.6	How HAWC FEB intially processes analog PMT signals. Signals are split through an amplifier and discriminator circuit. Each path is designated for ei- ther the HIGH or LOW threshold for the signal. The 2-edge event corresponds to LOW, while the 4 edge corresponds to HIGH. . . . .	25
204	Figure 3.7	An particle shower incident on WCDs. Secondary particles of an air shower travel in a cone centered on primary incident particle. Reconstruction of the initial angle is possible with arrival time of hits in PMTs inside WCDs. Figure from [33]. . . . .	27
208	Figure 3.8	Charge deposition in each PMT for a reconstructed gamma-ray event. WCDs are outlined in black surrounding the 4 smaller circles that represent PMTs. The color scale indicates the charge deposition in each PMT. The best shower core fit from SFCF is noted with a red star in the center of the dashed circle [34].	28
212	Figure 3.9	Simulated normalized energy distribution of each $f_{\text{hit}}$ bin defined in Tab. 3.1. Monte Carlo simulation of gamma-rays with $E^{-2.63}$ spectral shape and sim- ulated source at 20° declination. Figure from [34]. . . . .	30
215	Figure 3.10	Neural Network energy estimator performance compared to true energy. The dotted line is the identity line where the estimator and injection agree. Gam- ma/hadron separation cuts were applied with the energy estimation. Figure pulled from [37] . . . . .	32
219	Figure 3.11	Lateral distribution functions (LDFs) for cosmic ray (left) and a photon can- didate from the Crab Nebula (right). Cosmic ray LDF has clearly isolated hits far from the reconstructed shower core. Gamma-ray shower shows a more cuspy event [34]. . . . .	33

223	Figure 5.1 Sensitivities of five gamma-ray experiments compared to percentages of the 224 Crab nebula's emission and dark matter annihilation. Solid lines present 225 estimated sensitivities to power law spectra [FACT CHECK THIS]for each 226 experiment. Green lines are Fermi-LAT sensitivities where lighter green is 227 the sensitivity to the galactic center and dark green is its sensitivity to higher 228 declinations. Orange, red, and purple solid lines represent the MAGIC, HESS, 229 and VERITAS 50 hour sensitivities respectively. The maroon and brown lines 230 are the HAWC 1 year and 5 year sensitivities. Across four decades of gamma- 231 ray energy, these experiments have similar sensitivities on the order $10^{-12}$ 232 erg cm $^{-2}$ s $^{-1}$ . The dotted lines are estimated dark matter fluxes assuming 233 $m_\chi = 5$ TeV DM annihilating to bottom quarks (red), tau leptons (blue), 234 and W bosons (green). Faded gray lines outline percentage flux of the Crab 235 nebula. Figure is an augmented version of [40] . . . . .	38
236	Figure 5.2 Effect of Electroweak (EW) corrections on expected DM annihilation spec- 237 trum for $\chi\chi \rightarrow W^-W^+$ . Solid lines are spectral models that consider EW 238 corrections. Dash-dot lines are spectral models without EW corrections. Red 239 lines are models for $M_\chi = 1$ TeV. Blue lines represent models for $M_\chi = 100$ 240 TeV. All models are sourced from the PPPC4DMID [58]. . . . .	42
241	Figure 5.3 $\frac{dJ}{d\Omega}$ maps for Segue1 (top) and Coma Berenices (bottom). Origin is centered 242 on the specific dwarf spheroidal galaxies (dSph). X and Y axes are the angular 243 separation from the center of the dwarf. Profile is truncated at the scale radius. 244 Plots of the remaining 11 dSph HAWC studied are linked in Fig. A.1. . . . .	44
245	Figure 5.4 Illustration of the combination technique showing a comparison between 246 $-2 \ln \lambda$ provided by four instruments (colored lines) from the observation 247 of the same dSph without any $J$ nuisance and their sum, <i>i.e.</i> the resulting 248 combined likelihood (thin black line). According to the test statistics of 249 Equation (5.7), the intersection of the likelihood profiles with the line $-2 \ln \lambda$ 250 = 2.71 indicates the 95% C.L. upper limit on $\langle \sigma v \rangle$ . The combined likelihood 251 (thin black line) shows a smaller value of upper limit on $\langle \sigma v \rangle$ than those 252 derived by individual instruments. We also show how the uncertainties on 253 the $J$ factor effects the combined likelihood and degrade the upper limit on 254 $\langle \sigma v \rangle$ (thick black line). All likelihood profiles are normalized so that the global 255 minimum $\widehat{\langle \sigma v \rangle}$ is 0. We note that each profile depends on the observational 256 conditions in which a target object was observed. The sensitivity of a given 257 instrument can be degraded and the upper limits less constraining if the 258 observations are performed in non-optimal conditions such as a high zenith 259 angle or a short exposure time. . . . .	50
260	Figure 5.5 . . . . .	53

261	Figure 5.6 HAWC TS values for best fit $\langle\sigma v\rangle$ versus $m_\chi$ for seven SM annihilation channels with $J$ factors from $\mathcal{GS}$ . The solid black line shows the combined best fit TS values. The colored, dashed lines are the TS values for each of the 13 sources HAWC studied.	54
265	Figure 5.7 HAWC Brazil bands at 95% confidence level on $\langle\sigma v\rangle$ versus DM mass for seven annihilation channels with $J$ -factors from $\mathcal{GS}$ [69]. The solid line represents the combined limit from 13 dSphs. The dashed line is the expected limit. The green band is the 68% containment. The yellow band is the 95% containment.	55
270	Figure 5.8 Upper limits at 95% confidence level on $\langle\sigma v\rangle$ in function of the DM mass for eight annihilation channels, using the set of $J$ factors from Ref. [69] ( $\mathcal{GS}$ set in Table 5.1). The black solid line represents the observed combined limit, the black dashed line is the median of the null hypothesis corresponding to the expected limit, while the green and yellow bands show the 68% and 95% containment bands. Combined upper limits for each individual detector are also indicated as solid, colored lines. The value of the thermal relic cross-section in function of the DM mass is given as the red dotted-dashed line [70].	56
279	Figure 5.9 Same as Fig. 5.8, using the set of $J$ factors from Ref. [63, 71] ( $\mathcal{B}$ set in Table 5.1).	57
280	Figure 5.10 Comparisons of the combined limits at 95% confidence level for each of the eight annihilation channels when using the $J$ factors from Ref. [69] ( $\mathcal{GS}$ set in Table 5.1), plain lines, and the $J$ factor from Ref. [63, 71] ( $\mathcal{B}$ set in Table 5.1), dashed lines. The cross-section given by the thermal relic is also indicated [70].	59
284	Figure 5.11 Comparisons of the combined limits at 95% confidence level for a point source analysis and extended source using [69] $\mathcal{GS}$ J-factor distributions and PPPC [58] annihilation spectra. Shown are the limits for Segue1 which will have the most significant impact on the combined limit. 6 of the 7 DM annihilation channels are shown. Solid lines are extended source studies. Dashed lines are point source studies. Overall, the extended source analysis improves the limit by a factor of 2.	61
291	Figure 5.12 Same as Fig. 5.11 on Coma Berenices. This dSph also contributes significantly to the limit. The limits are identical in this case.	62
293	Figure 5.13 Comparison of combined limits when correcting for HAWC's pointing systematic. All DM annihilation channels are shown. The solid black line is the ratio between published limit to the declination corrected limit. The blue solid line or "Combined_og" represented the limits computed for Glory Duck. The solid orange line or "Combined_ad" represented the limits computed after correcting for the pointing systematic.	63

299	Figure 5.14 Differential map of $dJ/\Omega$ from model built in Section 5.8.1 and profiles 300 provided directly from authors. (Top) Differential from Segue1. (bottom) 301 Differential from Coma Berenices. Note that their scales are not the same. 302 Segue1 shows the deepest discrepancies which is congruent with its large 303 uncertainties. Both models show anuli where unique models become apparent. . . . .	64
304	Figure 5.15 HAWC limits for Coma Berenices (top) and Segue1 (bottom) for two different 305 map sets. Blue lines are limits calculated on maps with poor model repre- 306 sentation. Orange lines are limits calculated on spatial profiles provided by 307 the authors of [59]. Black line is the ratio of the poor spatial model limits to 308 the corrected spatial models. The left y-axis measures $\langle\sigma v\rangle$ for the blue and 309 orange lines. The right y-axis measures the ratio and is unitless. . . . .	65
310	Figure 5.16 Comparisons between the $J$ -factors versus the angular radius for the com- 311 putation of $J$ factors from Ref. [69] ( $\mathcal{GS}$ set in Table 5.1) in blue and for 312 the computation from Ref. [63, 71] ( $\mathcal{B}$ set in Tab. 5.1) in orange. The solid 313 lines represent the central value of the $J$ -factors while the shaded regions 314 correspond to the $1\sigma$ standard deviation. . . . .	67
315	Figure 5.17 Comparisons between the $J$ -factors versus the angular radius for the com- 316 putation of $J$ factors from Ref. [69] ( $\mathcal{GS}$ set in Tab. 5.1) in blue and for the 317 computation from Ref. [63, 71] ( $\mathcal{B}$ set in Tab. 5.1) in orange. The solid 318 lines represent the central value of the $J$ -factors while the shaded regions 319 correspond to the $1\sigma$ standard deviation. . . . .	68
320	Figure 6.1 Spectral hypotheses from PPPC [58] and HDM [79] for DM annihilation: $\chi\chi \rightarrow W^-W^+$ . Solid lines are spectral models with EW corrections from the 321 PPPC. Dash-dot lines are spectral models from HDM. Red lines are models 322 for $M_\chi = 1$ TeV. Blue lines represent models for $M_\chi = 100$ TeV. . . . .	73
324	Figure 6.2 Photon spectra for $\chi\chi \rightarrow \gamma\gamma$ (left) and $\chi\chi \rightarrow ZZ$ (right) after Gaussian 325 convolution of line features. Both spectra have $\delta$ -features at photon energies 326 equal to the DM mass. Bluer lines are annihilation spectra with lower DM 327 mass. Redder lines are spectra from larger DM mass. All spectral models are 328 sourced from the Heavy Dark Matter models [79]. Axes are drawn roughly 329 according to the energy sensitivity of HAWC. . . . .	74
330	Figure 6.3 $\frac{dJ}{d\Omega}$ maps for Coma Berenices, Draco, Segue1, and Sextans. Columns are 331 divided for the $\pm 1\sigma$ uncertainties in $dJ/d\Omega$ around the mean value from $\mathcal{LS}$ 332 [80]. Origin is centered on the specific dwarf spheroidal galaxies (dSph). $\theta$ 333 and $\phi$ axes are the angular separation from the center of the dwarf. Profiles 334 are truncated at $1^\circ$ and flattened beyond. . . . .	76

335	Figure 6.4	Infographic on how jobs and DM computation was organized in Section 5.3. Jobs were built for each permutation of CHANS and SOURCES shown by the left block in the figure. Each job, which took on the order 2 hrs to compute, had the following work flow: 1. Import HAWC analysis software, 2 min to run. 2. Load HAWC count maps, 5 min to run. 3. Load HAWC energy and spatial resolutions, 4 min. 5. Load DM spatial source templates and spectral models, less than 1 s. 6. Perform likelihood fit on data and model, about 8 min per DM mass. 7. Write results to file, less than 1s. . . . .	78
343	Figure 6.5	Graphic of Gustafson parallel coding pattern. $f_s$ is the fraction of a program, in time, spent on serial computation. $f_p$ is the fraction of computing time that is parallelizable. $T_p$ is the total time for a parallel program to run. $T_1$ is the total time for a parallel program to run if only 1 processor is allocated. $P_N$ is the $N$ -th processor where it's row is the computation the processor performs. The Gustafson pattern is most similar to what is implemented for this analysis. Figure is pulled from [82]. . . . .	79
350	Figure 6.6	Task chart for one multithreaded job developed for this project. Green blocks indicate a shared resource across the threads AND computation performed serially. Red blocks indicate functional parallel processing within each thread. 3 threads are represented here, yet many more can be employed during the full analysis. Jobs are defined by the SOURCE as these require unique maps to be loaded into the likelihood estimator. The $m_\chi$ , CHAN, and $\langle\sigma v\rangle$ variables are entered into the thread pool and allocated as evenly as possible across the threads. . . . .	81
358	Figure 6.7	HAWC upper limits at 95% confidence level on $\langle\sigma v\rangle$ versus $m_\chi$ for $\chi\chi \rightarrow b\bar{b}$ , $t\bar{t}$ , $u\bar{u}$ , $d\bar{d}$ , $s\bar{s}$ , $c\bar{c}$ , $gg$ , $W^+W^-$ , and $hh$ . Limits are with $\mathcal{LS}$ $J$ -factors [80]. The solid line represents the observed combined limit. Dashed lines represent limits from individual dSphs. . . . .	84
362	Figure 6.8	HAWC upper limits at 95% confidence level on $\langle\sigma v\rangle$ versus $m_\chi$ for $\chi\chi \rightarrow \nu_e\bar{\nu}_e$ , $\nu_\mu\bar{\nu}_\mu$ , $\nu_\tau\bar{\nu}_\tau$ , $e\bar{e}$ , $\mu\bar{\mu}$ , $\tau\bar{\tau}$ , $\gamma\gamma$ and $ZZ$ . Limits use $\mathcal{LS}$ $J$ -factors [80]. The solid line represents the observed combined limit. Dashed lines represent limits from individual dSphs. . . . .	85
366	Figure 6.9	HAWC TS values for best fit $\langle\sigma v\rangle$ versus $m_\chi$ for SM annihilation channels: $\chi\chi \rightarrow b\bar{b}$ , $t\bar{t}$ , $u\bar{u}$ , $d\bar{d}$ , $s\bar{s}$ , $c\bar{c}$ , $gg$ , $W^+W^-$ , and $hh$ . Limits use $\mathcal{LS}$ $J$ -factors. The solid black line shows the combined best fit TS values. The colored, dashed lines are the TS values from each dSph. . . . .	86
370	Figure 6.10	HAWC TS values for best fit $\langle\sigma v\rangle$ versus $m_\chi$ for SM annihilation channels: $\chi\chi \rightarrow \nu_e\bar{\nu}_e$ , $\nu_\mu\bar{\nu}_\mu$ , $\nu_\tau\bar{\nu}_\tau$ , $e\bar{e}$ , $\mu\bar{\mu}$ , $\tau\bar{\tau}$ , $\gamma\gamma$ and $ZZ$ . Limits use $\mathcal{LS}$ $J$ -factors. The solid black line shows the combined best fit TS values. The colored, dashed lines are the TS values from each dSph. . . . .	87

374	Figure 6.11 Comparison of HAWC limits from this analysis to Glory Duck (Fig. 5.5) for 3 dSphs and 3 DM annihilation channels: $b\bar{b}$ , $\tau\bar{\tau}$ , and $e\bar{e}$ . Each sector shows the 95% confidence limit from Glory Duck (blue line) and this analysis (orange line) in the top plot. The lower plot features the ratio in log scale of Glory Duck to this analysis in a red solid line. Horizontal dashed lines are for ratios of 1.0 (black) and $\sqrt{2}$ (blue). Ratios larger than 1.0 are for limits smaller, or stricter, than Glory Duck. Ratios larger than $\sqrt{2}$ indicates limits are stricter than a simple doubling of the Glory Duck data. . . . .	89
382	Figure 7.1 Neutrino spectra at production (left panels) and after oscillation at Earth (right panels). Blue, orange, and green lines are the $\nu_e$ , $\nu_\mu$ , and $\nu_\tau$ spectra respectively. Top panels show the spectra in $\frac{dN}{dE}$ . Lower panels plot the flavor ratio to $\nu_e + \nu_\mu + \nu_\tau$ . SM annihilation channels $b\bar{b}$ , $\tau\bar{\tau}$ , and $\nu_\mu\bar{\nu}_\mu$ are shown for $M_\chi = 1$ PeV, TeV, and EeV. . . . .	94
387	Figure 7.2 Signal recovery for 100 TeV DM annihilation into $\nu_\mu\bar{\nu}_\mu$ for a source at Dec = $16.06^\circ$ . $n_{\text{inj}}$ is the number of injected signal events in simulation. $n_s$ is the number of reconstructed signal events from the simulation data. Although the uncertainties are small and tight, the reconstructed $n_s$ are systematically underestimated. . . . .	95
392	Figure 7.3 Left panel shows the two kernels overlaying the original spectrum from $\chi$ arony after propagation to Earth [85]. The vertical red line indicates where the original neutrino line is maximized. Blue line is the output from $\chi$ aroy. Green line is the spectrum after convolution with a flat kernel. Orange line is the spectrum after Gaussian convolution. Right panel shows the signal recovery of the spectral model using the Gaussian kernel with parameters enumerated above. . . . .	96
399	Figure 7.4 Example spline that failed the fit. Failed splined are corrected on a case by case basis unless the SM channel has a systematic problem fitting the splines. In this case, I made a bookkeeping error and loaded the incorrect spectral model	98
402	Figure 7.5 Summary of input spectral models that were smoothed with Gaussian kernels. Spectral models are for $\chi\chi \rightarrow e\bar{e}, \mu\bar{\mu}, \tau\bar{\tau}, \nu_e\bar{\nu}_e, \nu_\mu\bar{\nu}_\mu$ , and $\nu_\tau\bar{\nu}_\tau$ . These spectra are the composite ( $\nu_\mu + \nu_\tau$ ) of neutrino flavors. Every spectral model used for this analysis is featured as a colored solid line. Bluer lines are for low $m_\chi$ models. $m_\chi$ ranges from 681 GeV to 100 PeV. HDM [79], $\chi$ aroy [85], and Photospline [89] are used to generate these spectra. Energy (x-axis) was chosen to roughly represent the energy sensitivity of NST. . . . .	99

409	Figure 7.6 Test statistic (TS) distributions for Segue 1 and $\chi\chi \rightarrow b\bar{b}$ . Each subplot, 410 except the final, is the TS distribution for a specific DM mass listed in the 411 subplot. Orange dashed lines are the traces for a $\chi^2$ distribution with 1 degree 412 of freedom. $\epsilon[\cdot]$ is the fraction of trials smaller than the bracketed value. The 413 final subplot features the all DM spectral models, similar to Fig. 7.5, used as 414 input for the TS distributions. . . . .	102
415	Figure 7.7 Same as Fig. 7.6 for Segue 1 $\chi\chi \rightarrow \tau\bar{\tau}$ . . . . .	103
416	Figure 7.8 Same as Fig. 7.6 for Segue 1 $\chi\chi \rightarrow \nu_\mu\bar{\nu}_\mu$ . . . . .	104
417	Figure 7.9 Same as Fig. 7.6 for Ursa Major II 1 $\chi\chi \rightarrow b\bar{b}$ . . . . .	105
418	Figure 7.10 Same as Fig. 7.6 for Ursa Major II 1 $\chi\chi \rightarrow \tau\bar{\tau}$ . . . . .	106
419	Figure 7.11 Same as Fig. 7.6 for Ursa Major II 1 $\chi\chi \rightarrow \nu_\mu\bar{\nu}_\mu$ . . . . .	107
420	Figure 7.12 Same as Fig. 7.6 for 15, GS J-factor, stacked sources and $\chi\chi \rightarrow b\bar{b}$ . . . . .	108
421	Figure 7.13 Same as Fig. 7.6 for 15, GS J-factor, stacked sources and $\chi\chi \rightarrow t\bar{t}$ . . . . .	109
422	Figure 7.14 Same as Fig. 7.6 for 15, GS J-factor, stacked sources and $\chi\chi \rightarrow u\bar{u}$ . . . . .	110
423	Figure 7.15 Same as Fig. 7.6 for 15, GS J-factor, stacked sources and $\chi\chi \rightarrow d\bar{d}$ . . . . .	111
424	Figure 7.16 Same as Fig. 7.6 for 15, GS J-factor, stacked sources and $\chi\chi \rightarrow e\bar{e}$ . . . . .	112
425	Figure 7.17 Same as Fig. 7.6 for 15, GS J-factor, stacked sources and $\chi\chi \rightarrow \mu\bar{\mu}$ . . . . .	113
426	Figure 7.18 Same as Fig. 7.6 for 15, GS J-factor, stacked sources and $\chi\chi \rightarrow \tau\bar{\tau}$ . . . . .	114
427	Figure 7.19 Same as Fig. 7.6 for 15, GS J-factor, stacked sources and $\chi\chi \rightarrow W^+W^-$ . . . . .	115
428	Figure 7.20 Same as Fig. 7.6 for 15, GS J-factor, stacked sources and $\chi\chi \rightarrow ZZ$ . . . . .	116
429	Figure 7.21 Same as Fig. 7.6 for 15, GS J-factor, stacked sources and $\chi\chi \rightarrow \nu_e\bar{\nu}_e$ . . . . .	117
430	Figure 7.22 Same as Fig. 7.6 for 15, GS J-factor, stacked sources and $\chi\chi \rightarrow \nu_\mu\bar{\nu}_\mu$ . . . . .	118

431	Figure 7.23 Signal Recovery study for an analysis with 15 stacked sources using the $\mathcal{GS}$	120
432	$J$ -factors [59]. Above shows 14 studies for DM mass ranging between 1	
433	TeV and 20 PeV for $\chi\chi \rightarrow \mu_\mu\overline{\mu_\mu}$ . The bottom right subplot features every	
434	spectral model used as input for the remaining subplots. The remaining	
435	subplots show $n_{\text{inj}}$ as the number of signal events injected into background	
436	simulation. Whereas, $n_s$ is the number of signal events recovered from	
437	analyzing the injected simulation. Blue line represents the median values of	
438	100 simulations. Light blue bands show the $1\sigma$ statistical uncertainty around	
439	the median. . . . .	
440	Figure 7.24 Same as Fig. 7.23 but for $\chi\chi \rightarrow t\bar{t}$ (top) and $b\bar{b}$ (bottom). . . . .	121
441	Figure 7.25 IceCube North Sky Track Sensitivities. Each panel shows sensitivity curves	
442	for various DM annihilation channels. Sensitivities are for the velocity-	
443	weighted cross-section $\langle\sigma v\rangle$ versus $m_\chi$ . Dotted, colored lines are sensitivities	
444	for individual sources. Solid white lines are for the combined sensitivity of	
445	all 15 $\mathcal{GS}$ sources used in this study. . . . .	123
446	Figure 7.26 Same as Fig. 7.25 for three additional DM annihilation channels. . . . .	124
447	Figure 7.27 Panel A: Neutrino's from the Northern sky and incident on the IceCube	
448	detector will travel through the Earth. How much of the Earth these neutrinos	
449	travels is a function of zenith from the vertical axis. Panel B: SM prediction of	
450	neutrino transmission probabilities for neutrinos arriving at $90^\circ - 180^\circ$ zenith	
451	and with 100 GeV to 100 PeV energies. High-energy neutrinos traversing	
452	the whole Earth are completely absorbed, whereas low-energy neutrinos pass	
453	through unimpeded. Neutrinos coming from above the horizon will arrive	
454	unimpeded for all neutrino energies. Figure pulled from [92]. . . . .	125
455	Figure 7.28 $\langle\sigma v\rangle$ sensitivities for 5 imaginary sources with $\log_{10} J = 19.42 \log_{10}(\text{GeV}^2\text{cm}^{-5})$ .	
456	Each imaginary source shares a declination with a source in Tab. 5.1 . . . . .	126
457	Figure 8.1 The prompt electron neutrino and photon spectrum resulting from the decay	
458	of a 2EeV DM particle to $\nu_e\overline{\nu}_e$ , as currently being searched for at IceCube	
459	[5]. Solid curves represent the results of this work, and predict orders of	
460	magnitude more flux at certain energies than the dashed results of Pythia 8.2,	
461	one of the only existing methods to generate spectra at these masses. In both	
462	cases energy conservation is satisfied: there is a considerable contribution to	
463	a $\delta$ -function at $x = 1$ , associated with events where an initial W or Z was never	
464	emitted and thus no subsequent shower developed. Large disagreements are	
465	generically observed at these masses for electroweak dominated channels,	
466	while the agreement is better for colored initial SM states. . . . .	128
467	Figure 8.2 TODO: neutrino and bb plot with nu Sensitivities[NEEDS A SOURCE][FACT	
468	CHECK THIS] . . . . .	129

469	Figure A.1	Sister figure to Figure 5.3. Sources in the first row from left to right: Bootes I, Canes Venatici I, II. In second row: Draco, Hercules, Leo I. In the first row: Leo II, Leo IV, Sextans. In the final row: Ursa Major I, Ursa Major II. . . . .	130
472	Figure B.1	Sister figure to Figure 6.2 for remaining SM primary annihilation channels studied for this thesis. These did not require any post generation smoothing and so are directly pulled from [79] with a binning scheme most helpful for a HAWC analysis. . . . .	131
476	Figure B.2	Comparison of HAWC limits from this analysis to Glory Duck (Fig. 5.5) for Coma Berenices and 7 DM annihilation channels. . . . .	141
478	Figure B.3	Same as Fig. B.2 but for Segue 1. . . . .	142
479	Figure B.4	Same as Fig. B.2 but for Sextans. . . . .	143
480	Figure C.1	Current status of spline tables according to constraints defined by Tab. 7.1. Green splines are splines that passed under the GOOD tolerance. Yellow are splines that are OK. Red are splines that FAIL. All yellow splines were inspected individually before running the analysis. Splines were made for the $\mu$ (PID 14; top panel) flavor and $\tau$ (PID 16; bottom panel) neutrino flavors. . . . .	147
485	Figure C.2	Sister figure to Fig. 7.5 for annihilation channels that did not require kernel smoothing. These spectra are the composite ( $\nu_\mu + \nu_\tau$ ) of neutrino flavors. Every spectral model used for this analysis is featured as a colored solid line. Bluer lines are for lower DM mass spectral models. DM masses range from 681 GeV to 100 PeV. . . . .	148
490	Figure C.3	Same as Fig. 7.23 but for Segue 1 and $\chi\chi \rightarrow b\bar{b}$ . . . . .	149
491	Figure C.4	Same as Fig. 7.23 but for Segue 1 and $\chi\chi \rightarrow t\bar{t}$ . . . . .	150
492	Figure C.5	Same as Fig. 7.23 but for Segue 1 and $\chi\chi \rightarrow \nu_\mu\bar{\nu}_\mu$ . . . . .	151
493	Figure C.6	Same as Fig. 7.23 but for Ursa Major II and $\chi\chi \rightarrow b\bar{b}$ . . . . .	152
494	Figure C.7	Same as Fig. 7.23 but for Ursa Major II and $\chi\chi \rightarrow t\bar{t}$ . . . . .	153
495	Figure C.8	Same as Fig. 7.23 but for Ursa Major II and $\chi\chi \rightarrow \nu_\mu\bar{\nu}_\mu$ . . . . .	154
496	Figure C.9	IceCube North Sky Track Sensitivities for $n_s/\langle N \rangle$ . $n_s$ values are the counts fed into Eq. (7.8) to produce Fig. 7.26 and Fig. 7.25. . . . .	155
498	Figure C.10	Same as Fig. C.9 for three additional DM annihilation channels. . . . .	156

**LIST OF ABBREVIATIONS**

- 500 **MSU** Michigan State University  
501 **LANL** Los Alamos National Laboratory  
502 **DM** Dark Matter  
503 **SM** Standard Model  
504 **HAWC** High Altitude Water Cherenkov Observatory  
505 **dSph** Dwarf Spheroidal Galaxy

506

## **CHAPTER 1**

### **INTRODUCTION**

507 Is the text not rendering right? Ah ok it knows im basically drafting the doc still

## CHAPTER 2

508

### DARK MATTER IN THE COSMOS

509 **2.1 Introduction**

510 The dark matter problem can be summarized in part by the following thought experiment.

511 Let us say you are the teacher for an elementary school classroom. You take them on a field  
512 trip to your local science museum and among the exhibits is one for mass and weight. The exhibit  
513 has a gigantic scale, and you come up with a fun problem for your class.

514 You ask your class, "What is the total weight of the classroom? Give your best estimation to  
515 me in 30 minutes, and then we'll check your guess on the scale. If your guess is within 10% of the  
516 right answer, we will stop for ice cream on the way back."

517 The students are ecstatic to hear this, and they get to work. The solution is some variation of  
518 the following strategy. The students should give each other their weight or best guess if they do  
519 not know. Then, all they must do is add each student's weight and get a grand total for the class.  
520 The measurement on the giant scale should show the true weight of the class. When comparing  
521 the measured weight to your estimation, multiply the measurement by  $1.0 \pm 0.1$  to get the  $\pm 10\%$   
522 tolerances for your estimation.

523 Two of your students, Sandra and Mario, return to you with a solution.

524 They say, "We weren't sure of everyone's weight. We used 65 lbs. for the people we didn't  
525 know and added everyone who does know. There are 30 of us, and we got 2,000 lbs.! That's a ton!"

526 You estimated 1,900 lbs. assuming the average weight of a student in your class was 60 lbs.  
527 So, you are pleased with Sandra's and Mario's answer. You instruct your students to all gather on  
528 the giant scale and read off the weight together. To all your surprise, the scale reads *10,000 lbs.*!  
529 10,000 is significantly more than a 10% error from 2,000. In fact, it is approximately 5 times more  
530 massive than either your or your students' estimates. You think to yourself and conclude there  
531 must be something wrong with the scale. You ask an employee to check the scale and verify it is  
532 well calibrated. They confirm that the scale is in working order. You weigh a couple of students  
533 individually to assess that the scale is well calibrated. Sandra weighs 59 lbs., and Mario weighs

534 62 lbs., typical weights for their age. You then weigh each student individually and see that their  
535 weights individually do not deviate greatly from 60 lbs. So, where does all the extra weight come  
536 from?

537 This thought experiment serves as an analogy to the Dark Matter problem. The important  
538 substitution to make however is to replace the students with stars and the classroom with a galaxy,  
539 say the Milky Way. Individually the mass of stars is well measured and defined with the Sun as our  
540 nearest test case. However, when we set out to measure the mass of a collection of stars as large as  
541 galaxies, our well-motivated estimation is wildly incorrect. There simply is no way to account for  
542 this discrepancy except without some unseen, or dark, contribution to mass and matter in galaxies.  
543 I set out in my thesis to narrow the possibilities of what this Dark Matter could be.

544 This chapter is organized like the following... **TODO: Text should look like ... Chapter x has**  
545 **blah blah blah.**

## 546 2.2 Dark Matter Basics

547 Presently, a more compelling theory of cosmology that includes Dark Matter (DM) in order  
548 to explain a variety of observations is  $\Lambda$  Cold Dark Matter, or  $\Lambda$ CDM. I present the evidence  
549 supporting  $\Lambda$ CDM in Section 2.3 yet discuss the conclusions of the  $\Lambda$ CDM model here. According  
550 to  $\Lambda$ CDM fit to observations on the Cosmic Microwave Background (CMB), DM is 26.8% of the  
551 universe's current energy budget. Baryonic matter, stuff like atoms, gas, and stars, contributes to  
552 4.9% of the universe's current energy budget [1, 2, 3].

553 DM is dark; it does not interact readily with light at any wavelength. DM also does not interact  
554 noticeably with the other standard model forces (Strong and Weak) at a rate that is readily observed  
555 [3]. DM is cold, which is to say that the average velocity of DM is below relativistic speeds [1].  
556 'Hot' DM would not likely manifest the dense structures we observe like galaxies, and instead  
557 would produce much more diffuse galaxies than what is observed [3, 1]. DM is old; it played a  
558 critical role in the formation of the universe and the structures within it [1, 2].

559 Observations of DM have so far been only gravitational. The parameter space available to what  
560 DM could be therefore is extremely broad. The broad DM parameter space is iteratively tested in

561 DM searches by supposing a hypothesis that has not yet been ruled out and performing observations  
562 to test them. When the observations yield a null result, the parameter space is constrained further.  
563 I present some approaches for DM searches in Section 2.4.

564 **2.3 Evidence for Dark Matter**

565 Dark Matter (DM) has been a looming problem in physics for almost 100 years. Anomalies  
566 have been observed by astrophysicists in galactic dynamics as early as 1933 when Fritz Zwicky  
567 noticed unusually large velocity dispersion in the Coma cluster. Zwicky's measurement was the  
568 first recorded to use the Virial theorem to measure the mass fraction of visible and invisible matter  
569 in celestial bodies [4]. From Zwicky in [5], "*If this would be confirmed, we would get the surprising*  
570 *result that dark matter is present in much greater amount than luminous matter.*" Zwicky's and  
571 others' observation did not instigate a crisis in astrophysics because the measurements did not  
572 entirely conflict with their understanding of galaxies [4]. In 1978, Rubin, Ford, and Norbert  
573 measured rotation curves for ten spiral galaxies [6]. Rubin et al.'s 1978 publication presented a  
574 major challenge to the conventional understanding of galaxies that could no longer be dismissed by  
575 measurement uncertainties. Evidence has been mounting ever since for this exotic form of matter.  
576 The following subsections provide three compelling pieces of evidence in support of the existence  
577 of DM.

578 **2.3.1 First Clues: Stellar Velocities**

579 Zwicky, and later Rubin, measured the stellar velocities of various galaxies to estimate their  
580 virial mass. The Virial Theorem upon which these observations are interpreted is written as

$$2T + V = 0. \quad (2.1)$$

581 Where  $T$  is the kinetic energy and  $V$  is the potential energy in a self-gravitating system. The  
582 classical Newton's law of gravity from stars and gas was used for gravitational potential modeled in  
583 the observed galaxies:

$$V = -\frac{1}{2} \sum_i \sum_{j \neq i} \frac{m_i m_j}{r_{ij}}. \quad (2.2)$$

584 Zwicky et al. measured just the velocities of stars apparent in optical wavelengths [5]. Rubin et al.  
 585 added by measuring the velocity of the hydrogen gas via the 21 cm emission line of Hydrogen [6].  
 586 The velocities of the stars and gas are used to infer the total mass of galaxies and galaxy clusters  
 587 via Equation (2.1). An inferred mass is obtained from the luminosity of the selected sources. The  
 588 two inferences are compared to each other as a luminosity to mass ratio which typically yielded [1]

$$\frac{M}{L} \sim 400 \frac{M_{\odot}}{L_{\odot}} \quad (2.3)$$

589  $M_{\odot}$  and  $L_{\odot}$  referring to stellar mass and stellar luminosity, respectively. These ratios clearly indicate  
 590 a discrepancy in apparent light and mass from stars and gas and their velocities.

591 Rubin et al. [6] demonstrated that the discrepancy was unlikely to be an underestimation of  
 592 the mass of the stars and gas. The inferred "dark" mass was up to 5 times more than the luminous  
 593 mass. This dark mass also needed to extend well beyond the extent of the luminous matter.

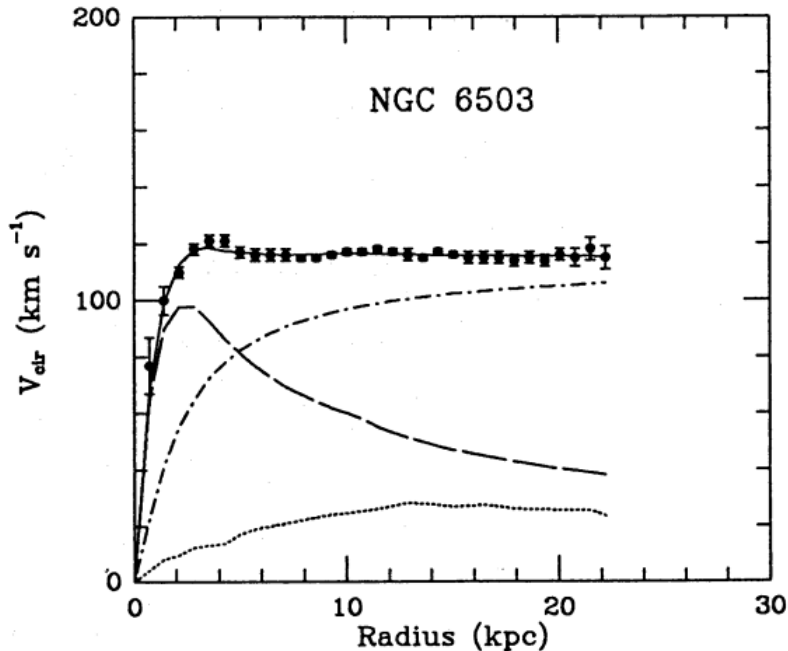


Figure 2.1 Rotation curve fit to NGC 6503 from [7]. Dashed line is the contribution from visible matter. Dotted curves are from gas. Dash-dot curves are from dark matter (DM). Solid line is the composite contribution from all matter and DM sources. Data are indicated with bold dots with error bars. Data agree strongly with a matter + DM composite prediction.

594 Figure 2.1 features one of many rotation curves plotted from the stellar velocities within galaxies.

595 The measured rotation curves mostly feature a flattening of velocities at higher radius which is not  
596 expected if the gravity was only coming from gas and luminous matter. The extension of the  
597 flat velocity region also indicates that the DM is distributed far from the center of the galaxy.  
598 Modern velocity measurements include significantly larger objects, galactic clusters, and smaller  
599 objects, dwarf galaxies. Yet, measurements along this regime are leveraging the Virial theorem  
600 with Newtonian potential energies. We know Newtonian gravity is not a comprehensive description  
601 of gravity. New observational techniques have been developed since 1978, and those are discussed  
602 in the following sections.

603 **2.3.2 Evidence for Dark Matter: Gravitational Lensing**

604 Modern evidence for dark matter comes from new avenues beyond stellar velocities. Grav-  
605 itational lensing from DM is a new channel from general relativity. General relativity predicts  
606 aberrations in light caused by massive objects. In recent decades we have been able to measure the  
607 lensing effects from compact objects and DM halos. Figure 2.2 shows how different massive ob-  
608 jects change the final image of a faraway galaxy resulting from gravitational lensing. Gravitational  
609 lensing developed our understanding of dark matter in two important ways.

610 Gravitational lensing provides additional compelling evidence for DM. The observation of two  
611 merging galactic clusters in 2006, shown in Figure 2.3, provided a compelling argument for DM  
612 outside the Standard Model. These clusters merged recently in astrophysical time scales. Galaxies  
613 and star cluster have mostly passed by each other as the likelihood of their collision is low. Therefore,  
614 these massive objects will mostly track the highest mass, dark and/or baryonic, density. Yet, the  
615 intergalactic gas is responsible for the majority of the baryonic mass in the systems [4]. These gas  
616 bodies will not phase through and will heat up as they collide together. The hot gas is located via  
617 x-ray emission from the cluster. Two observations of the clusters were performed independently of  
618 each other.

619 The first was the lensing of light around the galaxies due to their gravitational influences.  
620 When celestial bodies are large enough, the gravity they exert bends space and time itself. The  
621 warped space-time lenses light and will deflect in an analogous way to how glass lenses will bend

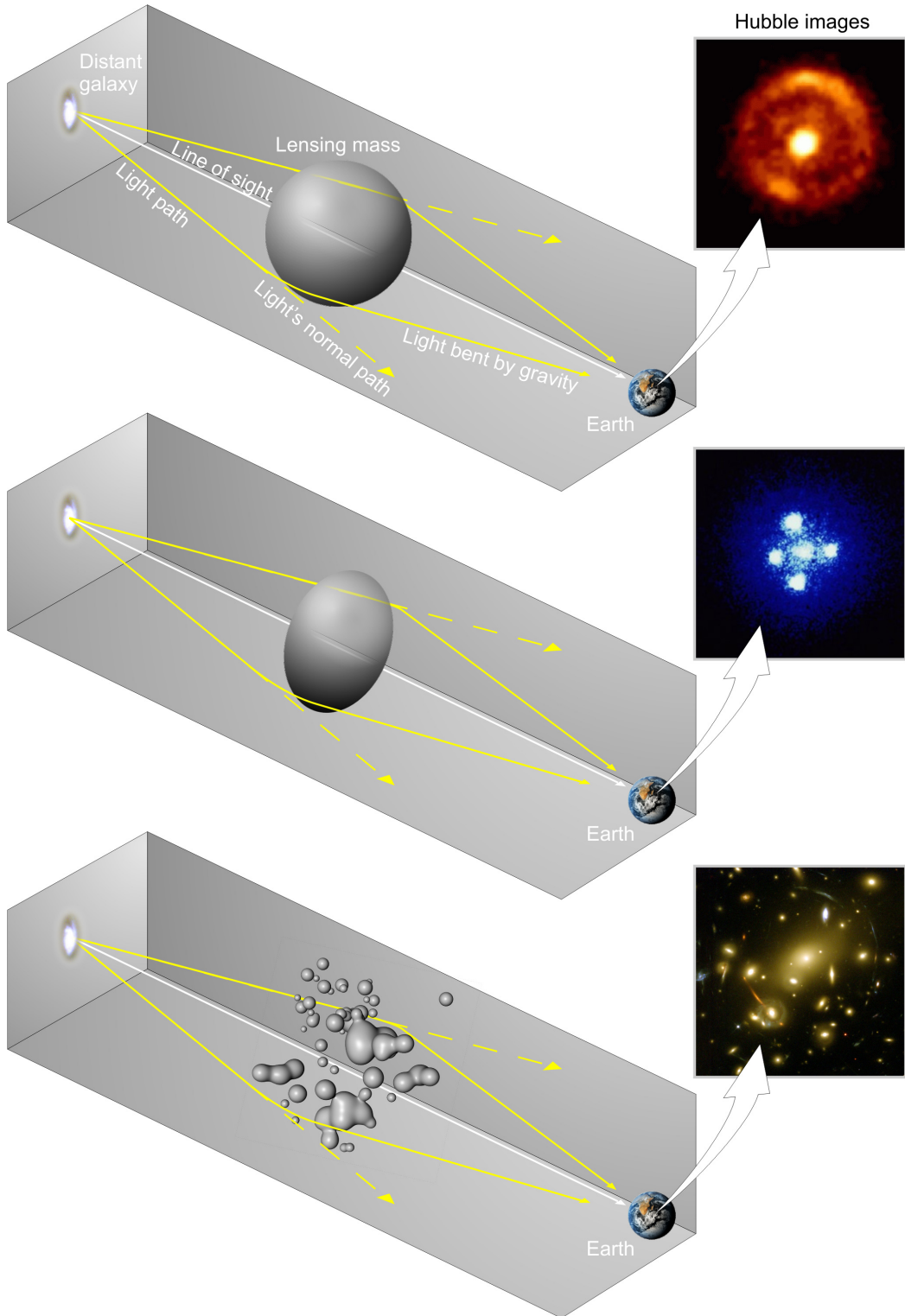


Figure 2.2 Light from distant galaxy is bent in unique ways depending on the distribution of mass between the galaxy and Earth. Yellow dashed lines indicate where the light would have gone if the matter were not present [8].

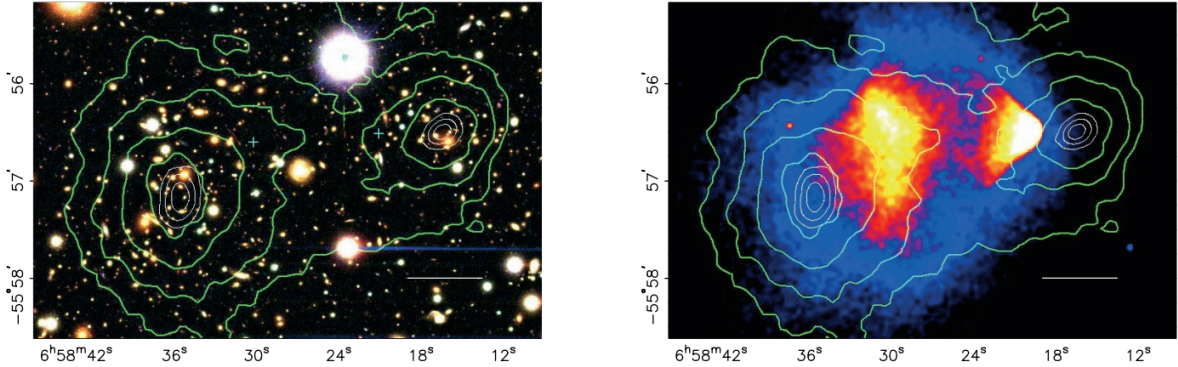


Figure 2.3 (left) Optical image of galactic cluster 1E0657-558. (right) X-ray image of the cluster with redder meaning hotter and higher baryon density. (both) Green contours are reconstruction of gravity contours from weak lensing. White rings are the best fit mass maxima at 68.3%, 95.5%, and 99.7% confidence. The matter maxima of the clusters are clearly separated from x-ray maxima. [9]

622 light, see Figure 2.2. With a sufficient understanding of light sources behind a massive object, we  
 623 can reconstruct the contours of the gravitational lenses. The gradient of the contours shown in  
 624 Figure 2.3 then indicates how dense the matter is and where it is.

625 The x-ray emission can then be observed from the clusters. Since these galaxies are mostly gas  
 626 and are merging, then the gas should be getting hotter. If they are merging, the x-ray emissions  
 627 should be the strongest where the gas is mostly moving through each other. Hence, X-ray emission  
 628 maps out where the gas is in the merging galaxy cluster.

629 The lensing and x-ray observations were done on the Bullet cluster featured on Figure 2.3.  
 630 The x-ray emissions do not align with the gravitational contours from lensing. The incongruence  
 631 in mass density and baryon density suggests that there is a lot of matter somewhere that does  
 632 not interact with light. Moreover, this dark matter cannot be baryonic [9]. The Bullet Cluster  
 633 measurement did not really tell us what DM is exactly, but it did give the clue that DM also does  
 634 not interact with itself very strongly. If DM did interact strongly with itself, then it would have been  
 635 more aligned with the x-ray emission [9]. There have been follow-up studies of galaxy clusters with  
 636 similar results. The Bullet Cluster and others like it provide a persuasive case against something  
 637 possibly amiss in our gravitational theories.

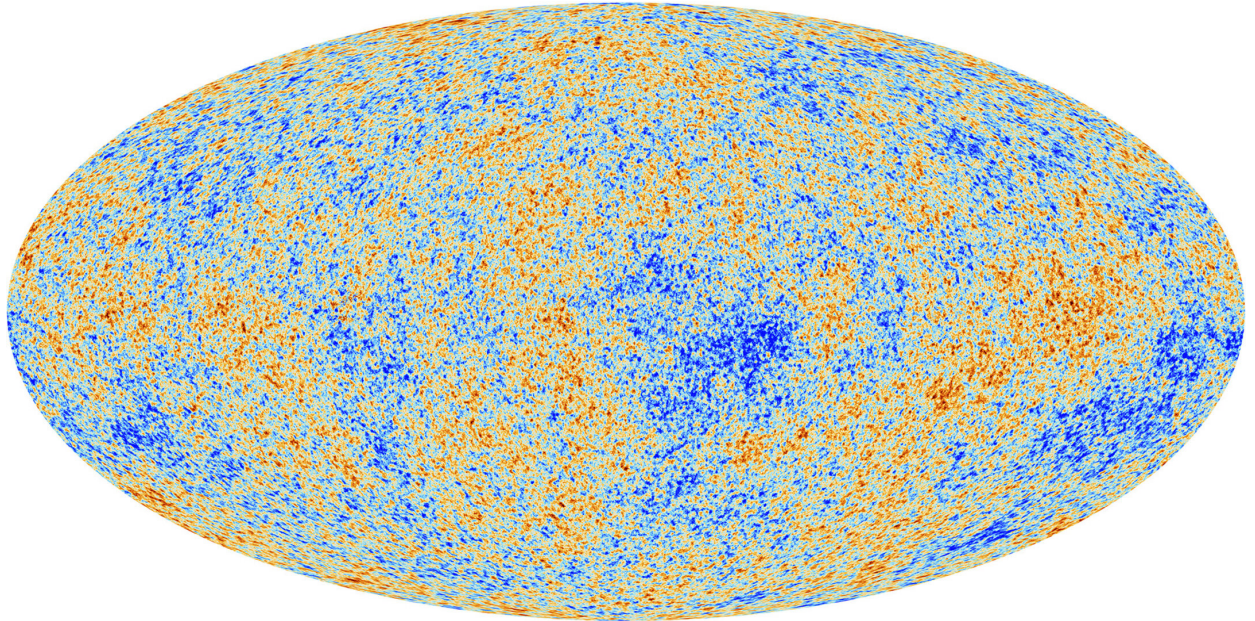


Figure 2.4 Plank CMB sky. Sky map features small variations in temperature in primordial light. These anisotropies are used to make inferences about the universe's energy budget and developmental history. [10]

638     **2.3.3 Evidence for Dark Matter: Cosmic Microwave Background**

639       The Cosmic Microwave Background (CMB) is the primordial light from the early universe  
640       when Hydrogen atoms formed from the free electron and proton soup in the early universe. The  
641       CMB is the earliest light we can observe; released when the universe was about 380,000 years old.  
642       Then we look at how the simulated universes look like compared to what we see. Figure 2.4 is the  
643       most recent CMB image from the Plank satellite after subtracting the average value and masking the  
644       galactic plane [10]. Redder regions indicate a slightly hotter region in the CMB, and blue indicates  
645       colder. The intensity variations are on the order of 1 in 1000 with respect to the average value.

646       The Cosmic Microwave Background shows that the universe had DM in it from an incredibly  
647       early stage. To measure the DM, Dark Energy, and matter fractions of the universe from the CMB,  
648       the image is analyzed into a power spectrum, which shows the amplitude of the fluctuations as  
649       a function of spherical multipole moments.  $\Lambda$ CDM provides the best fit to the power spectra of  
650       the CMB as shown in Figure 2.5. The CMB power spectrum is quite sensitive to the fraction  
651       of each energy contribution in the early universe. Low  $l$  modes are dominated by variations  
652       in gravitational potential. Intermediate  $l$  emerge from oscillations in photon-baryon fluid from

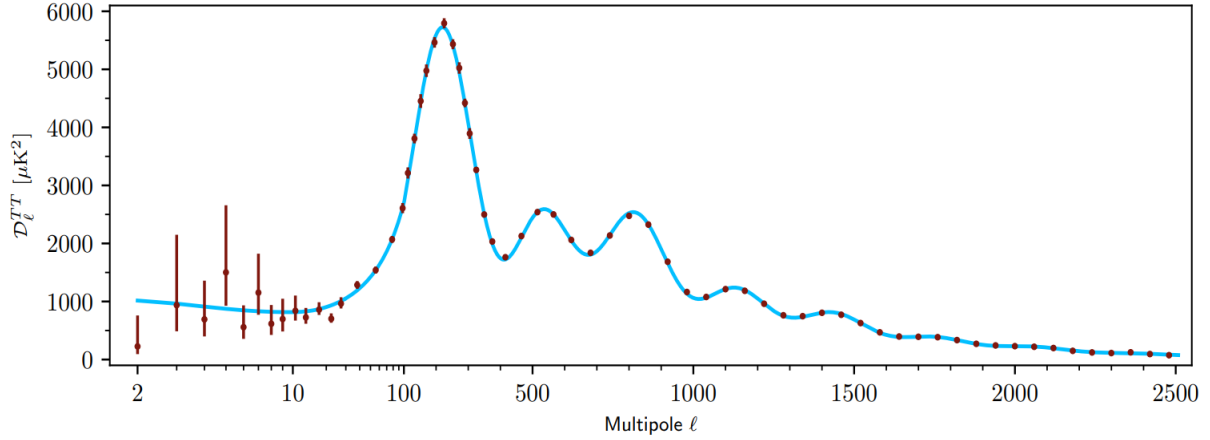


Figure 2.5 Observed Cosmic Microwave Background power spectrum as a function of multipole moment from Plank [10]. Blue line is best fit model from  $\Lambda$ CDM. Red points and lines are data and error, respectively.

653 competing baryon pressures and gravity. High  $l$  is a damped region from the diffusion of photons  
 654 during electron-proton recombination. [1]

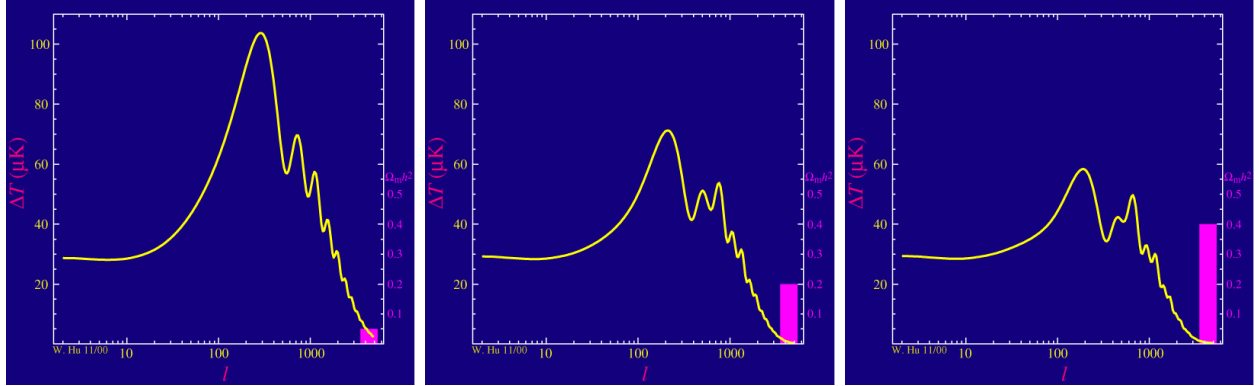


Figure 2.6 Predicted power spectra of CMB for different  $\Omega_m h^2$  values for fixed baryon density from [11]. (left) Low  $\Omega_m h^2$  increases the prominence of first and second peaks. (middle)  $\Omega_m h^2$  is most similar to the observed power spectrum. The second and third peaks are similar in height. (right)  $\Omega_m h^2$  is large which suppresses the first peak and raises the prominence of the third peak.

655 The harmonics would look quite different for a universe with less DM. Figure 2.6 demonstrates  
 656 the effect  $\Omega_m h^2$  has on the expected power spectrum for fixed baryon matter density. [11] Sweeping  
 657  $\Omega_m h^2$  in this way clearly shows the effect dark matter has on the CMB power spectrum. The  
 658 observations fit well with the  $\Lambda$ CDM model, and the derived fractions are as follows. The matter  
 659 fraction:  $\Omega_m = 0.3153$ ; and the baryon fraction:  $\Omega_b = 0.04936$  [10]. Plank's observations also  
 660 provide a measure of the Hubble constant,  $H_0$ .  $H_0$  especially has seen a growing tension in the

661 past decade that continues to deepened with observations from instruments like the James Webb  
662 Telescope [12, 13]. As Hubble tensions deepen, we may find that perhaps  $\Lambda$ **CDM**, despite its  
663 successes, is missing some critical physics.

664 Overall, the Newtonian motion of stars in galaxies, weak lensing from galactic clusters, and  
665 power spectra from primordial light form a compelling body of research in favor of dark matter.  
666 It takes another leap of theory and experimentation to make observations of DM that are non-  
667 gravitational in nature. In Section 2.3, the evidence for DM implies strongly that the DM is matter  
668 and not a lost parameter in the gravitational fields between massive objects. Finally, if we take one  
669 axiom: that this matter has quantum behavior, such as being described by some Bohr wavelength  
670 and abiding by some fermion or boson statistics; then we arrive at particle dark matter. One particle  
671 DM hypothesis is the Weakly Interacting Massive Particle (WIMP). This DM candidate theory is  
672 discussed further in the next section and is the focus of this thesis.

673 **2.4 Searching for Dark Matter: Particle DM**

674 Section 2.4 shows the Standard Model of particle physics and is currently the most accurate  
675 model for the dynamics of fundamental particles like electrons and photons. The current status  
676 of the SM does not have a viable DM candidate. When looking at the standard model, we can  
677 immediately exclude any charged particle because charged particles interact strongly with light.  
678 Specifically, this will rule out the following charged, fundamental particles:  $e, \mu, \tau, W, u, d, s, c, t, b$   
679 and their corresponding antiparticles. Recalling from Section 2.2 that DM must be long-lived and  
680 stable over the age of the universe which excludes all SM particles with decay half-lives at or shorter  
681 than the age of the universe. The lifetime constraint additionally eliminates the  $Z$  and  $H$  bosons.  
682 Finally, the candidate DM needs to be somewhat massive. Recall from Section 2.2 that DM is cold  
683 or not relativistic through the universe. This eliminates the remaining SM particles:  $\nu_{e,\mu,\tau}, g, \gamma$  as  
684 DM candidates. Because there are no DM candidates within the SM, the DM problem strongly  
685 hints to physics beyond the SM (BSM).

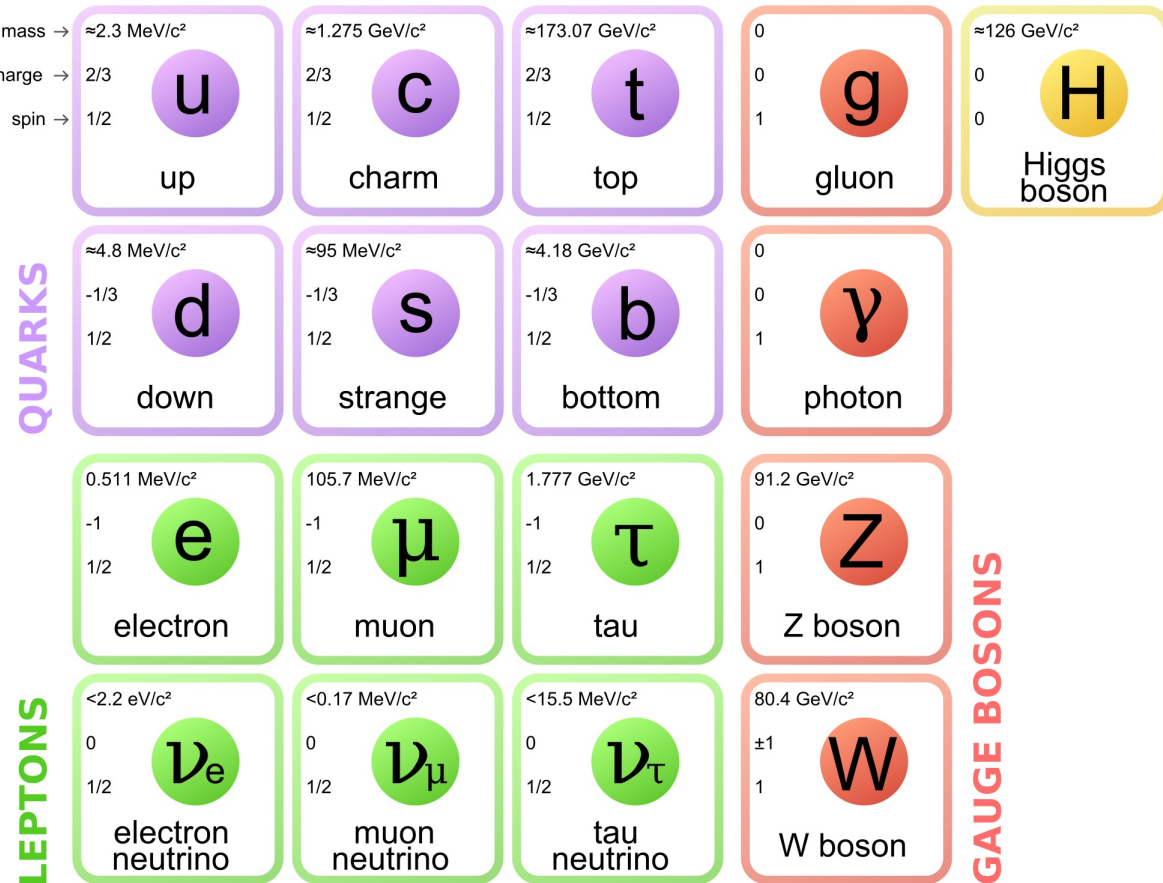


Figure 2.7 The Standard Model (SM) of particle physics. Figure taken from <http://www.quantumdiaries.org/2014/03/14/the-standard-model-a-beautiful-but-flawed-theory/>

### 686 2.4.1 Shake it, Break it, Make it

687 When considering DM that couples in some way with the SM, the interactions are roughly  
 688 demonstrated by interaction demonstrated in Figure 2.8. The figure is a simplified Feynman  
 689 diagram where the arrow of time represents the interaction modes of: **Shake it, Break it, Make it**.

690 **Shake it** refers to the direct detection of dark matter. Direct detection interactions start with  
 691 a free DM particle and an SM particle. The DM and SM interact via elastic or inelastic collision  
 692 and recoil away from each other. The DM remains in the dark sector and imparts some momentum  
 693 onto the SM particle. The hope is that the momentum imparted onto the SM particle is sufficiently  
 694 high enough to pick up with extremely sensitive instruments. Because we cannot create the DM in  
 695 the lab, a direct detection experiment must wait until DM is incident on the detector. Most direct  
 696 detection experiments are therefore placed in low-background environments with inert detection

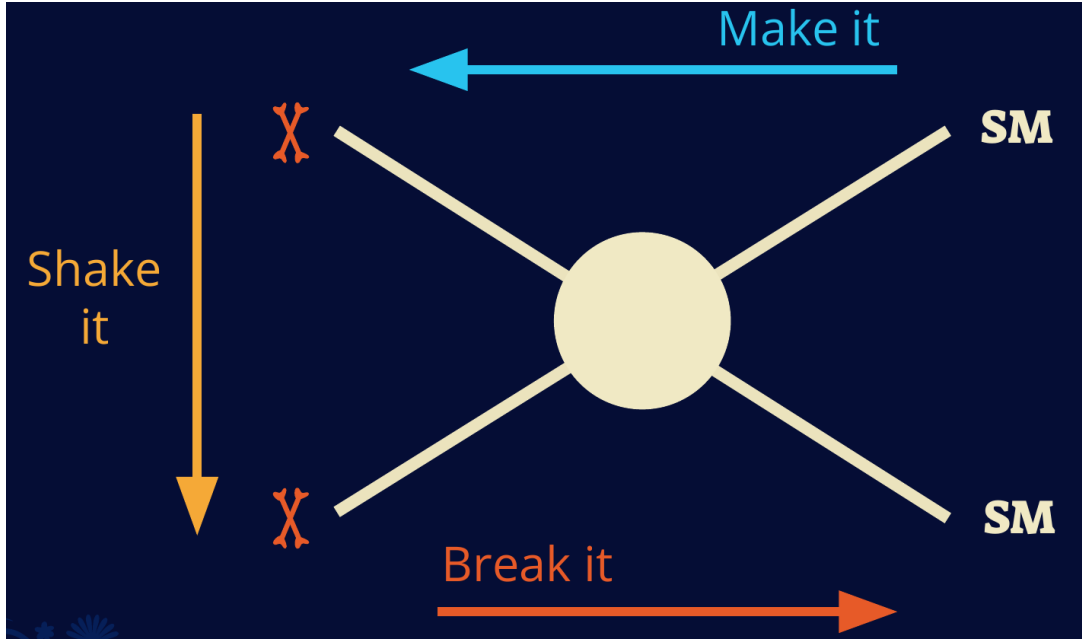


Figure 2.8 Simplified Feynman diagram demonstrating different ways DM can interact with SM particles. The 'X's refer to the DM particles whereas the SM refer to fundamental particles in the SM. The large circle in the center indicates the vertex of interaction and is purposely left vague. The colored arrows refer to different directions of time as well as their respective labels. The arrows indicate the initial and final state of the DM -SM interaction in time.

697 media like the noble gas Xenon. [14]

698       **Make it** refers to the production of DM from SM initial states. The experiment starts with  
 699 particles in the SM. These SM particles are accelerated to incredibly high energies and then collide  
 700 with each other. In the confluence of energy, DM hopefully emerges as a byproduct of the SM  
 701 annihilation. Often it is the collider experiments that are energetic enough to hypothetically produce  
 702 DM. These experiments include the world-wide collaborations ATLAS and CMS at CERN where  
 703 proton collide together at extreme energies. The DM searches, however, are complex. DM likely  
 704 does not interact with the detectors and lives long enough to escape the detection apparatus of  
 705 CERN's colliders. This means any DM production experiment searches for an excess of events  
 706 with missing momentum or energy in the events. An example event with missing transverse  
 707 momentum is shown in Figure 2.9. The missing momentum with no particle tracks implies a  
 708 neutral particle carried the energy out of the detector. However, there are other neutral particles  
 709 in the SM, like neutrons or neutrinos, so any analysis has to account for SM signatures of missing

710 momentum. [15]

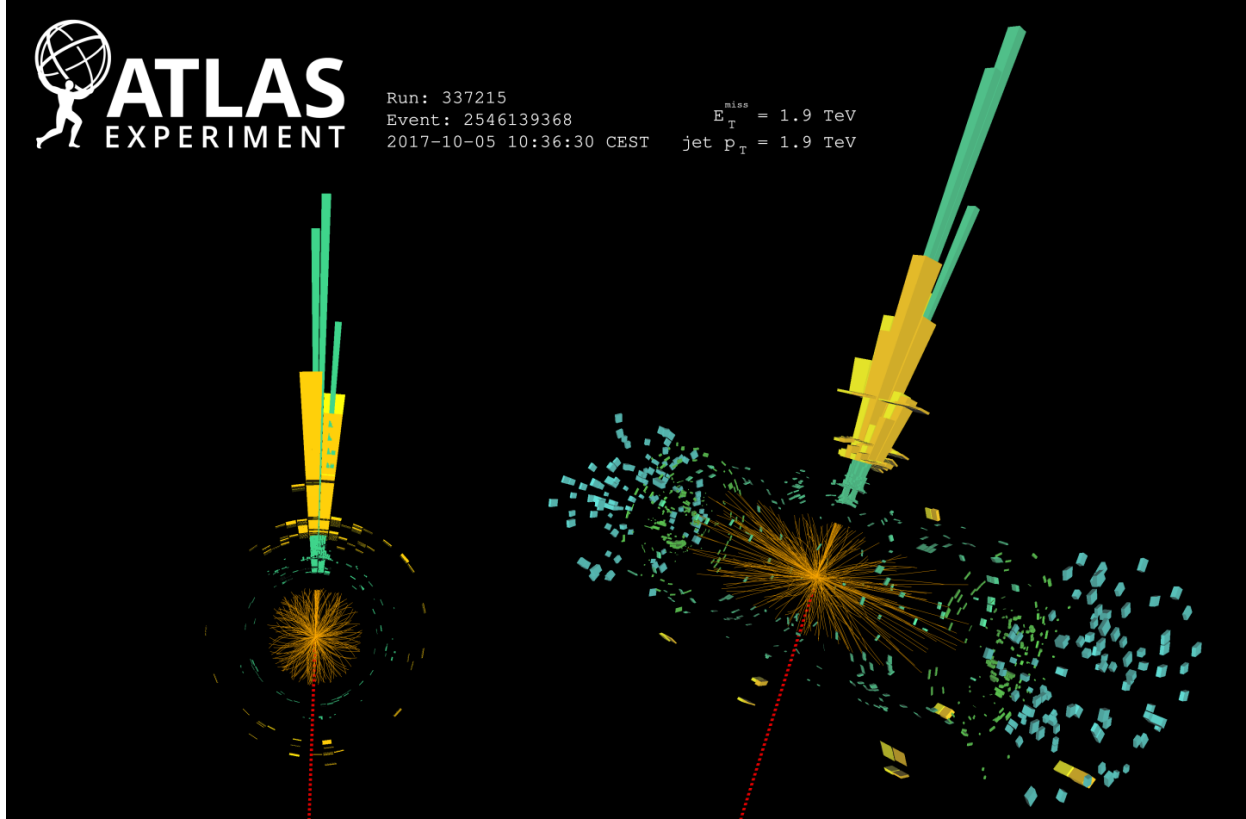


Figure 2.9 A single jet event in ATLAS detector from 2017 [16]. Jet momentum was observed to be 1.9 TeV. Missing transverse momentum was observed to be 1.9 TeV compared to the initial transverse momentum of the event was 0. Implied MET is traced by a red dashed line in event display.

711 **2.4.2 Break it: Standard Model Signatures of Dark Matter through Indirect Searches**

712 **Break it** refers to the creation of SM particles from the dark sector, and it is the primary focus  
713 of this thesis. The interaction begins with DM or in the dark sector. The hypothesis is that this  
714 DM will either annihilate with itself or decay and produce an SM byproduct. This method is  
715 often referred to as the Indirect Detection of DM because we have no lab to directly control or  
716 manipulate the DM. Therefore, most indirect DM searches are performed using observations of  
717 known DM densities among the astrophysical sources. The strength is that we have the whole of the  
718 universe and its 13.6-billion-year lifespan to use as a detector and particle accelerator. Additionally,  
719 locations of dark matter are well cataloged since it was astrophysical observations that presented

720 the problem of DM in the first place.

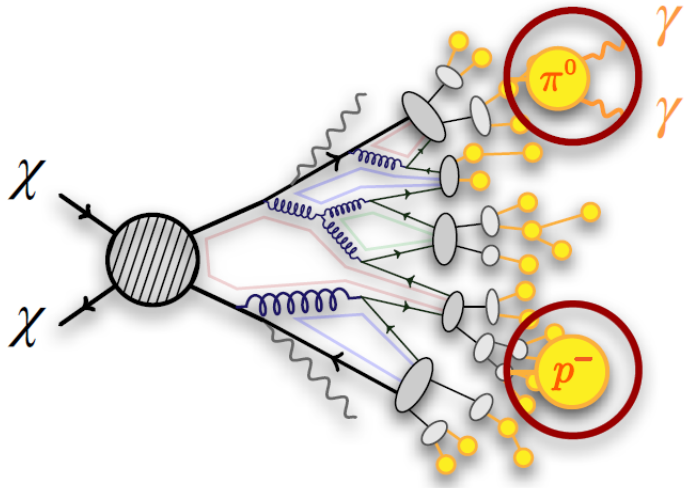


Figure 2.10 More detailed pseudo-Feynman diagram of particle cascade from dark matter annihilation into 2 quarks. The quarks hadronize and down to stable particles like  $\gamma$  or the anti-proton ( $p^-$ ). Diagram pulled from ICRC 2021 presentation on DM annihilation search [17].

721 However, anything can happen in the universe. There are many difficult to deconvolve back-  
722 grounds when searching for DM. One prominent example is the galactic center. We know the  
723 galactic center has a large DM content because of stellar kinematics in our Milky Way and DM halo  
724 simulations. Yet, any signal from the galactic center is challenging to parse apart from the extreme  
725 environment of our supermassive black hole, unresolved sources, and diffuse emission from the  
726 interstellar medium [18]. Despite the challenges, any DM model that yields evidence in the other  
727 two observation methods, **Shake it or Make it** must be corroborated with indirect observations of  
728 the known DM sources. Without corroborating evidence, DM observation in the lab is hard-pressed  
729 to demonstrate that it is the model contributing to the DM seen at the universal scale.

730 In the case of WIMP DM, signals are described in terms of primary SM particles produced  
731 from DM decay or annihilation. The SM initial state particles are then simulated down to stable  
732 final states such as the  $\gamma$ ,  $\nu$ ,  $p$ , or  $e$  which can traverse galactic lengths to reach Earth.

733 Figure 2.10 shows the quagmire of SM particles that emerges from SM initial states that are not  
734 stable [17]. There are many SM particles with varying energies that can be produced in such an

735 interaction. For any arbitrary DM source and stable SM particle, the SM flux from DM annihilating  
 736 to a neutral particle in the SM,  $\phi$ , from a region in the sky is described by the following.

$$\frac{d\Phi_\gamma}{dE_\gamma} = \frac{\langle\sigma v\rangle}{8\pi m_\chi^2} \frac{dN_\gamma}{dE_\gamma} \times \int_{\text{source}} d\Omega \int_{l.o.s} \rho_\chi^2 dl(r, \theta') \quad (2.4)$$

737 In Equation (5.1),  $\langle\sigma v\rangle$  is the velocity-weighted annihilation cross-section of DM to the SM.  $m_\chi$   
 738 refers to the mass of DM, noted with Greek letter  $\chi$ .  $\frac{dN_\phi}{dE_\phi}$  is the N particle flux weighted by the  
 739 particle energy. An example is provided in Figure 2.11 for the  $\gamma$  final state. The integrated terms  
 740 are performed over the solid angle,  $d\Omega$ , and line of sight, l.o.s.  $\rho$  is the density of DM for a  
 741 location  $(r, \theta')$  in the sky. The terms left of the '×' are often referred to as the particle physics  
 742 component. The terms on the right are referred to as the astrophysical component. For decaying  
 743 DM, the equation changes to...

$$\frac{d\Phi_\phi}{dE_\phi} = \frac{1}{4\pi\tau m_\chi} \frac{dN_\phi}{dE_\phi} \times \int_{\text{source}} d\Omega \int_{l.o.s} \rho_\chi dl(r, \theta') \quad (2.5)$$

744 In Equation (2.5),  $\tau$  is the decay lifetime of the DM. Just as in Equation (5.1), the left and right  
 745 terms are the particle physics and the astrophysical components respectively. The integrated  
 746 astrophysical component of Equation (5.1) is often called the J-Factor. Whereas the integrated  
 747 astrophysical component of Equation (2.5) is often called the D-Factor.

748 Exact DM  $\text{DM} \rightarrow \text{SM SM}$  branching ratios are not known, so it is usually assumed to go 100%  
 749 into an SM particle/anti-particle. Additionally, when a DM annihilation or decay produces one of  
 750 the neutral, long-lived SM particles ( $\nu$  or  $\gamma$ ), the particle is traced back to a DM source. For DM  
 751 above GeV energies, there are very few SM processes that can produce particles with such a high  
 752 energy. Seeing such a signal would almost certainly be an indication of the presence of dark matter.  
 753 Fortunately, the universe provides us with the largest volume and lifetime ever for a particle physics  
 754 experiment.

## 755 2.5 Sources for Indirect Dark Matter Searches

756 The first detection of DM relied on optical observations. Since then, we have developed new  
 757 techniques to find DM dense regions. As described in Section 2.3.1, many DM dense regions were  
 758 through observing galactic rotation curves. Our Milky Way galaxy is among DM dense regions

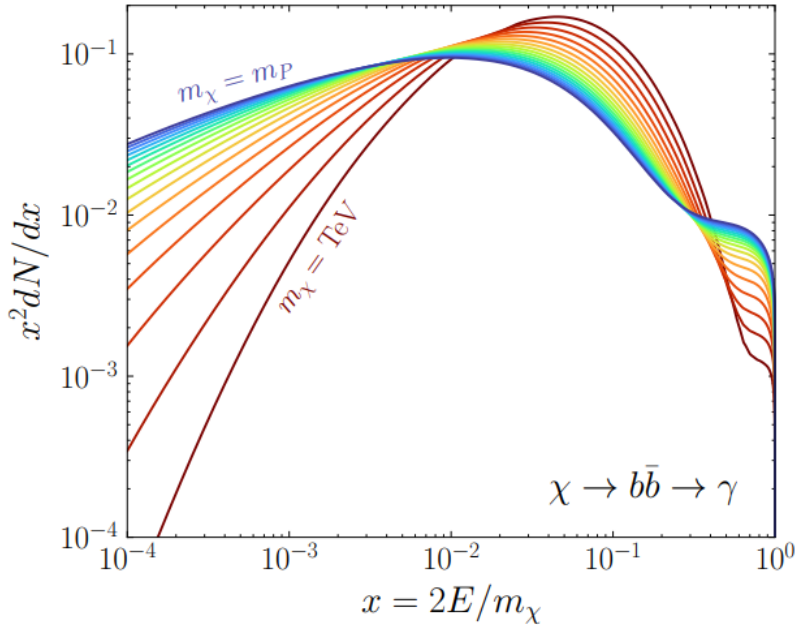


Figure 2.11 Dark Matter (DM) decay spectrum for  $b\bar{b}$  initial state and  $\gamma$  final state. Redder spectra are for larger DM masses. Bluer spectra are light DM masses.  $x$  is a unitless factor defined as the ratio of the mass of DM,  $m_\chi$ , and the final state particle energy  $E_\gamma$ . Figure from [19].

discovered, and it is the largest nearby DM dense region to look at. Additionally, the DM halo surrounding the Milky Way is clumpy [18]. There are regions in the DM halo of the Milky Way that have more DM than others that have captured gas over time. These sub-halos were dense enough to collapse gas and form stars. These apparent sub galaxies are known as dwarf spheroidal galaxies and are the main sources studied in this thesis. Each source type comes with different trade-offs. Galactic Center studies will be very sensitive to the assumed distribution of DM. The central DM density can vary substantially as demonstrated in Figure 2.12. At distances close to the center of the galaxy, or small  $r$ , the differences in DM densities can be 3-4 orders of magnitude. Searches toward the galactic center will therefore be quite sensitive to the assumed DM distribution.

Searches toward Dwarf Spheroidal Galaxies (dSph's) suffer from uncertainties in the DM density less than the galactic center studies. This is mostly from their diminutive size being smaller than the angular resolution of most  $\gamma$ -ray observatories [18]. The DM content dSph's are typically determined with the Virial theorem, Equation (2.1), and are usually majority DM [18] in mass. DSph's tend to be ideal sources to look at for DM searches. Their environments are quiet with little

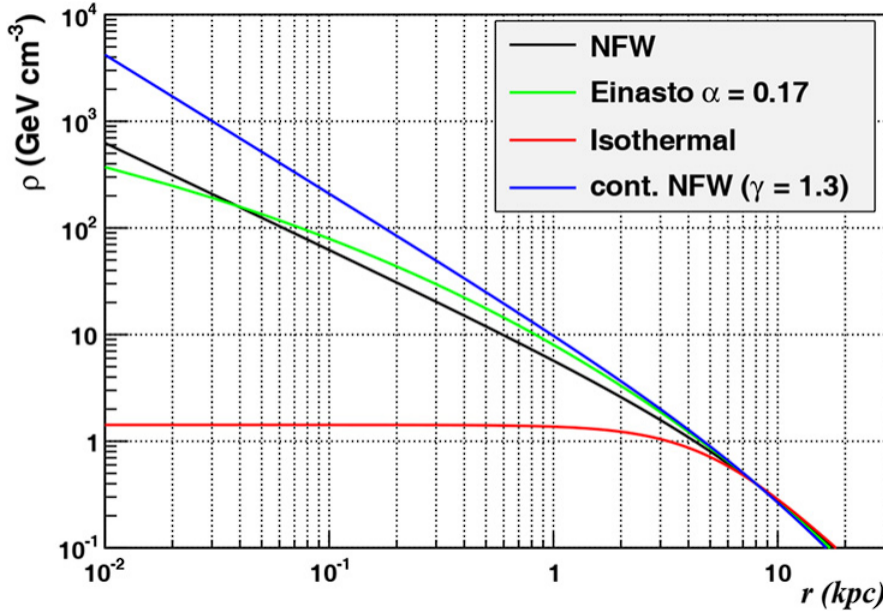


Figure 2.12 Different dark matter density profiles compared. Some models produce exceptionally large densities at small  $r$  [20].

773 astrophysical background. Unlike the galactic center, the most active components of dSph's are the  
 774 stars within them versus a violent accretion disc around a black hole. All this together means that  
 775 dSph's are among the best sources to look at for indirect DM searches. dSph's are the targets of  
 776 focus for this thesis.

## 777 2.6 Multi-Messenger Dark Matter

778 Astrophysics entered a new phase in the past few decades that leverages our increasing sensitivity  
 779 to SM channels and general relativity (GR). Up until the 21st century, astrophysical observations  
 780 were performed with photons ( $\gamma$ ) only. Astrophysics with this 'messenger' is fairly mature now.  
 781 Novel observations of the universe have since only adjusted the sensitivity of the wavelength of  
 782 light that is observed except at MeV energies. Gems like the CMB [10], and more have ultimately  
 783 been observations of different wavelengths of light. Multi-messenger astrophysics proposes using  
 784 other SM particles such the  $p^{+-}$ , or  $\nu$  or gravitation waves predicted by general relativity.

785 The experiment LIGO had a revolutionary discovery in 2016 with the first detection of a binary  
 786 black hole merger [21]. This opened the collective imagination to observing the universe through  
 787 gravitational waves. There has also been a surge of interest in the neutrino ( $\nu$ ) sector. IceCube

788 demonstrated that we are sensitive to neutrinos in regions that correlate with significant photon  
 789 emission like the galactic plane [22]. Neutrinos, like gravitational waves and light, travel mostly  
 790 unimpeded from their source to our observatories. This makes pointing to the originating source  
 791 of these messengers much easier than it is for cosmic rays which are deflected from their source by  
 792 magnetic fields.

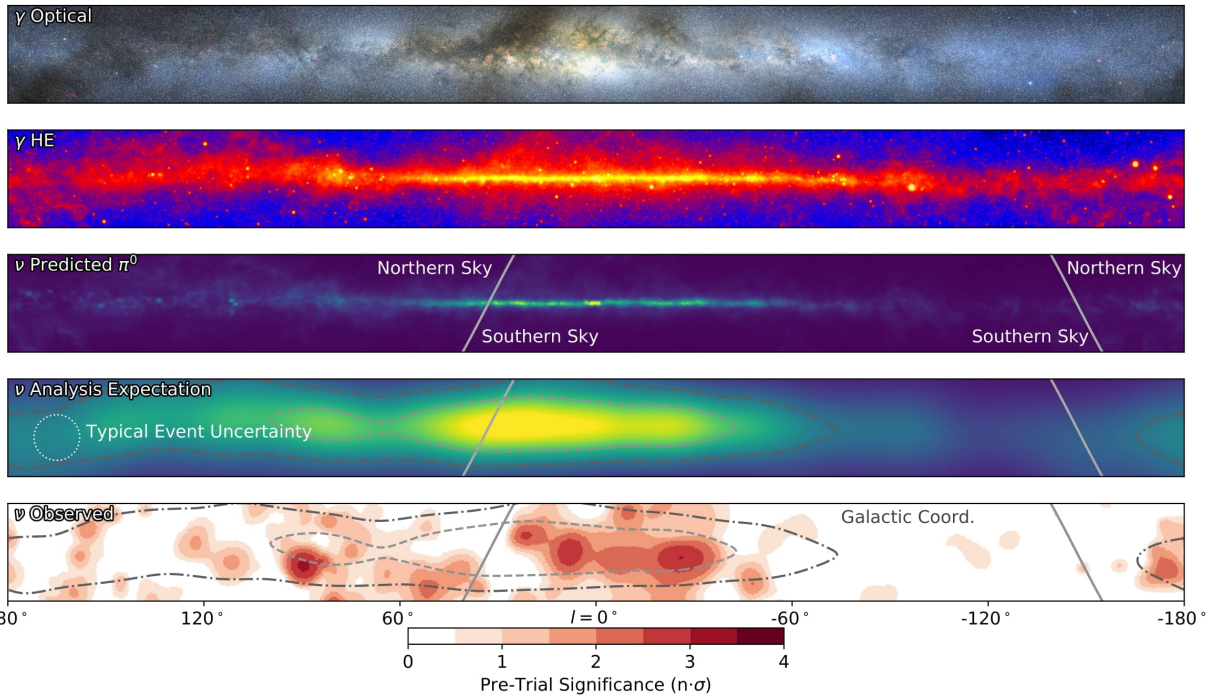


Figure 2.13 The Milky Way Galaxy in photons ( $\gamma$ ) and neutrinos ( $\nu$ ) [22]. The Galactic center is at  $l=0^\circ$  and is the brightest region in all panels. (top) An Optical color image of the Milky Way galaxy seen from Earth. Clouds of gas and dust obscure some light from stars. (2nd down) Integrated flux of  $\gamma$ -rays observed by the Fermi-LAT telescope [23]. (middle) Expected neutrino emission that corresponds with Fermi-LAT observations. (2nd up) Expected neutrino emission profile after considering detector systematics of IceCube. (bottom) Observed neutrino emission from region of the galactic plane. Substantial neutrino emission was detected.

793 The IceCube collaboration recently published a groundbreaking result of the Milky Way in  
 794 neutrinos. The recent result from IceCube, shown in Figure 2.13, proves that we can make  
 795 observations under different messenger regimes. The top two panels show the appearance of the  
 796 galactic plane to different wavelengths of light. Some sources are more apparent in some panels,  
 797 while others are not. This new channel is powerful because neutrinos are readily able to penetrate  
 798 through gas and dust in the Milky Way. This new image also refines our understanding of how high

799 energy particles are produced. For example, the fit to IceCube data prefers neutrino production  
 800 from the decay of  $\pi^0$  [22].

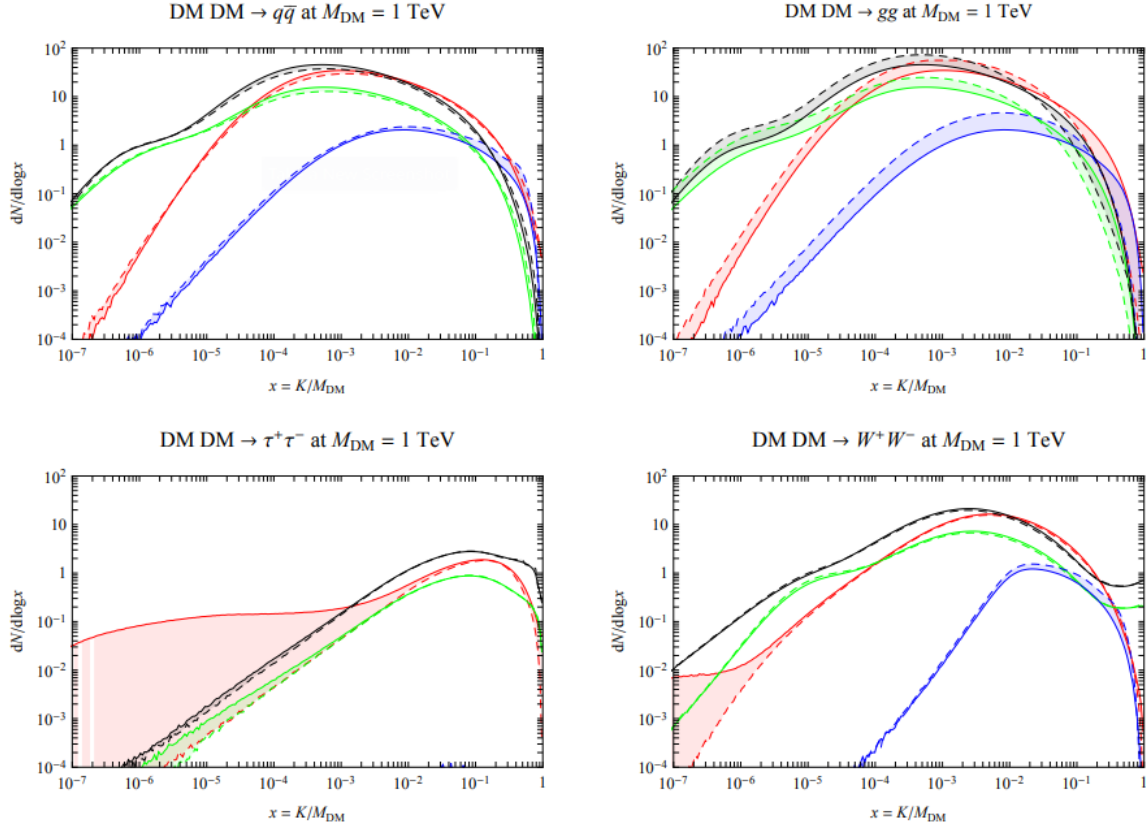


Figure 2.14 Dark Matter annihilation spectra for different final state particle and standard model annihilation channels [24]. Photons (red),  $e^\pm$  (green),  $\bar{p}$  (blue),  $\nu$  (black).

801 Exposing our observations to more cosmic messengers greatly increases our sensitivity to  
 802 rare processes. In the case of DM, Figure 2.14, there are many SM particles produced in DM  
 803 annihilation. Among the final state fluxes are gammas and neutrinos. Charged particles are also  
 804 produced however they would not likely make it to Earth since they will be deflected by magnetic  
 805 fields between the source and Earth. This means observatories that can see the neutral messengers  
 806 are especially good for DM searches and for combining data for a multi-messenger DM search.

## CHAPTER 3

807

### HIGH ALTITUDE WATER CHERENKOV (HAWC) OBSERVATORY

808



Figure 3.1 Photo of the HAWC detector that I took on May 17, 2023. Main array is centered in the photo and comprised of the larger tanks. Outriggers are the smaller tanks around the main array.

809

The High Altitude Water Cherenkov (HAWC) Observatory is a specialized instrument designed

810

for the observation of high energy gamma-rays and cosmic rays [25]. Located on the Sierra

811

Negra volcano in Mexico, HAWC observes gamma rays and cosmic rays in the energy range of

812

approximately 100 GeV to 100's of TeV. HAWC is strategically situated to maximize observational

813

efficiency due to its high altitude. At an elevation of 4,100 meters, it monitors about two-thirds of

814

the sky every day with an uptime above 90%. This capability is essential for studying high-energy

815

astrophysical phenomena.

816

HAWC consists of 300 water Cherenkov detectors (WCDs) spread over  $22,000 \text{ m}^2$ . Each main

817

array detector is filled with purified water and equipped with four, upward-facing photomultiplier

818

tubes (PMTs). See Fig. 3.3 for schematic of WCDs. These PMTs detect Cherenkov radiation from

819

charged particles passing through the tanks. These charged particles are generated when a high

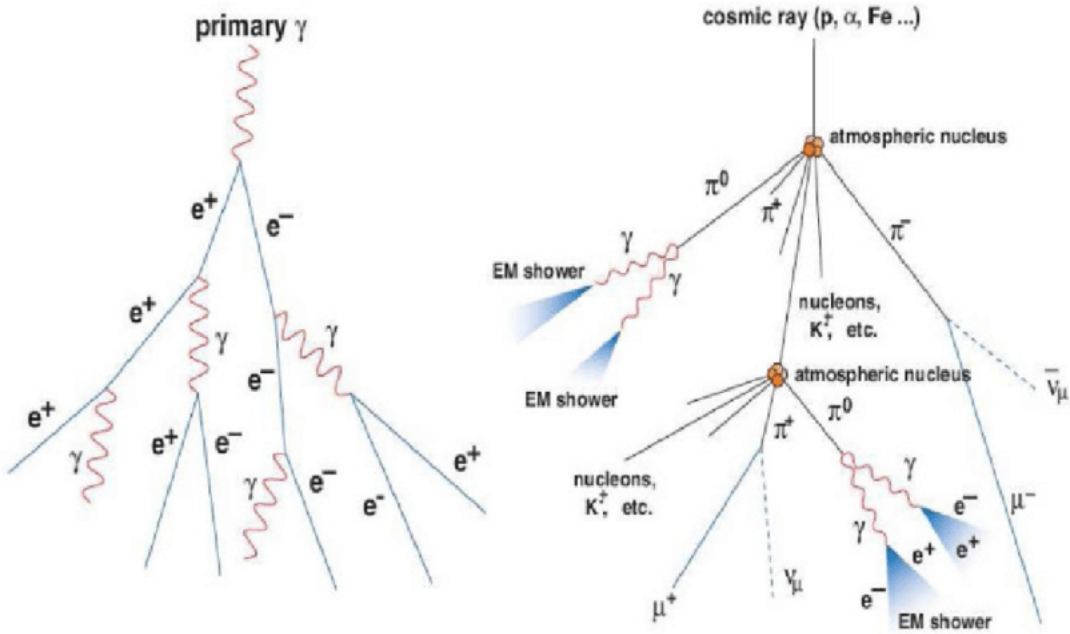


Figure 3.2 A particle physics illustration of high energy particle showers. Left shower is an electromagnetic shower from a high energy gamma-ray. Most particles in the shower will be a combination of photons and charged leptons, in this case electrons ( $e$ ). Right figure shows a cosmic ray particle shower. The cosmic ray will produce many more types of particles including pions ( $\pi$ ), neutrinos, and charged leptons. Figured pulled from [26].

820 energy gamma or cosmic ray collides with gas in the atmosphere to create a charged particle shower,  
 821 see Fig. 3.2. The observatory includes a separate tank configuration which are referred to as the  
 822 outriggers. They are a secondary array of 345 smaller WCD's. Surrounding the main array, each  
 823 outrigger tank measures 1.55 meters in diameter and height and contain a single upward-facing  
 824 eight-inch PMT. This add-on increases the instrumented footprint fourfold. The outriggers are  
 825 meant to improve the reconstruction of showers extending beyond the main array, especially for  
 826 events above 10 TeV. However, at the time of writing this thesis, the outriggers have not been fully  
 827 integrated into HAWC's reconstruction software.

### 828 3.1.1 Construction and Hardware

829 Each main array WCD, see Fig. 3.3, is a cylindrical tank with dimensions of 7.3 m in diameter  
 830 and 5.4 m in height and filled with 180,000 L of water [25]. The metal shell of these tanks is made  
 831 from bolted together, corrugated, galvanized steel panels. The tanks are placed into 0.6 m deep

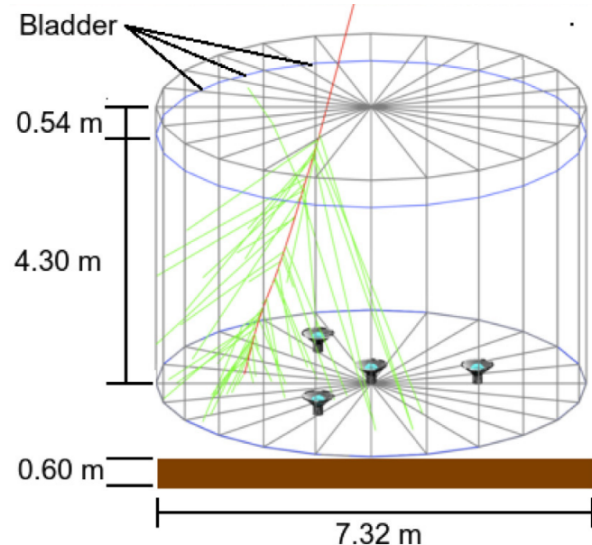


Figure 3.3 The WCDs. Left image features several WCDs looking from within the main array of HAWC. Right image shows a schematic of a WCD pulled from [25].

832 trenches filled with rammed earth to secure it against seismic activity [27]. The interior of each  
 833 tank is lined with a black, low-density polyethylene bladder, designed to be impermeable to external  
 834 light and to prevent reflection of Cherenkov light within the tank. This bladder is approximately 0.4  
 835 mm thick and composed of two layers of three-substrate film. To further minimize light penetration,  
 836 a black agricultural foil covers the bladder. The ground and walls inside the tank are protected  
 837 with felt and sand to safeguard against punctures. The tanks are filled 4.5 m deep of purified water,  
 838 achieving a photon attenuation length for Cherenkov photons that exceeds the tank's dimensions  
 839 [27]. This purification level ensures the optimal detection environment for the photons generated  
 840 by traversing charged particles.

841 At the base of each tank, four photomultiplier tubes (PMTs) are installed to detect the Cherenkov  
 842 radiation emitted by charged particles in water. Three 8-inch diameter PMTs surround a larger  
 843 10 inch PMT from Hamamatsu [28]. The variation in PMT response is carefully accounted for  
 844 in event reconstruction algorithms. Signals from the PMTs traverse 610 ft cables to the counting  
 845 house, where they are processed by Front-End Boards (FEBs), see Figs. 3.4 and 3.5. These FEBs,  
 846 along with Time to Digital Converters (TDCs), digitize the signals and manage the high voltage  
 847 supply to the PMTs.

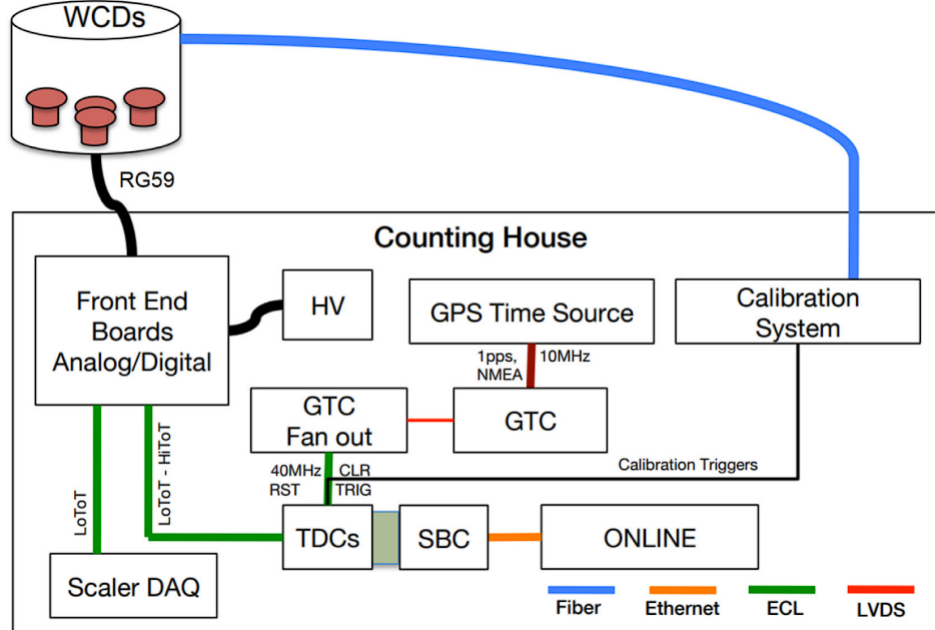


Figure 3.4 Overview of HAWC control and data electronics. The LoToT and HiToT threshold signals are discussed in Section 3.1.2. Figure from [27]

### 848 3.1.2 Data Acquisition and Signal Processing

849 The HAWC data acquisition (DAQ) and signal processing systems convert the physical detection  
 850 of particles into analyzable data. This process involves a series of steps from initial signal detection  
 851 by PMTs to digital conversion and preliminary analysis, see Figs. 3.5 and 3.6.

852 Once the signal from the PMTs arrive at the counting house, they enter the Front-End Boards  
 853 (FEBs). The FEBs are responsible for the initial processing of these signals, which includes  
 854 amplification and integration [30]. Each PMT signal is compared against preset LOW/HIGH  
 855 voltage thresholds in the FEBs, see Fig. 3.6, identifying signals that correspond to about 1/4 and  
 856 4 photoelectrons, respectively. This differentiation allows the system to gauge the strength of  
 857 the detected Cherenkov radiation. The processed signals are then digitized by Time to Digital  
 858 Converters (TDCs). These converters measure the time over threshold (ToT) for each signal, a  
 859 parameter that reflects both the duration and amplitude of the signal. This digitization facilitates  
 860 reconstruction of the original event for translating the physical interactions within the detectors into  
 861 data [27, 29, 30].

862 Synchronization across the HAWC observatory is maintained by a central GPS Timing and

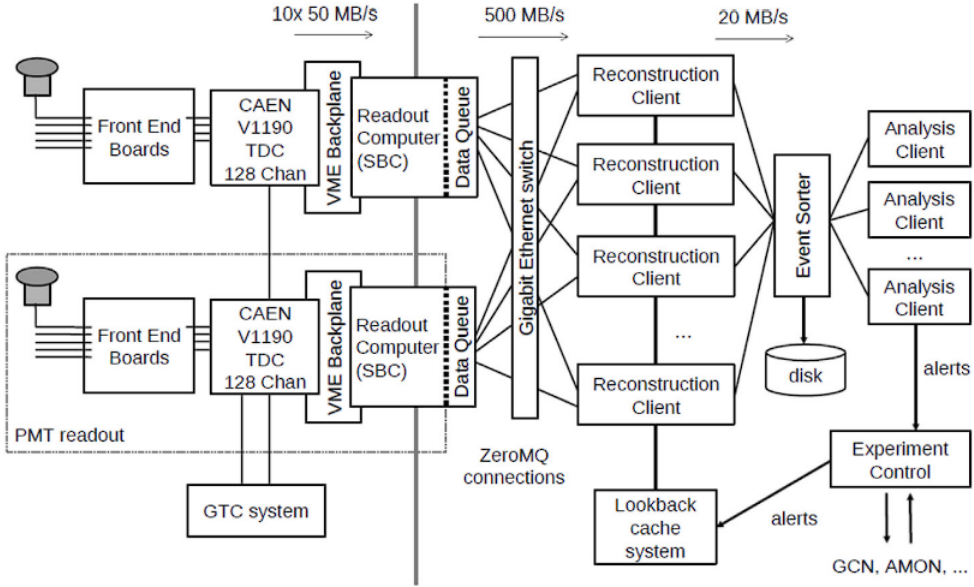


Figure 3.5 Schematic of data flow in HAWC data acquisition and online processing system. Pulled from [29].

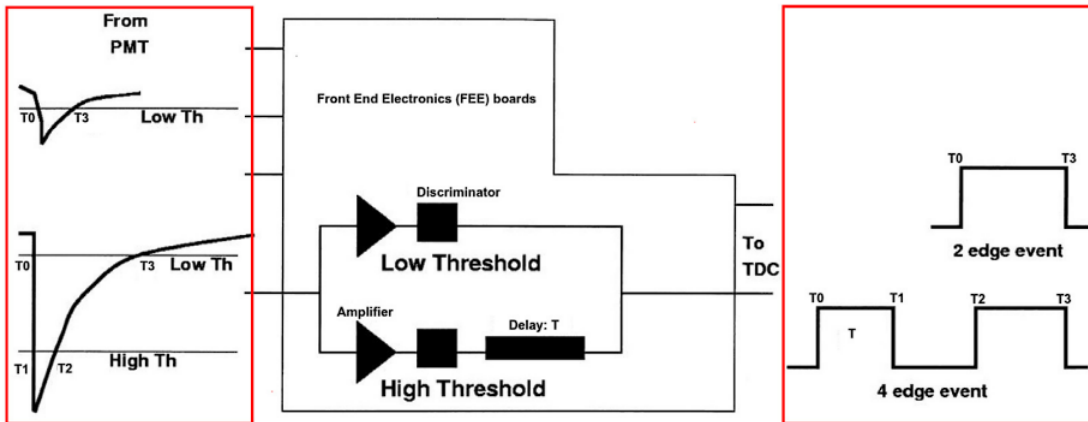


Figure 3.6 How HAWC FEB intially processes analog PMT signals. Signals are split through an amplifier and discriminator circuit. Each path is designated for either the HIGH or LOW threshold for the signal. The 2-edge event corresponds to LOW, while the 4 edge corresponds to HIGH.

863 Control (GTC) system, which achieves a timing resolution of 98 ps. This high-resolution timing  
864 is vital for accurately reconstructing the timing and location of air showers initiated by cosmic  
865 and gamma rays. The GTC system ensures that all components of the DAQ operate in unison to  
866 preserve the temporal integrity of the detected events [27, 31].

867 Once digitized, the data are transferred to an online event reconstruction system. This system  
868 runs the Reconstruction Client, which utilizes the raw PMT data to reconstruct the characteristics  
869 of the air showers, such as their direction and energy [29]. The capacity for real-time analysis  
870 allows HAWC to promptly respond to astrophysical phenomena like Gamma Ray Bursts (GRBs)  
871 and to participate in multi-messenger astronomy by following up on alerts from other observatories.  
872 This real-time processing system is designed to handle high data throughput, using ZeroMQ [32]  
873 for efficient data transfer between software components. Analysis Clients perform specific online  
874 analyses that require immediate data, including monitoring for GRBs, solar flare activity, and  
875 participation in global efforts to track gravitational waves and neutrinos [27].

876 The DAQ system is overseen by an Experiment Control system and crew that manage the  
877 operational aspects of data collection. This includes initiating and terminating data collection  
878 runs and monitoring the experiment for errors. In the event of a system crash, often caused by  
879 environmental factors such as lightning, the Experiment Control system is designed to automatically  
880 restart the experiment and minimize downtime [27, 29].

### 881 **3.2 Event Reconstruction**

882 Event reconstruction at the HAWC Observatory is a critical procedure that converts the raw data  
883 from the observatory’s WCDs into a coherent framework for understanding cosmic and gamma-  
884 ray events. This process includes several distinct steps. Core Fitting determines the geometric  
885 center of the air shower on the detector plane. Angle Reconstruction assesses the trajectory of the  
886 incoming particle, revealing its origin in the sky. Energy Estimation is performed using both  $f$ -hit  
887 and Neural Network (NN) methods to quantify the energy of the detected events. Gamma/Hadron  
888 discrimination differentiates between gamma-ray and hadronic cosmic ray initiated showers, a vital  
889 step for astrophysical interpretations. Each of these steps is integral to the observatory’s objective

890 of investigating the high-energy universe and enable the transformation of signals into detailed  
 891 insights about high energy cosmic phenomena.

892 **3.2.1 Core Fitting**

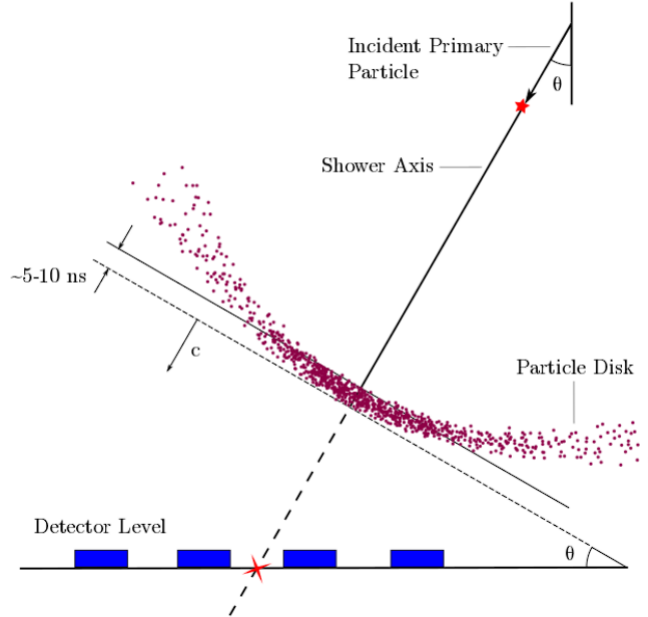


Figure 3.7 An air shower incident on WCDs. Secondary particles of an air shower travel in a cone centered on primary incident particle. Reconstruction of the initial angle is possible with arrival time of hits in PMTs inside WCDs. Figure from [33].

893 In the study of air showers, accurately determining the location of the air shower core on the  
 894 ground is crucial for reconstructing the direction of the originating primary particle. An illustration  
 895 of this can be seen in a HAWC event plot, Figs. 3.2 and 3.11, where the lateral charge distribution  
 896 across the array is displayed. The core is identified and marked with a red star, reconstructed using  
 897 a predetermined functional form, Eq. (3.1).

898 We model signal  $S_i$  from the  $i$ th PMT is given by the following equation:

$$S_i = S(A, \tilde{x}, \tilde{x}_i) = A \left( \frac{1}{2\pi\sigma^2} e^{-\frac{|\vec{x}_i - \vec{x}|^2}{2\sigma^2}} + \frac{N}{(0.5 + |\vec{x}_i - \vec{x}|/R_m)^3} \right) \quad (3.1)$$

899 In this model,  $\tilde{x}$  represents the core location and  $\tilde{x}_i$  is the position of the  $i$ th PMT.  $R_m$  stands for  
 900 the Molière radius, which is approximately 120 meters at the altitude of HAWC.  $\sigma$  is the standard  
 901 deviation of the Gaussian distribution.  $N$  is the normalization factor for the tail of the distribution.

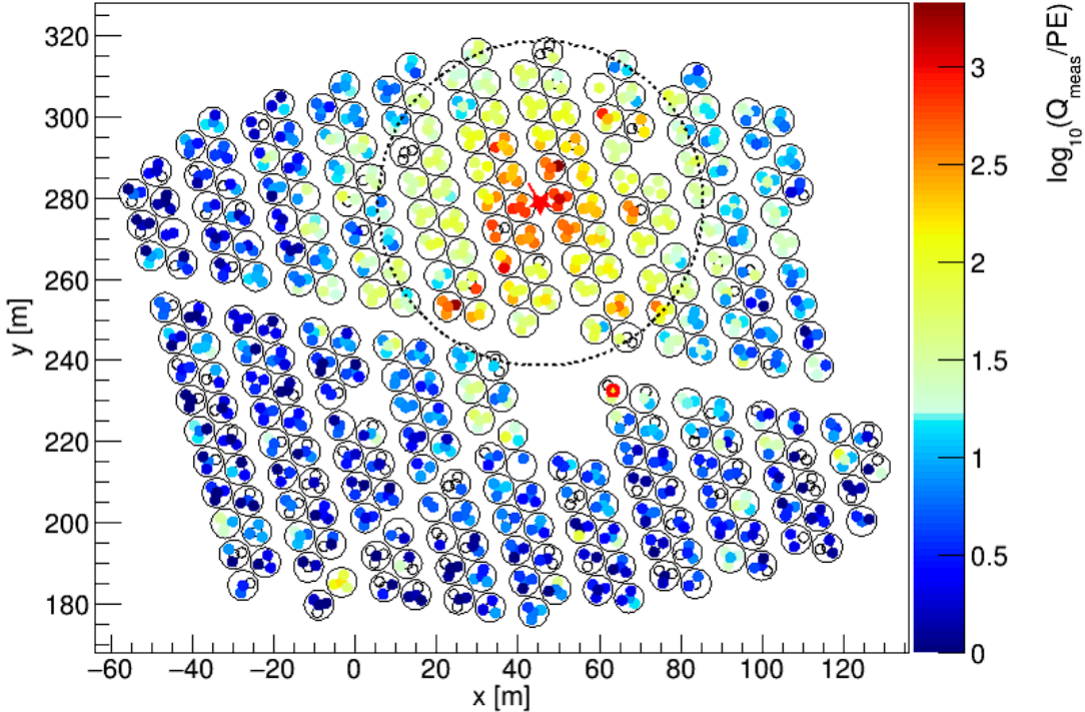


Figure 3.8 Charge deposition in each PMT for a reconstructed gamma-ray event. WCDs are outlined in black surrounding the 4 smaller circles that represent PMTs. The color scale indicates the charge deposition in each PMT. The best shower core fit from SFCF is noted with a red star in the center of the dashed circle [34].

902 The equation incorporates fixed values of  $\sigma = 10$  m and  $N = 5 \cdot 10^{-5}$ . This leaves the core location  
 903 and overall amplitude  $A$  as the free parameters to be determined during fitting.

904 The chosen functional form for the Super Fast Core Fit (SFCF) algorithm is a simplified version  
 905 of a modified Nishimura-Kamata-Greisen (NKG) function [35], selected for its computational  
 906 efficiency which is essential for rapid fitting of air shower cores. The SFCF form allows numerical  
 907 minimization to converge more quickly due to the function's simplicity, the analytical computation  
 908 of its derivatives, and the absence of a pole at the core location [34]. Figure 3.8 provides a  
 909 visualization of a recorded event, with the plot depicting the charge recorded by each PMT as a  
 910 function of the distance to the reconstructed shower core. Through the application of the SFCF,  
 911 core locations can be identified with a median error of approximately 2 m for large events and about  
 912 4 m for smaller ones, assuming the gamma-ray event core impacts directly upon the HAWC detector  
 913 array [34]. It is noted that as the core's distance from the main array increases, the precision in

914 locating the core diminishes [34], highlighting the importance of proximity in the accuracy of core  
915 reconstruction.

916 **3.2.2 Angle Reconstruction**

917 After establishing the core position, the next step is angle reconstruction. This process deter-  
918 mines the primary particle's trajectory. The angle of arrival is indicative of the originating gamma  
919 ray's direction. It correlates to the cosmic source of the gamma-ray. We deduce this angle using  
920 the timing of PMT hits [34].

921 The air shower's front is conically shaped, not flat. This shape arises from the travel patterns  
922 of secondary particles. An event example is illustrated in Fig. 3.7. Far from the core, secondary  
923 particles undergo multiple scattering. They also travel longer distances [36]. Particle sampling  
924 decreases with distance from the core. This decrease results in measurable delays in arrival times  
925 [36, 34]. Simulations provide a corrective measure for these effects. The correction is a function of  
926 shower parameters [34]. It adjusts both curvature and sampling. The distance from the shower core  
927 and the charge recorded by PMTs are crucial to this correction. A function based on simulation  
928 and Crab Nebula observations is used for this purpose [34]. This curvature correction allows us to  
929 fit the particle front as a plane wave.

930 Corrections lead to the  $\chi^2$  minimization step. This technique fits a plane to the timing data of  
931 the PMTs. It then calculates the shower's angle of arrival. The zenith and azimuth angles are the  
932 results of this fit [36]. The local angles are converted to celestial coordinates. These coordinates  
933 allow correlation with gamma-ray sources. Right ascension (RA) and declination (Dec) are used  
934 for this purpose. RA is akin to longitude, and Dec to latitude.

935 The reconstructed angle's resolution ranges from  $0.1^\circ$  to  $1^\circ$ . This range depends on the incoming  
936 particle's energy and zenith angle [36]. The analysis uses a curvature/sampling correction. This  
937 correction applies a quadratic function based on distance from the core [34]. The adjustment  
938 improves angular resolution. However, discrepancies between simulation and observation persist.  
939 These discrepancies introduce systematic errors into HAWC analyses [34].

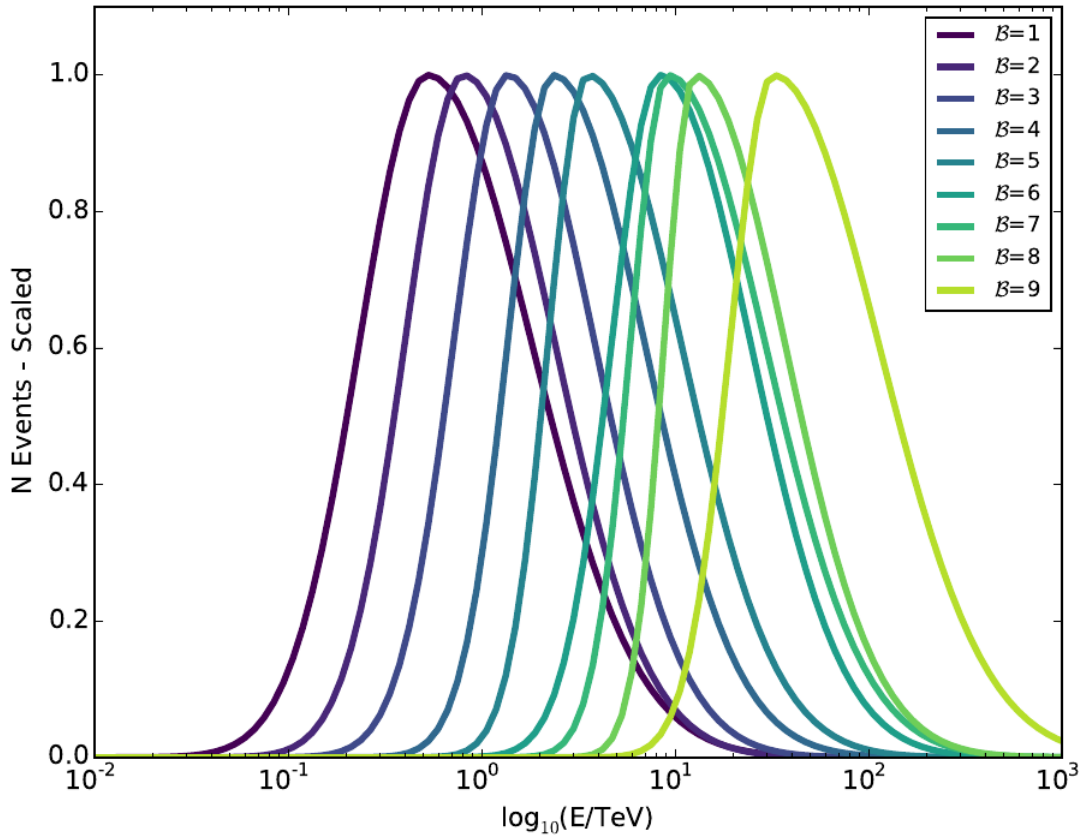


Figure 3.9 Simulated normalized energy distribution of each  $f_{\text{hit}}$  bin defined in Tab. 3.1. Monte Carlo simulation of gamma-rays with  $E^{-2.63}$  spectral shape and simulated source at  $20^\circ$  declination. Figure from [34].

Bin	Lower Edge %	Upper Edge %	$\Theta_{68}$ ( $^\circ$ )
1	6.7	10.5	1.05
2	10.5	16.2	0.69
3	16.2	24.7	0.50
4	24.7	35.6	0.39
5	35.6	48.5	0.30
6	48.5	61.8	0.28
7	61.8	74.0	0.22
8	74.0	84.0	0.20
9	84.0	100	0.17

Table 3.1 Definitions of  $f_{\text{hit}}$  energy estimator bins. Bins are defined by the fraction of available PMTs that are triggered during an air shower event. The angular resolution,  $\Theta_{68}$ , is the bin containing 68% of events [34].

940    **3.2.3  $f_{\text{hit}}$  Energy Estimation**

941    The HAWC Observatory quantifies the primary particle energy of air showers using a metric  
942    known as  $f_{\text{hit}}$ . This ratio compares the count of PMTs involved in the event reconstruction to the  
943    total number of functional PMTs at the time [34]. The main array consists of about 1200 PMTs,  
944    but the count may vary due to maintenance or other operational factors.

945    Events are stratified into several  $f_{\text{hit}}$  bins. Each bin corresponds to a specific range of angular  
946    resolutions, enabling a structured approach to event analysis based on the extent of the shower  
947    footprint, see Tab. 3.1. The  $f_{\text{hit}}$  metric, while effective, has several limitations. It is dependent on  
948    the zenith angle and the spectral characteristics presumed for the observed source. The variable  
949    also reaches a saturation point around 10 TeV, after which the detector's ability to discriminate  
950    between higher energy levels diminishes [34]. Furthermore, the energy distribution for each  $f_{\text{hit}}$   
951    bin is notably broad, see Fig. 3.9. In response to these limitations, HAWC has developed more  
952    intricate algorithms for energy estimation. These algorithms incorporate the zenith angle and  
953    the distribution of charge around the shower core for a more accurate assessment of the primary  
954    particle's energy, particularly at energies surpassing 10 TeV [36].

955    The relationship between  $f_{\text{hit}}$  and primary energy is complex. Atmospheric attenuation can  
956    cause high-energy showers to present a smaller footprint, misrepresenting their energy in the  $f_{\text{hit}}$   
957    metric. This effect is captured in simulations that chart the actual energy distribution across  $f_{\text{hit}}$   
958    categories [36]. Such distributions vary with the declination of the source and the theoretical  
959    energy spectrum used in the model.

960    **3.2.4 Neural Network Energy Estimation**

961    The energy estimation for photon events at the HAWC Observatory is refined through an  
962    artificial neural network (NN) algorithm. This method, based on the Toolkit for Multivariate  
963    Analysis NN, adopts a multilayer-perceptron model with logistic activation functions across its  
964    layers. The structure includes two hidden layers, the first with 15 nodes and the second with 14,  
965    designed to process input variables through a neural network optimized to estimate primary particle  
966    energies [38].

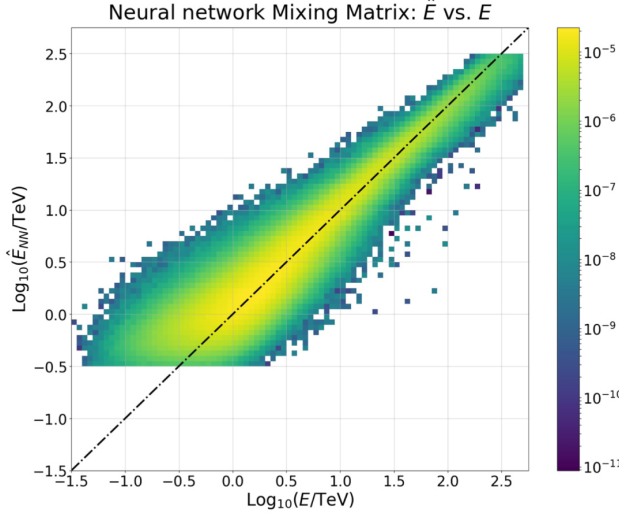


Figure 3.10 Neural Network energy estimator performance compared to true energy. The dotted line is the identity line where the estimator and injection agree. Gamma/hadron separation cuts were applied with the energy estimation. Figure pulled from [37]

967        The NN is trained to minimize a specific error function that measures discrepancies between the  
 968        NN's energy predictions and the actual energies from Monte Carlo simulations. This minimization  
 969        targets an error function that incorporates the relative importance of each event, weighting more  
 970        the importance to mimic an  $E^{-2}$  power law spectrum. This approach helps achieve a uniform  
 971        error rate across energies ranging from 1 to 100 TeV. The optimization process leverages the  
 972        Broyden-Fletcher-Goldfarb-Shanno algorithm that calibrates the NN's 479 weights [37].

973        The spectral analysis employs a binned likelihood method, using a forward-folding technique  
 974        to accommodate the energy estimate's bias and resolution [37]. This establishes a 2D binning  
 975        scheme that categorizes events by both their  $f_{\text{hit}}$  value and estimated energy. The decision to use  
 976        this scheme over a simple energy-based binning lies in the correlation between gamma/hadron  
 977        separation parameters and the angular resolution with both the size and energy of the event. The  
 978        spectrum of interest is partitioned into nine  $f_{\text{hit}}$  bins, each further divided into 12 energy bins,  
 979        spanning from 0.316 TeV to 316 TeV, encompassing a total of 108 bins [37]. However, not all  
 980        bins contribute to the final estimate. Bins with low event populations or insufficient Monte Carlo  
 981        simulation are excluded. This approach focuses on the central 99% of events by estimated energy  
 982        within each  $f_{\text{hit}}$  bin, effectively removing outliers [37].

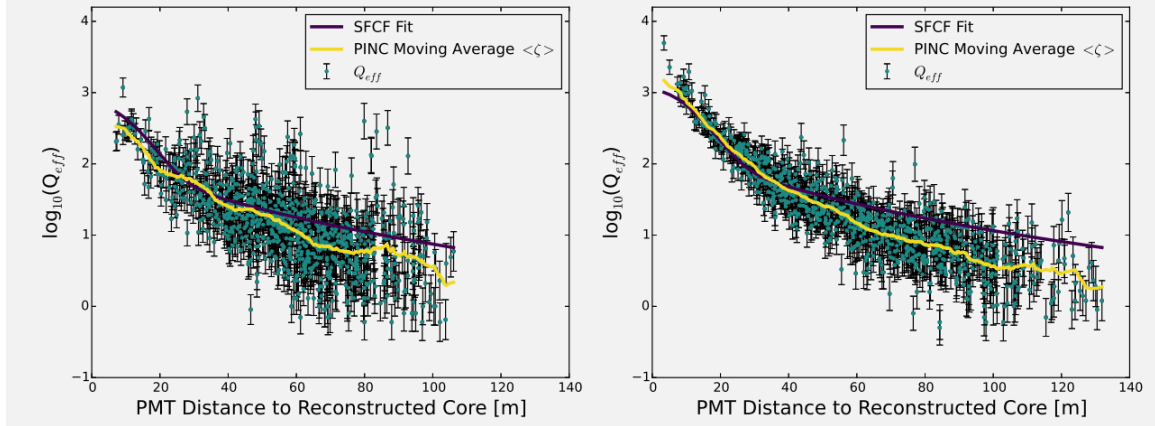


Figure 3.11 Lateral distribution functions (LDFs) for cosmic ray (left) and a photon candidate from the Crab Nebula (right). Cosmic ray LDF has clearly isolated hits far from the reconstructed shower core. Gamma-ray shower shows a more cuspy event [34].

983     Input variables for the NN are selected to capture key characteristics of the air shower: energy  
 984     deposition, containment, and atmospheric attenuation. The algorithm calculates energy deposition  
 985     using the fraction of PMTs and tanks activated, alongside the logarithm of the normalization from  
 986     the lateral distribution fit. Containment is inferred from the distance between the shower core and  
 987     the array's center, while atmospheric attenuation is evaluated using the reconstructed zenith angle  
 988     and a detailed analysis of the shower's lateral charge distribution [38, 37].

989     This refined NN energy estimation methodology is an integral component of HAWC's toolkit,  
 990     enabling precise analysis of high-energy gamma-ray events. It represents a significant advancement  
 991     in the field by more accurately mapping observed shower characteristics to primary particle energies.

### 992     **3.2.5 G/H Discrimination**

993     At the HAWC Observatory, distinguishing between air showers initiated by gamma rays and  
 994     those by hadronic cosmic rays is fundamental for astrophysical data purity. The separation process  
 995     leverages differences in shower characteristics: electromagnetic showers from gamma rays typically  
 996     display fewer muons and a smoother lateral distribution, whereas hadronic showers are more chaotic  
 997     due to the abundance of muons and hadronic sub-showers.

998     Two primary parameters facilitate the identification of cosmic-ray events [34]:

999       Compactness (C): This parameter evaluates the charge captured by PMTs, particularly focusing  
 1000      on the PMT with the highest effective charge beyond a 40-meter radius from the shower core.

1001 Compactness is inversely proportional to this effective charge, as higher charges at extended  
1002 distances from the core are indicative of hadronic showers. It is mathematically expressed as:

$$C = \frac{N_{\text{hit}}}{CxPE_{40}} \quad (3.2)$$

1003 where  $N_{\text{hit}}$  is the number of PMTs hit and  $CxPE_{40}$  is the effective charge measured outside a 40 m  
1004 radius from the shower cores [34].

1005 PINCness (P): PINCness quantifies the "clumpiness" of a shower using the charges recorded  
1006 by PMTs and is short for Parameter for Identifying Nuclear Cosmic Rays. It is computed from the  
1007 logarithm of the effective charge,  $Q_{\text{eff},i}$ , of each PMT hit,  $i$ , compared to an expected average for  
1008 that annular region. A higher PINCness suggests a less smooth distribution, typical of hadronic  
1009 showers. The formula is:

$$P = \frac{1}{N} \sum_{i=0}^N \frac{(\zeta_i - \langle \zeta \rangle)^2}{\sigma_{\zeta_i}^2} \quad (3.3)$$

1010 where  $\zeta_i = \log_{10}(Q_{\text{eff},i})$ . The average,  $\langle \zeta \rangle$  is the average over an annular region surrounding the  
1011 shower core. The errors,  $\sigma_{\zeta_i}$ , are computed and allocated from gamma-ray candidates close to the  
1012 Crab.

1013 These parameters are tested and modeled in simulations and with observational data near the  
1014 Crab Nebula. Figure 3.11 illustrating the lateral distributions for representative cosmic-ray and  
1015 photon candidate showers, as well as the distribution of these discrimination parameters, affirm  
1016 their efficacy [34].

1017 The discrimination technique has remained consistent, but cut values have been reoptimized  
1018 for the 2D bins based on  $f_{\text{hit}}$  and NN estimated energy. This refinement enhances the selection  
1019 of high-energy events. Each bin ensures at least 50% efficiency for gamma-ray detection, with  
1020 efficiencies extending up to nearly 100% in certain bins [34, 37].

### 1021 3.3 Background Estimation: Direct Integration

1022 The ratio of cosmic rays to gamma rays can be as high as 10,000 to 1, depending on the energy.  
1023 At HAWC, we confront a significant challenge even after gamma/hadron cuts: our gamma-ray data  
1024 is still inundated with cosmic-ray events. To tackle this, we rely on the direct integration method

1025 developed by Milagro [39]. This method capitalizes on the cosmic rays' isotropic nature resulting  
1026 from their deflection by interstellar magnetic fields.

1027 The direct integration method estimates background events by integrating over a stable two-  
1028 hour period of detector operation. The expected number of background events at a particular sky  
1029 coordinate  $(\phi, \theta)$  is determined by integrating the normalized detector's efficiency with the all-sky  
1030 event rate:

$$N_{\text{exp}}(\phi, \theta) = \int \int E(\text{ha}, \theta) \cdot R(t) dt \quad (3.4)$$

1031 Here,  $E(\text{ha}, \theta)$ , represents the detector's efficiency, which varies with local coordinates (hour angle  
1032 and declination).  $R(t)$  is the event rate as a function of time [39].

1033 Our background estimation is expected to falter in high-energy ranges where cosmic-ray events  
1034 are less frequent due to enhanced gamma/hadron discrimination. Sparsity in our background and  
1035 data also arise at the limits of HAWC's sensitivity and during short-term analyses of transient events.  
1036 HAWC addresses these issues by using a pixel size of  $0.5^\circ$  in our direct integration to maintain  
1037 robustness in our estimation [34, 36]. In constructing the background model, it's crucial to exclude  
1038 areas of the sky with known gamma-ray sources. Regions containing the Crab Nebula, Mrk 421,  
1039 Mrk 501, and the Galactic Plane are masked to prevent their significant gamma-ray signals from  
1040 biasing our background estimate [34].

1041

## CHAPTER 4

### ICECUBE NEUTRINO OBSERVATORY

1042 **4.1 The Detector**

1043 **4.2 Events Reconstruction and Data Acquisition**

1044 **4.2.1 Angle**

1045 **4.2.2 Energy**

1046 **4.3 Northern Test Site**

1047 **4.3.1 PIgeon remote dark rate testing**

1048 **4.3.2 Bulkhead Construction**

## CHAPTER 5

### 1049      **GLORY DUCK: MULTI-WAVELENGTH SEARCH FOR DARK MATTTER** 1050      **ANNIHILATION TOWARDS DWARF SPHEROIDAL GALAXIES**

#### 1051    **5.1 Introduction**

1052      The field of astrophysics now has several instruments and observatories sensitive to high energy  
1053      gamma-rays. The energy sensitivity for the modern gamma-ray program spans many orders of  
1054      magnitude. Figure 5.1 demonstrates these comparable sensitivities across energies for the five  
1055      experiments: Fermi-LAT, HAWC, HESS, MAGIC, and VERITAS.

1056      Each of the five experiments featured in Figure 5.1 have independently searched for DM  
1057      annihilation from dwarf spheroidal galaxies (dSph) and set limits on annihilation cross-section of  
1058      WIMPs. Intriguingly, there are regions of substantial overlap in their energy sensitivities. This  
1059      clearly motivates an analysis that combines data from these five. Each experiment has unique  
1060      gamma-ray detection methods and their weaknesses and strengths can be leveraged with each other.  
1061      The HAWC gamma-ray observatory is extensively introduced in chapter 3, so it is not introduced  
1062      here. A brief description of the remaining experiments are in the following paragraphs.

1063      The Large Area Telescope (LAT) is a pair conversion telescope mounted on the NASA Fermi  
1064      satellite in orbit  $\sim$ 550 km above the Earth [41]. LAT's field of view covers about 20% of the  
1065      whole sky, and it sweeps the whole sky approximately every 3 hours. LAT's gamma-ray energy  
1066      sensitivity ranges from 20 MeV up to 1 TeV. Previous DM searches towards dSphs using Fermi-LAT  
1067      are published in [42] and [43].

1068      The High Energy Spectroscopic System (HESS), Major Atmospheric Gamma Imaging  
1069      Cherenkov (MAGIC), and Very Energetic Radiation Imaging Telescope Array System (VERI-  
1070      TAS) are arrays of Imaging Atmospheric Cherenkov Telescopes (IACT). These telescopes observe  
1071      the Cherenkov light emitted from gamma-ray showers in the Earth's atmosphere. The field of  
1072      view for these telescopes is no larger than  $5^\circ$  with energy sensitivities ranging from 30 GeV up  
1073      to 100 TeV [44, 45, 46]. IACTs are able to make precise observations in selected regions of the  
1074      sky, however can only be operated in ideal dark conditions. HESS's observations of the dwarves

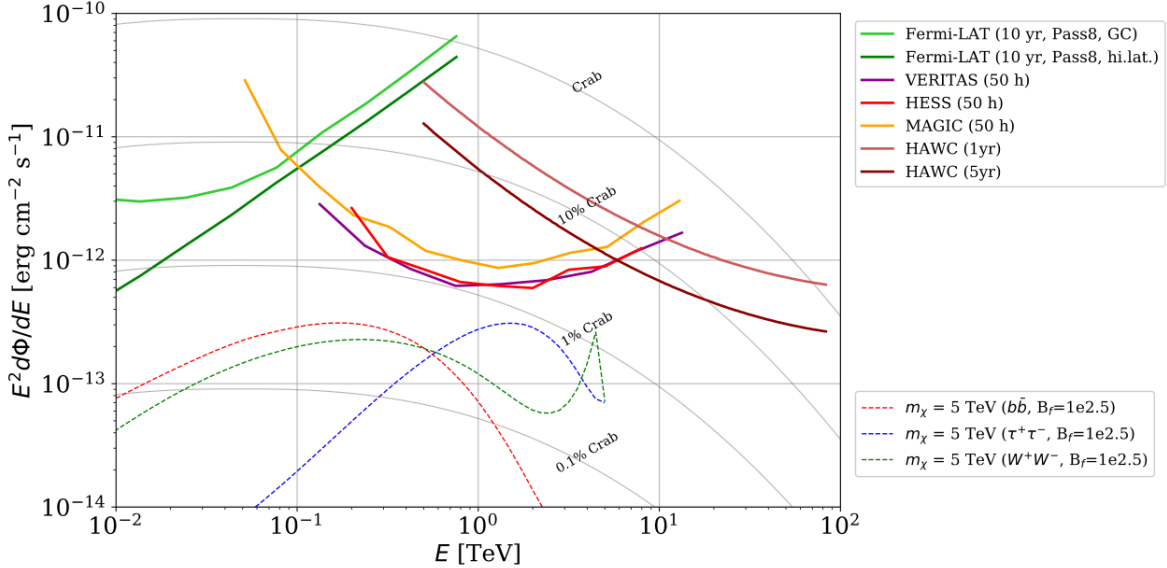


Figure 5.1 Sensitivities of five gamma-ray experiments compared to percentages of the Crab nebula’s emission and dark matter annihilation. Solid lines present estimated sensitivities to power law spectra [FACT CHECK THIS] for each experiment. Green lines are Fermi-LAT sensitivities where lighter green is the sensitivity to the galactic center and dark green is its sensitivity to higher declinations. Orange, red, and purple solid lines represent the MAGIC, HESS, and VERITAS 50 hour sensitivities respectively. The maroon and brown lines are the HAWC 1 year and 5 year sensitivities. Across four decades of gamma-ray energy, these experiments have similar sensitivities on the order  $10^{-12}$  erg  $\text{cm}^{-2}\text{s}^{-1}$ . The dotted lines are estimated dark matter fluxes assuming  $m_\chi = 5$  TeV DM annihilating to bottom quarks (red), tau leptons (blue), and W bosons (green). Faded gray lines outline percentage flux of the Crab nebula. Figure is an augmented version of [40]

1075 Sculptor and Carina were between January 2008 and December 2009. HESS’s observations of  
 1076 Coma Berenices were taken from 2010 to 2013, and Fornax was observed in 2010 [47, 48, 49].  
 1077 MAGIC provided deep observations of Segue1 between 2011 and 2013 [50]. MAGIC also provides  
 1078 data for three additional dwarves: Coma Berenices, Draco, and Ursa Major II where observations  
 1079 were made in: January - June 2019 [51], March - September 2018 [51], and 2014 - 2016 [52]  
 1080 respectively. VERITAS provided data for Boötes I, Draco, Segue 1, and Ursa Minor from 2009 to  
 1081 2016 [53].

1082 This chapter presents the Glory Duck analysis, the name given for the search for dark matter  
 1083 annihilation from dSph by combining data from the five gamma-ray observatories: Fermi-LAT,  
 1084 HAWC, HESS, MAGIC, and VERITAS. Specifically, the methods in analysis and modeling are  
 1085 presented for the HAWC gamma-ray observatory. This work will be published in the Journal of

1086 Cosmology and Astroparticle Physics and presented at the International Cosmic Ray Conference  
1087 in 2019, 2021, and 2023 [54, 55, 56] and others.

1088 **5.2 Dataset and Background**

1089 This section enumerates the data analysis and background estimation methods used for HAWC's  
1090 study of dSphs. Section 5.2.1 and Section 5.2.2 are most useful for fellow HAWC collaborators  
1091 looking to replicate the Glory Duck analysis.

1092 **5.2.1 Itemized HAWC files**

1093 These files are only available withing HAWC's internal documentation and collaborators. They  
1094 are not meant for public access, and are presented here so that HAWC collaborators can reproduce  
1095 results accurately.

- 1096 • Detector Response: [response\\_aerie\\_svn\\_27754\\_systematics\\_best\\_mc\\_test\\_nobr](#)  
1097 [oadpulse\\\_10pctlogchargesmearing\\_0.63qe\\_25kHzNoise\\_run5481\\_curvature](#)  
1098 [0\\_index3.root](#)
- 1099 • Data Map: [maps-20180119/liff/maptree\\_1024.root](#)
- 1100 • Spectral Dictionary: [DM\\_CirrelliSpectrum\\_dict\\_gammas.npy](#)
- 1101 • Analysis wiki: [https://private.hawc-observatory.org/wiki/index.php/Glory\\_Duck\\_Multi-Experiment\\_Dark\\_Matter\\_Search](https://private.hawc-observatory.org/wiki/index.php/Glory_Duck_Multi-Experiment_Dark_Matter_Search)

1103 **5.2.2 Software Tools and Development**

1104 This analysis was performed using HAL and 3ML [34, 57] in Python version 2. I built software  
1105 to implement the *A Poor Particle Physicist Cookbook for Dark Matter Indirect Detection* (PPPC)  
1106 [58] DM spectral model and dSphs spatial model from [59] for HAWC analysis. A NumPy version  
1107 of this dictionary was made for both Py2 and Py3. The code base for creating this dictionary is  
1108 linked on my GitLab sandbox:

- 1109 • Py2: [Dictionary Generator \(Deprecated\)](#)

- 1110 • Py3: [PPPC2Dict](#)

1111     The analysis was performed using the  $f_{hit}$  framework as used and described in the HAWC Crab  
1112 paper [34]. The Python2 NumPy dictionary file for gamma-ray final states is `dmCirSpecDict.npy`.  
1113 The corresponding Python3 file is `DM_CirrelliSpectrum_dict_gammas.npy`. These files can  
1114 also be used for decay channels and the PPPC describes how [58]. All other software used for data  
1115 analysis, DM profile generation, and job submission to SLURM are also kept in my sandbox for  
1116 [the Glory Duck](#) project.

### 1117 5.2.3 Data Set and Background Description

1118     The HAWC data maps used for this analysis contain 1017 days of data between runs 2104  
1119 (2014-11-26) and 7476 (2017-12-20). They were generated from pass 4.0 reconstruction. The  
1120 analysis is performed using the  $f_{hit}$  energy binning scheme with bins (1-9) similar to what was done  
1121 for the Crab and previous HAWC dSph analysis [34, 60]. Bin 0 was excluded as it has substantial  
1122 hadronic contamination and poor angular resolution.

1123     This analysis was done on dSphs because of their large DM mass content relative to baryonic  
1124 mass. We consider the following to estimate the background to this study.

- 1125     • The dSphs' angular extent are small relative to HAWC's spatial resolution, so the analysis is  
1126         not sensitive to large or small scale anisotropies.
- 1127     • The dSphs used in this analysis are off the galactic plane and therefore not contaminated by  
1128         diffuse emission from the galaxy.
- 1129     • The dSphs are baryonically faint relative to their expected dark matter content and are not  
1130         expected to contain high energy gamma-ray sources.

1131     Therefor we make no additional assumptions on the background from our sources and use  
1132 HAWC's standard direct integration method for background estimation [34]. The largest background  
1133 under this consideration is from an isotropic flux of cosmic rays. The contamination of this hadronic  
1134 flux is worse at lower energies where HAWC's gamma/hadron discrimination worse. It is possible

1135 for gamma rays from DM annihilation to scatter in transit to HAWC via Inverse Compton Scattering  
1136 (ICS). This was investigated and its impact on the flux is negligible. Supporting information on  
1137 this is in Section 5.7.1

1138 **5.3 Analysis**

1139 The expected differential photon flux from DM-DM annihilation to standard model particles,  
1140  $d\Phi_\gamma/dE_\gamma$ , over solid angle,  $\Omega$ , is described by the familiar equation.

$$\frac{d\Phi_\gamma}{dE_\gamma} = \frac{\langle\sigma v\rangle}{8\pi m_\chi^2} \frac{dN_\gamma}{dE_\gamma} \times \int_{\text{source}} d\Omega \int_{l.o.s} dl \rho_\chi^2 J(r, \theta') \quad (5.1)$$

1141 Where  $\langle\sigma v\rangle$  is the velocity weighted annihilation cross-section.  $\frac{dN}{dE}$  is the expected differential  
1142 number of photons produced at each energy per annihilation.  $m_\chi$  is the rest mass of the supposed  
1143 DM particle.  $\rho_\chi$  is the DM density.  $J$  is the astrophysical J-factor and is defined as

$$J = \int d\Omega \int_{l.o.s} dl \rho_\chi^2(r, \theta') \quad (5.2)$$

1144  $l$  is the distance to the source from Earth.  $r$  is the radial distance from the center of the source.  $\theta'$  is  
1145 the half angle defining a cone containing the DM source. How each component is synthesized and  
1146 considered for HAWC's analysis is presented in the following sections. Section 5.3.1 presents the  
1147 particle physics model for DM annihilation. Section 5.3.2 presents the spatial distributions built  
1148 for each dSph.

1149 **5.3.1  $\frac{dN_\gamma}{dE_\gamma}$  - Particle Physics Component**

1150 For these spectra, we import the PPPC with Electroweak (EW) corrections [58]. Public versions  
1151 of the imported tables are provided by the [authors online](#). The spectrum is implemented as a model  
1152 script in astromodels for 3ML. The EW corrections were previously not considered for HAWC and  
1153 are significant for DM annihilating to EW coupled SM particles such as all leptons, and the  $\gamma$ ,  
1154  $Z$ , and  $W$  bosons [60]. Figure 5.2 demonstrates the significance of EW corrections for W boson  
1155 annihilation. Across EW SM channels, the gamma-ray spectra become harder than spectra without  
1156 EW corrections. Tables from the PPPC were reformatted into Python NumPy dictionaries for  
1157 collaboration-wide use. A class in astromodels was developed to include the EW correction from  
1158 the PPPC and is aptly named `PPPCSpectra` within `DM_models.py`.

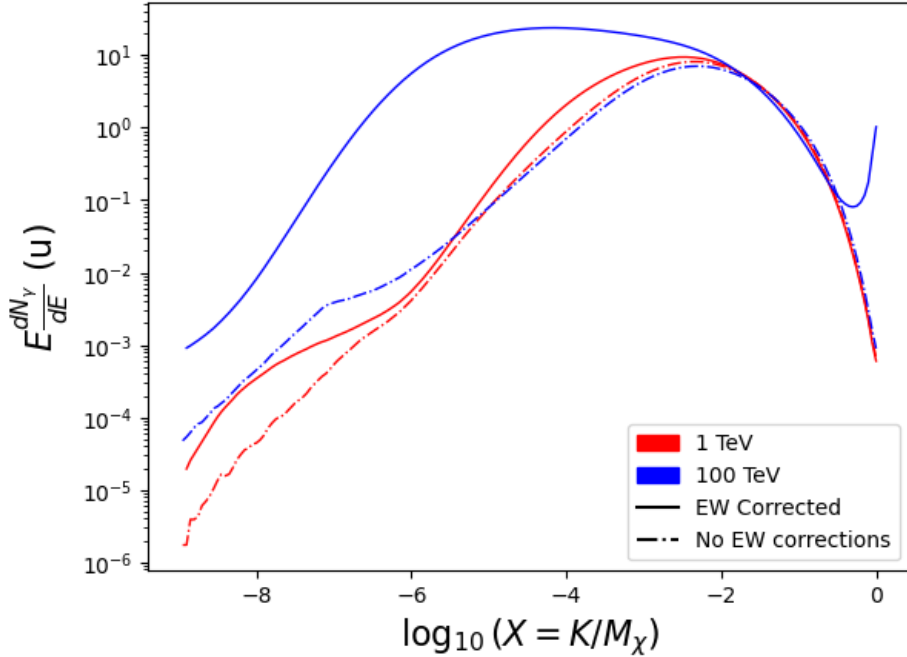


Figure 5.2 Effect of Electroweak (EW) corrections on expected DM annihilation spectrum for  $\chi\chi \rightarrow W^-W^+$ . Solid lines are spectral models that consider EW corrections. Dash-dot lines are spectral models without EW corrections. Red lines are models for  $M_\chi = 1$  TeV. Blue lines represent models for  $M_\chi = 100$  TeV. All models are sourced from the PPPC4DMID [58].

### 1159 5.3.2 J- Astrophysical Component

1160 The J-factor profiles for each source are imported from Geringer-Sameth (referred to with  $\mathcal{GS}$ )  
 1161 [59].  $\mathcal{GS}$  fits the Zhao DM profile to the dSphs which has a DM density described as [61]

$$\rho(r) = \frac{\rho_0}{(r/R_s)^\gamma (1 + (r/R_s)^\alpha)^{(\beta-\gamma)}}. \quad (5.3)$$

1162  $R_s$  is the scale radius and free parameter in the model.  $\gamma$  is the logarithmic slope in the region  
 1163  $r \ll R_s$ .  $\beta$  is the logarithmic slope in the region  $r \gg R_s$ .  $\alpha$  is known as the sharpness of transition  
 1164 where  $r \approx R_s$ . The classic Navarro-Frenk-White [62] (NFW) can be retrieved from Zhao by fixing  
 1165  $(\alpha, \beta, \gamma) = (1, 3, 1)$ .

1166  $\mathcal{GS}$  best fits were pulled from the publication as  $J(\theta)$ , where  $\theta$  is the angular separation from  
 1167 the center of the source. HAWC requires maps in terms of  $\frac{dJ}{d\Omega}$ , so the conversion from the maps  
 1168 was done in the following way...

1169 First, convert the angular distances to solid angles

$$\Omega = 2 \cdot \pi(1 - \cos(\theta)) \quad (5.4)$$

1170 which reduces with a small angle approximation to  $\pi\theta^2$ . Next, the central difference for both the  
1171  $\Delta J$  and  $\Delta\Omega$  value were calculated from the discretized  $J(\theta)$  with the central difference stencil:

$$\Delta\phi_i = \phi_{i+1} - \phi_{i-1} \quad (5.5)$$

1172 Where  $\phi$  is either  $\Omega$  or  $J$ . These were done separately in case the grid spacing in  $\theta$  was not uniform.  
1173 Finally, these lists are divided so that we are left with an approximation of the  $dJ/d\Omega$  profile that  
1174 is a function of  $\theta$ . Admittedly, this is an approximation method for the map which introduces small  
1175 errors compared to the true profile estimate. This was checked as a systematic against the author's  
1176 profiling of the spatial distribution and is documented in Section 5.8.1.

1177 With  $\frac{dJ}{d\Omega}(\theta)$ , a map is generated, first by filling in the north-east quadrant of the map. This  
1178 quadrant is then reflected twice, vertically then horizontally, to fill the full map. Maps are then  
1179 normalized by dividing the discrete 2D integral of the map. The 2D integral was a simple height  
1180 of bins, Newton's integral:

$$p^2 \cdot \sum_{i,j=0}^{N,M} \frac{dJ}{d\Omega}(\theta_{i,j}, \phi_{i,j}) \quad (5.6)$$

1181 These maps are HEALpix maps with NSIDE 16384 and saved in the .fits format. The hyper fine  
1182 resolution was selected to better preserve the total expected counts after integrating Eq. (5.1) with  
1183 the detector response.

1184 Another DM spatial distribution model from Bonnivard ( $\mathcal{B}$ ) [63] was used for the Glory Duck  
1185 study. However, to save computational time, limits from  $\mathcal{GS}$  were scaled to  $\mathcal{B}$  instead of each  
1186 experiment performing a full study a second time. How these models compare is demonstrated  
1187 for each dSph in Figure 5.16 and Figure 5.17 Plots of these maps are provided for each source  
1188 in chapter A Examples of the two most impactful dSphs derived from  $\mathcal{GS}$ , Segue1 and Coma  
1189 Berenices are featured in Figure 5.3

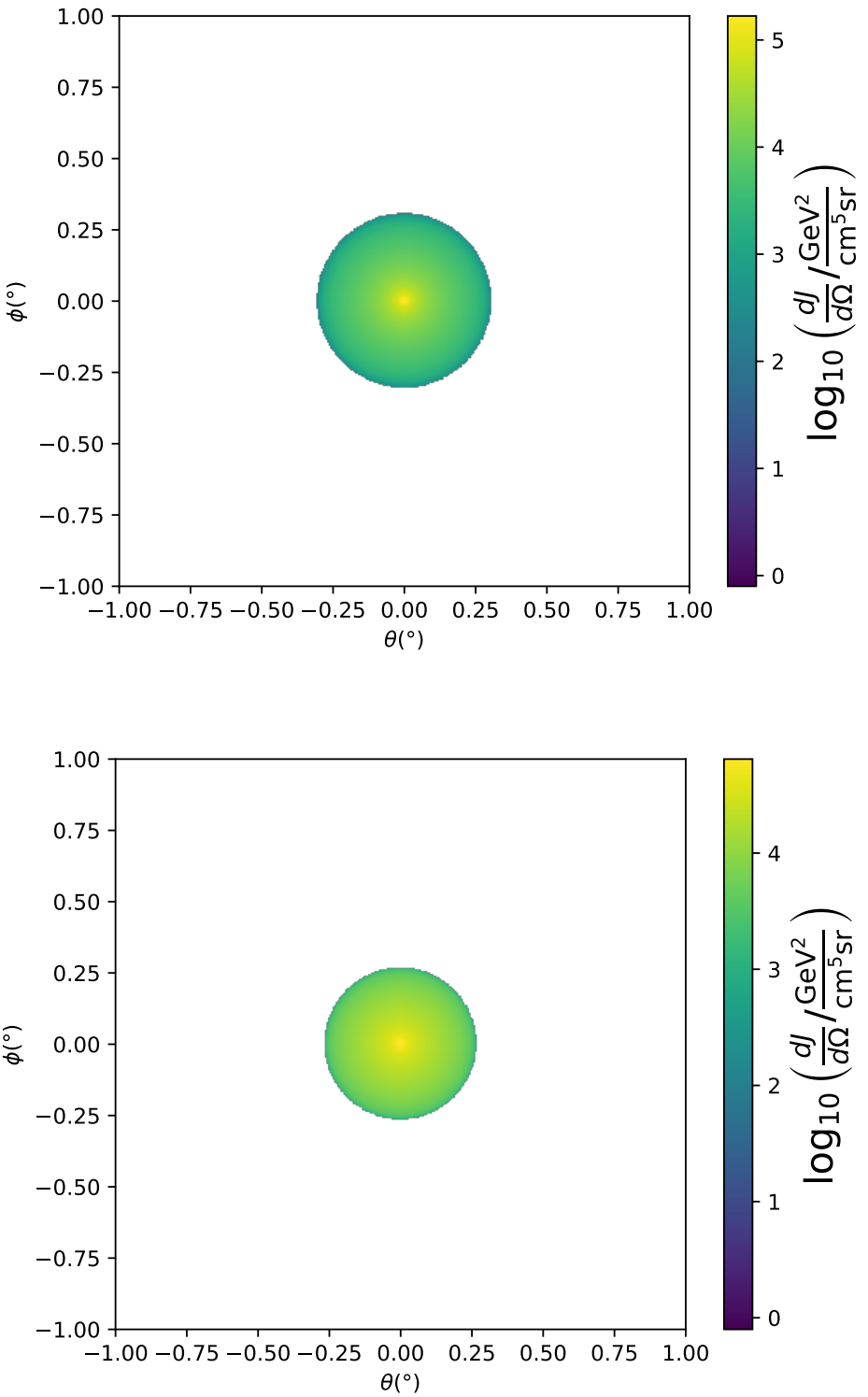


Figure 5.3  $\frac{dJ}{d\Omega}$  maps for Segue1 (top) and Coma Berenices (bottom). Origin is centered on the specific dwarf spheroidal galaxies (dSph). X and Y axes are the angular separation from the center of the dwarf. Profile is truncated at the scale radius. Plots of the remaining 11 dSph HAWC studied are linked in Fig. A.1.

1190 **5.3.3 Source Selection and Annihilation Channels**

1191 We use many of the dSphs presented in HAWC’s previous dSph DM search [60]. HAWC’s  
1192 sources for Glory Duck include Boötes I, Coma Berenices, Canes Venatici I + II, Draco, Hercules,  
1193 Leo I, II, + IV, Segue 1, Sextans, and Ursa Major I + II. A full description of all sources used  
1194 in Glory Duck is found in Table 5.1. Triangulum II was excluded from the Glory Duck analysis  
1195 because of large uncertainties in its  $J$  factor. Ursa Minor was excluded from HAWC’s contribution  
1196 to the combination because the source extension model extended Ursa Minor beyond HAWC’s field  
1197 of view. Ursa Minor was not expected to contribute significantly to the combined limit, so work  
1198 was not invested in a solution to include Ursa Minor.

1199 This analysis improves on the previous HAWC dSph paper [60] in the following ways. Pre-  
1200 viously, the dSphs were treated and implemented as point sources. For this analysis, dSphs are  
1201 modeled and treated as extended source. The impact of this change with respect to the upper limit  
1202 is source dependent and is explored in Section 5.7.2. Previously, the particle physics model used for  
1203 gamma-ray spectra from DM annihilation did not have EW corrections where the PPPC includes  
1204 them. Finally, the gamma-ray ray dataset is much larger. The study performed here analyzes over  
1205 1000 days of data compared to 507.

1206 The SM annihilation channels probed for the Glory Duck combination include  $b\bar{b}$ ,  $e\bar{e}$ ,  $\mu\bar{\mu}$ ,  $\tau\bar{\tau}$ ,  
1207  $t\bar{t}$ ,  $W^+W^-$ , and  $ZZ$ . A summary of all sources, with a description of each experiments’ sensitivity  
1208 to the source, is provided in Table 5.2.

1209 **5.4 Likelihood Methods**

1210 **5.4.1 HAWC Likelihood**

1211 For every analysis bin in energy,  $f_{hit}$  bins (1-9), and location, we can expect  $N$  signal events and  
1212  $B$  background events. The expected number of excess signal events from dark matter annihilation,  
1213  $S$ , is estimated by convolving Equation (5.1) with HAWC’s energy response and pixel point spread  
1214 functions. I then compute the test statistic (TS) with the log-likelihood ratio test,

$$TS_{\max} = -2 \ln \left( \frac{\mathcal{L}_0}{\mathcal{L}^{\max}} \right) \quad (5.7)$$

Table 5.1 Summary of the relevant properties of the dSphs used in the present work. Column 1 lists the dSphs. Columns 2 and 3 present their heliocentric distance and galactic coordinates, respectively. Columns 4 and 5 report the  $J$ -factors of each source given from the  $\mathcal{GS}$  and  $\mathcal{B}$  independent studies and their estimated  $\pm 1\sigma$  uncertainties. The values  $\log_{10} J$  ( $\mathcal{GS}$  set) [59] correspond to the mean  $J$ -factor values for a source extension truncated at the outermost observed star. The values  $\log_{10} J$  ( $\mathcal{B}$  set) [63] are provided for a source extension at the tidal radius of each dSph. **Bolded sources are within HAWC's field of view and provided to the Glory Duck analysis.**

Name	Distance (kpc)	$l, b$ ( $^{\circ}$ )	$\log_{10} J$ ( $\mathcal{GS}$ set) $\log_{10}(\text{GeV}^2\text{cm}^{-5}\text{sr})$	$\log_{10} J$ ( $\mathcal{B}$ set) $\log_{10}(\text{GeV}^2\text{cm}^{-5}\text{sr})$
<b>Boötes I</b>	66	358.08, 69.62	$18.24^{+0.40}_{-0.37}$	$18.85^{+1.10}_{-0.61}$
<b>Canes Venatici I</b>	218	74.31, 79.82	$17.44^{+0.37}_{-0.28}$	$17.63^{+0.50}_{-0.20}$
<b>Canes Venatici II</b>	160	113.58, 82.70	$17.65^{+0.45}_{-0.43}$	$18.67^{+1.54}_{-0.97}$
Carina	105	260.11, -22.22	$17.92^{+0.19}_{-0.11}$	$18.02^{+0.36}_{-0.15}$
<b>Coma Berenices</b>	44	241.89, 83.61	$19.02^{+0.37}_{-0.41}$	$20.13^{+1.56}_{-1.08}$
<b>Draco</b>	76	86.37, 34.72	$19.05^{+0.22}_{-0.21}$	$19.42^{+0.92}_{-0.47}$
Fornax	147	237.10, -65.65	$17.84^{+0.11}_{-0.06}$	$17.85^{+0.11}_{-0.08}$
<b>Hercules</b>	132	28.73, 36.87	$16.86^{+0.74}_{-0.68}$	$17.70^{+1.08}_{-0.73}$
<b>Leo I</b>	254	225.99, 49.11	$17.84^{+0.20}_{-0.16}$	$17.93^{+0.65}_{-0.25}$
<b>Leo II</b>	233	220.17, 67.23	$17.97^{+0.20}_{-0.18}$	$18.11^{+0.71}_{-0.25}$
<b>Leo IV</b>	154	265.44, 56.51	$16.32^{+1.06}_{-1.70}$	$16.36^{+1.44}_{-1.65}$
Leo V	178	261.86, 58.54	$16.37^{+0.94}_{-0.87}$	$16.30^{+1.33}_{-1.16}$
Leo T	417	214.85, 43.66	$17.11^{+0.44}_{-0.39}$	$17.67^{+1.01}_{-0.56}$
Sculptor	86	287.53, -83.16	$18.57^{+0.07}_{-0.05}$	$18.63^{+0.14}_{-0.08}$
<b>Segue I</b>	23	220.48, 50.43	$19.36^{+0.32}_{-0.35}$	$17.52^{+2.54}_{-2.65}$
Segue II	35	149.43, -38.14	$16.21^{+1.06}_{-0.98}$	$19.50^{+1.82}_{-1.48}$
<b>Sextans</b>	86	243.50, 42.27	$17.92^{+0.35}_{-0.29}$	$18.04^{+0.50}_{-0.28}$
<b>Ursa Major I</b>	97	159.43, 54.41	$17.87^{+0.56}_{-0.33}$	$18.84^{+0.97}_{-0.43}$
<b>Ursa Major II</b>	32	152.46, 37.44	$19.42^{+0.44}_{-0.42}$	$20.60^{+1.46}_{-0.95}$
Ursa Minor	76	104.97, 44.80	$18.95^{+0.26}_{-0.18}$	$19.08^{+0.21}_{-0.13}$

Table 5.2 Summary of dSph observations by each experiment used in this work. A ‘-’ indicates the experiment did not observe the dSph for this study. For Fermi-LAT, the exposure at 1 GeV is given. For HAWC,  $|\Delta\theta|$  is the absolute difference between the source declination and HAWC latitude. HAWC is more sensitive to sources with smaller  $|\Delta\theta|$ . For IACTs, we show the zenith angle range, the total exposure, the energy range, the angular radius  $\theta$  of the signal or ON region, the ratio of exposures between the background-control (OFF) and signal (ON) regions ( $\tau$ ), and the significance of gamma-ray excess in standard deviations,  $\sigma$ .

Source name	Fermi-LAT	HAWC	H.E.S.S, MAGIC, VERITAS						
	Exposure ( $10^{11}$ s m $^2$ )	$ \Delta\theta $ (°)	IACT	Zenith (°)	Exposure (h)	Energy range (GeV)	$\theta$ (°)	$\tau$	$S$ ( $\sigma$ )
Boötes I	2.6	4.5	VERITAS	15 – 30	14.0	100–41000	0.10	8.6	-1.0
Canes Venatici I	2.9	14.6	–	–	–	–	–	–	–
Canes Venatici II	2.9	15.3	–	–	–	–	–	–	–
Carina	3.1	–	H.E.S.S.	27 – 46	23.7	310 – 70000	0.10	18.0	-0.3
Coma Berenices	2.7	4.9	H.E.S.S.	47 – 49	11.4	550 – 70000	0.10	14.4	-0.4
Draco	3.8	38.1	MAGIC	5 – 37	49.5	60 – 10000	0.17	1.0	–
			MAGIC	29 – 45	52.1	70 – 10000	0.22	1.0	–
			VERITAS	25 – 40	49.8	120 – 70000	0.10	9.0	-1.0
Fornax	2.7	–	H.E.S.S.	11 – 25	6.8	230 – 70000	0.10	45.5	-1.5
Hercules	2.8	6.3	–	–	–	–	–	–	–
Leo I	2.5	6.7	–	–	–	–	–	–	–
Leo II	2.6	3.1	–	–	–	–	–	–	–
Leo IV	2.4	19.5	–	–	–	–	–	–	–
Leo V	2.4	–	–	–	–	–	–	–	–
Leo T	2.6	–	–	–	–	–	–	–	–
Sculptor	2.7	–	H.E.S.S.	10 – 46	11.8	200 – 70000	0.10	19.8	-2.2
Segue I	2.5	2.9	MAGIC	13 – 37	158.0	60 – 10000	0.12	1.0	-0.5
			VERITAS	15 – 35	92.0	80 – 50000	0.10	7.6	0.7
Segue II	2.7	–	–	–	–	–	–	–	–
Sextans	2.4	20.6	–	–	–	–	–	–	–
Ursa Major I	3.4	32.9	–	–	–	–	–	–	–
Ursa Major II	4.0	44.1	MAGIC	35 – 45	94.8	120 – 10000	0.30	1.0	-2.1
Ursa Minor	4.1	–	VERITAS	35 – 45	60.4	160 – 93000	0.10	8.4	-0.1

1215 where  $\mathcal{L}_0$  is the null hypothesis, or no DM emission, likelihood.  $\mathcal{L}^{\max}$  is the best fit signal  
 1216 hypothesis where  $\langle\sigma v\rangle$  maximizes the likelihood. We calculate the likelihood of each source and  
 1218 model, assuming events are Poisson distributed, with

$$\mathcal{L} = \prod_i \frac{(B_i + S_i)^{N_i} e^{-(B_i + S_i)}}{N_i!} \quad (5.8)$$

1219 where  $S_i$  is the sum of expected number of signal counts.  $B_i$  is the number of background counts  
 1220 observed.  $N_i$  is the total number of counts.

1221 I also calculate an upper limit on  $\langle\sigma v\rangle$  by calculating the 95% confidence level (CL). For the  
 1222 CL, we define a parameter,  $TS_{95}$ , as

$$TS_{95} \equiv \sum_{\text{bins}} \left[ 2N \ln \left( 1 + \frac{\epsilon S_{\text{ref}}}{B} \right) - 2\epsilon S_{\text{ref}} \right] \quad (5.9)$$

1223 where the expected signal counts from a dSph is scaled by  $\epsilon$ .  $S_{\text{ref}}$  is the expected number of excess  
 1224 counts in a bin from DM emission from a dSph with a corresponding annihilation cross-section,  
 1225  $\langle\sigma v\rangle$ . We scan  $\epsilon$  such that

$$2.71 = TS_{\max} - TS_{95} \quad (5.10)$$

1226 HAWC's exclusive results are provided in Section 5.5.

#### 1227 5.4.2 Glory Duck Joint Likelihood

1228 The joint likelihood for the 5-experiment combination was done similarly as Section 5.4.1. We  
 1229 calculate upper limits on  $\langle\sigma v\rangle$  from the TS, Eq. (5.7), and define the likelihood ratio more generally

$$\lambda(\langle\sigma v\rangle | \mathcal{D}_{\text{dSphs}}) = \frac{\mathcal{L}(\langle\sigma v\rangle; \hat{\nu} | \mathcal{D}_{\text{dSphs}})}{\mathcal{L}(\widehat{\langle\sigma v\rangle}; \hat{\nu} | \mathcal{D}_{\text{dSphs}})} \quad (5.11)$$

1230  $\mathcal{D}_{\text{dSphs}}$  is the totality of observations across experiments and dSphs.  $\nu$  are the nuisance parameters  
 1231 which are the  $J$  factors in this study.  $\widehat{\langle\sigma v\rangle}$  and  $\hat{\nu}$  are the respective estimate that maximize  $\mathcal{L}$   
 1232 globally. Finally,  $\hat{\nu}$  is the set of nuisance parameters that maximize  $\mathcal{L}$  for a fixed value of  $\langle\sigma v\rangle$ .

1233 The *complete* joint likelihood,  $\mathcal{L}$  that encompasses all observations from all instruments and  
 1234 dSphs can be factorized into *partial* functions for each dSph  $l$  (with  $\mathcal{L}_{\text{dSph},l}$ ) and its  $J$  factor ( $\mathcal{J}_l$ ):

$$\mathcal{L}(\langle\sigma v\rangle; \nu | \mathcal{D}_{\text{dSphs}}) = \prod_{l=1}^{N_{\text{dSphs}}} \mathcal{L}_{\text{dSph},l}(\langle\sigma v\rangle; J_l, \nu_l | \mathcal{D}_l) \times \mathcal{J}_l(J_l | J_{l,\text{obs}}, \sigma_{\log J_l}). \quad (5.12)$$

1235 For this study,  $N_{\text{dSphs}} = 20$  is the number of dSphs studied.  $\mathcal{D}_l$  are the gamma-ray observations  
 1236 of dSph,  $l$ .  $\nu_l$  are the nuisance parameters modifying the gamma-ray observations of dSph,  $l$ ,  
 1237 but excludes  $\mathcal{J}_l$ .  $\mathcal{J}_l$  is the  $J$  factor for dSph,  $l$ , as defined in Equation (5.2), and it is a nuisance  
 1238 parameter whose value is unknown.  $\log_{10} J_{l,\text{obs}}$  and  $\sigma_{\log J_l}$  are obtained by fitting a log-normal  
 1239 function of  $J_{l,\text{obs}}$  to the posterior distribution of  $J_l$  [64].  $\log_{10} J_{l,\text{obs}}$  and  $\sigma_{\log J_l}$  values are provided  
 1240 in Table 5.1. The term  $\mathcal{J}_l$  constraining  $J_l$  is written as:

$$\mathcal{J}_l(J_l | J_{l,\text{obs}}, \sigma_{\log J_l}) = \frac{1}{\ln(10)J_{l,\text{obs}}\sqrt{2\pi}\sigma_{\log J_l}} \exp\left(-\frac{(\log_{10} J_l - \log_{10} J_{l,\text{obs}})^2}{2\sigma_{\log J_l}^2}\right). \quad (5.13)$$

1241 Both the  $\mathcal{GS}$  and  $\mathcal{B}$ , displayed in Table 5.1, sets of  $J$  factors are used in this analysis. Equation (5.13)  
 1242 is also normalized, so it can also be interpreted as a probability density function (PDF) for  $J_{l,\text{obs}}$ .  
 1243 From Equation (5.1), we can also see that  $\langle\sigma v\rangle$  and  $J_l$  are degenerate when computing  $\mathcal{L}_{\text{dSph},l}$ .  
 1244 Therefore, as noted in [65], it is sufficient to compute  $\mathcal{L}_{\text{dSph},l}$  versus  $\langle\sigma v\rangle$  for a fixed value of  $J_l$ .  
 1245 We used  $J_{l,\text{obs}}(\mathcal{GS})$  reported in Tab. 5.1, in order to perform the profile of  $\mathcal{L}$  with respect to  $J_l$ .  
 1246 The degeneracy implies that for any  $J'_l \neq J_{l,\text{obs}}$  (in practice in our case we used  $J'_l = J_{l,\text{obs}}(\mathcal{B})$  to  
 1247 compute results from a different set of  $J$  factors):

$$\mathcal{L}_{\text{dSph},l}(\langle\sigma v\rangle; J'_l, \nu_l | \mathcal{D}_l) = \mathcal{L}_{\text{dSph},l}\left(\frac{J'_l}{J_{l,\text{obs}}} \langle\sigma v\rangle; J_{l,\text{obs}}, \nu_l | \mathcal{D}_l\right), \quad (5.14)$$

1248 which is a straightforward rescaling operation that reduces the computational needs of the profiling  
 1249 operation since:

$$\mathcal{L}(\langle\sigma v\rangle; \hat{\nu} | \mathcal{D}_{\text{dSphs}}) = \prod_{l=1}^{N_{\text{dSphs}}} \max_{J_l} \left[ \mathcal{L}_{\text{dSph},l}(\langle\sigma v\rangle; J_l, \hat{\nu}_l | \mathcal{D}_l) \times \mathcal{J}_l(J_l | J_{l,\text{obs}}, \sigma_{\log J_l}) \right]. \quad (5.15)$$

1250 In addition, Eq. (5.14) enables the combination of data from different gamma-ray instruments and  
 1251 observed dSphs via tabulated values of  $\mathcal{L}_{\text{dSph},l}$ , or equivalently of  $\lambda$  from Eq. (5.11) as was done in  
 1252 this work, versus  $\langle\sigma v\rangle$ .  $\mathcal{L}_{\text{dSph},l}$  is computed for a fixed value of  $J_l$  and profiled with respect to all  
 1253 instrumental nuisance parameters  $\nu_l$ , these nuisance parameters are discussed in more detail below.  
 1254 These values are produced by each detector independently and therefore there is no need to share  
 1255 sensitive low-level information used to produce them, such as event lists. Figure 5.4 illustrates the  
 1256 multi-instrument combination technique used in this study with a comparison of the upper limit

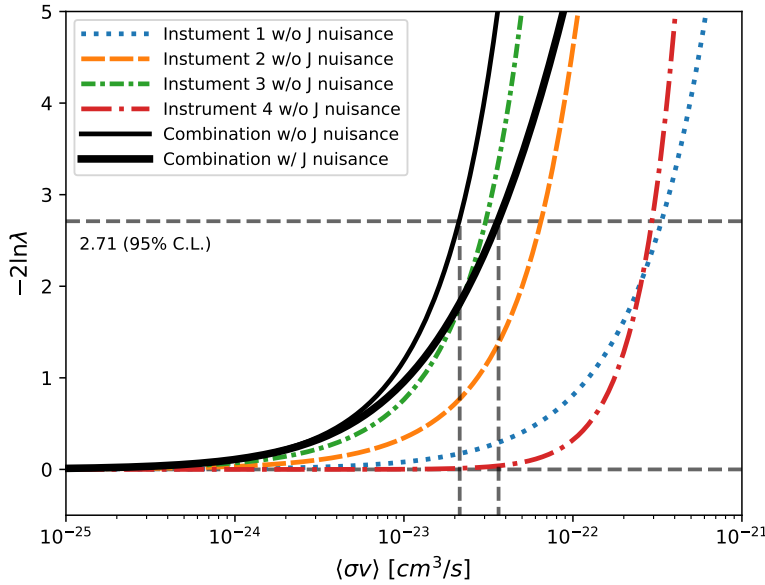


Figure 5.4 Illustration of the combination technique showing a comparison between  $-2 \ln \lambda$  provided by four instruments (colored lines) from the observation of the same dSph without any  $J$  nuisance and their sum, *i.e.* the resulting combined likelihood (thin black line). According to the test statistics of Equation (5.7), the intersection of the likelihood profiles with the line  $-2 \ln \lambda = 2.71$  indicates the 95% C.L. upper limit on  $\langle\sigma v\rangle$ . The combined likelihood (thin black line) shows a smaller value of upper limit on  $\langle\sigma v\rangle$  than those derived by individual instruments. We also show how the uncertainties on the  $J$  factor effects the combined likelihood and degrade the upper limit on  $\langle\sigma v\rangle$  (thick black line). All likelihood profiles are normalized so that the global minimum  $\widehat{\langle\sigma v\rangle}$  is 0. We note that each profile depends on the observational conditions in which a target object was observed. The sensitivity of a given instrument can be degraded and the upper limits less constraining if the observations are performed in non-optimal conditions such as a high zenith angle or a short exposure time.

1257 on  $\langle\sigma v\rangle$  obtained from the combination of the observations of four experiments towards one dSph  
 1258 versus the upper limit from individual instruments. It also shows graphically the effect of the  
 1259  $J$ -factor uncertainty on the combined observations.

1260 The *partial* joint likelihood function for gamma-ray observations of each dSph ( $\mathcal{L}_{\text{dSph},l}$ ) is  
 1261 written as the product of the likelihood terms describing the  $N_{\text{exp},l}$  observations performed with  
 1262 any of our observatories:

$$\mathcal{L}_{\text{dSph},l} (\langle\sigma v\rangle; J_l, \nu_l | \mathcal{D}_l) = \prod_{k=1}^{N_{\text{exp},l}} \mathcal{L}_{lk} (\langle\sigma v\rangle; J_l, \nu_{lk} | \mathcal{D}_{lk}), \quad (5.16)$$

1263 where each  $\mathcal{L}_{lk}$  term refers to an observation of the  $l$ -th dSph with associated  $k$ -th instrument

1264 responses.  $N_{\text{exp},l}$  varies from dSph to dSph and can be inferred from Table 5.2.

1265     Each collaboration separately analyzes their data for  $\mathcal{D}_{lk}$  corresponding to dSph  $l$  and gamma-  
 1266     ray detector  $k$ , using as many common assumptions as possible in the analysis. HAWC's treatment  
 1267     was described earlier in Section 5.4.1 whereas the specifics of the remaining experiments is left to  
 1268     the publication. We compute the values for the likelihood functions  $\mathcal{L}_{lk}$  (see Eq. (5.16)) for a fixed  
 1269     value of  $J_l$  and profile over the rest of the nuisance parameters  $\nu_{lk}$ . Then, values of  $\lambda$  from Eq. (5.11)  
 1270     are computed as a function of  $\langle \sigma v \rangle$ , and shared using a common format. Results are computed for  
 1271     seven annihilation channels,  $W^+W^-$ ,  $ZZ$ ,  $b\bar{b}$ ,  $t\bar{t}$ ,  $e^+e^-$ ,  $\mu^+\mu^-$ , and  $\tau^+\tau^-$  over 62  $m_\chi$  values between  
 1272     5 GeV and 100 TeV provided in [58]. The  $\langle \sigma v \rangle$  range is defined between  $10^{-28}$  and  $10^{-18} \text{cm}^3 \cdot \text{s}^{-1}$ ,  
 1273     with 1001 logarithmically spaced values. The likelihood combination, i.e. Equation (5.12), and  
 1274     profile over the  $J$ -factor to compute the profile likelihood ratio  $\lambda$ , Equation (5.11), are carried out  
 1275     with two different public analysis software packages, namely `gLike` [66] and `LklCom` [67], that  
 1276     provide the same results [68].

1277     As mentioned previously, each experiment computes the  $\mathcal{L}_{lk}$  from Equation (5.11) differently.  
 1278     The remainder of this section highlights the differences in this calculation across the experiments.  
 1279     Four experiments, namely *Fermi*-LAT, H.E.S.S., HAWC and MAGIC, use a binned likelihood to  
 1280     compute the  $\mathcal{L}_{lk}$ . For these experiments, for each observation  $\mathcal{D}_{lk}$  of a given dSph  $l$  carried out  
 1281     using a given gamma-ray detector  $k$ , the binned likelihood function is:

$$\mathcal{L}_{lk} (\langle \sigma v \rangle; J_l, \nu_{lk} | \mathcal{D}_{lk}) = \prod_{i=1}^{N_E} \prod_{j=1}^{N_P} \left[ \mathcal{P}(s_{lk,ij}(\langle \sigma v \rangle, J_l, \nu_{lk}) + b_{lk,ij}(\nu_{lk}) | N_{lk,ij}) \right] \times \mathcal{L}_{lk,\nu} (\nu_{lk} | \mathcal{D}_{\nu_{lk}}) \quad (5.17)$$

1282     where  $N_E$  and  $N_P$  are the number of considered bins in reconstructed energy and arrival direction,  
 1283     respectively;  $\mathcal{P}$  represents a Poisson PDF for the number of gamma-ray candidate events  $N_{lk,ij}$   
 1284     observed in the  $i$ -th bin in energy and  $j$ -th bin in arrival direction, when the expected number is  
 1285     the sum of the expected mean number of signal events  $s_{ij}$  (produced by DM annihilation) and of  
 1286     background events  $b_{ij}$ ;  $\mathcal{L}_{lk,\nu}$  is the likelihood term for the extra  $\nu_{lk}$  nuisance parameters that vary  
 1287     from one instrument  $k$  to another. The expected counts for signal events  $s_{ij}$  for a given dSph  $l$  and

1288 detector  $k$  is given by:

$$s_{ij}(\langle\sigma\nu\rangle, J) = \int_{E'_{\min,i}}^{E'_{\max,i}} dE' \int_{P'_{\min,j}}^{P'_{\max,j}} d\Omega' \int_0^\infty dE \int_{\Delta\Omega_{tot}} d\Omega \int_0^{T_{\text{obs}}} dt \frac{d^2\Phi(\langle\sigma\nu\rangle, J)}{dEd\Omega} \text{IRF}(E', P' | E, P, t) \quad (5.18)$$

1289 where  $E'$  and  $E$  are the reconstructed and true energies,  $P'$  and  $P$  the reconstructed and true  
1290 arrival directions;  $E'_{\min,i}$ ,  $P'_{\min,j}$ ,  $E'_{\max,i}$ , and  $P'_{\max,j}$  are their lower and upper limits of the  $i$ -th  
1291 energy bin and the  $j$ -th arrival direction bin;  $T_{\text{obs}}$  is the (dead-time corrected) total observation  
1292 time;  $t$  is the time along the observations;  $d^2\Phi/dEd\Omega$  is the DM flux in the source region (see  
1293 Equation (5.1)); and  $\text{IRF}(E', P' | E, P, t)$  is the IRF, which can be factorized as the product of the  
1294 effective collection area of the detector  $A_{\text{eff}}(E, P, t)$ , the PDFs for the energy estimator  $f_E(E' | E, t)$ ,  
1295 and arrival direction  $f_P(P' | E, P, t)$  estimators. Note that for Fermi-LAT, HAWC, MAGIC, and  
1296 VERITAS the effect of the finite angular resolution is taken into account through the convolution  
1297 of  $d\Phi/dEd\Omega$  with  $f_P$  in Equation (5.18), whereas in the cases of H.E.S.S.  $f_P$  is approximated by a  
1298 delta function. This approximation has been made in order to maintain compatibility of the result  
1299 with what has been previously published. The difference introduced by this approximation is  $< 5\%$   
1300 for all considered dSphs. A more comprehensive review of the differences between the analyses of  
1301 different instruments can be found in [40].

## 1302 5.5 HAWC Results

1303 13 of the 20 dSphs considered for the Glory Duck analysis are within HAWC's field of view.  
1304 These dSph are analyzed for emission from DM annihilation according to the likelihood method  
1305 described in Section 5.4. The 13 likelihood profiles are then stacked to synthesize a combined  
1306 limit on the dark matter cross-section,  $\langle\sigma\nu\rangle$ . This combination is done for the 7 SM annihilation  
1307 channels used in the Glory Duck analysis. Figure 5.5 shows the combined limit for all annihilation  
1308 channels with HAWC only observations. We also perform 300 studies of Poisson trials on the  
1309 background. These trials are used to produce HAWC sensitivities with  $\pm 1\sigma$  and  $\pm 2\sigma$  uncertainty  
1310 bands which were shared with the other collaborators for combination. The results on fitting to  
1311 HAWC's Poisson trials of the DM hypothesis is shown in Figure 5.7 for all the DM annihilation  
1312 channels studied for Glory Duck.

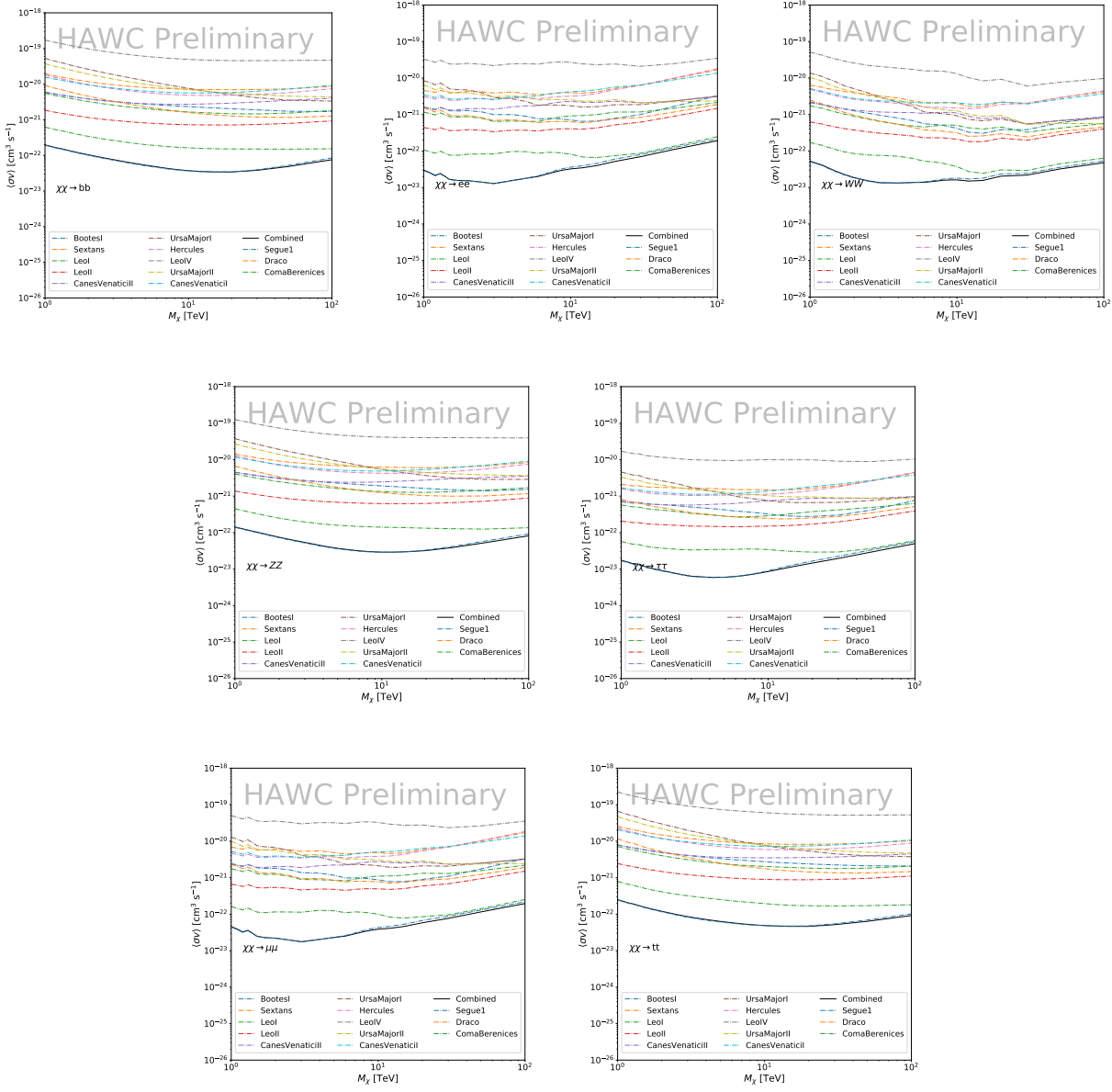


Figure 5.5

1313     No DM was found in HAWC observations. HAWC's limits are dominated by the dSphs Segue1  
 1314     and Coma Berenices. The remaining 11 dSphs do not contribute significantly to the limit because  
 1315     they are at high zenith and/or have much smaller  $J$  factors. Even though some remaining dSphs  
 1316     have large  $J$  factors, they are towards the edge of HAWC's field of view where HAWC analysis is  
 1317     less sensitive.

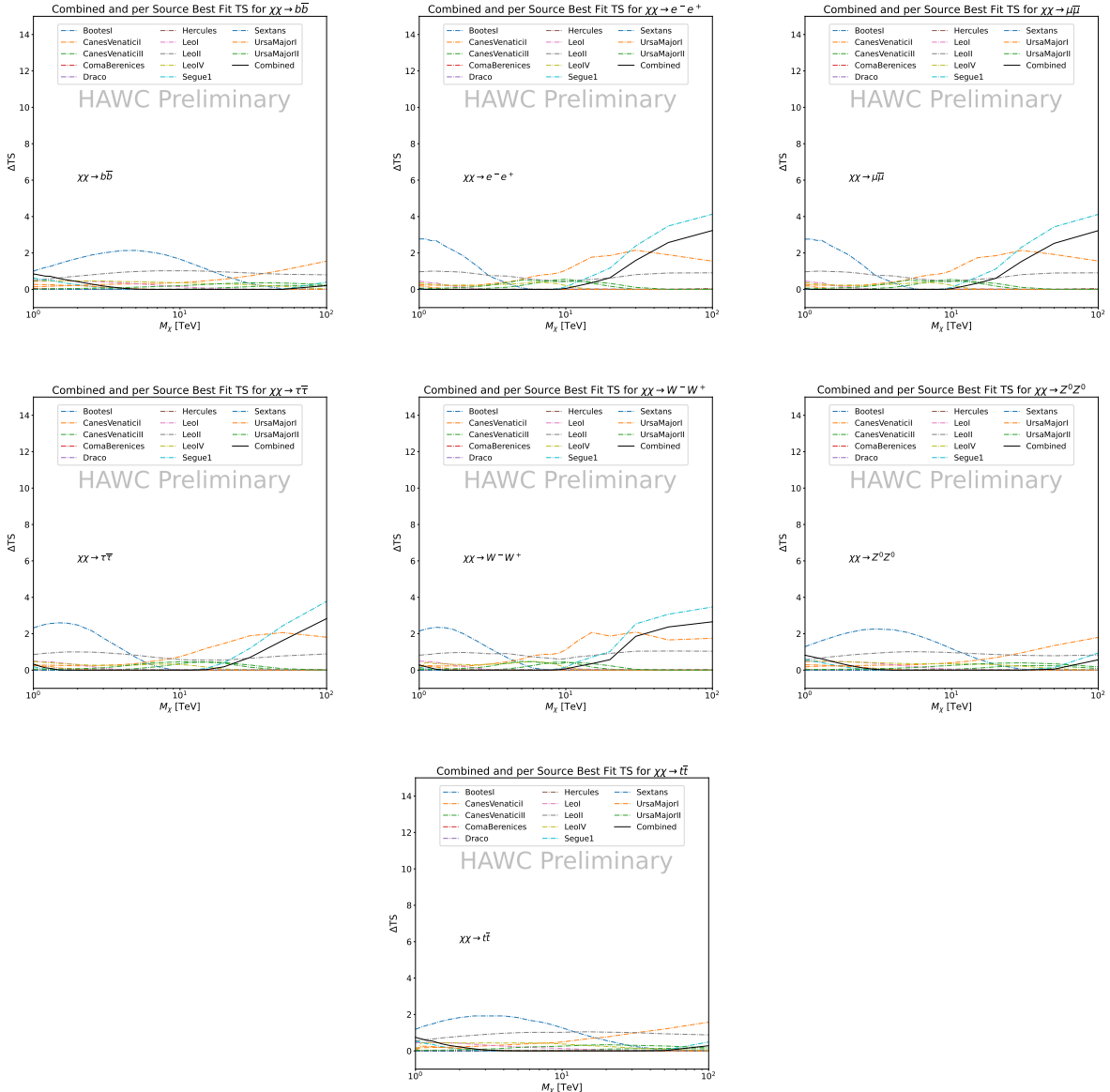


Figure 5.6 HAWC TS values for best fit  $\langle\sigma v\rangle$  versus  $m_\chi$  for seven SM annihilation channels with  $J$  factors from  $\mathcal{GS}$ . The solid black line shows the combined best fit TS values. The colored, dashed lines are the TS values for each of the 13 sources HAWC studied.

## 1318 5.6 Glory Duck Combined Results

1319 The crux of this analysis is that HAWC's results are combined with 4 other gamma-ray observa-  
 1320 tories: Fermi-LAT, H.E.S.S., MAGIC, and VERITAS. No significant DM emission was observed  
 1321 by any of the five instruments. We present the upper limits on  $\langle\sigma v\rangle$  assuming seven independent  
 1322 DM self annihilation channels, namely  $W^+W^-$ ,  $Z^+Z^-$ ,  $b\bar{b}$ ,  $t\bar{t}$ ,  $e^+e^-$ ,  $\mu^+\mu^-$ , and  $\tau^+\tau^-$ . The 68%

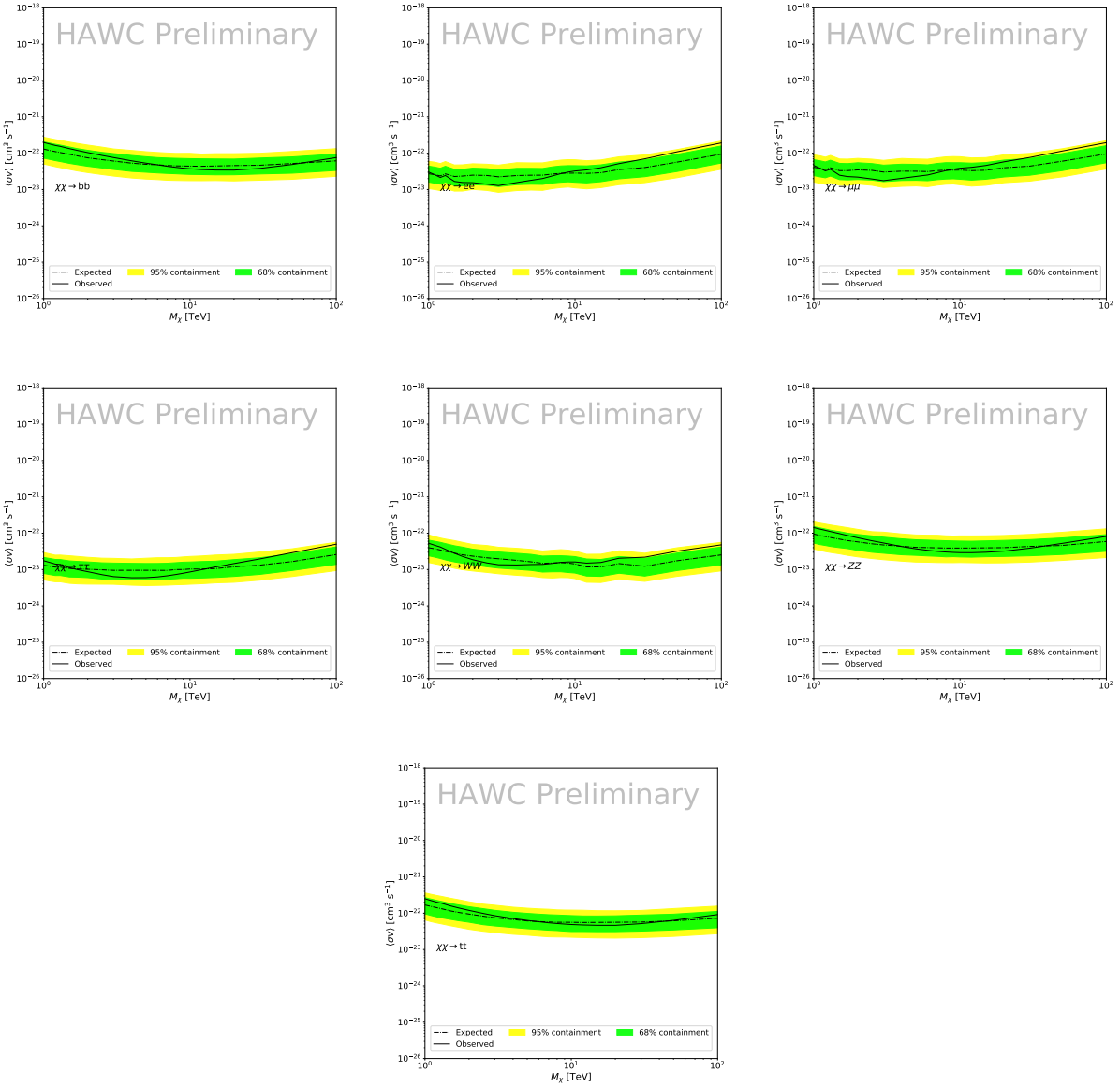


Figure 5.7 HAWC Brazil bands at 95% confidence level on  $\langle\sigma v\rangle$  versus DM mass for seven annihilation channels with  $J$ -factors from GS [69]. The solid line represents the combined limit from 13 dSphs. The dashed line is the expected limit. The green band is the 68% containment. The yellow band is the 95% containment.

1323 and 95% containment bands are produced from 300 Poisson realizations of the null hypothesis  
 1324 corresponding to each of the combined datasets. These 300 realizations are combined identically  
 1325 to dSph observations. The containment bands and the median are extracted from the distribution  
 1326 of resulting limits on the null hypothesis. These 300 realizations are obtained either by fast simu-  
 1327 lations of the OFF observations, for H.E.S.S., MAGIC, VERITAS, and HAWC, or taken from real

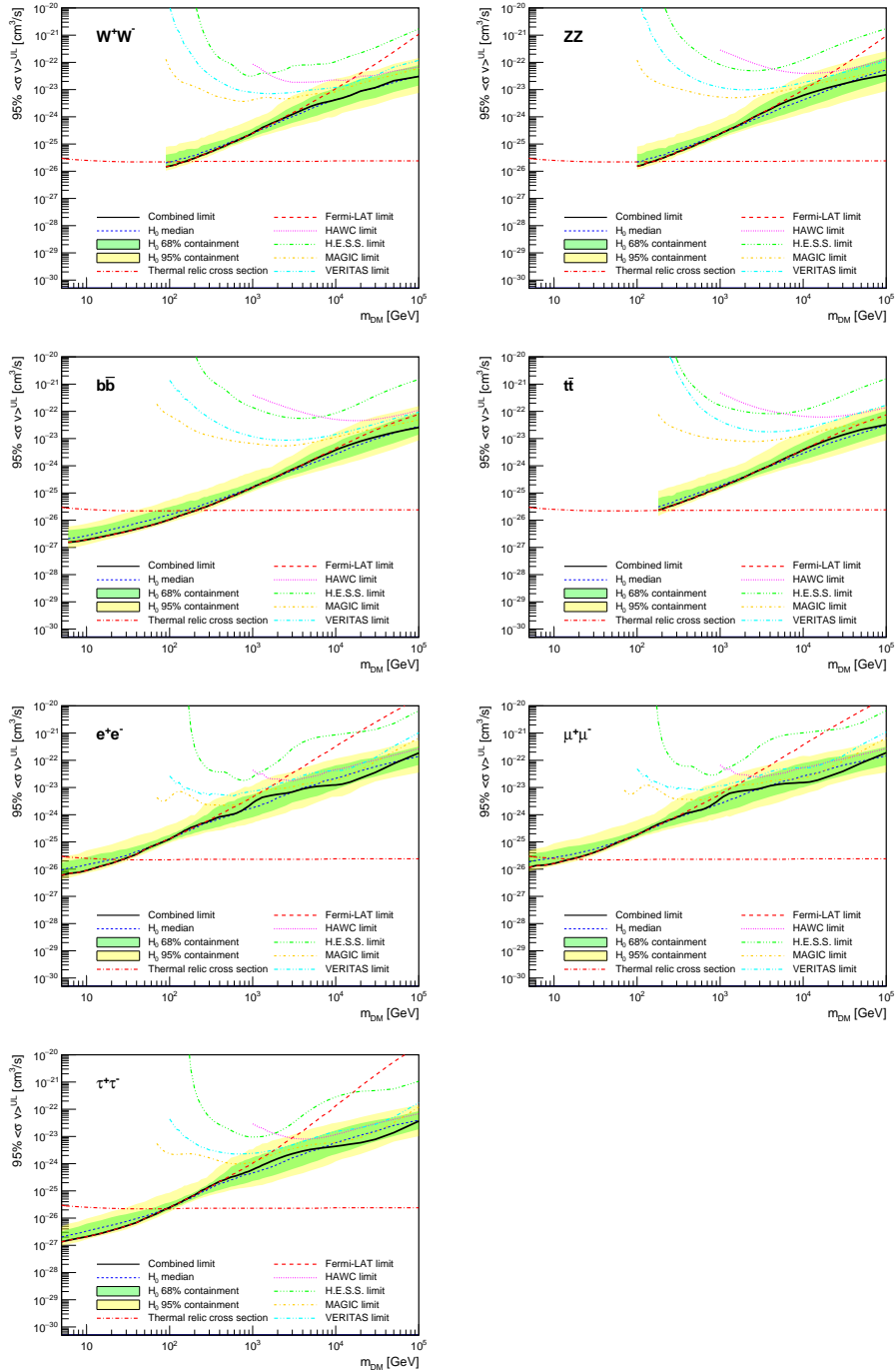


Figure 5.8 Upper limits at 95% confidence level on  $\langle\sigma v\rangle$  in function of the DM mass for eight annihilation channels, using the set of  $J$  factors from Ref. [69] ( $\mathcal{GS}$  set in Table 5.1). The black solid line represents the observed combined limit, the black dashed line is the median of the null hypothesis corresponding to the expected limit, while the green and yellow bands show the 68% and 95% containment bands. Combined upper limits for each individual detector are also indicated as solid, colored lines. The value of the thermal relic cross-section in function of the DM mass is given as the red dotted-dashed line [70].

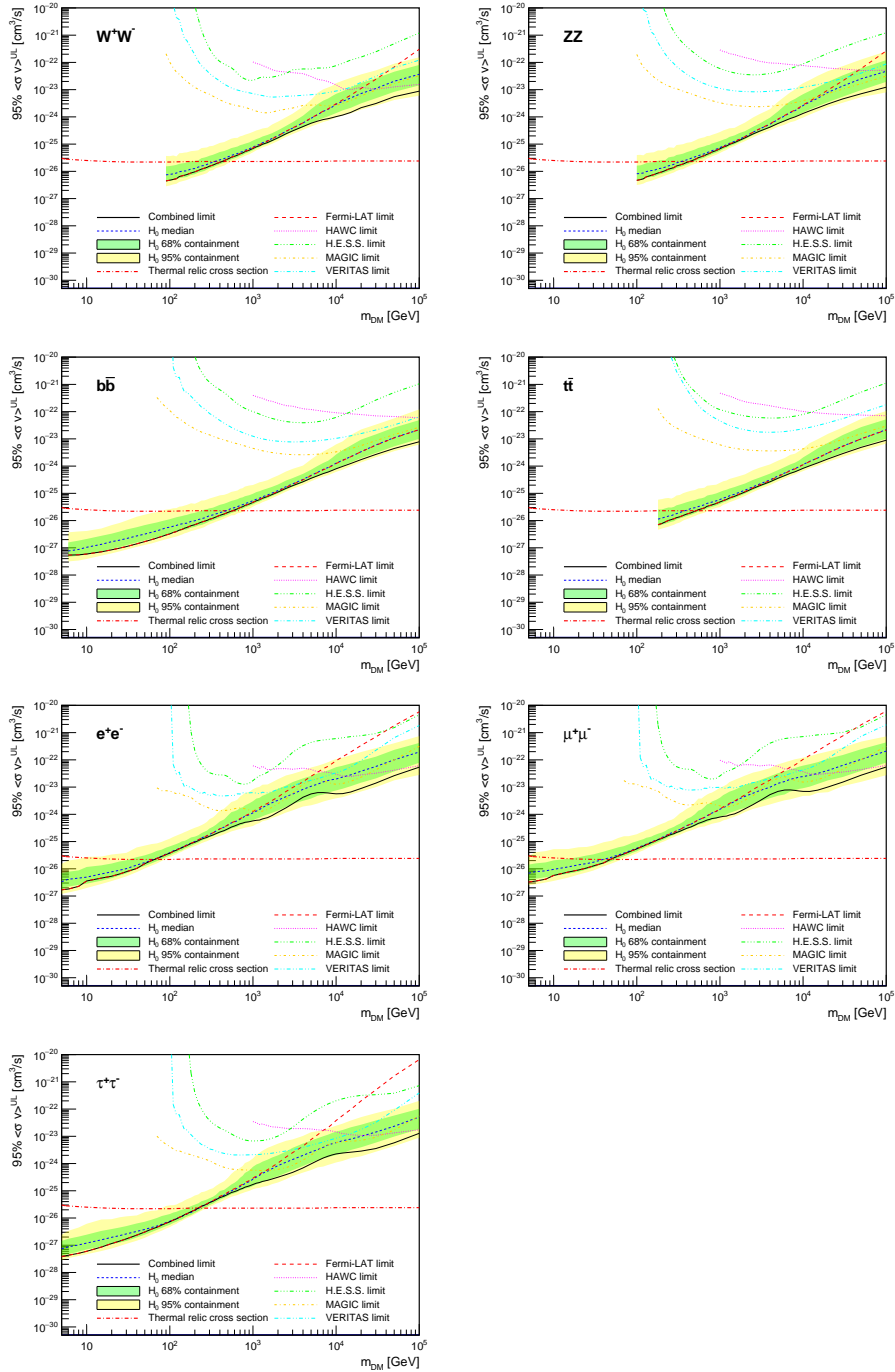


Figure 5.9 Same as Fig. 5.8, using the set of  $J$  factors from Ref. [63, 71] ( $\mathcal{B}$  set in Table 5.1).

1328 observations of empty fields of view in the case of Fermi-LAT [64, 72, 73].

1329 The obtained limits are shown in Figure 5.8 for the  $\mathcal{GS}$  set of  $J$ -factors [69] and in Figure 5.9  
1330 for the  $\mathcal{B}$  set of  $J$ -factors [63, 71]. The combined limits are presented with their 68% and 95%  
1331 containment bands, and are expected to be close to the median limit when no signal is present.

1332 We observe agreement with the null hypothesis for all channels, within  $2\sigma$  standard deviations,  
1333 between the observed limits and the expectations given by the median limits. Limits obtained from  
1334 each detector are also indicated in the figures, where limits for all dSphs observed by the specific  
1335 instrument have been combined.

1336 Below  $\sim 300$  GeV, the *Fermi*-LAT dominates the DM limits for all annihilation channels. From  
1337  $\sim 300$  GeV to  $\sim 2$  TeV, *Fermi*-LAT continues to dominate for the hadronic and bosonic DM channels,  
1338 yet the IACTs (H.E.S.S., MAGIC, and VERITAS) and *Fermi*-LAT all contribute to the limit for  
1339 leptonic DM channels. For DM masses between  $\sim 2$  TeV to  $\sim 10$  TeV, the IACTs dominate leptonic  
1340 DM annihilation channels, whereas both the *Fermi*-LAT and the IACTs dominate bosonic and  
1341 hadronic DM annihilation channels. From  $\sim 10$  TeV to  $\sim 100$  TeV, both the IACTs and HAWC  
1342 contribute significantly to the leptonic DM limit. For hadronic and bosonic DM, the IACTs and  
1343 *Fermi*-LAT both contribute strongly.

1344 We notice that the limits computed using the  $\mathcal{B}$  set of  $J$ -factor are always better compared to the  
1345 ones calculated with the  $\mathcal{GS}$  set. For the  $W^+W^-$ ,  $Z^+Z^-$ ,  $b\bar{b}$ , and  $t\bar{t}$  channels, the ratio between the  
1346 limits computed with the two sets of  $J$ -factor is varying between a factor of  $\sim 3$  and  $\sim 5$  depending  
1347 on the energy, with the largest ratio around 10 TeV. For the channels  $e^+e^-$ ,  $\mu^+\mu^-$ , and  $\tau^+\tau^-$ , the  
1348 ratio lies between  $\sim 2$  to  $\sim 6$ , being maximum around 1 TeV. Examining Figure 5.16 and Figure 5.17  
1349 in Section 5.8, these differences are explained by the fact that the  $\mathcal{B}$  set provides higher  $J$ -factors  
1350 for the majority of the studied dSphs, with the notable exception of Segue I. The variation on the  
1351 ratio of the limits for the two sets is due to different dSph dominating the limits depending on the  
1352 energy. One set,  $\mathcal{B}$ , pushes the range of which thermal cross-section which can be excluded to  
1353 higher mass. This comparison demonstrates the magnitude of systematic uncertainties associated  
1354 with the choice of the  $J$ -factor calculation. The  $\mathcal{GS}$  and  $\mathcal{B}$  sets present a difference in the limits for  
1355 all channels of about This difference is explained, see Figure 5.16 and Figure 5.17, by the fact that  
1356 the  $\mathcal{B}$  set provides higher  $J$ -factors for all dSph except for Segue I.

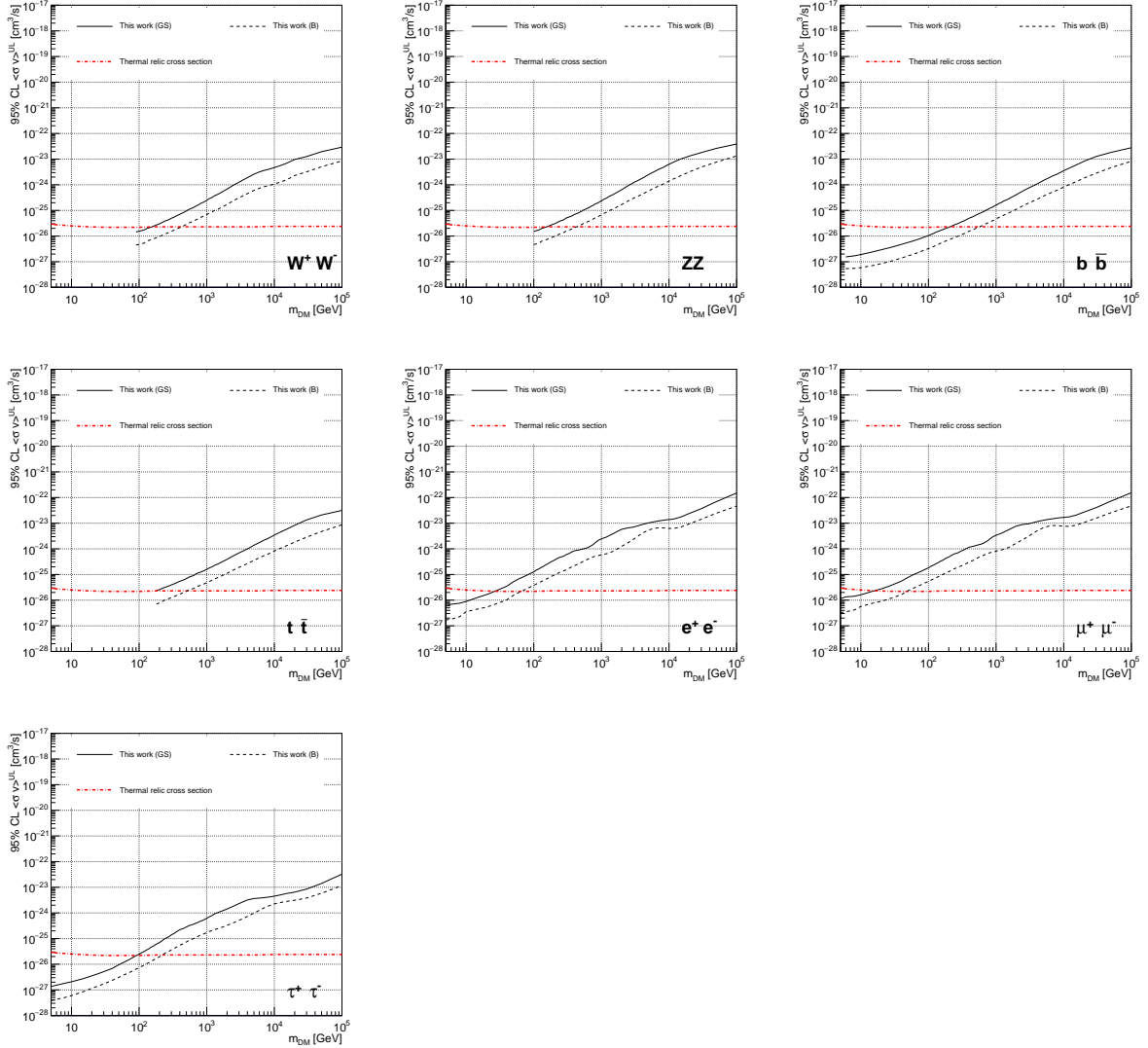


Figure 5.10 Comparisons of the combined limits at 95% confidence level for each of the eight annihilation channels when using the  $J$  factors from Ref. [69] ( $\mathcal{GS}$  set in Table 5.1), plain lines, and the  $J$  factor from Ref. [63, 71] ( $\mathcal{B}$  set in Table 5.1), dashed lines. The cross-section given by the thermal relic is also indicated [70].

## 1357 5.7 HAWC Systematics

### 1358 5.7.1 Inverse Compton Scattering

1359 The DM-DM annihilation channels produce many high energy electrons regardless of the  
 1360 primary annihilation channel. These high energy electrons can produce high energy gamma-rays  
 1361 through Inverse Compton Scattering (ICS). If this effect is strong, it would change the morphology  
 1362 of the source and increase the total expected gamma-ray counts from any source. The PPPC [58]

1363 provides tools in Mathematica for calculating the impact of ICS for an arbitrary location in the  
1364 sky for a specified annihilation channel. We calculated the change in gamma-ray counts for DM  
1365 annihilation to primary  $e\bar{e}$  for RA and Dec corresponding to Segue1 and Coma Berenices. These  
1366 dSphs were chosen because they are the strongest contributors to the limit.  $e\bar{e}$  was selected because  
1367 it would have the largest number of high energy electrons. The effect was found to be on the order  
1368 of  $10^{-7}$  on the gamma-ray spectrum. As a result, this systematic is not considered in our analysis.

1369 **5.7.2 Point Source Versus Extended Source Limits**

1370 The previous DM search toward dSph approximated the dSphs as point sources [60]. In  
1371 this analysis, the dSphs are implemented as extended with J-factor distributions following those  
1372 produced by [69]. The resolution of the cited map is much finer than HAWC's angular resolution.  
1373 The vast majority of the J-factor distribution is represented on the central HAWC pixel of the dSph  
1374 spatial map. However, the neighboring 8 pixels are not negligible and contribute to our limit.

1375 Figure 5.11 shows a substantial improvement to the limit for Segue1. Fig. 5.12 however showed  
1376 identical limits. These disparities are best explained by the relative difference in their J-Factors.  
1377 Both dSphs pass almost overhead the HAWC detector, however Segue1 has the larger J-Factor  
1378 between the two. Adjacent pixels to the central pixel will therefore contribute to the limits. This is  
1379 the case for other dSph that are closer to the zenith of the HAWC detector.

1380 Comparison plots for all sources and the combined limit can be found in the sandbox for the  
1381 Glory Duck project.

1382 **5.7.3 Impact of Pointing Systematic**

1383 During the analysis it was discovered that directional reconstruction of gamma-rays had a  
1384 systematic bias at large zenith angles. Slides describing this systematic can be found [here](#). Shown  
1385 on the presentation is dependence on the pointing systematic on declination. New spatial profiles  
1386 were generated for every dSph and limits were computed for the adjusted declination.

1387 Section 5.7.3 demonstrates the impact of this systematic for all DM annihilation channels  
1388 studied by HAWC. The impact is a tiny improvement, yet mostly identical, to the combined limits.

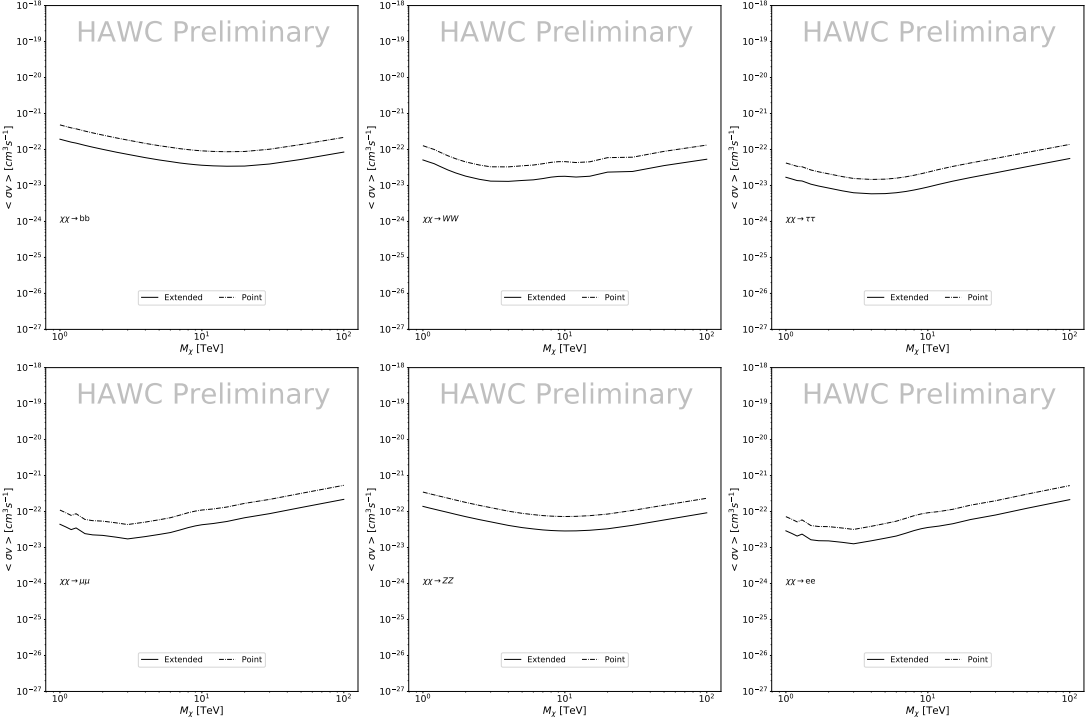


Figure 5.11 Comparisons of the combined limits at 95% confidence level for a point source analysis and extended source using [69]  $\mathcal{GS}$  J-factor distributions and PPPC [58] annihilation spectra. Shown are the limits for Segue1 which will have the most significant impact on the combined limit. 6 of the 7 DM annihilation channels are shown. Solid lines are extended source studies. Dashed lines are point source studies. Overall, the extended source analysis improves the limit by a factor of 2.

## 1389 5.8 J-factor distributions

### 1390 5.8.1 Numerical integration of $\mathcal{GS}$ maps

1391 It was discovered well after the HAWC analysis was completed that the published tables from  
 1392  $\mathcal{GS}$  [59] quoted median  $J$ -factors were computed in a non-trivial manner. The assumption myself  
 1393 and collaborators had been that the published tables represented the  $J$ -factor as a function of  $\theta$  for  
 1394 the best global fit model on a per-source basis. However, this is not the case. Instead, what is  
 1395 published are the best fit model for each dwarf that only considers stars up to the angular separation  
 1396  $\theta$ . Therefore, the model is changing for each value of  $\theta$  for each dwarf. Yet, the introduced features  
 1397 from unique models at each  $\theta$  are much smaller than the angular resolution of HAWC. It is not  
 1398 expected for these effects to impact the limits and TS greatly as a result.

1399 Median  $J$ -factor model profiles were provided by the authors. New maps were generated

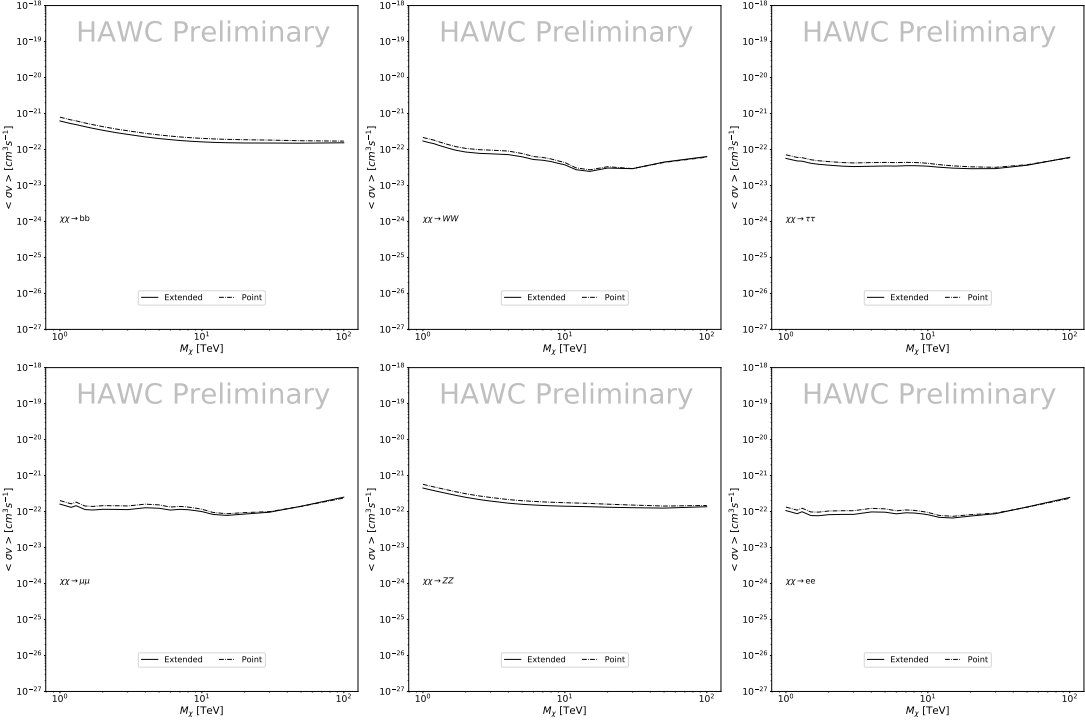


Figure 5.12 Same as Fig. 5.11 on Coma Berenices. This dSph also contributes significantly to the limit. The limits are identical in this case.

1400 and analyzed for Segue1 and Coma Berenices. Figure 5.14 shows the differential between maps  
 1401 generated with the method from Section 5.8.1 and from the authors of [59]. These maps were  
 1402 reanalyzed for all SM DM annihilation channels. Upper limits for these channels are shown in  
 1403 Figure 5.15

1404 From Figure 5.15, we can see that the impact of these model difference was no substantial.  
 1405 The observed impact was a fractional effect which is much smaller than the impact from selecting  
 1406 another DM spatial distribution model as was shown in Figure 5.10.

### 1407 **5.8.2 $\mathcal{GS}$ Versus $\mathcal{B}$ spatial models**

1408 We show in this appendix a comparison between the  $J$ -factors computed by Geringer-Sameth  
 1409 *et al.* [69] (the  $\mathcal{GS}$  set) and the ones computed by Bonnivard *et al.* [63, 71] (the  $\mathcal{B}$  set). The  
 1410  $\mathcal{GS}$   $J$ -factors are computed through a Jeans analysis of the kinematic stellar data of the selected  
 1411 dSphs, assuming a dynamic equilibrium and a spherical symmetry for the dSphs. They adopted  
 1412 the generalized DM density distribution, known as Zhao-Hernquist, introduced by [61], carrying

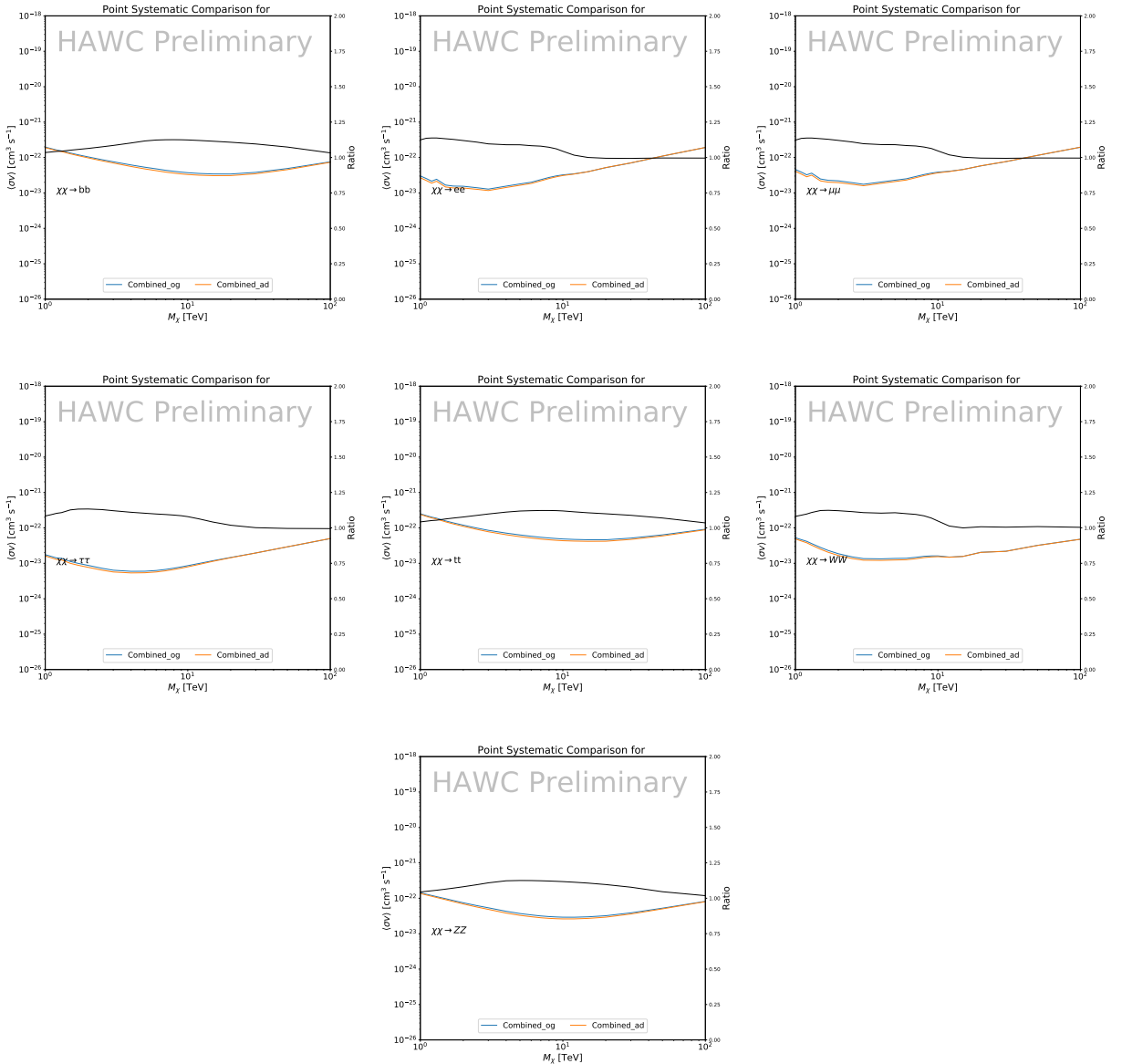


Figure 5.13 Comparison of combined limits when correcting for HAWC's pointing systematic. All DM annihilation channels are shown. The solid black line is the ratio between published limit to the declination corrected limit. The blue solid line or "Combined\_og" represented the limits computed for Glory Duck. The solid orange line or "Combined\_ad" represented the limits computed after correcting for the pointing systematic.

1413 three additional index parameters to describe the inner and outer slopes, and the break of the  
 1414 density profile. Such a profile parametrization allows the reduction of the theoretical bias from  
 1415 the choice of a specific radial dependency on the kinematic data. In other words, the increase of  
 1416 free parameters with the use of the Zhao-Hernquist profile allows a better description of the mass

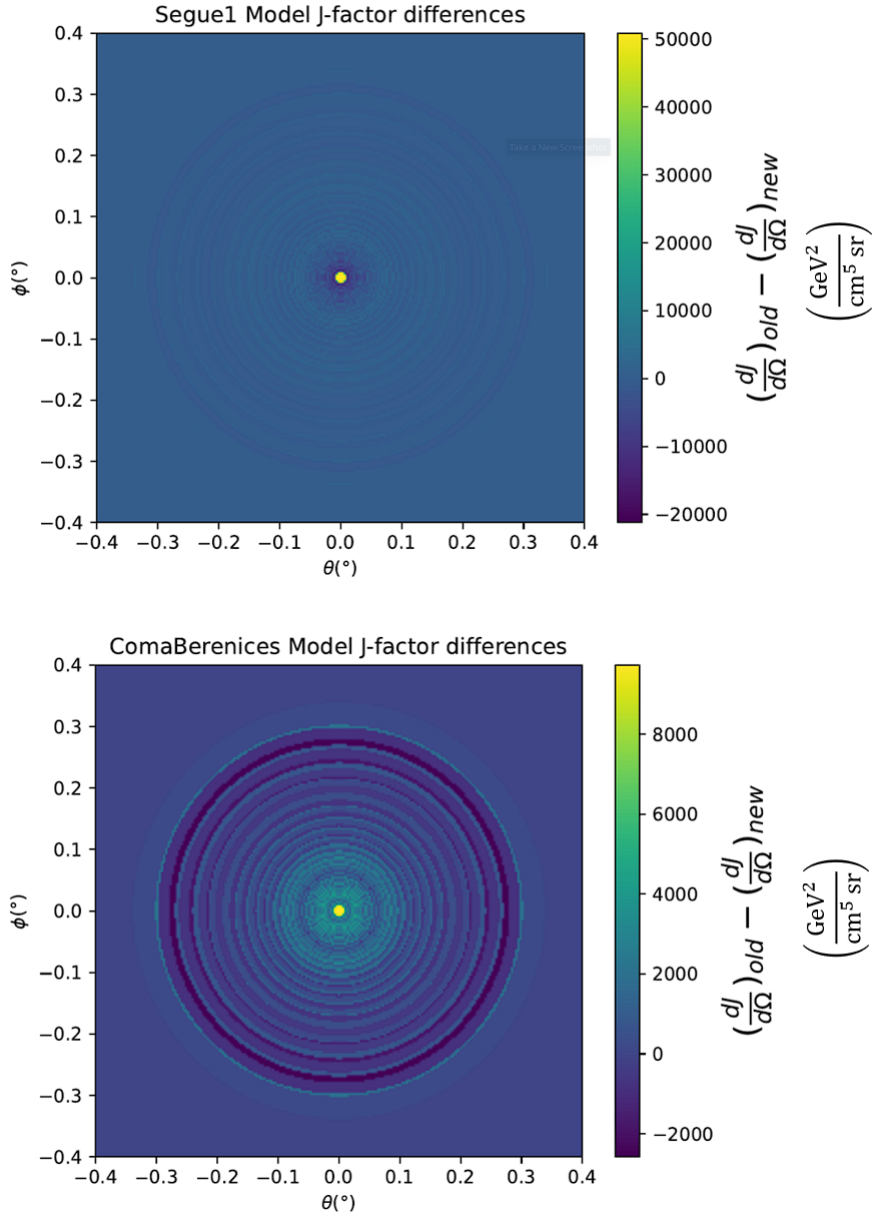


Figure 5.14 Differential map of  $dJ/\Omega$  from model built in Section 5.8.1 and profiles provided directly from authors. (Top) Differential from Segue1. (bottom) Differential from Coma Berenices. Note that their scales are not the same. Segue1 shows the deepest discrepancies which is congruent with its large uncertainties. Both models show anuli where unique models become apparent.

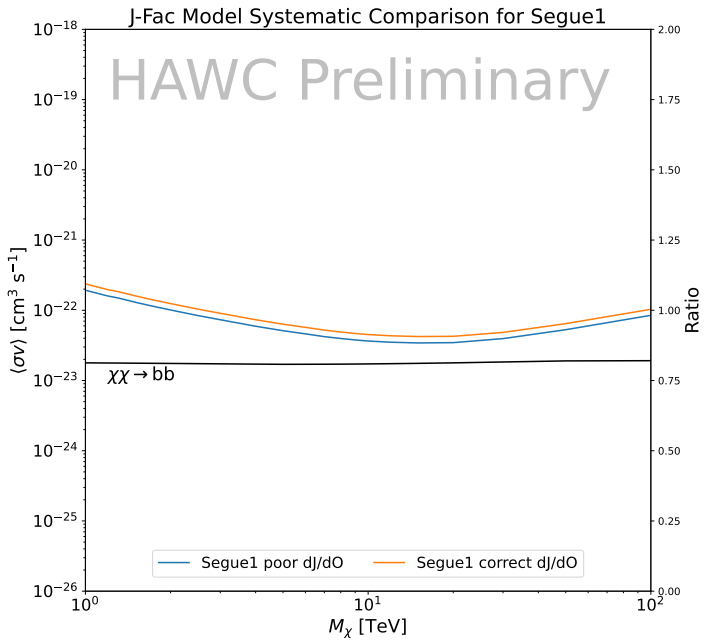
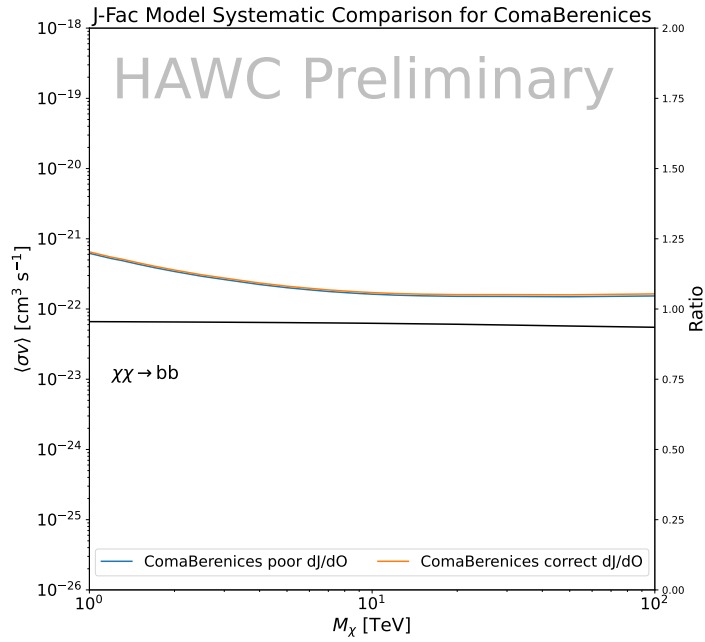


Figure 5.15 HAWC limits for Coma Berenices (top) and Segue1 (bottom) for two different map sets. Blue lines are limits calculated on maps with poor model representation. Orange lines are limits calculated on spatial profiles provided by the authors of [59]. Black line is the ratio of the poor spatial model limits to the corrected spatial models. The left y-axis measures  $\langle \sigma v \rangle$  for the blue and orange lines. The right y-axis measures the ratio and is unitless.

1417 density distribution of dark matter.

1418 In addition, a constant velocity anisotropy profile and a Plummer light profile [74] for the stellar  
1419 distribution were assumed. The velocity anisotropy profile depends on the radial and tangential  
1420 velocity dispersion. However, its determination remains challenging since only the line-of-sight  
1421 velocity dispersion can be derived from velocity measurements. Therefore, the parametrization of  
1422 the anisotropy profile is obtained from simulated halos (see [75] for more details). They provide the  
1423 values of the  $J$ -factors of regions extending to various angular radius up to the outermost member  
1424 star.

1425 The  $\mathcal{B}$   $J$ -factors were computed through a Jeans analysis taking into account the systematic  
1426 uncertainties induced by the DM profile parametrization, the radial velocity anisotropy profile, and  
1427 the triaxiality of the halo of the dwarf galaxies. They performed a more complete study of the dSph  
1428 kinematics and dynamics than  $\mathcal{GS}$  for the determination of the  $J$ -factor. Conservative values of the  
1429  $J$ -factors where obtained using an Einasto DM density profile [76], a realistic anisotropy profile  
1430 known as the Baes & Van Hese profile [77] which takes into account that the inner regions can be  
1431 significantly non-isotropic, and a Zhao-Hernquist light profile [61].

1432 For both sets,  $J$ -factor values are provided for all dSphs as a function of the radius of the  
1433 integration region [69, 63, 71]. Table 5.1 shows the heliocentric distance and Galactic coordinates  
1434 of the twenty dSphs, together with the two sets of  $J$ -factor values integrated up to the outermost  
1435 observed star for  $\mathcal{GS}$  and the tidal radius for  $\mathcal{B}$ . Both  $J$ -factor sets were derived through a Jeans  
1436 analysis based on the same kinematic data, except for Draco where the measurements of [78] have  
1437 been adopted in the computation of the  $\mathcal{B}$  value. The computations for producing the  $\mathcal{GS}$  and  $\mathcal{B}$   
1438 samples differ in the choice of the DM density, velocity anisotropy, and light profiles, for which the  
1439 set  $\mathcal{B}$  takes into account some sources of systematic uncertainties.

1440 Figure 5.16 and Figure 5.17 show the comparisons for the  $J$ -factor versus the angular radius  
1441 for each of the 20 dSphs used in this study. The uncertainties provided by the authors are also  
1442 indicated in the figures. For the  $\mathcal{GS}$  set, the computation stops at the angular radius corresponding  
1443 to the outermost observed star, while for the  $\mathcal{B}$  set, the computation stops at the angular radius

1444 corresponding to the tidal radius.

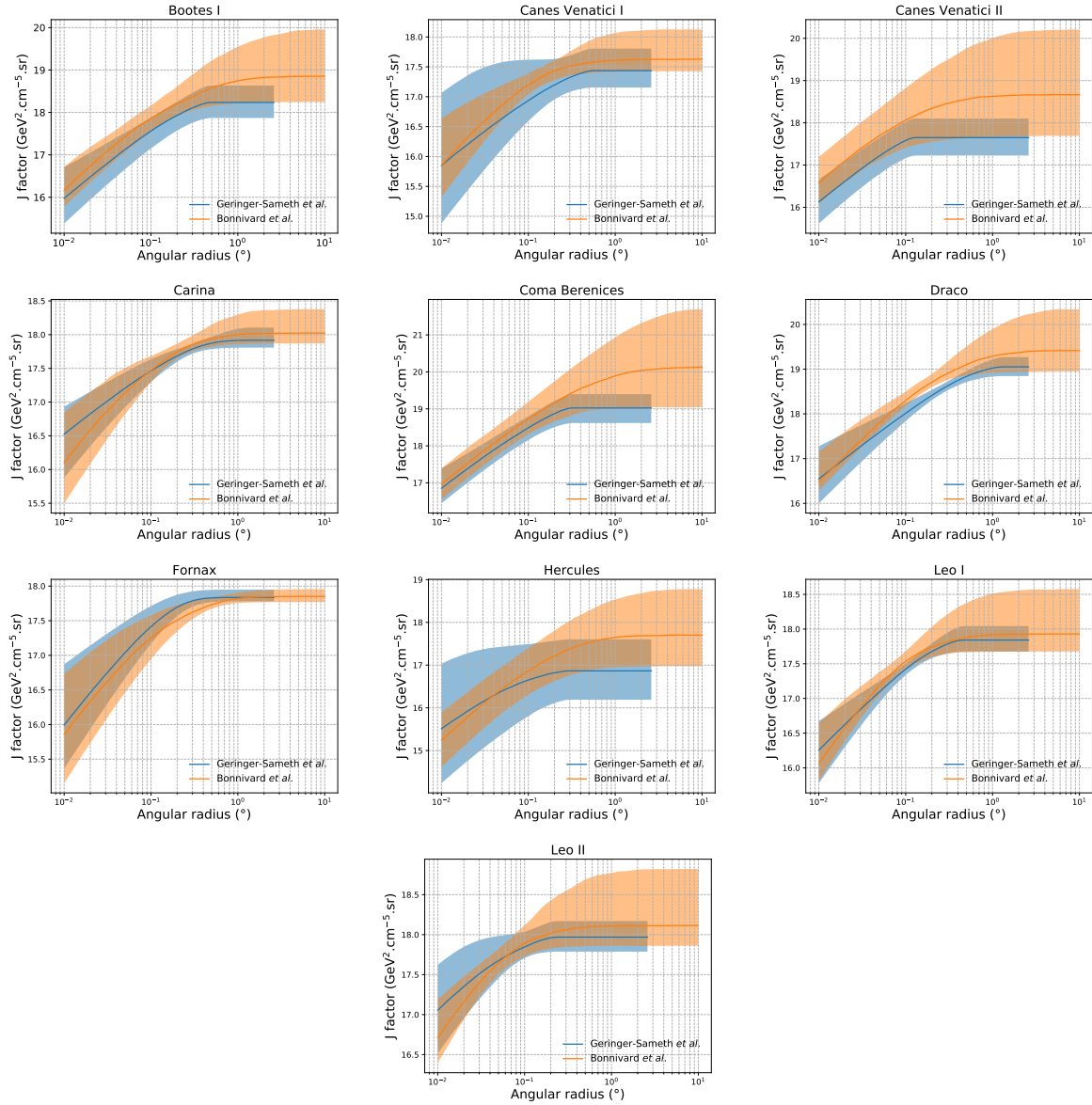


Figure 5.16 Comparisons between the  $J$ -factors versus the angular radius for the computation of  $J$  factors from Ref. [69] ( $\mathcal{GS}$  set in Table 5.1) in blue and for the computation from Ref. [63, 71] ( $\mathcal{B}$  set in Tab. 5.1) in orange. The solid lines represent the central value of the  $J$ -factors while the shaded regions correspond to the  $1\sigma$  standard deviation.

## 1445 5.9 Discussion and Conclusions

1446 In this multi-instrument analysis, we have used observations of 20 dSphs from the gamma-ray  
 1447 telescopes Fermi-LAT, H.E.S.S., MAGIC, VERITAS, and HAWC to perform a collective DM  
 1448 search annihilation signals. The data were combined across sources and detectors to significantly

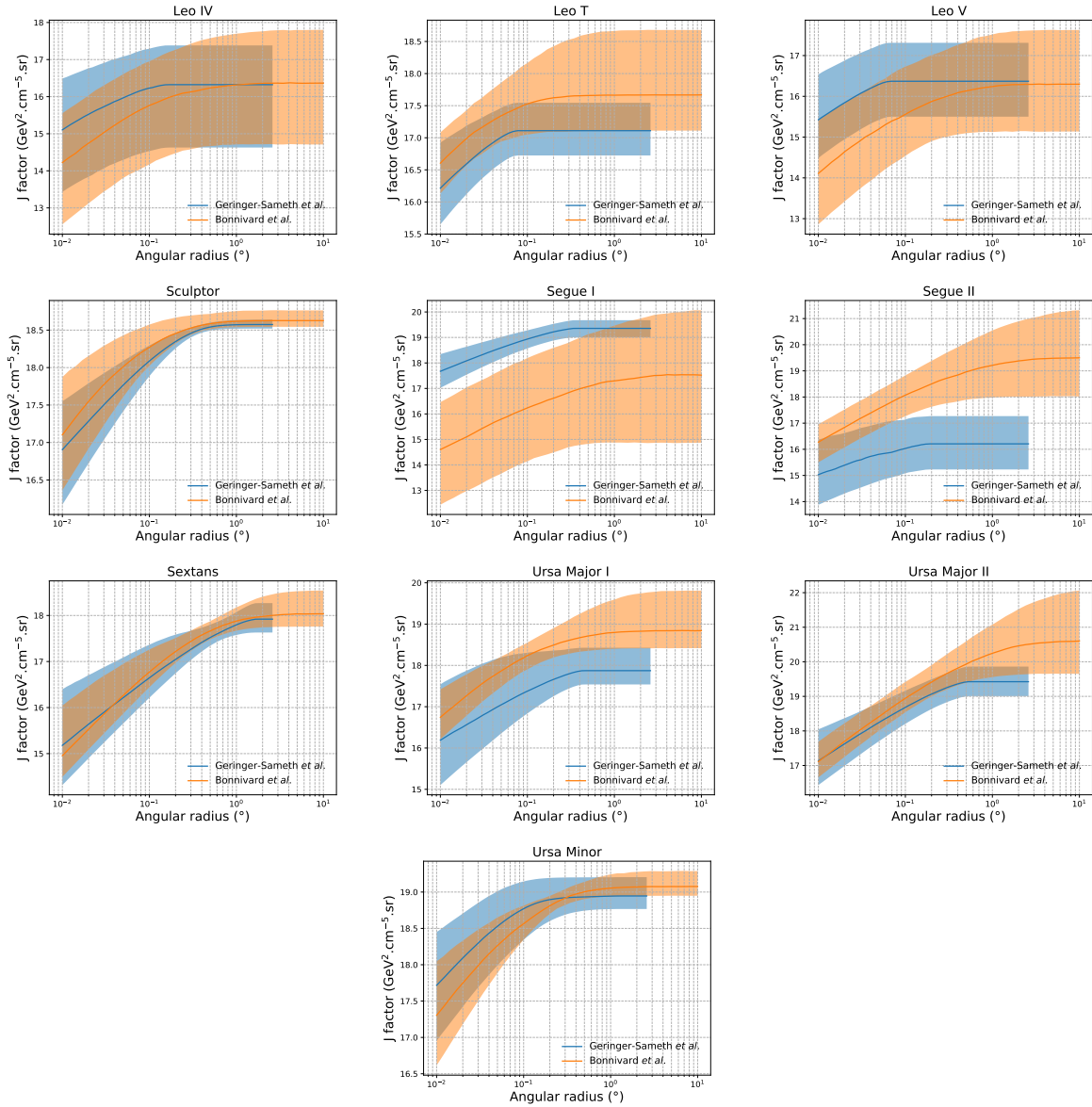


Figure 5.17 Comparisons between the  $J$ -factors versus the angular radius for the computation of  $J$  factors from Ref. [69] ( $\mathcal{GS}$  set in Tab. 5.1) in blue and for the computation from Ref. [63, 71] ( $\mathcal{B}$  set in Tab. 5.1) in orange. The solid lines represent the central value of the  $J$ -factors while the shaded regions correspond to the  $1\sigma$  standard deviation.

1449 increase the sensitivity of the search. We have observed no significant deviation from the null, no  
 1450 DM hypothesis, and so present our results in terms of upper limits on the annihilation cross-section  
 1451 for seven potential DM annihilation channels.  
 1452 Fermi-LAT brings the most stringent constraints for continuum channels below approximately  
 1453 1 TeV. The remaining detectors dominate at higher energies. Overall, for multi-TeV DM mass,

1454 the combined DM constraints from all five telescopes are 2-3 times stronger than any individual  
1455 telescope for multi-TeV DM.

1456     Derived from observations of many dSphs, our results produce robust limits given the DM  
1457 content of the dSphs is relatively well constrained. The obtained limits span the largest mass  
1458 range of any WIMP DM search. Our combined analysis improves the sensitivity over previously  
1459 published results from each detector which produces the most stringent limits on DM annihilation  
1460 from dSphs. These results are based on deep exposures of the most promising known dSphs with  
1461 the currently most sensitive gamma-ray instruments. Therefore, our results constitute a legacy of  
1462 a generation of gamma-ray instruments on WIMP DM searches towards dSphs. Our results will  
1463 remain the reference in the field until a new generation of more sensitive gamma-ray instruments  
1464 begin operations, or until new dSphs with higher  $J$ -factors are discovered.

1465     This analysis serves as a proof of concept for future multi-instrument and multi-messenger  
1466 combination analyses. With this collaborative effort, we have managed to sample over four orders  
1467 in magnitude in gamma-ray energies with distinct observational techniques. Determining the nature  
1468 of DM continues to be an elusive and difficult problem. Larger datasets with diverse measurement  
1469 techniques could be essential to tackling the DM problem. A future collaboration using similar  
1470 techniques as the ones described in this paper could grow even beyond gamma rays. The models we  
1471 used for this study include annihilation channels with neutrinos in the final state. Advanced studies  
1472 could aim to merge our results with those from neutrino observatories with large data sets. Efforts  
1473 are already underway to add data from the IceCube, ANTARES, and KM3NeT observatories to  
1474 these gamma-ray results.

1475     From this work, a selection of the best candidates for observations, according to the latest  
1476 knowledge on stellar dynamics and modelling techniques for the derivation of the  $J$ -factors on  
1477 the potential dSphs targets, is highly desirable at the time that new experiments are starting their  
1478 dark matter programs using dSphs. Given the systematic uncertainty inherent to the derivation of  
1479 the  $J$ -factors, an informed observational strategy would be to select both objects with the highest  
1480  $J$ -factors that could lead to DM signal detection, and objects with robust  $J$ -factor predictions, i.e.

1481 with kinematic measurements on many bright stars, which would strengthen the DM interpretation  
1482 reliability of the observation outcome.

1483 This analysis combines data from multiple telescopes to produce strong constraints on astro-  
1484 physical objects. From this perspective, these methods can be applied beyond just DM searches.  
1485 Almost every astrophysical study can benefit from multi-telescope, multi-wavelength gamma-ray  
1486 studies. We have enabled these telescopes to study the cosmos with greater precision and detail.  
1487 Many astrophysical searches can benefit from multi-instrument gamma-ray studies, for which our  
1488 analysis lays the foundation.

## CHAPTER 6

### MULTITHREADING HAWC ANALYSES FOR DARK MATTER SEARCHES

#### 6.1 Introduction

HAWC's current software suite, plugins to 3ML and HAL [68, 34], do not fully utilize computational advancements of recent decades. Said advancements include the proliferation of Graphical Processing Units (GPUs), and multithreading on multicore processors. The analysis described in chapter 5 took up to 3 months of wall time waiting for the full gambit of data analysis and simulation of background to compute. Additionally, with the updated 2D energy binning scheme,  $f_{\text{hit}}$  and Neural Network (NN), the time needed to compute expected to grow. Although excessive computing time was, in part, from an intense use of a shared computing cluster, it was evident that there was room for improvement. In HAWC's next generation dSph DM search, I decided to develop codes that would utilize the multicore processors on modern high performance computing clusters. The results of this work are featured in this chapter and brought a human timing improvement to computation that scales approximately as  $1/N$  where  $N$  is the number of threads.

#### 6.2 Dataset and Background

This section enumerates the data and background methods used for HAWC's multithreaded study of dSphs. Section 6.2.1 and Section 6.2.2 are most useful for fellow HAWC collaborators looking to replicate a multithreaded dSph DM search.

##### 6.2.1 Itemized HAWC files

These files are only available within HAWC's internal documentation and collaborators. They are not meant for public access, and are presented here so that HAWC collaborators can reproduce results accurately.

- Detector Resolution: `refit-Pass5-Final-NN-detRes-zenith-dependent.root`
- Data Map: `Pass5-Final-NN-maptree-ch103-ch1349-zenith-dependent.root`
- Spectral Dictionary: `HDMspectra_dict_gamma.npy`

1513 **6.2.2 Software Tools and Development**

1514 This analysis was performed using HAL and 3ML [34, 57] in Python3. I built software  
1515 in collaboration with Michael Martin and Letrell Harris to implement the *Dark Matter Spectra*  
1516 *from the Electroweak to the Planck Scale* (HDM) [79] and dSphs spatial model from [80] for  
1517 HAWC analysis. A NumPy dictionary of HDM, `HDMspectra_dict_gamma.npy`, was made for  
1518 portability within the collaboration. These dictionaries were generated from the [git repository](#) [79].  
1519 The analysis was performed using the Neural Network energy estimator for Pass 5.F. A description  
1520 of this estimator was provided in chapter 3. [TODO: Define a subsection when it's written](#), and its  
1521 key, relevant improvements are an improved energy estimation and improved sensitivities at higher  
1522 zenith angles. All other software used for data analysis, DM profile generation, and job submission  
1523 to SLURM are also kept in my sandbox in the [Dark Matter HAWC](#) project. The above repository  
1524 also incorporates the model inputs used previously in Glory Duck, described in chapter 5, so Glory  
1525 Duck remains compatible with modern software.

1526 **6.2.3 Data Set and Background Description**

1527 The HAWC data maps used for this analysis contain 2565 days of data between runs 2104 and  
1528 7476. They were generated from pass 5.f reconstruction. The analysis is performed using the NN  
1529 energy estimator with bin list:

1530 `B1C0Ea, B1C0Eb, B1C0Ec, B1C0Ed, B1C0Ee, B2C0Ea, B2C0Eb, B2C0Ec, B2C0Ed, B2C0Ee,`  
1531 `B3C0Ea, B3C0Eb, B3C0Ec, B3C0Ed, B3C0Ee, B3C0Ef, B4C0Eb, B4C0Ec, B4C0Ed, B4C0Ee,`  
1532 `B4C0Ef, B5C0Ec, B5C0Ed, B5C0Ee, B5C0Ef, B5C0Eg, B6C0Ed, B6C0Ee, B6C0Ef, B6C0Eg,`  
1533 `B6C0Eh, B7C0Ee, B7C0Ef, B7C0Eg, B7C0Eh, B7C0Ei, B8C0Ee, B8C0Ef, B8C0Eg, B8C0Eh,`  
1534 `B8C0Ei, B8C0Ej, B9C0Ef, B9C0Eg, B9C0Eh, B9C0Ei, B9C0Ej, B10C0Eg, B10C0Eh,`  
1535 `B10C0Ei, B10C0Ej, B10C0Ek, B10C0El`

1536 Bin 0 was excluded as it has substantial hadronic contamination and poor angular resolution.

1537 Background considerations and source selection was identical to Section 5.2.3, and no additional  
1538 arguments are provided here. Many of the HAWC systematics explored in Section 5.7 also apply

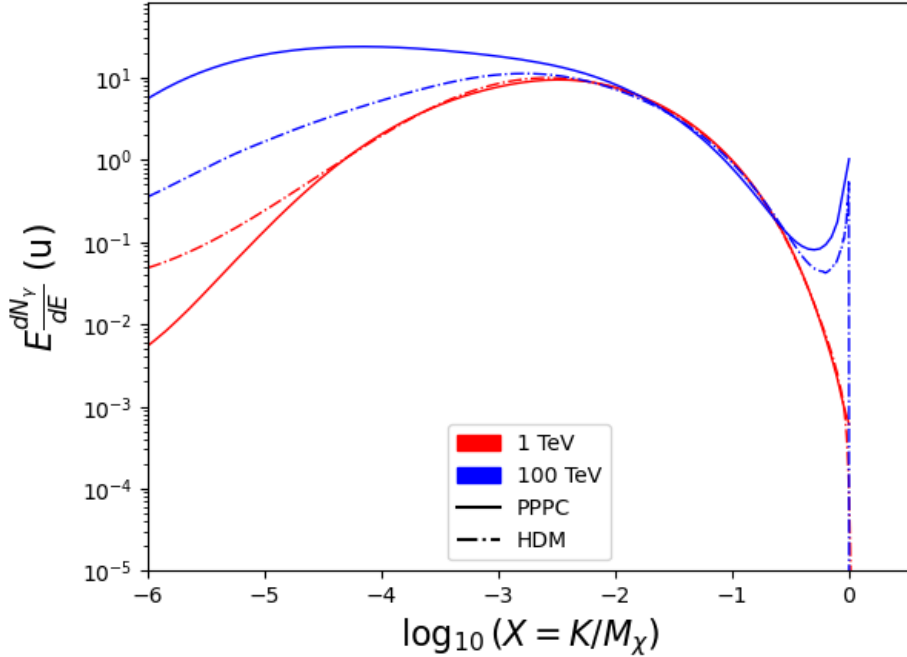


Figure 6.1 Spectral hypotheses from PPPC [58] and HDM [79] for DM annihilation:  $\chi\chi \rightarrow W^-W^+$ . Solid lines are spectral models with EW corrections from the PPPC. Dash-dot lines are spectral models from HDM. Red lines are models for  $M_\chi = 1$  TeV. Blue lines represent models for  $M_\chi = 100$  TeV.

1539 for this DM search and are not added upon here.

1540 **6.3 Analysis**

1541 The analysis and its systematics are almost identical to Section 5.3. Importantly, we use the  
 1542 same **TODO: fix this ref** Equation (5.1) and Equation (5.2) for estimating the gamma-ray flux at  
 1543 HAWC from our sources.

1544 **6.3.1  $\frac{dN_\gamma}{dE_\gamma}$  - Particle Physics Component**

1545 For these spectra, we import HDM with Electroweak (EW) corrections and additional correc-  
 1546 tions for neutrinos above the EW scale [79]. The spectra are implemented as a model script in  
 1547 astromodels for 3ML. A comprehensive description of EW corrections and neutrino considerations  
 1548 are provided later in Sec. 8.

1549 Figure 6.1 demonstrates the impact of changes implemented in HDM on DM annihilation to W  
 1550 bosons. A class in astromodels was developed to include HDM and is aptly named **HDMspectra**  
 1551 within `DM_models.py`. The SM DM annihilation channels studied here are  $\chi\chi \rightarrow$ :

1552       $e^+e^-$ ,  $\mu^+\mu^-$ ,  $\tau^+\tau^-$ ,  $b\bar{b}$ ,  $t\bar{t}$ ,  $gg$ ,  $W^+W^-$ ,  $ZZ$ ,  $c\bar{c}$ ,  $u\bar{u}$ ,  $d\bar{d}$ ,  $s\bar{s}$ ,  $\nu_e\bar{\nu}_e$ ,  $\nu_\mu\bar{\nu}_\mu$ ,  $\nu_\tau\bar{\nu}_\tau$ ,  $\gamma\gamma$ ,  $hh$ .

1553 For  $\gamma\gamma$  and  $ZZ$ , a substantial fraction of the signal photons are expected to have  $E_\gamma = m_\chi$  [79].  
 1554 This introduces  $\delta$ -function that is much narrower than the energy resolution of the HAWC detector.  
 1555 To ensure that this feature is not lost in the likelihood fits, the 'line' feature is convolved with a  
 1556 Gaussian kernel with a  $1\sigma$  width of  $0.05 \cdot m_\chi$  and total kernel window of  $\pm 4\sigma$ . This differs from  
 1557 HAWC's previous line study where 30% of HAWC's energy resolution was used for the kernel [81].  
 1558 The NN energy estimator's strength compared to  $f_{\text{hit}}$  at low gamma-ray energy enables narrower  
 1559 kernels [79].  $\chi\chi \rightarrow \gamma\gamma$  and  $ZZ$  spectral hypotheses are shown in Figure 6.2. We did not explore  
 1560 how well we reconstruct injected signal events for various kernels widths. This is a systematic  
 1561 that should be tested before publication to journal. Spectral models for the remaining annihilation  
 1562 channels are plotted for each  $m_\chi$  in Figure B.1.

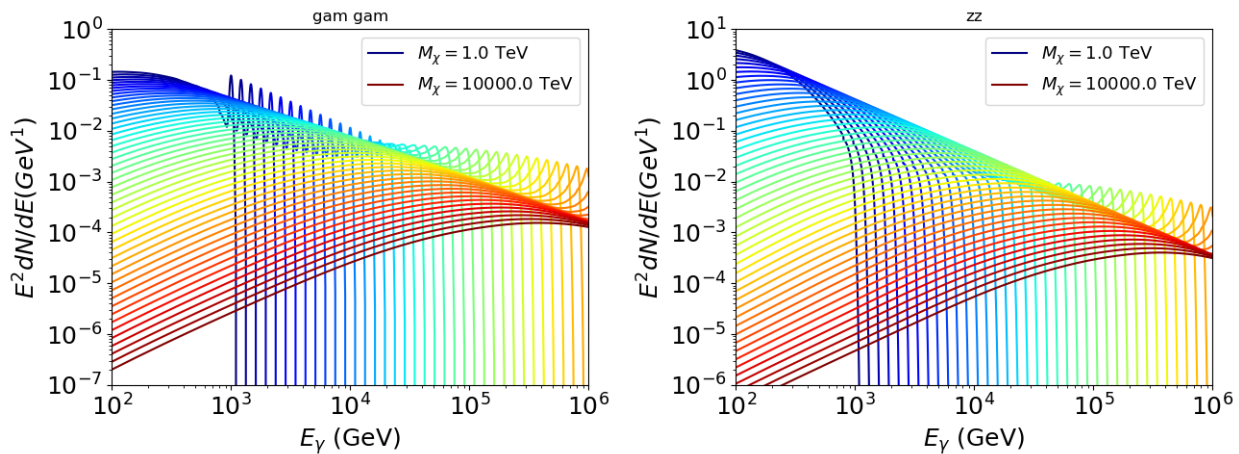


Figure 6.2 Photon spectra for  $\chi\chi \rightarrow \gamma\gamma$  (left) and  $\chi\chi \rightarrow ZZ$  (right) after Gaussian convolution of line features. Both spectra have  $\delta$ -features at photon energies equal to the DM mass. Bluer lines are annihilation spectra with lower DM mass. Redder lines are spectra from larger DM mass. All spectral models are sourced from the Heavy Dark Matter models [79]. Axes are drawn roughly according to the energy sensitivity of HAWC.

1563 **6.3.2 J Astrophysical Components**

1564 The J-factor profiles for each source are imported from Louis Strigari et al. (referred to with  
 1565  $\mathcal{LS}$ ) [80]. The  $\mathcal{LS}$  catalog fits a Navarro–Frenk–White (NFW) [62] spatial DM distributions to

1566 the dSphs which has a DM density of

$$\rho(r) = \frac{\rho_0}{\frac{r}{R_s} \left(1 + \frac{r}{R_s}\right)^2}. \quad (6.1)$$

1567  $\rho_0$  and the scale radius,  $R_s$  are free parameters fit for each dSph.  $r$  is the distance from the center  
1568 of the dSph.

1569 Profiles in  $\frac{dJ}{d\Omega}(\theta)$  up to an angular separation  $\theta = 0.5^\circ$  were provided directly from the authors.  
1570 Map generation from these profiles were almost identical to Section 5.3.2 except that a higher order  
1571 trapezoidal integral was used for the normalization of the square, uniformly-spaced map:

$$p^2 \cdot \sum_{i=0}^N \sum_{j=0}^M w_{i,j} \frac{dJ}{d\Omega}(\theta_{i,j}, \phi_{i,j}) \quad (6.2)$$

1572  $p$  is the angular side of one pixel in the map.  $w_{i,j}$  is a weight assigned the following ways:

1573  $w_{i,j} = 1$  if  $(\theta_{i,j}, \phi_{i,j})$  is fully within the region of integration

1574  $w_{i,j} = 1/2$  if  $(\theta_{i,j}, \phi_{i,j})$  is on an edge of the region of integration

1575  $w_{i,j} = 1/4$  if  $(\theta_{i,j}, \phi_{i,j})$  is on a corner of the region of integration

1576 Figure 6.3 shows the median and  $\pm 1\sigma$  maps used as input for this DM annihilation study.

### 1577 6.3.3 Source Selection and Annihilation Channels

1578 HAWC's sources for this multithreaded analysis include Coma Berenices, Draco, Segue 1, and  
1579 Sextans.  $\mathcal{LS}$  observed up to 43 sources in its publication, however only 4 of the best fit profiles  
1580 were provided at the time this thesis was written. A full description of each source used in this  
1581 analysis is found in Table 6.1.

1582 This analysis improves on chapter 5 in the following ways. Previously, the particle physics  
1583 model used for gamma-ray spectra from DM annihilation was from the PPPC [58] which missed  
1584 important considerations relevant for the neutrino sector. HDM is used to account for this shortfall  
1585 [79]. HDM also models DM to the Planck scale which permits HAWC to probe PeV scale DM. For  
1586 this study, we sample DM masses: 1 TeV - 10 PeV with 6 mass bins per decade in DM mass. In

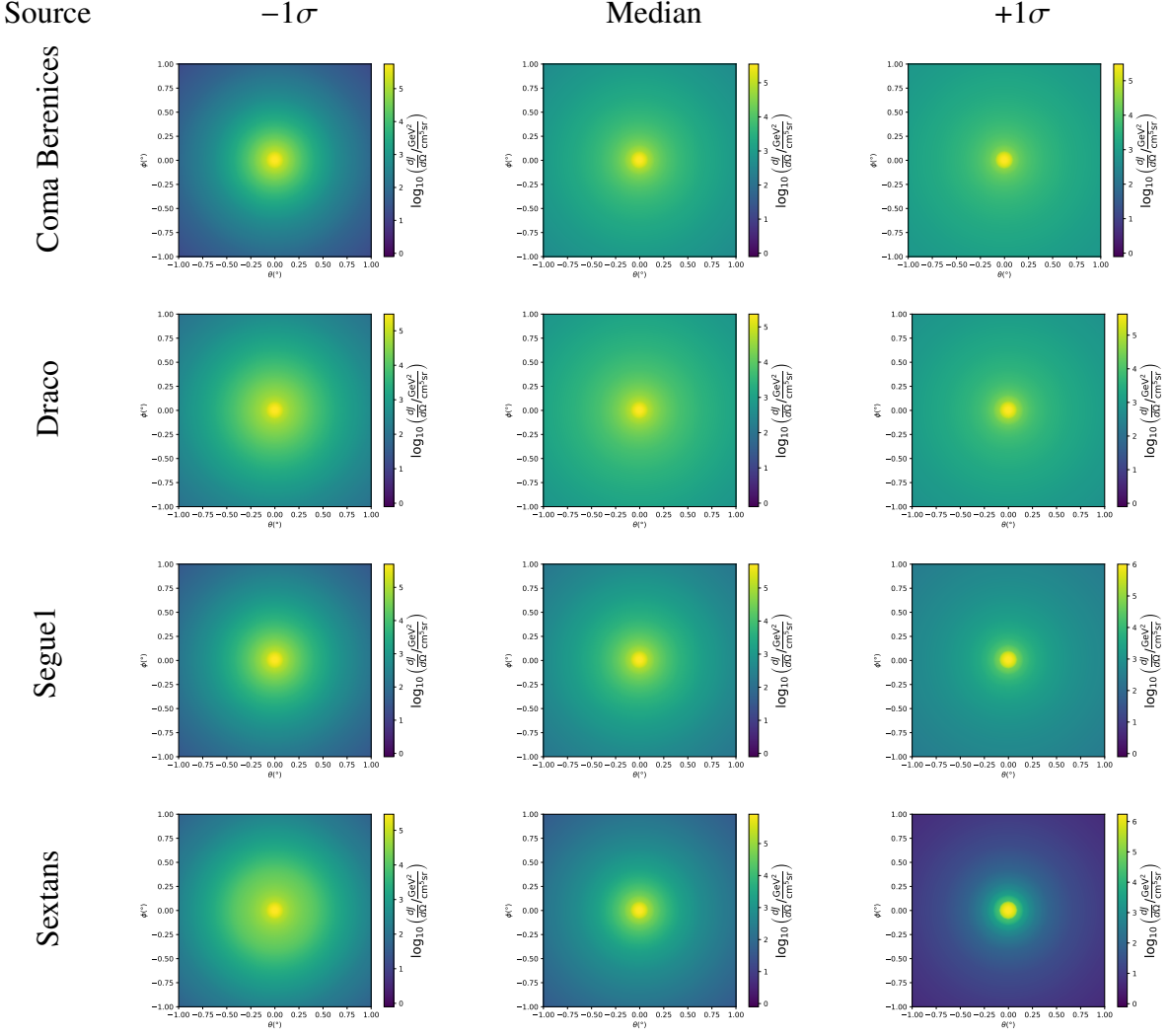


Figure 6.3  $\frac{dJ}{d\Omega}$  maps for Coma Berenices, Draco, Segue1, and Sextans. Columns are divided for the  $\pm 1\sigma$  uncertainties in  $dJ/d\Omega$  around the mean value from  $\mathcal{LS}$  [80]. Origin is centered on the specific dwarf spheroidal galaxies (dSph).  $\theta$  and  $\phi$  axes are the angular separation from the center of the dwarf. Profiles are truncated at  $1^\circ$  and flattened beyond.

1587 the case of line spectra ( $\chi\chi \rightarrow \gamma\gamma$ , or  $ZZ$ ), we double the mass binning to 12 DM mass bins per  
 1588 decade in DM mass.

1589  $\mathcal{LS}$  provides 25 sources within HAWC's field of view. Additionally, NFW [62] DM distributions  
 1590 have fewer parameters than Zhao [61], so  $\mathcal{LS}$  fits ultra-faint dwarves which expands the number of  
 1591 sources. However, all sources were not provided by the authors in time for the completion of this  
 1592 dissertation. Finally, the gamma-ray ray dataset is much larger. The study performed here analyzes  
 1593 2565 days of data compared to 1017 days analyzed in chapter 5.

1594 **6.4 Likelihood Methods**

1595 These are identical to Section 5.4.1 and no additional changes are made to the likelihood. Bins  
1596 in this analysis are expanded to include HAWC’s NN energy estimator.

1597 **6.5 Computational Methods: Multithreading**

1598 Previously, as in Section 5.3, the likelihood was minimized for one model at a time. One model  
1599 in this case representing a DM annihilation channel (CHAN), DM mass ( $m_\chi$ ), and dSph ((SOURCE)).  
1600 In an effort to conserve human and CPU time, jobs submitted for high performance computing  
1601 contained a list of  $m_\chi$  to iterate over for likelihood fitting. Jobs were then trivially parallelized  
1602 for each permutation of the two lists: CHANS and SOURCES. The lists for CHANS and SOURCES are  
1603 found in Section 6.3.1 and Table 6.1, respectively. Initially, 11  $m_\chi$  were serially sampled for one  
1604 job defined by a [CHAN, SOURCE] tuple. Computing the likelihoods would take between 1.5 to 2 hrs,  
1605 stochastically, for a job. We expect to compute likelihoods for data and 300 Poisson background  
1606 trials. The estimated CPU time based on the above for all CHAN (N = 17) and SOURCE (M = 25)  
1607 was estimated to 127,925 jobs. In total, 1,407,175 likelihood fits and profiles would be computed  
1608 for the 11 mass bins we wished to study. The estimated CPU time ranged between 8k CPU days  
1609 to 10k CPU days. Human time is more challenging to estimate as job allocation is stochastic and  
1610 highly dependent on what other users are submitting. Yet, it is unlikely that all jobs would run  
1611 simultaneously. Therefore, we can expect human time to be about as long as was seen in chapter 5

Name	Distance (kpc)	$l, b$ ( $^\circ$ )	$\log_{10} J$ ( $\mathcal{LS}$ set) $\log_{10}(\text{GeV}^2 \text{cm}^{-5} \text{sr})$
Coma Berenices	44	241.89, 83.61	$19.00^{+0.36}_{-0.35}$
Draco	76	86.37, 34.72	$18.83^{+0.12}_{-0.12}$
Segue I	23	220.48, 50.43	$19.12^{+0.49}_{-0.58}$
Sextans	86	243.50, 42.27	$17.73^{+0.13}_{-0.12}$

Table 6.1 Summary of the relevant properties of the dSphs used in the present work. Column 1 lists the dSphs. Columns 2 and 3 present their heliocentric distance and galactic coordinates, respectively. Column 4 reports the  $J$ -factors of each source given from the  $\mathcal{LS}$  studies and estimated  $\pm 1\sigma$  uncertainties. The values  $\log_{10} J$  ( $\mathcal{LS}$  set) [80] correspond to the mean  $J$ -factor values for a source extension truncated at  $0.5^\circ$ .

1612 which was on the order of months to fully compute on a smaller analysis. A visual aid to describe  
1613 how jobs were organized is provided in Figure 6.4.

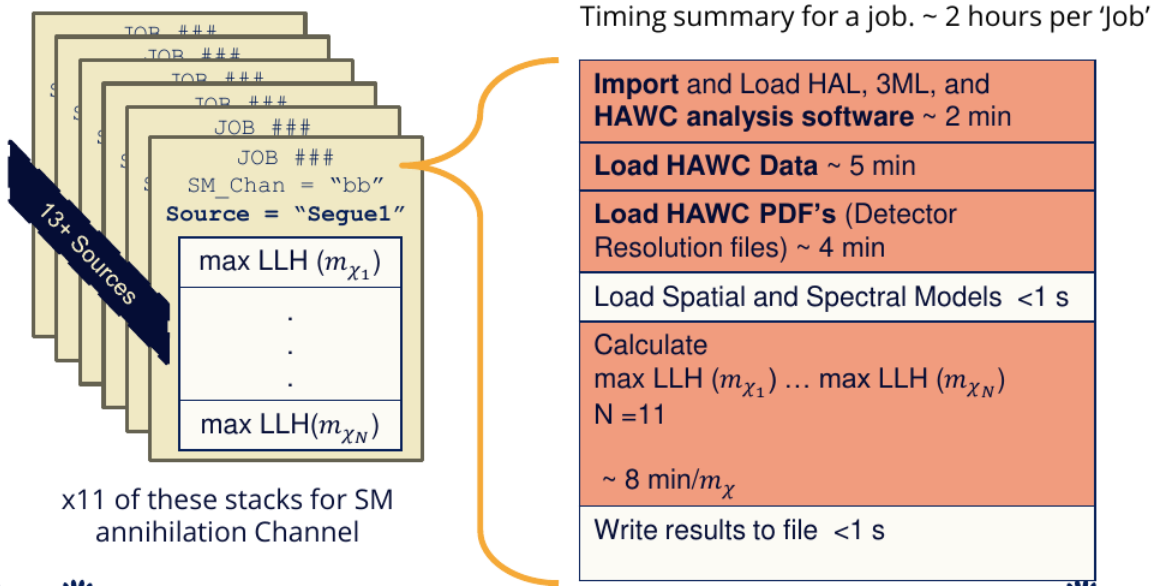


Figure 6.4 Infographic on how jobs and DM computation was organized in Section 5.3. Jobs were built for each permutation of CHANS and SOURCES shown by the left block in the figure. Each job, which took on the order 2 hrs to compute, had the following work flow: 1. Import HAWC analysis software, 2 min to run. 2. Load HAWC count maps, 5 min to run. 3. Load HAWC energy and spatial resolutions, 4 min. 5. Load DM spatial source templates and spectral models, less than 1 s. 6. Perform likelihood fit on data and model, about 8 min per DM mass. 7. Write results to file, less than 1s.

1614 The computational needs for this next generation DM analysis are extreme and is unlike other  
1615 analyses performed on HAWC. It became clear that there was a lot to gain from optimizing how  
1616 the likelihoods are computed. This section discusses how multi-threading was applied to solve and  
1617 reduce HAWC's computing of likelihoods for large parameter spaces like in DM searches.

### 1618 6.5.1 Relevant Foundational Information

1619 The profiling of the likelihood for HAWC is done via gradient descent where the normalization  
1620 of Equation (5.1) (linearly correlated with  $\langle \sigma v \rangle$ ) is rescaled in the descent. Additionally, we sample  
1621 the likelihood space for a defined list of  $\langle \sigma v \rangle$ 's described in Section 5.4.2. The time to compute  
1622 these values is not predictable or consistent because many variables can change across the full  
1623 model-space. Comprehensively, these variables are:

1624     •  $m_\chi$  : DM rest mass  
 1625     • CHAN : DM annihilation channel in SM.  
 1626     • SOURCE : dSph. Involves a spatial template AND coordinate in HAWC data.  
 1627     •  $\langle\sigma v\rangle$ : Effectively the flux normalization and free parameter in the likelihood fit.  
 1628   Therefore, we develop an asynchronous, functional-parallel coding pattern. Asynchronous meaning  
 1629   the instructions within a function are independent and permitted to be out of sync with sibling  
 1630   computations. Functional-parallel meaning that instructions are the subject of parallelization  
 1631   rather than threading the likelihood computation. This is close to trivial parallelization seen in  
 1632   Figure 6.4 except that we seek to consolidate the loading stages (software, data, and detector  
 1633   resolution loading). Multiple asynchronous threads are expected to reduce total serial processing  
 1634   time and total overhead across the entire project in addition to saving human time.

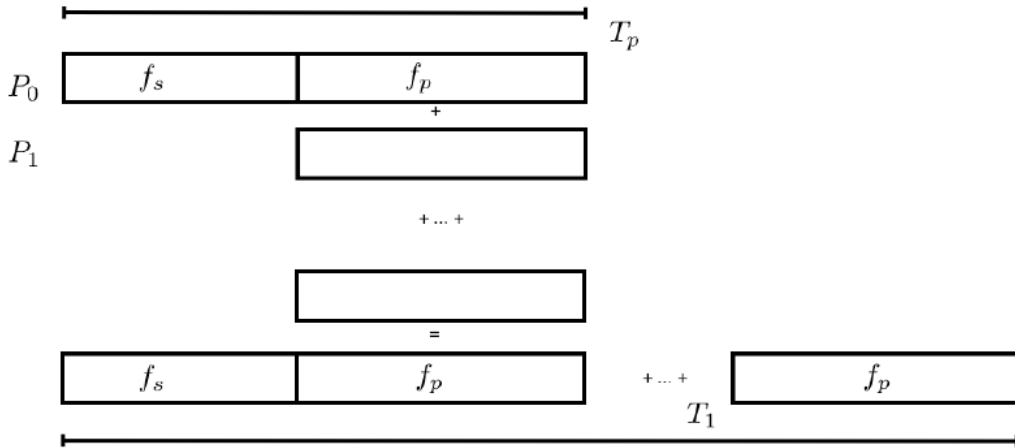


Figure 6.5 Graphic of Gustafson parallel coding pattern.  $f_s$  is the fraction of a program, in time, spent on serial computation.  $f_p$  is the fraction of computing time that is parallelizable.  $T_p$  is the total time for a parallel program to run.  $T_1$  is the total time for a parallel program to run if only 1 processor is allocated.  $P_N$  is the  $N$ -th processor where it's row is the computation the processor performs. The Gustafson pattern is most similar to what is implemented for this analysis. Figure is pulled from [82].

1635   We need a way to measure and compare the expected speedup and efficiency gain for this  
 1636   asynchronous coding pattern. I pull inspiration for timing measurement from [82] and use *Amdahl's*

1637 law with hybrid programming. Hybrid programming meaning that the computation is a mix of  
 1638 distributed and shared memory programming. If we assume the code is fully parallelizable over  $p$   
 1639 processors and  $c$  threads, the ideal speedup is simply  $pc$ , and ideal run-time is  $T_1/(pc)$ .  $T_1$  is the  
 1640 total time for a parallel program to run if only 1 processor is allocated. However, the coding pattern  
 1641 contains some amount of unavoidable serial computation, as shown in Figure 6.5. In our case, the  
 1642 run time,  $T_{p,c}$ , is estimated to be

$$T_{p,c} = \frac{T_1}{pc} (1 + F_s(c - 1)). \quad (6.3)$$

1643  $F_s$  is the fraction of CPU time dedicated to serial computation. The expected speedup,  $S_{p,c}$ , is

$$S_{p,c} \equiv \frac{T_1}{T_{p,c}} = \frac{pc}{1 + F_s(c - 1)}. \quad (6.4)$$

1644 From Equation (6.4), we can see that the speed-up scales with  $p/F_s$ . We are free to minimize  $F_s$   
 1645 asymptotically by enlarging the total models that are submitted to the thread pool, thereby shrinking  
 1646 the CPU fraction dedicated to serial operation. We are also free to define exactly how many threads  
 1647 and processors we utilize, yet eventually hit a hard cap at the hardware available on our computing  
 1648 cluster. HAWC uses Intel Xeon™processors with 48 cores and 96 threads. We see that a successful  
 1649 code will scale well as the expected speedup is inversely correlated with  $F_s$ . As the total number  
 1650 of models sampled grows, the speedup will also.

## 1651 6.5.2 Implementation

1652 The multithreaded code was written in Python3 and is documented in the `dark_matter_hawc`  
 1653 [repository](#) within the script named `mpu_analysis.py`. A version of the script as of April 25  
 1654 **TODO: make sure to update on this date** is also provided in Section B.2. It has many dependencies  
 1655 including the HAWC analysis software. Figure 6.6 displays the workflow of a job with 3 threads.  
 1656 Within a job, SOURCE is kept fixed and CHANS remains 17 elements long. More  $m_\chi$  are sampled  
 1657 from 11 bins up to 49 (for  $\gamma\gamma$  and ZZ) and 25 (for remaining CHANS) which amounts to 12 or 6  
 1658 mass bins per decade.  $m_\chi$  and CHANS are permuted into a 473 element list which is split evenly  
 1659 across N threads where N is [2, 8, 16]. For each  $m_\chi$ -CHAN tuple, 1001  $\langle\sigma v\rangle$  values are sampled in

Timing summary for a multi-threaded job.

Import and Load HAL, 3ML, and <b>HAWC analysis software</b> ~ 2 min		
Load HAWC Data ~ 5 min		
Load HAWC PDF's (Detector Resolution files) ~ 4 min		
Load Spatial Model < 1s		
Load Spectra Models <1 s	Load Spectra Models <1 s	Load Spectra Models <1 s
Calculate max LLH (Chan_0, $m_{\chi_1}$ ) ... max LLH (Chan_?, $m_{\chi_N}$ ) N = TOTAL/N_THREADS  ~ 8 min/Spec_model	Calculate max LLH (Chan_?, $m_{\chi_1}$ ) ... max LLH (Chan_?, $m_{\chi_N}$ ) N = TOTAL/N_THREADS  ~ 8 min/Spec_model	Calculate max LLH (Chan_?, $m_{\chi_1}$ ) ... max LLH (Chan_?, $m_{\chi_N}$ ) N = TOTAL/N_THREADS  ~ 8 min/Spec_model
Write results to file <1 s	Write results to file <1 s	Write results to file <1 s
Join Threads and terminate < 1s		

Figure 6.6 Task chart for one multithreaded job developed for this project. Green blocks indicate a shared resource across the threads AND computation performed serially. Red blocks indicate functional parallel processing within each thread. 3 threads are represented here, yet many more can be employed during the full analysis. Jobs are defined by the SOURCE as these require unique maps to be loaded into the likelihood estimator. The  $m_{\chi}$ , CHAN, and  $\langle \sigma v \rangle$  variables are entered into the thread pool and allocated as evenly as possible across the threads.

- 1660 the likelihood, and the value of  $\langle \sigma v \rangle$  that maximizes the likelihood is found. Although rare, fits  
 1661 that failed are handled on a case by case basis.

### 1662 6.5.3 Performance

M Tasks	$T_{p,c}$ (hr:min:s)			
	$T_{1,1}$	$T_{1,2}$	$T_{1,8}$	$T_{1,16}$
50	1:40:37.5	0:52:43.7	0:19:13.8	0:13:44.0
74	2:22:30.0	1:15:00.6	0:25:21.3	0:15:49.8
100	(3:07:51.9)	1:40:10.5	0:30:44.4	0:20:01.4
200	(6:02:20.6)	-	1:00:32.0	0:30:35.0
473	(13:58:40.3)	-	2:01:41.4	1:07:53.2

Table 6.2 Timing summaries for analyses for serial and multithreaded processes. M tasks is the number of functional-parallel tasks ran for the computation.  $T_{p,c}$  is a single run time in hours:minutes:seconds for runs utilizing  $p$  nodes and  $c$  threads. Runs are run interactively on the same computer to maximize consistency. Empty entries are indicated with '-'. (·) entries are estimated entries extrapolated from data earlier in the column.

- 1663 We see a significant reduction to wall time needed for our dSph analyses to run. Table 6.2

1664 shows the timing summaries for analyses of different sizes and thread counts. Additionally, the  
 1665 efficiency gained when consolidating the serial loading of data is also apparent in our ability to  
 1666 study many more tasks in about the same amount of wall time as a smaller serial computation. Trials  
 1667 represented in the table were run on an AMD Opteron® processor 6344 with 48 cores, 2 threads per  
 1668 core; 2.6 GHz clock. This is not the same architecture used for analysis on the HAWC computing  
 1669 cluster however they are similar enough that results shown here are reasonably representative of  
 1670 computing on the HAWC computing cluster. I use Tab. 6.2 for the inferences and conclusions in  
 1671 the following paragraphs.

1672 First, we want to find  $T_s$ , the time of serial computation. From Fig. 6.5, the timing for our  
 1673 coding pattern can be written as

$$T_s + Mt_p = T_{1,1}^M. \quad (6.5)$$

1674  $M$  is the number of functional-parallel tasks (represented as column 1 of Tab. 6.2), and  $t_p$  is the  
 1675 average time to complete a single parallel task.  $T_{1,1}^M$  is the total time for a parallel program to run if  
 1676 only 1 processor is allocated for  $M$  parallel task. With two runs of different  $M$  ( $M_1$  and  $M_2$ ), we  
 1677 can use a system of equations to compute

$$T_s = 803.1\text{s} \text{ and } t_p = 104.6\text{s} \quad (6.6)$$

1678 Now, we have specific estimation for the fraction of serial computing time,  $F_s$ :

$$F_s = \frac{803.1}{803.1 + 104.6 \cdot M}. \quad (6.7)$$

1679 The maximum  $M$  for this study is 473 which evaluates to:  $F_s = 0.016$  or 1.6% of computing time.  
 1680 Table 6.3 shows the resulting speedups.

1681 We see a speedup that generally exceeds expectations from Eq. (6.4) for real trail runs. We also  
 1682 see that there are diminishing returns as the number of threads increases. For small jobs with large  $c$ ,  
 1683 both the expected and observed speedup are significantly smaller than  $c$ . One thing not considered  
 1684 in Eq. (6.4) is the time incurred via communication latency. Communication latency increases  
 1685 with the number of threads and contributes to diminishing returns. Additionally, these values are

M Tasks	$F_s$	$S_{1,2}$	$S_{1,8}$	$S_{1,16}$
50	1.33 E-1	1.90 [1.76]	5.23 [4.14]	6.35 [5.34]
74	9.40 E-2	1.90 [1.83]	5.62 [4.82]	9.00 [6.64]
100	7.13 E-2	1.88 [1.87]	6.11 [5.34]	9.38 [7.73]
200	3.70 E-2	- [1.93]	5.98 [6.36]	11.85 [10.29]
473	1.60 E-2	- [1.97]	6.89 [7.20]	12.35 [12.91]

Table 6.3 Speed up summaries for analyses for serial and multithreaded processes. M tasks is the number of functional-parallel tasks ran for the computation.  $S_{p,c}$  is a single speedup comparison for runs utilizing  $p$  nodes and  $c$  threads. [·] are the estimated speedups calculated from Tab. 6.2, Eq. (6.7), and Eq. (6.4). Empty entries are indicated with '-'.

for single runs and do not consider the stochastic variation expected in a shared high performance computing resource. Therefor, these results are not strictly conclusive, yet demonstrate the merits of multi-threading. We see very clearly that there is a lot to gain, and this new coding pattern will expand HAWC's analysis capabilities.

## 6.6 Analysis Results

3 of the 43  $\mathcal{L}\mathcal{S}$  dSphs considered for the multithreaded analysis. These dSph are analyzed for emission from DM annihilation according to the likelihood method described in Section 5.4. The three likelihood profiles are then stacked to synthesize a combined limit on the dark matter annihilation cross-section,  $\langle\sigma v\rangle$ . This combination is done each of the 17 SM annihilation channels. Figure 6.7 and Fig. 6.8 show the combined limits for all annihilation channels with HAWC's observations. Test statistics of the best fit  $\langle\sigma v\rangle$  values for each  $m_\chi$  and CHAN are shown in Fig. 6.9 and Fig. 6.10. We also compare these limits to HAWC's Glory Duck limits shown in Section 5.5. The comparison to Glory Duck are featured in Fig. 6.11 for all the DM annihilation channels studied for Glory Duck. A full comparison is provided in the appendix in Fig. B.2, Fig. B.3, and Fig. B.4. Here, we show updated limits for  $\chi\chi \rightarrow b\bar{b}, e\bar{e}, \mu\bar{\mu}, \tau\bar{\tau}, t\bar{t}, W^+W^-$ ,  $\gamma\gamma$  and  $ZZ$ . For the first time ever, we show limits for  $\chi\chi \rightarrow c\bar{c}, s\bar{s}, u\bar{u}, d\bar{d}, \nu_e\bar{\nu}_e, \nu_\mu\bar{\nu}_\mu, \nu_\tau\bar{\nu}_\tau, gg$ , and  $hh$ .

No DM was found in HAWC observations. The largest excess found in HAWC data was for DM annihilating to  $W$ -bosons or  $\nu_e\bar{\nu}_e$  for  $m_\chi = 10$  TeV at significance  $2.11\sigma$  and  $2.14\sigma$  respectively. HAWC's limits and excesses are dominated by Segue1. Coma Berenices shows excesses at higher DM mass, yet no similar excesses were observed in Segue1 or Sextans. Sextans did not contribute

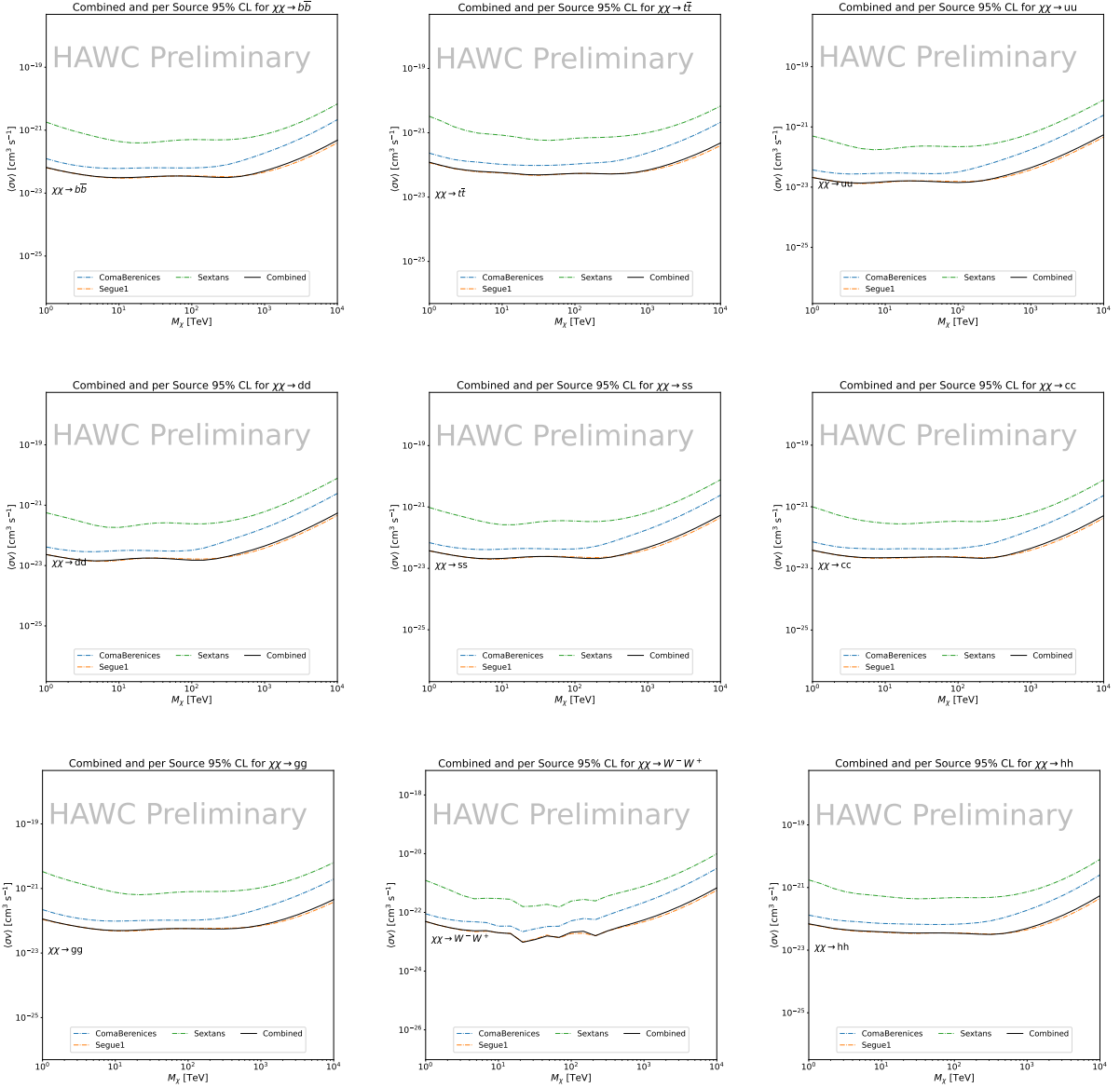


Figure 6.7 HAWC upper limits at 95% confidence level on  $\langle\sigma v\rangle$  versus  $m_\chi$  for  $\chi\chi \rightarrow b\bar{b}$ ,  $t\bar{t}$ ,  $u\bar{u}$ ,  $d\bar{d}$ ,  $s\bar{s}$ ,  $c\bar{c}$ ,  $gg$ ,  $W^+W^-$ , and  $hh$ . Limits are with  $\mathcal{L}\mathcal{S}$   $J$ -factors [80]. The solid line represents the observed combined limit. Dashed lines represent limits from individual dSphs.

1706 significantly to signal excesses or the combined limit as it is at high zenith. Draco was not included  
 1707 as the PDF of some of our analysis bins were wider than what is reasonable for a point source  
 1708 analysis. Draco is at a high zenith for HAWC, so the effort required to include it was not justified  
 1709 by the benefits.

1710 We did not generate background trials in time of writing this thesis. These are not shown and

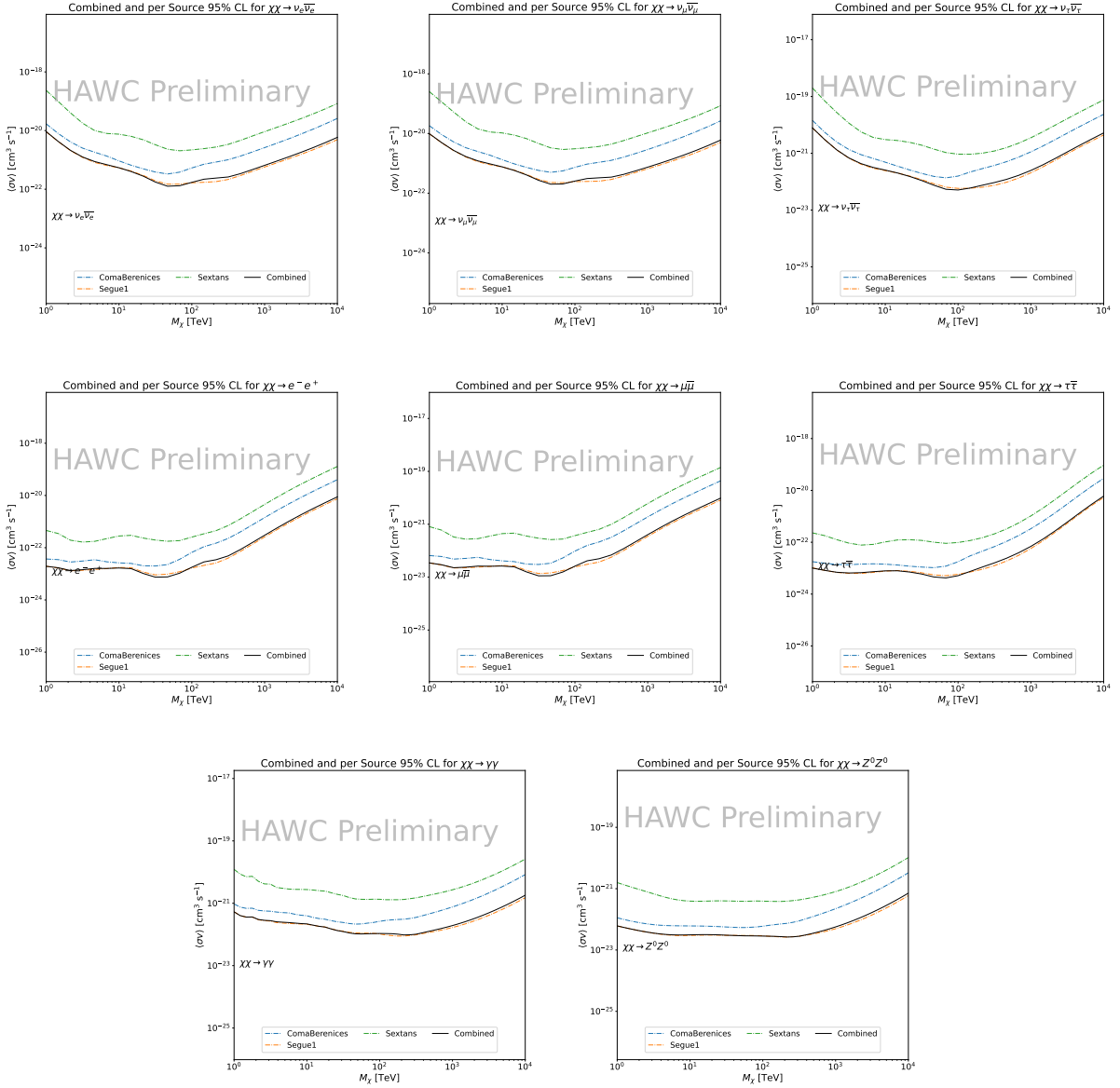


Figure 6.8 HAWC upper limits at 95% confidence level on  $\langle\sigma v\rangle$  versus  $m_\chi$  for  $\chi\chi \rightarrow \nu_e \bar{\nu}_e$ ,  $\nu_\mu \bar{\nu}_\mu$ ,  $\nu_\tau \bar{\nu}_\tau$ ,  $e \bar{e}$ ,  $\mu \bar{\mu}$ ,  $\tau \bar{\tau}$ ,  $\gamma\gamma$  and  $ZZ$ . Limits use  $\mathcal{L}S$   $J$ -factors [80]. The solid line represents the observed combined limit. Dashed lines represent limits from individual dSphs.

1711 are an immediate next step for this analysis before publication.

1712 When comparing these results to Section 5.5, we see an overall decrease to the confidence limit  
 1713 therefore improvement to HAWC's expected sensitivity. This improvement is generally stronger  
 1714 than a doubling of data, or a factor  $\sqrt{2}$  decrease. The comparison is somewhat complex and  
 1715 dependent on the dSph and SM annihilation channel. Figure 6.11 shows the comparisons of limits

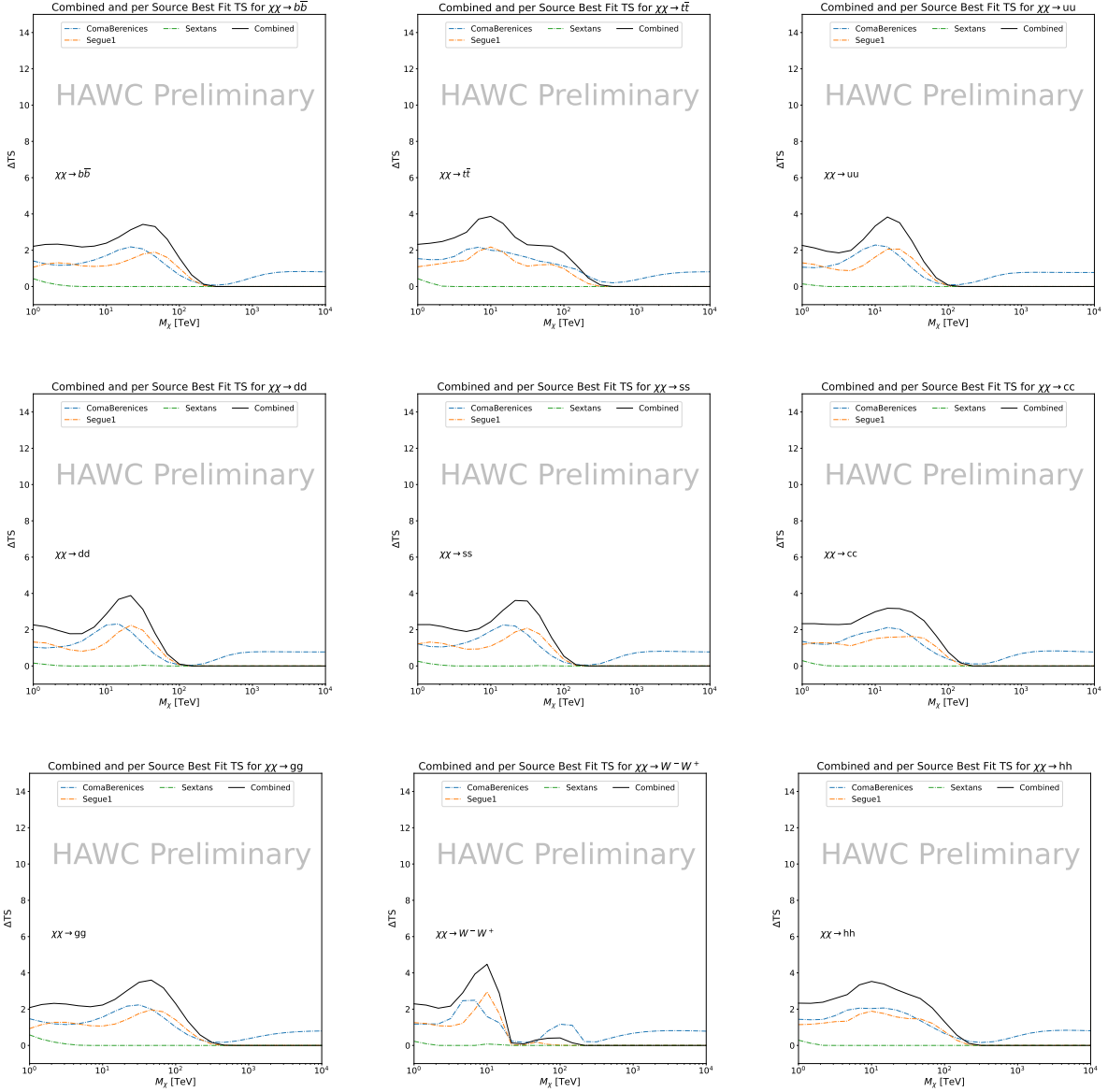


Figure 6.9 HAWC TS values for best fit  $\langle\sigma v\rangle$  versus  $m_\chi$  for SM annihilation channels:  $\chi\chi \rightarrow b\bar{b}$ ,  $t\bar{t}$ ,  $u\bar{u}$ ,  $d\bar{d}$ ,  $s\bar{s}$ ,  $c\bar{c}$ ,  $gg$ ,  $W^-W^+$ , and  $hh$ . Limits use  $\mathcal{LS}$   $J$ -factors. The solid black line shows the combined best fit TS values. The colored, dashed lines are the TS values from each dSph.

1716 calculated for this analysis and Glory Duck (Section 5.5). Segue 1 and Coma Berenices are low  
 1717 zenith where improvements to HAWC's analysis come only from energy estimation. Differences  
 1718 between these two are dominantly from their differences in  $J$ -factor, half-light radii of the dSphs,  
 1719 and the particle physics inputs. Substantial gains in HAWC's analysis methods (pass 5.F) were  
 1720 made at high zenith which is important for sources like Sextans. The HDM particle physics model

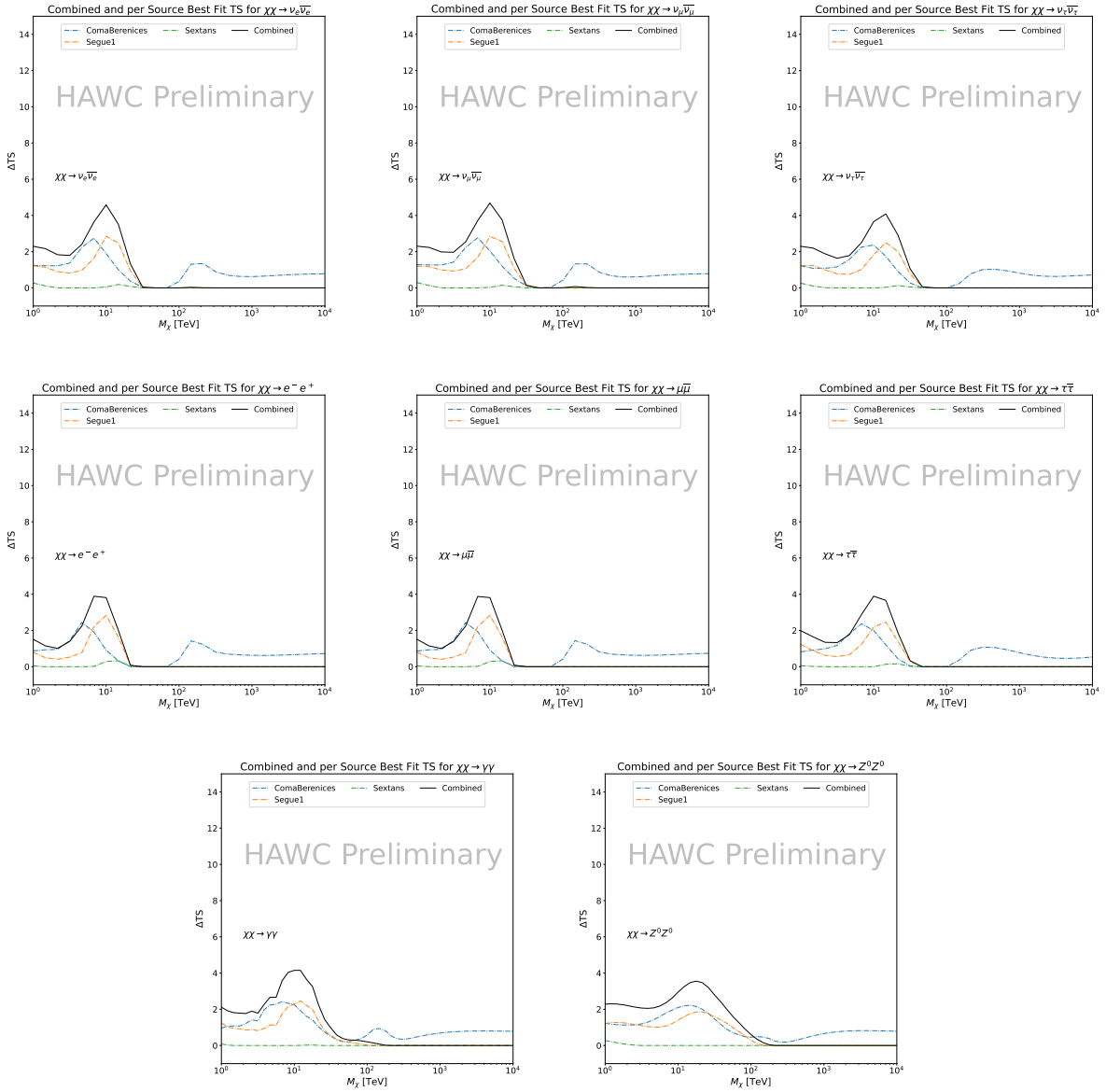


Figure 6.10 HAWC TS values for best fit  $\langle\sigma v\rangle$  versus  $m_\chi$  for SM annihilation channels:  $\chi\chi \rightarrow \nu_e \bar{\nu}_e$ ,  $\nu_\mu \bar{\nu}_\mu$ ,  $\nu_\tau \bar{\nu}_\tau$ ,  $e^- e^+$ ,  $\mu \bar{\mu}$ ,  $\tau \bar{\tau}$ ,  $\gamma\gamma$  and  $ZZ$ . Limits use  $\mathcal{LS}$   $J$ -factors. The solid black line shows the combined best fit TS values. The colored, dashed lines are the TS values from each dSph.

1721 produces almost identical spectra to the PPPC for  $\chi\chi \rightarrow e^- e^+$ . This channel can be used to  
 1722 compare limits between dSph spatial models. Overhead sources see minimal improvement to the  
 1723 limits, while high zenith sources see an order of magnitude improvement for all DM masses. Softer  
 1724 SM annihilation channels see broad improvements to the limit compared to harder channels.

1725 **6.7 Systematics**

1726     Systematics to this analysis are identical to what was performed earlier in Glory Duck, Sec-  
1727     tion 5.7. We are also sensitive to the choice in spatial template, and this was explored in Section 5.7.2  
1728     and Section 5.8.2.

1729 **6.8 Conclusion and Discussion**

1730     In this multithreaded analysis, we have used observations of 3 dSphs from HAWC to perform  
1731     a collective DM annihilation search towards dSphs. The data were combined across sources  
1732     to significantly increase the sensitivity of the search. Advanced computational techniques were  
1733     deployed to accelerate wall-time spent analyzing by an order of magnitude. We have observed  
1734     no significant deviation from the null, no DM hypothesis, and so present our results in terms of  
1735     upper limits on the velocity-weighted cross-section,  $\langle\sigma v\rangle$ , for seventeen potential DM annihilation  
1736     channels across four decades of DM mass.

1737     This analysis serves as a proof of concept for multithreaded HAWC analyses with large parameter  
1738     spaces. Larger datasets with fast techniques will be essential to tackling the DM problem. The  
1739     models we used for this study include annihilation channels with neutrinos in the final state.  
1740     Advanced studies could aim to merge our results with those from neutrino observatories with large  
1741     data sets.

1742     A full HAWC analysis will include systematic studies of the  $J$ -factor distributions. Additionally,  
1743     because of the timing reduction, the study can be doubled in size to include DM decay. We have not  
1744     yet received the remaining spatial profiles to the  $\mathcal{LS}$  catalog, and limits can be quickly computed  
1745     once these are received. Finally, statistical studies with Poisson variation of HAWC's background  
1746     are essential to a comprehensive understanding of our observed excesses.

Segue1

Coma Berenices

Sextans

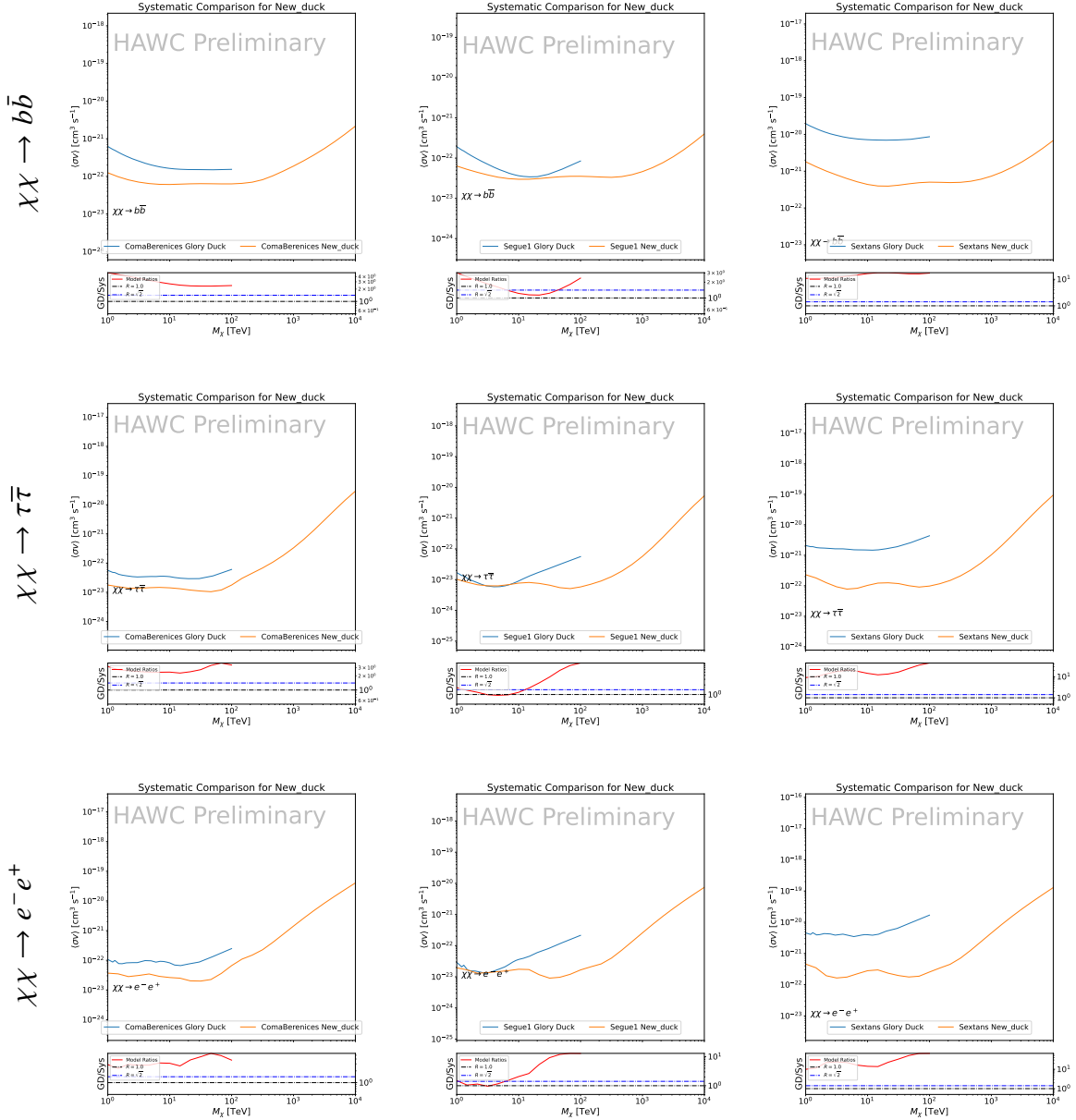


Figure 6.11 Comparison of HAWC limits from this analysis to Glory Duck (Fig. 5.5) for 3 dSphs and 3 DM annihilation channels:  $b\bar{b}$ ,  $\tau\bar{\tau}$ , and  $e\bar{e}$ . Each sector shows the 95% confidence limit from Glory Duck (blue line) and this analysis (orange line) in the top plot. The lower plot features the ratio in log scale of Glory Duck to this analysis in a red solid line. Horizontal dashed lines are for ratios of 1.0 (black) and  $\sqrt{2}$  (blue). Ratios larger than 1.0 are for limits smaller, or stricter, than Glory Duck. Ratios larger than  $\sqrt{2}$  indicates limits are stricter than a simple doubling of the Glory Duck data.

## CHAPTER 7

### HEAVY DARK MATTER ANNIHILATION SEARCH WITH ICECUBE'S NORTH SKY TRACK DATA

#### 7.1 Introduction

Neutrinos are another astrophysical messenger than can travel long distances without significant attenuation or deflection. Additionally, Neutrinos come in three flavors which triples the multiplicity of the particles we are searching for. Uniquely, they interact less readily than photons especially above PeV energies. Neutrinos therefore provide another window through which we can perform dark matter searches.

The previous IceCube DM annihilation analysis towards dwarf galaxies was performed in 2013 [83] which, in technical terms, is more than a minute ago. This is in spite of IceCube's crucial sensitivity afforded from neutrino spectral lines [84]. A lot has changed in IceCube since its previous DM annihilation search such as, additional strings, more sophisticated analysis methods, and more accurate theory modeling. It has come time for IceCube to make a DM dSph contribution.

IceCube is sensitive to annihilating DM for DM masses above 1 TeV. Additionally, IceCube's sensitivity is comparable gamma-ray observatories in spectral models that produce hard neutrino features. The goal of this analysis is to perform a DM annihilation search using the Northern Sky Tracks datasets. The search will only be towards dwarf spheroidal galaxies (dSph) for the strengths mentioned in Section 5.3.3. These sources are treated as point sources for IceCube with little loss to sensitivity or model dependence on how the DM is distributed. DM masses from 500 GeV to 100 PeV are considered for this analysis. Several DM annihilation channels available from the HDMspectra [79] are studied in this analysis. This chapter presents the analysis work for IceCube to update our DM searches toward dSphs.

#### 7.2 Dataset and Background

This section enumerates the data and background methods used for IceCube's study of dSphs. Section 7.2.1 and Section 7.2.2 are most useful for fellow IceCube collaborators looking to replicate this analysis.

1773 **7.2.1 Itemized IceCube files**

1774 These files are only available within IceCube’s internal documentation and wikis. They are not  
1775 meant for public access, and are presented here so that IceCube collaborators can reproduce results  
1776 accurately.

1777 • Software Environment: CVMFS Py3-v4.1.1

1778 • Data Sample: Northern Tracks NY86v5p1

1779 • Analysis Software: csky ([nu\\_dark\\_matter](#))

1780 • Analysis wiki: [https://wiki.icecube.wisc.edu/index.php/Dark\\_Matter\\_Annihilation\\_Search\\_towards\\_dwarf\\_spheroidals\\_with\\_NST\\_and\\_DNN\\_Cascades](https://wiki.icecube.wisc.edu/index.php/Dark_Matter_Annihilation_Search_towards_dwarf_spheroidals_with_NST_and_DNN_Cascades)

1782 • Project repository

1783 **7.2.2 Software Tools and Development**

1784 This analysis was performed inside IceCube’s CVMFS (3.4.1.1) software environment using  
1785 csky for likelihood calculations. Csky at first did not come with dark matter spectral models nor  
1786 could accommodate custom flux models. We developed these capacities for single source and  
1787 stacked source studies for this analysis. The analysis code is held in a separate repository from  
1788 csky. The [nu\\_dark\\_matter branch of csky](#) manages the input of custom dark matter spectra and  
1789 accompanied DM astrophysical source. Csky also enables the use of multithreading which was  
1790 shown to be crucial for DM searches (see Sec. 6). Csky then calculates likelihoods with a selected  
1791 data sample. The [IceCube Dark Matter dSph repository](#) manages the generation of spectral models  
1792 for neutrinos, physics parameter extraction from  $n_{\text{sig}}$ ,  $J$ -factor per source inputs, and bookkeeping  
1793 for the large parameter space. The project repository required a secondary software environment  
1794 for neutrino oscillations. How to launch and run those calculations are documented in the project  
1795 repository and the Docker image is additionally saved in Section C.1.

1796 **7.2.3 Data Set and Background Description**

1797 For this analysis, I use the Northern Sky Tracks (NST) Sample (Version V005-P01). The sample  
1798 contains up-going track-like events, usually from  $\nu_\mu$  and  $\nu_\tau$ , with a superior angular resolution  
1799 compared to the cascade dataset. This sample covers 10.4 years of data (IC86\_2011-2021). The  
1800 accepted neutrino energy range used for the analysis is unique from most other IceCube searches  
1801 because DM spectra are hard with large contributions close to  $E_\nu = m_\chi$ . Therefore, the sampled  
1802 energy range is  $1 < \log(E_\nu/\text{GeV}) < 9.51$  with step size 0.125.

1803 The strengths of a dwarf analysis is that there are no additional background considerations  
1804 beyond nominal, baseline background estimations (see Section 5.2.3). For NST, the nominal  
1805 contributions come from atmospheric neutrinos and isotropic astrophysical neutrinos. We estimate  
1806 the background by scrambling NST data along Right Ascension.

1807 **7.3 Analysis**

1808 The expected differential neutrino flux from DM-DM annihilation to standard model particles,  
1809  $d\Phi_\nu/dE_\nu$ , over solid angle,  $\Omega$  is described by the familiar equation.

$$\frac{d\Phi_\nu}{dE_\nu} = \frac{\langle\sigma\nu\rangle}{8\pi m_\chi^2} \frac{dN_\nu}{dE_\nu} \times \int_{\text{source}} d\Omega \int_{l.o.s} \rho_\chi^2 dl(r, \theta') \quad (7.1)$$

1810 This is identical to Eq. (5.1) except that there are 3 neutrino flavors, so there are a corresponding  
1811 3 flux equations. Section 5.3 has a complete description of each term in Eq. (7.1). Additionally,  
1812 neutrinos oscillate between flavors which needs to be considered for the expected neutrino flux  
1813 at Earth. Section 7.3.1 presents the particle physics model and processing for DM annihilation.  
1814 Section 7.3.2 presents the spatial distributions built for each dSph.

1815 **7.3.1  $\frac{dN_\nu}{dE_\nu}$  - Particle Physics Component**

1816 Neutrino spectra from heavy DM annihilation were generated using HDMspectra [79] and  
1817  $\chi$ arow [85]. HDMspectra has tables for the decay and annihilation of heavy DM for different  
1818 dark DM and SM primary annihilation channels. The simulation includes electroweak or gluon  
1819 radiative corrections and higher order loop corrections from the  $W$  and  $Z$  bosons ( $WWZ$  and  $WW\gamma$ ).  
1820 These corrections are especially important for accurately estimating the prompt neutrino flux. This

1821 publication also pushes the simulated DM mass to the Plank scale (1 EeV), however this study will  
1822 not explore that high.

1823 An important feature in the spectra is that neutrino line channels will be accompanied by a low  
1824 energy tail [79], see Fig. 7.1. Thus, the Earth will not fully attenuate a heavy neutrino line-like  
1825 signal from high declination sources where the neutrino flux must first traverse through the Earth.  
1826 The DM annihilation channels that feature lines include all leptonic channels:  $\nu_{e,\mu,\tau}$ ,  $e$ ,  $\mu$ , and  $\tau$ . We  
1827 use the `xarov` software to propagate and oscillate the neutrinos from the source to Earth. Because  
1828 these sources are quite large in absolute terms, and also far (order 10 kpc or more), the resulting  
1829 flavor spectra are the averages of the transition probabilities [85]:

$$P(\nu_\alpha \rightarrow \nu_\beta) \approx \begin{bmatrix} 0.55 & 0.18 & 0.27 \\ 0.18 & 0.44 & 0.38 \\ 0.27 & 0.38 & 0.35 \end{bmatrix} \quad (7.2)$$

1830 Examples of the spectra before and after propagation are shown in Fig. 7.1.

1831 When calculating the expected contribution to  $n_s$ , only  $\nu_\mu$  and  $\nu_\tau$  are considered as NST's  
1832 effective area to  $\nu_e$  is negligible [86]. Therefore, the expected composite neutrino spectrum is the  
1833 sum of the two flavors:  $\frac{dN\nu_\mu}{dE\nu_\mu} + \frac{dN\nu_\tau}{dE\nu_\tau}$ . The spectral tables are then converted to splines to condense  
1834 information, enable random sampling of the spectra, and reduce computing times. The spectral  
1835 splines are finally implemented as a DM class in csky.

### 1836 7.3.1.1 Treatment of Neutrino Line Features

1837 All DM annihilation channels into leptons  $\chi\chi \rightarrow [\nu_{e,\mu,\tau}, e, \mu, \tau]$  develop a prominent and  
1838 narrow spectral line feature. For all neutrino flavors, this line is visible and prominent in all  $m_\chi$   
1839 studied in this analysis. For charged leptons, the feature typically manifests at  $m_{ch} > 10$  TeV, yet  
1840 its prominence varies slightly between the flavors. Examples for lines in the annihilation spectra  
1841 with neutrinos or charged leptons are provided in Fig. 7.1.

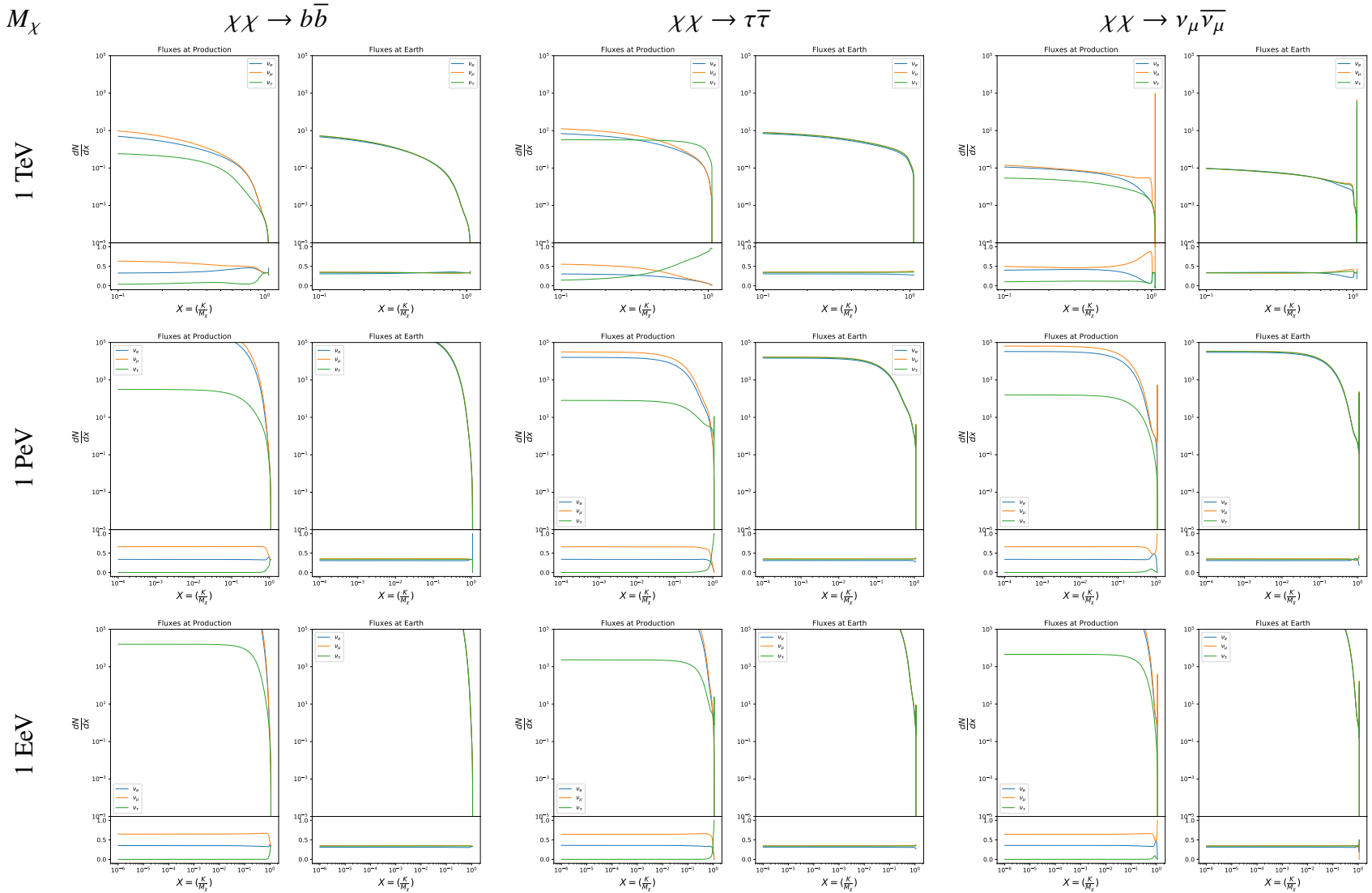


Figure 7.1 Neutrino spectra at production (left panels) and after oscillation at Earth (right panels). Blue, orange, and green lines are the  $\nu_e$ ,  $\nu_\mu$ , and  $\nu_\tau$  spectra respectively. Top panels show the spectra in  $\frac{dN}{dE}$ . Lower panels plot the flavor ratio to  $\nu_e + \nu_\mu + \nu_\tau$ . SM annihilation channels  $b\bar{b}$ ,  $\tau\bar{\tau}$ , and  $\nu_\mu \bar{\nu}_\mu$  are shown for  $M_\chi = 1$  Pev, TeV, and EeV.

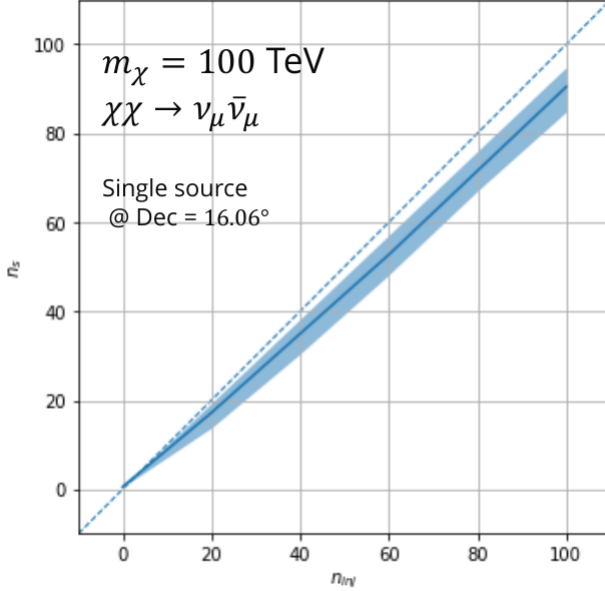


Figure 7.2 Signal recovery for 100 TeV DM annihilation into  $\nu_\mu \bar{\nu}_\mu$  for a source at Dec = 16.06°.  $n_{\text{inj}}$  is the number of injected signal events in simulation.  $n_s$  is the number of reconstructed signal events from the simulation data. Although the uncertainties are small and tight, the reconstructed  $n_s$  are systematically underestimated.

1842     The neutrino line feature is so narrow relative the sampled energy range that the random  
 1843     sampling of the spectra and likelihood fitting rarely capture the line in computation. As a result,  
 1844     often the best fit to simulation of background will always floor to TS = 0 and the signal recovery  
 1845     systematically underestimates the signal (see Fig. 7.2).

1846     To remedy this, we take a similar approach to the IceCube’s decay analysis [87] and the previous  
 1847     gamma-ray study in Section 6.3.1. Two smoothing kernels were tested (Gaussian and uniform)  
 1848     to widen the line feature. The widths were tuned such that the signal recovery approached unity  
 1849     for DM mass 100 TeV to 1 PeV for a source at Segue 1’s declination, 16.06°. Near horizon  
 1850     was chosen in order to isolate loss in signal recovery away from Earth’s attenuation of very high  
 1851     energy neutrinos and atmospheric backgrounds. The kernel convolution needed closely preserve  
 1852     the integrated counts of neutrinos. The optimized kernel parameters for all lines are summarized  
 1853     as:

- 1854     • Gaussian kernel with  $1\sigma$  width =  $1.75\text{E-}3 \cdot m_\chi$   
 1855     • Minimum energy included in convolution =  $\text{MIN}[0.995 \cdot m_\chi, E(\nu_{\text{line}}) - 4\sigma]$

- 1856 • Maximum energy included in convolution =  $\text{MAX}[1.005 \cdot m_\chi, E(\nu_{\text{line}}) + 4\sigma]$

1857 where  $E(\nu_{\text{line}})$  is the neutrino energy where the neutrino line is at the maximum.

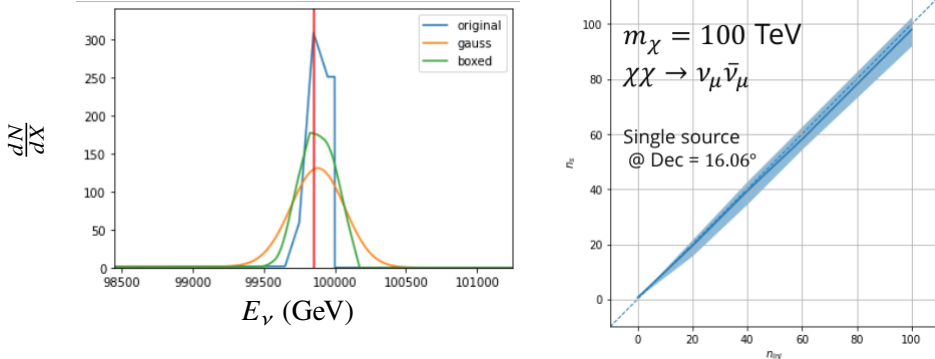


Figure 7.3 Left panel shows the two kernels overlaying the original spectrum from  $\chi\text{aron}\nu$  after propagation to Earth [85]. The vertical red line indicates where the original neutrino line is maximized. Blue line is the output from  $\chi\text{aron}\nu$ . Green line is the spectrum after convolution with a flat kernel. Orange line is the spectrum after Gaussian convolution. Right panel shows the signal recovery of the spectral model using the Gaussian kernel with parameters enumerated above.

1858 These parameters broadly improved the signal recovery of the line spectra. An example is in  
1859 Fig. 7.3. Analysis level signal recovery studies are expanded upon in Section 7.6.

### 1860 7.3.1.2 Spline Fitting

1861 In an effort to reduce computational work, memory burden, and align with point source methods  
1862 used for NGC1068 [88], spectral splines were created and adopted for estimating the neutrino flux  
1863 for the different spectral models. Software was written to generate, book keep, and calculate values  
1864 on the splines.

1865 When using splines, one has to be careful of the goodness to fit. The spline software used  
1866 here, Photospline [89], uses the penalized spline technique [90]. Through the penalized technique,  
1867 poor fits are penalized according to the accuracy of the nominal value, and the smoothness of the  
1868 first and second derivatives. However, this construction does not penalize on the integral of the  
1869 fit distribution which is critical in low signal studies, such as DM searches. There are additional  
1870 caveats when testing the goodness to fit to the MC generated above for all DM annihilation channels.

- 1871     • The splines must be Log10(\*) in Energy and dN/dX to account for the exponential nature of  
 1872       the flux.
- 1873     • The fidelity of the fit matters more at  $E_\nu \approx m_\chi$  where the model uncertainties are minimal  
 1874       and physical considerations (like the cut-off) are most important.
- 1875     • The fidelity of the fit matters less at low  $E_\nu$  as the model uncertainties are large AND  
 1876       IceCube's sensitivity diminishes significantly below 500 GeV.
- 1877     • Total integrated counts should be well-preserved.

1878   The resulting cost function was built to evaluate the goodness of spline fits to account for the above  
 1879   considerations.

$$e_i = x_i \cdot \left( \frac{dN_i}{dX_i} - 10^{\hat{e}_i} \right) \quad (7.3)$$

1880   Where  $\hat{e}_i$  is the spline estimator's value for  $x_i$ .  $x_i = E_{\nu_i}/m_\chi$ .  $\frac{dN_i}{dX_i}$  is the flux value from MC. I then  
 1881   take the RMS of the error distribution and the resulting value, err, is used to evaluate the fidelity of  
 1882   the spectral spline.

$$\text{err} = \sqrt{\frac{1}{x_{\max} - x_{\min}} \int_{x_{\min}}^{x_{\max}} e^2 dx} \quad (7.4)$$

1883    $x_{\min}$  and  $x_{\max}$  are the scope of the error evaluation and are provided in Tab. 7.1.

1884   Each SM channel had unique tolerances for 'err'. Channels with very hard cut-offs had looser  
 1885   tolerance for err because a significant error would be generated from single counts over/underes-  
 1886   timated at the cut-off. Soft channels do not share this issue, so the tolerance is much stricter. All  
 1887   annihilation channels from HDM are modeled well below IceCube's NST sensitivity which falls  
 1888   off substantially below 100 GeV [86]. We do not think it is necessary to evaluate the spline fits  
 1889   below 100 GeV and use this value as the default lower cut-off. Yet, HDM's model uncertainties  
 1890   at  $E_\nu < 10^{-6} \cdot m_\chi$  span an order of magnitude [79]. We also choose not to evaluate the splines  
 1891   below this critical value if it is within IceCube's sensitivity. Finally, the smoothing of the spectral  
 1892   lines in leptonic annihilation channels are ignored for evaluating the fit. We used the lower limit of

$\chi\chi \rightarrow$	GOOD	OK	FAIL	Limits of err calc [ $X_{min}, X_{max}$ ]
$Z^0 Z^0, W^+ W^-$	1.0E-3	1.0E-3, 1.0E-2	1.0E-2	MAX[100GeV/ $m_\chi$ , $10^{-6}$ ], 1.0
$t\bar{t}, hh$	1.0E-5	1.0E-5, 1.0E-4	1.0E-4	MAX[100GeV/ $m_\chi$ , $10^{-6}$ ], 1.0
$b\bar{b}, d\bar{d}, u\bar{u}$	9.0E-7	9.0E-7, 9.0E-6	9.0E-6	MAX[100GeV/ $m_\chi$ , $10^{-6}$ ], 1.0
$\nu\bar{\nu}_{e,\mu,\tau}$	1.0E-3	1.0E-3, 1.0E-2	1.0E-2	MAX[100GeV/ $m_\chi$ , $10^{-6}$ ], MIN[0.995, ( $E_n(\nu_{line}) - 4\sigma$ )/ $M_\chi$ ]
$e\bar{e}, \mu\bar{\mu}, \tau\bar{\tau}$	1.0E-3	1.0E-3, 1.0E-2	1.0E-2	MAX[100GeV/ $m_\chi$ , $10^{-6}$ ], MIN[0.995, ( $E_n(\nu_{line}) - 4\sigma$ )/ $M_\chi$ ]

Table 7.1 Spline err tolerances used for input in particle physics component to Eq. (5.1). Column 1 is the DM annihilation channel being fit. Columns 2, 3, and 4 are the tolerances for "GOOD" (pass), "OK" requires inspection, and "FAIL" (tune and refit) respectively. Column 5 has the X ranges over which the error is evaluated. MAX/MIN [ $\cdot, \cdot$ ] takes the maximum or minimum of the two enclosed values.

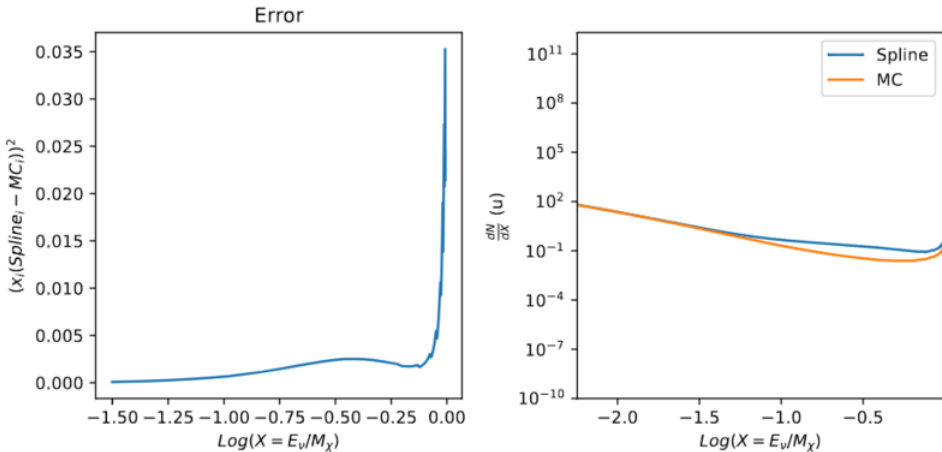


Figure 7.4 Example spline that failed the fit. Failed splines are corrected on a case by case basis unless the SM channel has a systematic problem fitting the splines. In this case, I made a bookkeeping error and loaded the incorrect spectral model

1893 the kernel mask as the upper limit of evaluation. Table 7.1 summarizes the tolerances for the DM  
1894 annihilation channels used for this analysis.

1895 The errors are then assesed in two ways. First, FAIL and OK are directly plotted with  $e_i$  as a  
1896 function of  $x$  with the full spline and MC. An example of a single failure is provided in Fig. 7.4.  
1897 Second, a summary plot of all the splines is plotted and colors coded. Figure C.1 are the spline  
1898 summaries as of writing this thesis. The goal broadly is to eliminate all red and inspect yellow  
1899 statuses.

1900 The  $\nu_e$  spectra at Earth are not considered in this analysis, so no work was done to refine the

1901 spline fits for this flavor. Finally, I perform a visual inspection of the splines to verify that the spline  
 1902 fitting did not introduce spurious features that would corrupt the likelihood fitting.

### 1903 7.3.1.3 Composite Neutrino Spectra

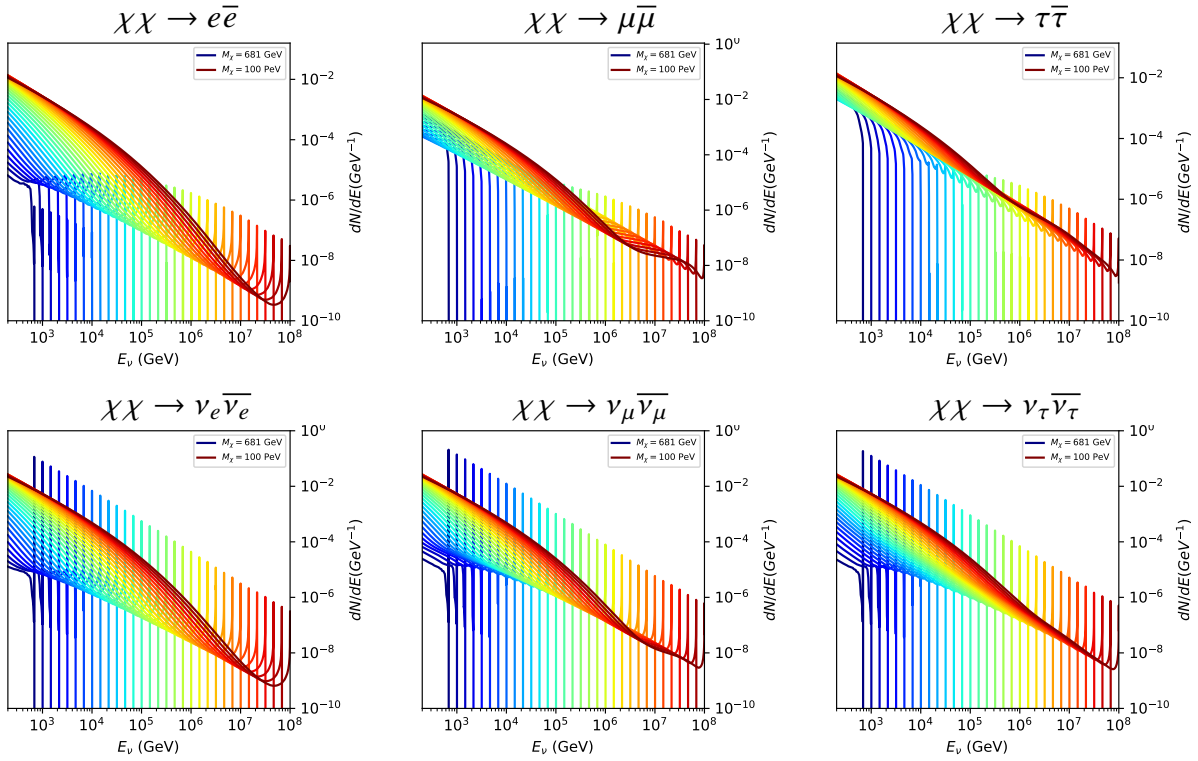


Figure 7.5 Summary of input spectral models that were smoothed with Gaussian kernels. Spectral models are for  $\chi\chi \rightarrow e\bar{e}$ ,  $\mu\bar{\mu}$ ,  $\tau\bar{\tau}$ ,  $\nu_e\bar{\nu}_e$ ,  $\nu_\mu\bar{\nu}_\mu$ , and  $\nu_\tau\bar{\nu}_\tau$ . These spectra are the composite ( $\nu_\mu + \nu_\tau$ ) of neutrino flavors. Every spectral model used for this analysis is featured as a colored solid line. Bluer lines are for low  $m_\chi$  models.  $m_\chi$  ranges from 681 GeV to 100 PeV. HDM [79],  $\chi$ arov [85], and Photospline [89] are used to generate these spectra. Energy (x-axis) was chosen to roughly represent the energy sensitivity of NST.

1904 With all the previously mentioned pieces, we are ready to fully assemble a comprehensive  
 1905 description of the particle physics term  $dN/dE$  in Eq. (7.1).

$$\frac{dN_\nu}{dE_\nu \oplus} = \left( \frac{dN_{\nu_e}}{dE_{\nu_e}} + \frac{dN_{\nu_\mu}}{dE_{\nu_\mu}} + \frac{dN_{\nu_\tau}}{dE_{\nu_\tau}} \right)_{\text{src}} \cdot \mathbf{P}(\nu_\alpha \rightarrow \nu_\beta) \quad (7.5)$$

1906 Figure 7.5 shows the spectral models that required Gaussian smoothing, the leptonic annihilation  
 1907 channels. The remaining models where the only processing were spline fitting and neutrino  
 1908 oscillation are documented in Section C.3. Notice that the different neutrino flavors are unique,

1909 especially in their low energy tails. Therefore, this analysis will be sensitive to DM annihilating to  
1910 the distinct neutrino flavors.

1911 **7.3.2 *J*- Astrophysical Component**

1912 For this analysis, we re-adopt the  $\mathcal{GS}$  model [59] used in Sec. 5 for dSphs. These models  
1913 are based on a modified Navarro-Frenk-White (NFW) profile where the indices of the NFW  
1914 (traditionally 1,3,1) are allowed to float. The angular width of these sources is much smaller than  
1915 the angular resolution of IceCube NST [88]. We therefore treat these sources as point sources  
1916 in this analysis, and forgo generating maps. These sources and the  $\mathcal{GS}$  model have already been  
1917 discussed at length in Section 5.3.2 and is not repeated here. IceCube uses identical sources to  
1918 Tab. 5.1 except we analyze source with declinations above  $0.0^\circ$ .

1919 **7.3.3 Source Selection and Annihilation Channels**

1920 We use all the dSphs presented in IceCube’s previous dSph DM search [83] and expand beyond  
1921 it. IceCube’s sources for this analysis studies include Boötes I, Canes Venatici I, Canes Venatici II,  
1922 Coma Berenices, Draco, Hercules, Leo I, Leo II, Leo V, Leo T, Segue 1, Segue 2, Ursa Major I,  
1923 Ursa Major II, and Ursa Minor. A full description of all sources used is in Table 5.1. Sources with  
1924 declinations less than 0.0 are excluded from this analysis.

1925 This analysis improves on the previous IceCube dSph paper [83] in the following ways. Previ-  
1926 ously, the IceCube detector was not yet completed to the 86 string configuration. Many more dSphs  
1927 will be observed, from 4 to 15. Previously, the particle physics model used for neutrino spectra  
1928 from DM annihilation did not have EW corrections where they are now included [79]. The spectral  
1929 models also predict substantial differences between the neutrino flavors, so this analysis will be the  
1930 first DM dwarf analysis to discriminate between primary neutrino flavors. The study performed  
1931 here studies 10.4 years of data.

1932 The SM annihilation channels probed for this study include  $\chi\chi \rightarrow$

1933  $b\bar{b}, t\bar{t}, u\bar{u}, d\bar{d}, e\bar{e}, \mu\bar{\mu}, \tau\bar{\tau}, ZZ, W^+W^-, \nu_e\bar{\nu}_e, \nu_\mu\bar{\nu}_\mu$ , and  $\nu_\tau\bar{\nu}_\tau$

1934 **7.4 Likelihood Methods**

1935 I use the Point-Source search likelihood which is widely used in IceCube analyses. The  
1936 likelihood function is defined as the following:

$$L(n_s) = \prod_{i=1}^N \left[ \frac{n_s}{N} S_i + \left(1 - \frac{n_s}{N}\right) B_i \right] \quad (7.6)$$

1937 where  $i$  is an event index,  $S$  and  $B$  are the signal PDF and background PDF respectively. For a joint  
1938 analysis where the sources are stacked the likelihood is expanded in the simplified way:

$$L(n_s) = \prod_{i=1}^{N_{\text{sources}}} L_i(n_s) \quad (7.7)$$

1939 Where  $L_i$  is the likelihood from the  $i$ -th source in the stacked analysis. The Test Statistic (TS)  
1940 definition remains the same as Eq. (5.7)

1941 **7.5 Background Simulation**

1942 Before we look at data, we must first analyze background and signal injection to validate our  
1943 analysis. We set out to characterize the TS distributions for each source, annihilation channel, and  
1944  $m_\chi$ . Previous IceCube DM searches [87, 91] showed TS distributions that did not behave according  
1945 to a  $\chi^2$  distribution with 1 degree of freedom. TS distributions can also vary significantly between  
1946 DM mass and annihilation models. Therefore, Wilk's theorem may not be applicable to the analysis.  
1947 Instead, a critical value is defined from many background trials. We study the TS distributions  
1948 first for each source, then for the stacked analysis. The following sections show the results of the  
1949 likelihood fitting for a suite of background trials.

1950 I assume that TS values are physical:  $TS \geq 0$ .  $\epsilon[x]$  indicate the fraction of events where  $TS < x$ .  
1951 For TS plots shown here, the decimal values of  $x$  are 1.0e-2 and 1.0e-3. Each subplot represents  
1952 a simulation of 100,000 data-scrambled background trials. Section 7.5.1 show the background TS  
1953 distributions obtained from Segue 1, a source with little Earth attenuation and large  $J$ -factor, and  
1954 Ursa Major II, which has similarly large  $J$ -factor but significantly more Earth attenuation, assuming  
1955 DM annihilation into  $b\bar{b}$ ,  $\tau\bar{\tau}$ , and  $\nu_\mu\bar{\nu}_\mu$ . I show the TS distributions of a stacked study of 15 sources  
1956 for all DM annihilation channels.

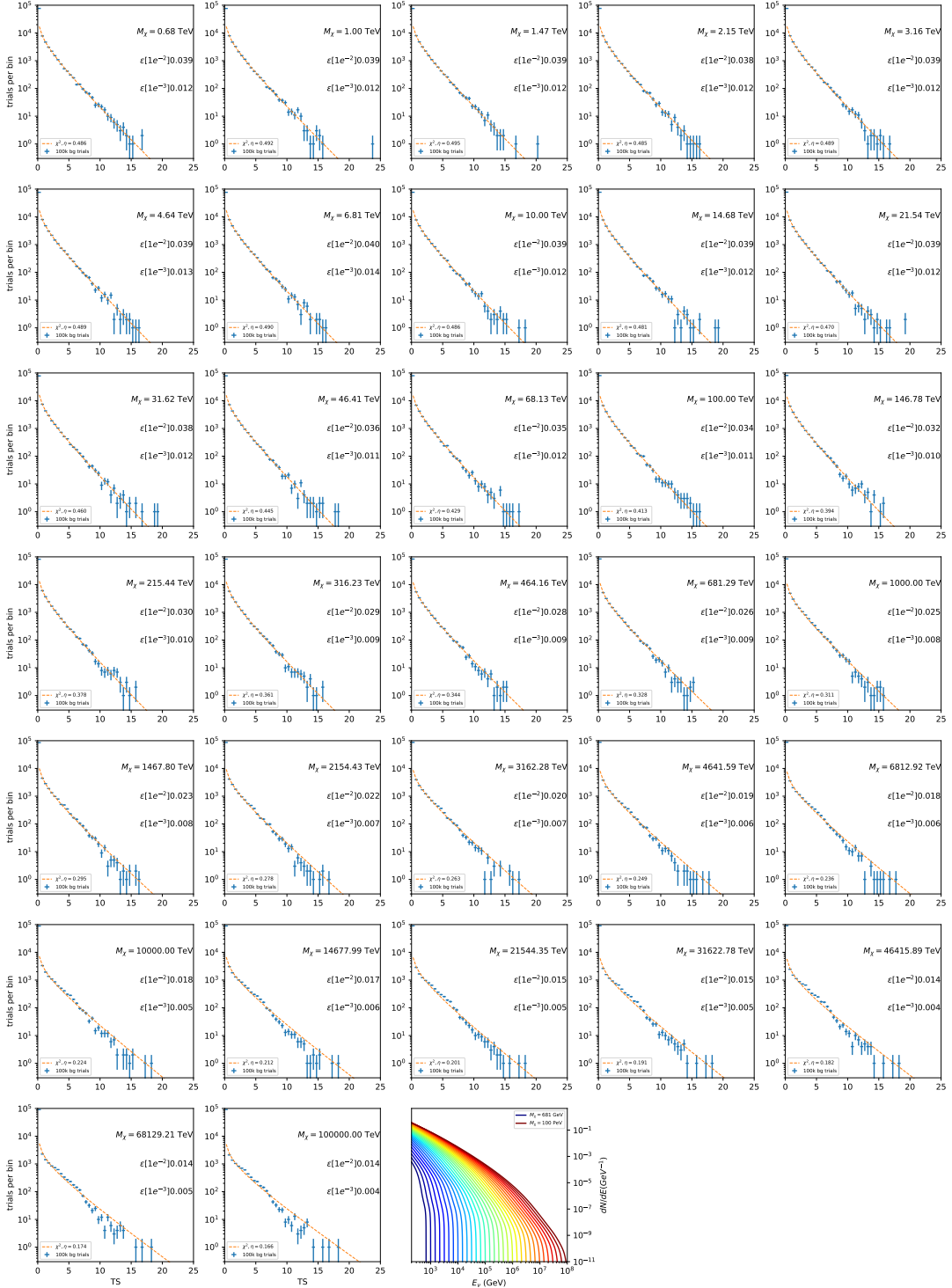


Figure 7.6 Test statistic (TS) distributions for Segue 1 and  $\chi\chi \rightarrow b\bar{b}$ . Each subplot, except the final, is the TS distribution for a specific DM mass listed in the subplot. Orange dashed lines are the traces for a  $\chi^2$  distribution with 1 degree of freedom.  $\epsilon[\cdot]$  is the fraction of trials smaller than the bracketed value. The final subplot features the all DM spectral models, similar to Fig. 7.5, used as input for the TS distributions.

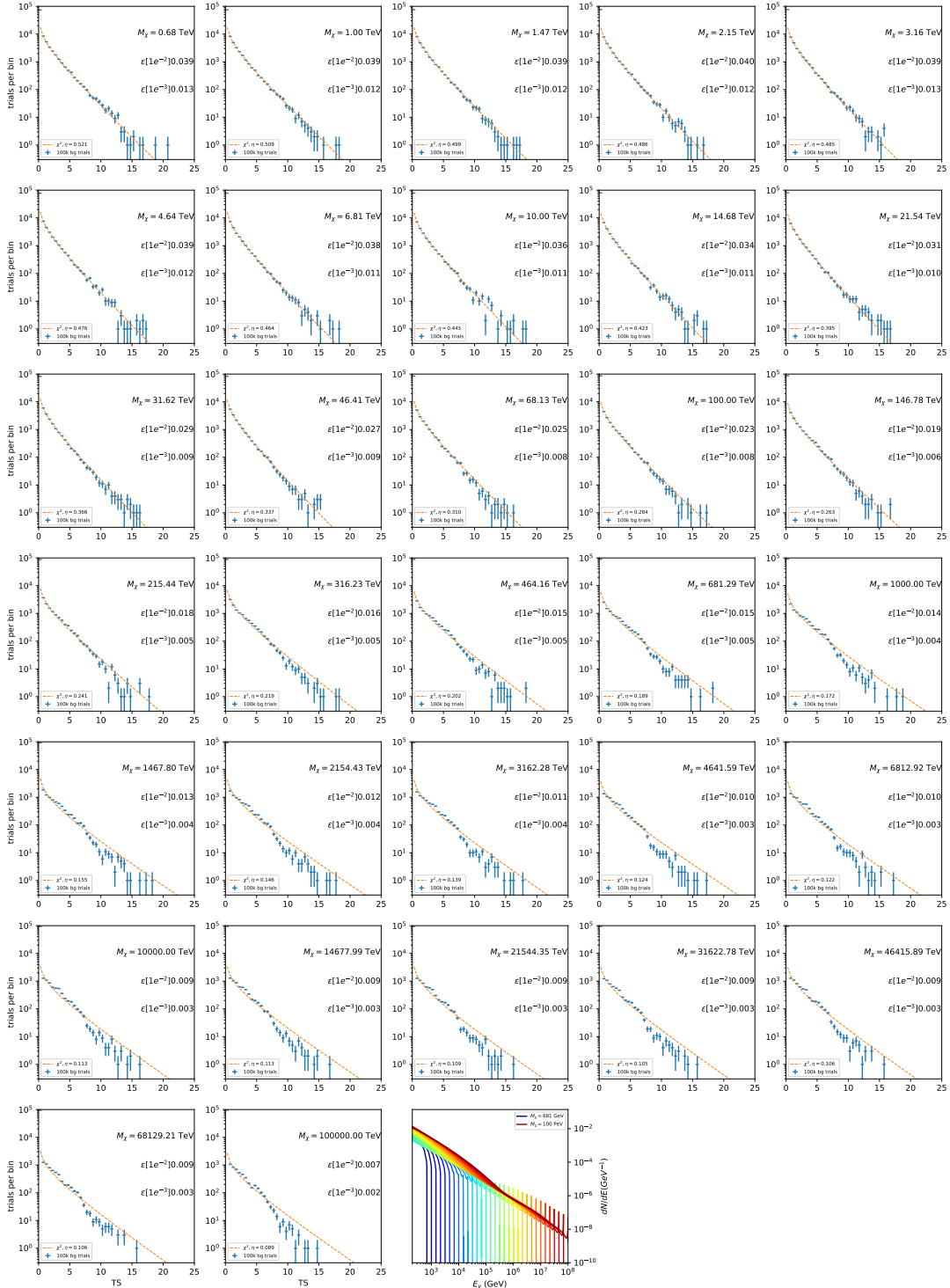


Figure 7.7 Same as Fig. 7.6 for Segue 1  $\chi\chi \rightarrow \tau\bar{\tau}$ .

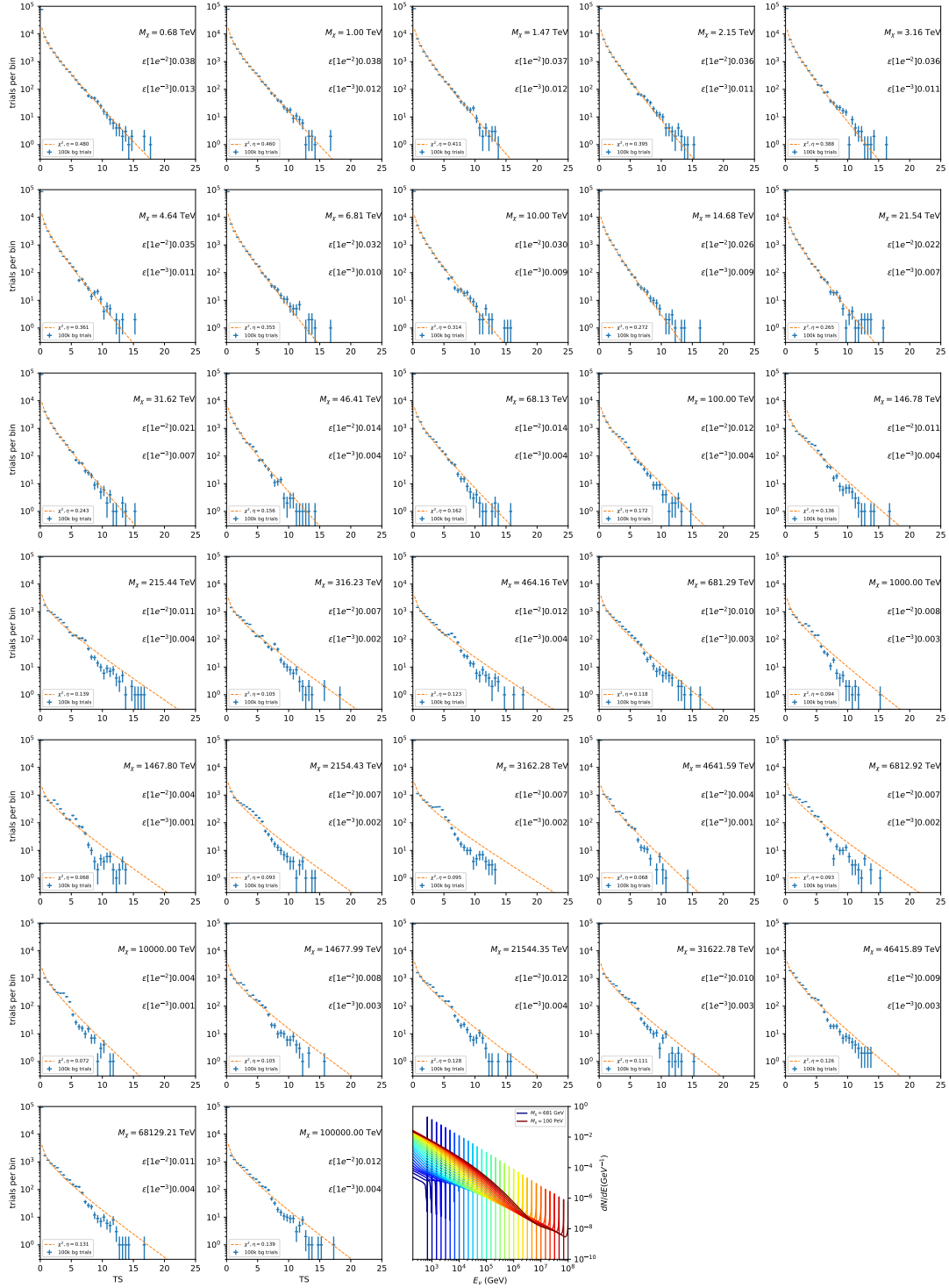


Figure 7.8 Same as Fig. 7.6 for Segue 1  $\chi\chi \rightarrow \nu_\mu\bar{\nu}_\mu$ .

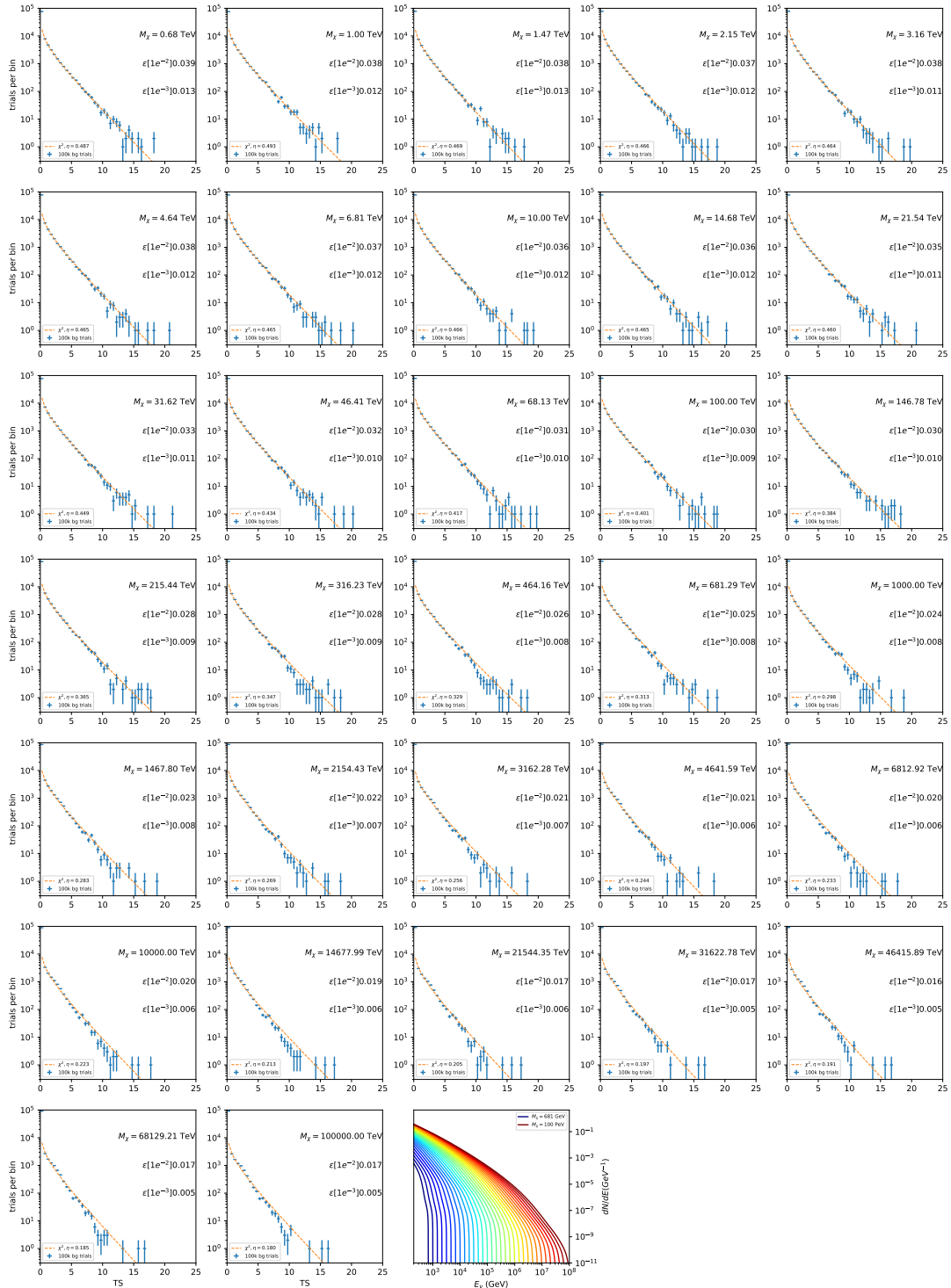


Figure 7.9 Same as Fig. 7.6 for Ursa Major II 1  $\chi\chi \rightarrow b\bar{b}$ .

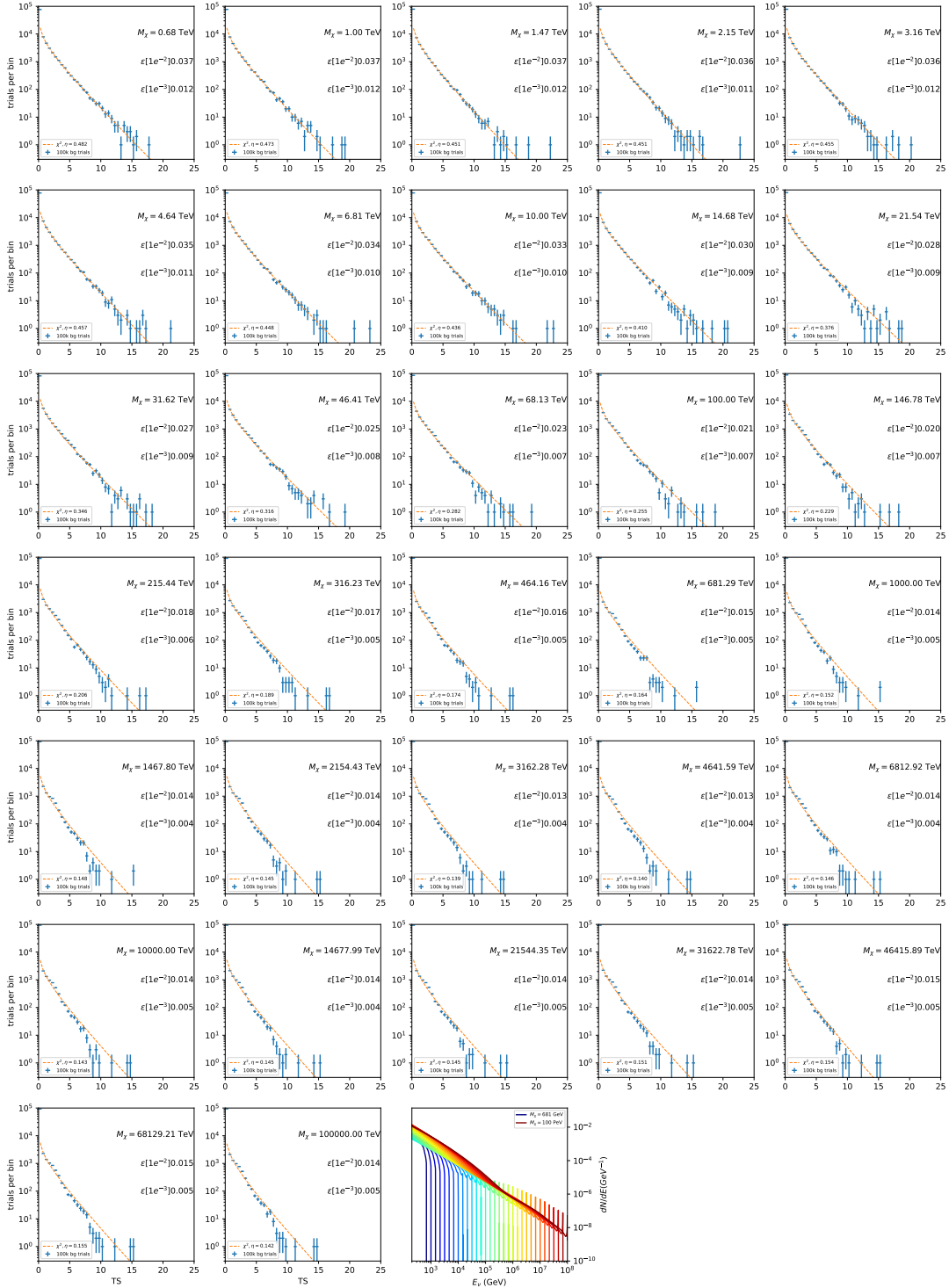


Figure 7.10 Same as Fig. 7.6 for Ursus Major II 1  $\chi\chi \rightarrow \tau\bar{\tau}$ .

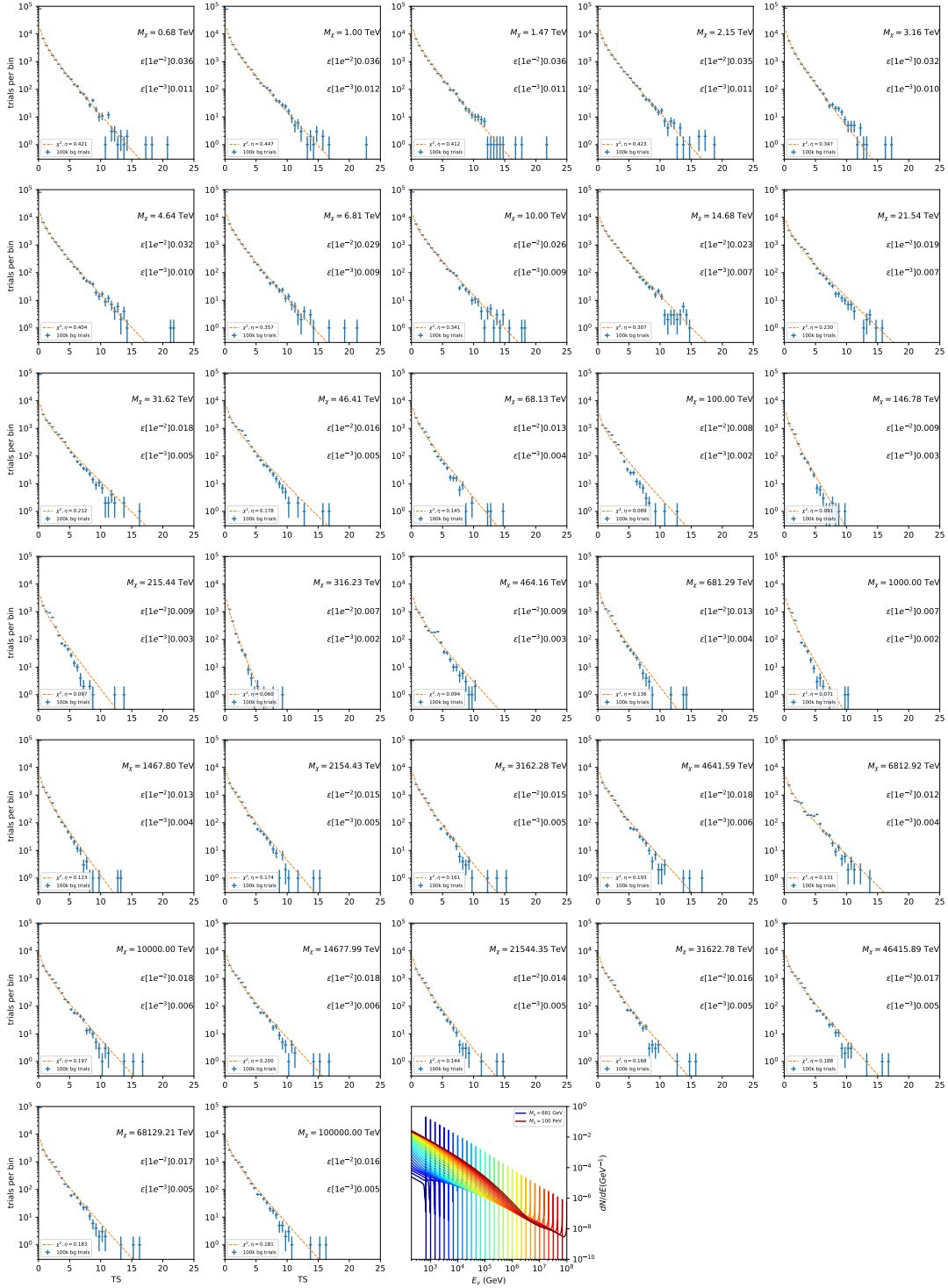


Figure 7.11 Same as Fig. 7.6 for Ursa Major II 1  $\chi\chi \rightarrow \nu_\mu\bar{\nu}_\mu$ .

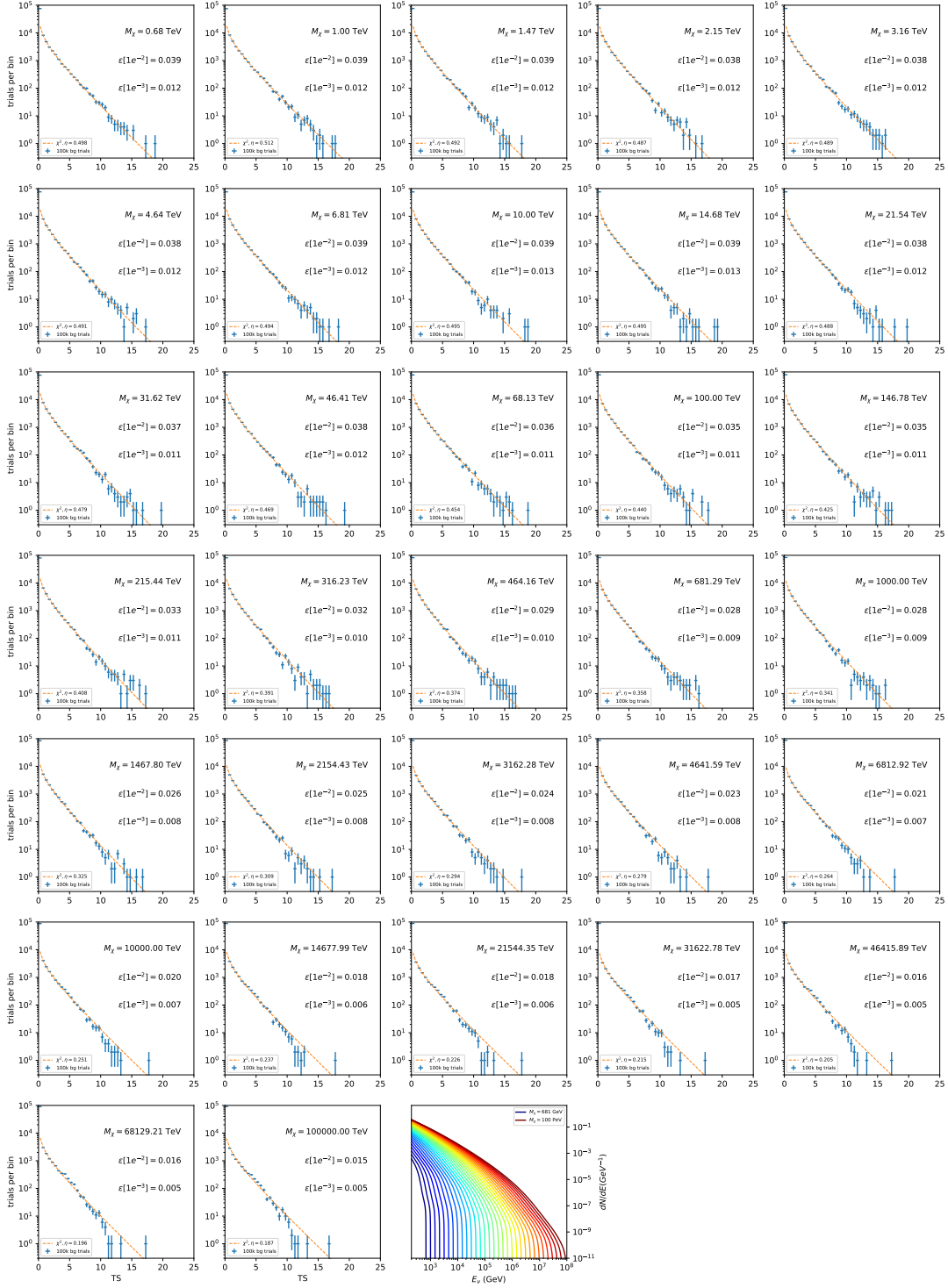


Figure 7.12 Same as Fig. 7.6 for 15,  $\mathcal{GS}$   $J$ -factor, stacked sources and  $\chi\chi \rightarrow b\bar{b}$ .

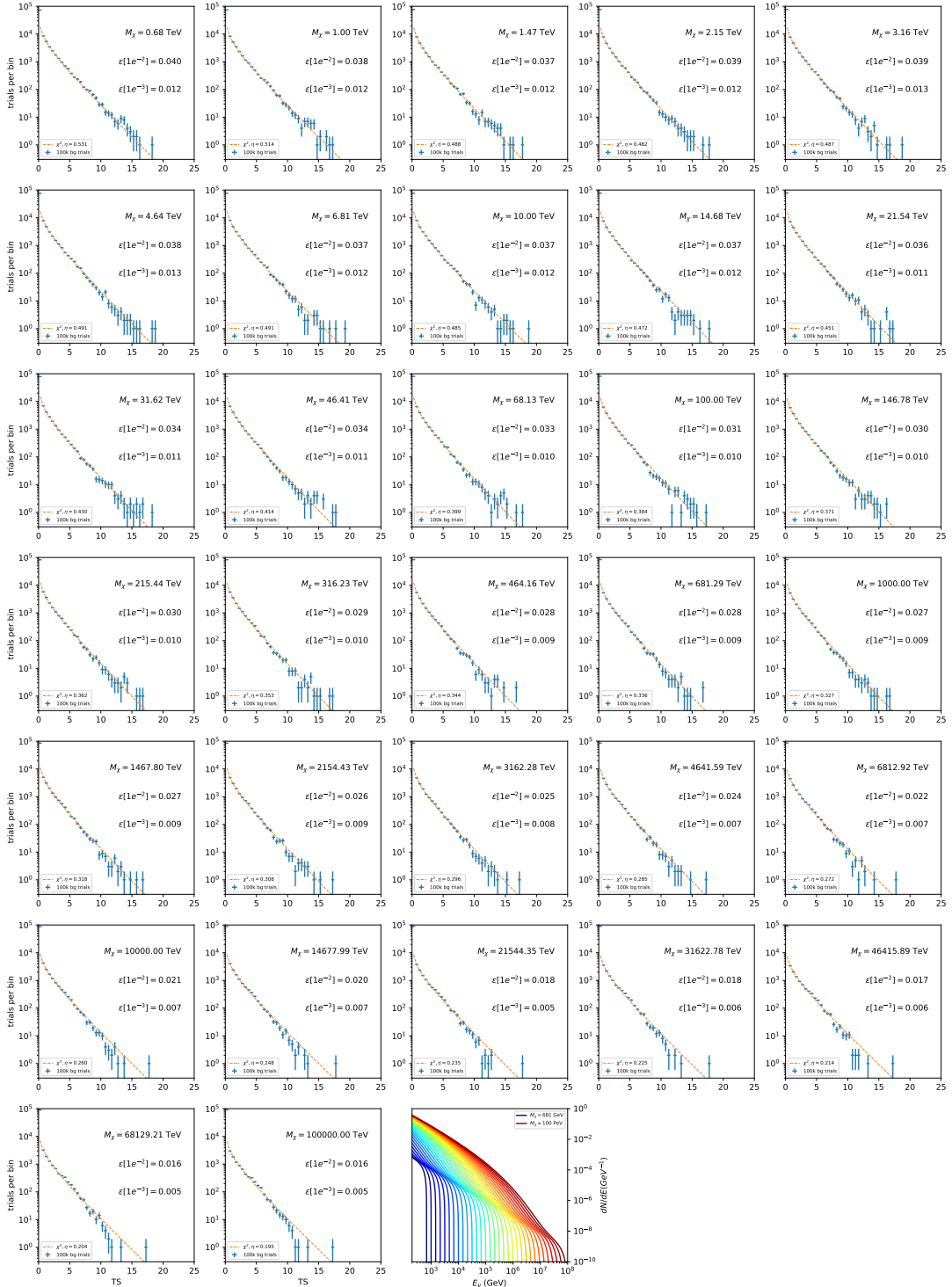


Figure 7.13 Same as Fig. 7.6 for 15,  $\mathcal{GS}$   $J$ -factor, stacked sources and  $\chi\chi \rightarrow t\bar{t}$ .

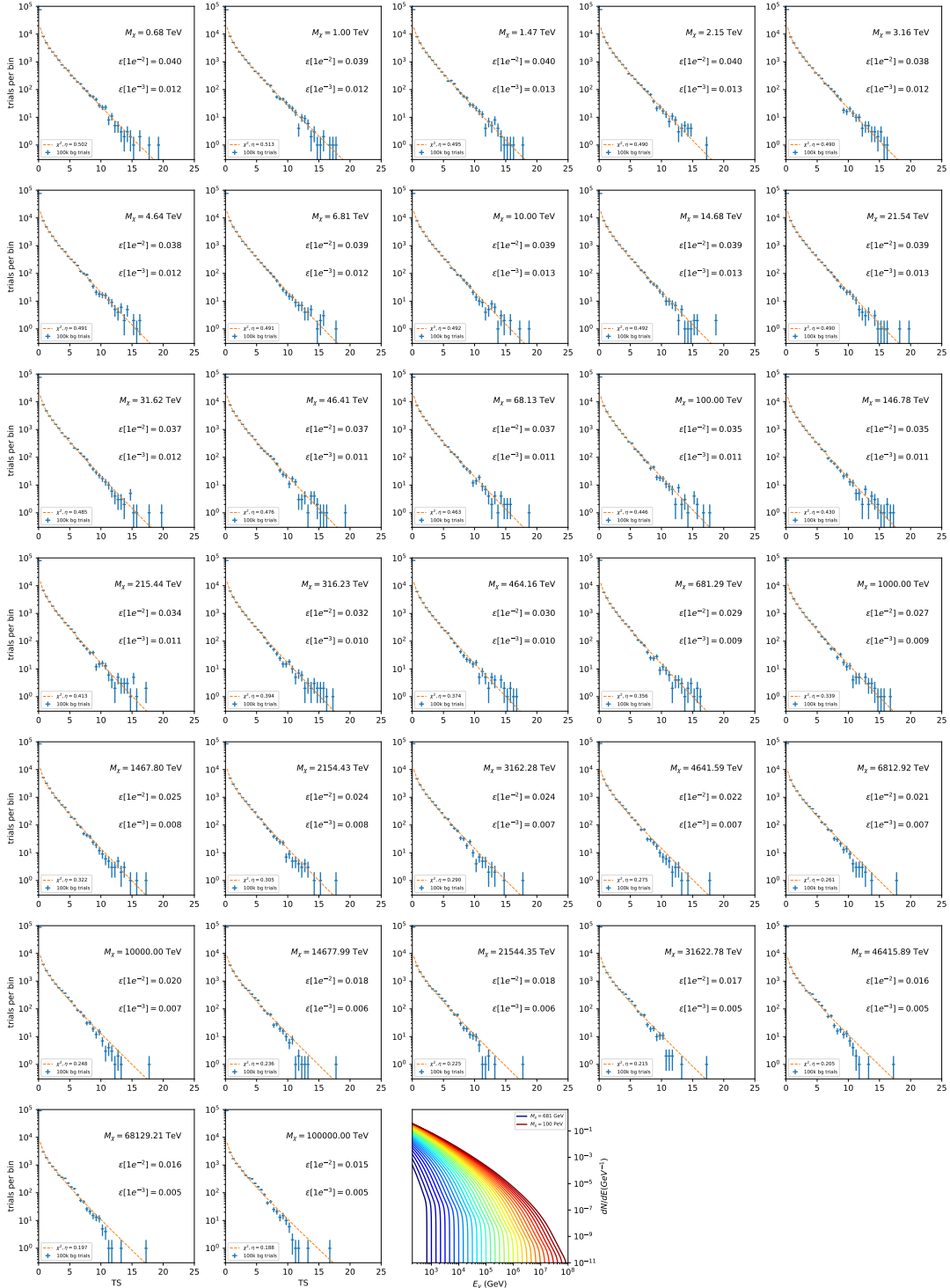


Figure 7.14 Same as Fig. 7.6 for 15,  $\mathcal{G}\mathcal{S}$   $J$ -factor, stacked sources and  $\chi\chi \rightarrow u\bar{u}$ .

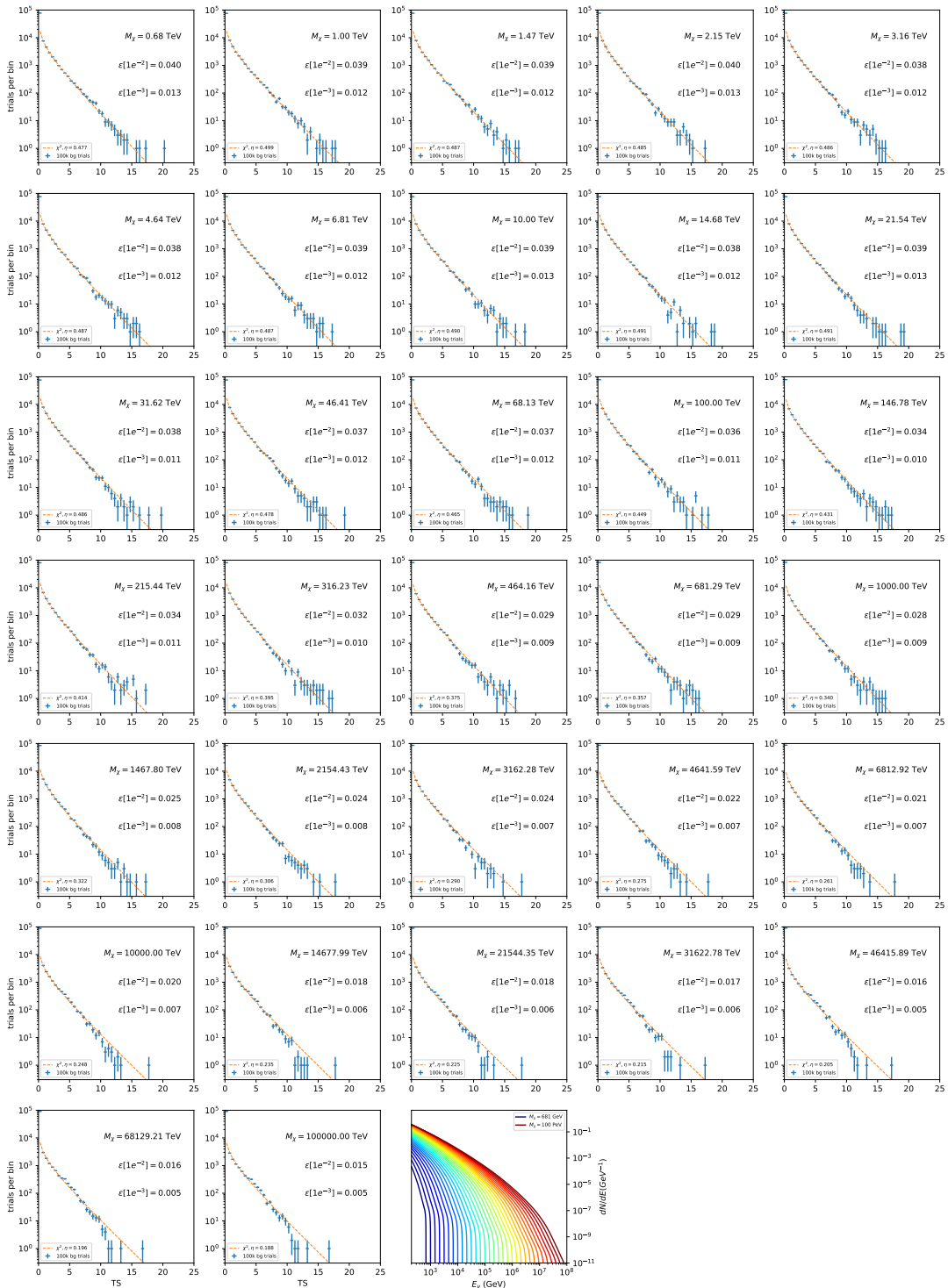


Figure 7.15 Same as Fig. 7.6 for 15,  $\mathcal{G}\mathcal{S}$  J-factor, stacked sources and  $\chi\chi \rightarrow d\bar{d}$ .

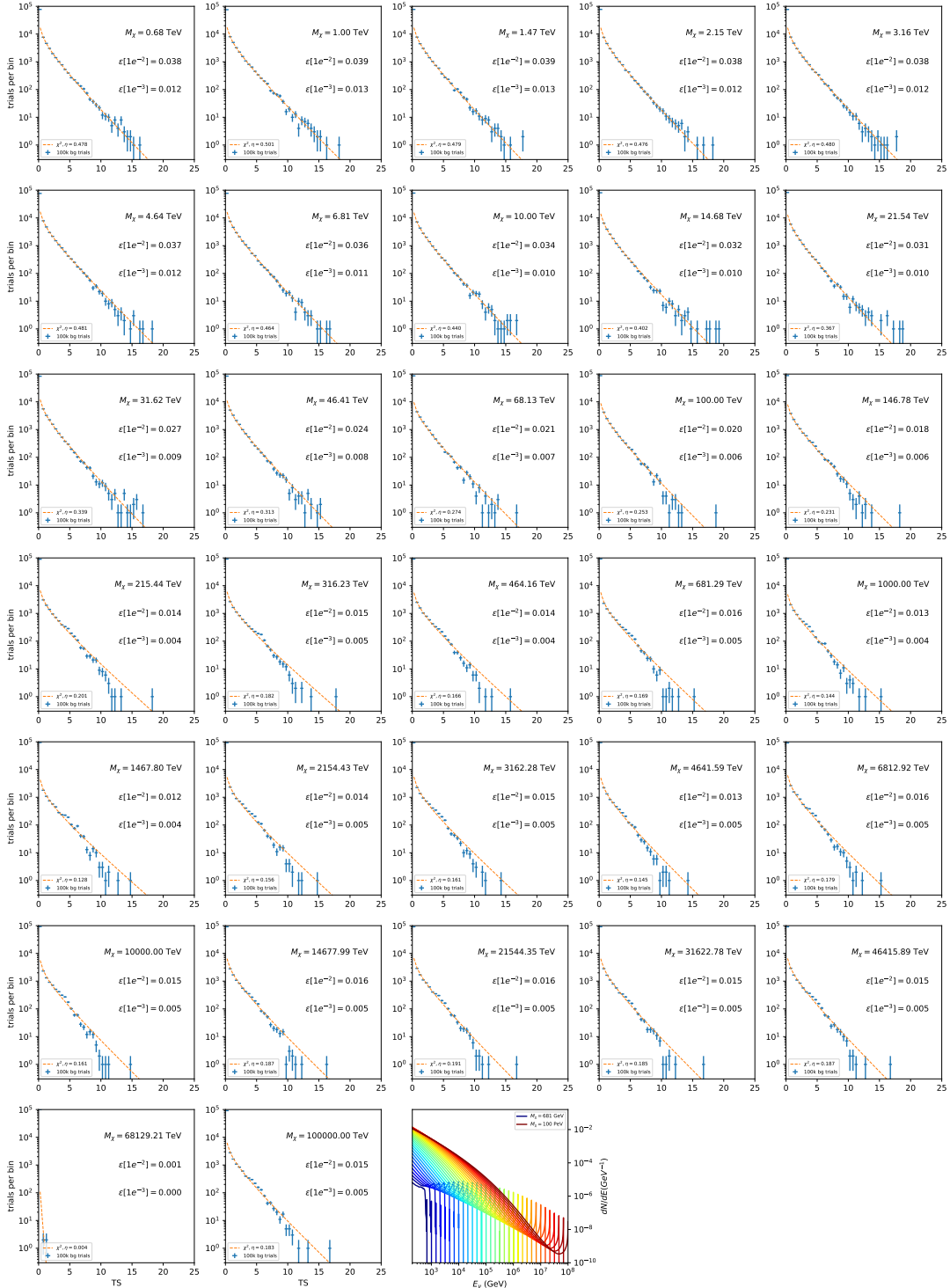


Figure 7.16 Same as Fig. 7.6 for 15,  $\mathcal{G}\mathcal{S}$  J-factor, stacked sources and  $\chi\chi \rightarrow e\bar{e}$ .

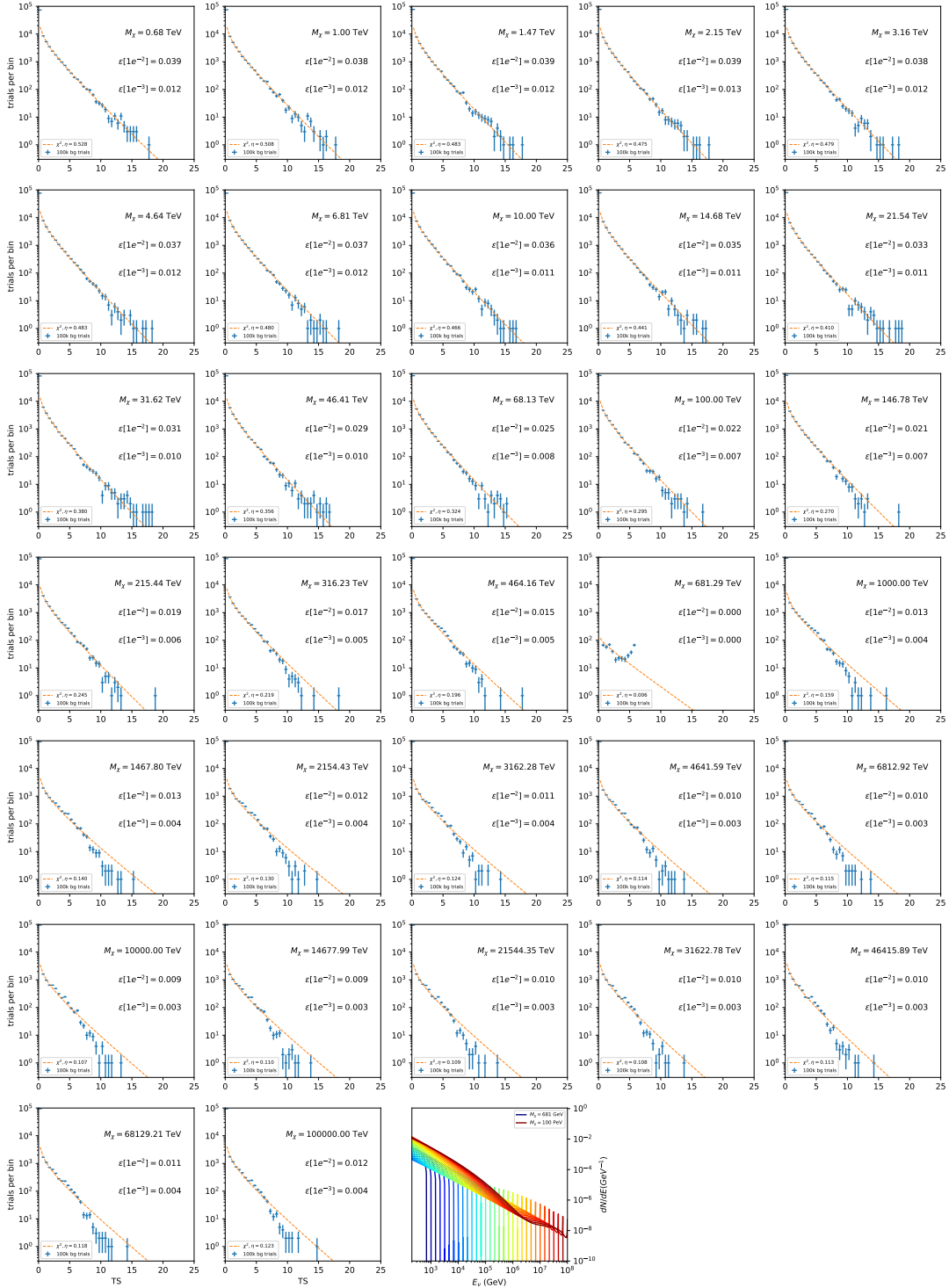


Figure 7.17 Same as Fig. 7.6 for 15,  $\mathcal{GS}$   $J$ -factor, stacked sources and  $\chi\chi \rightarrow \mu\bar{\mu}$ .

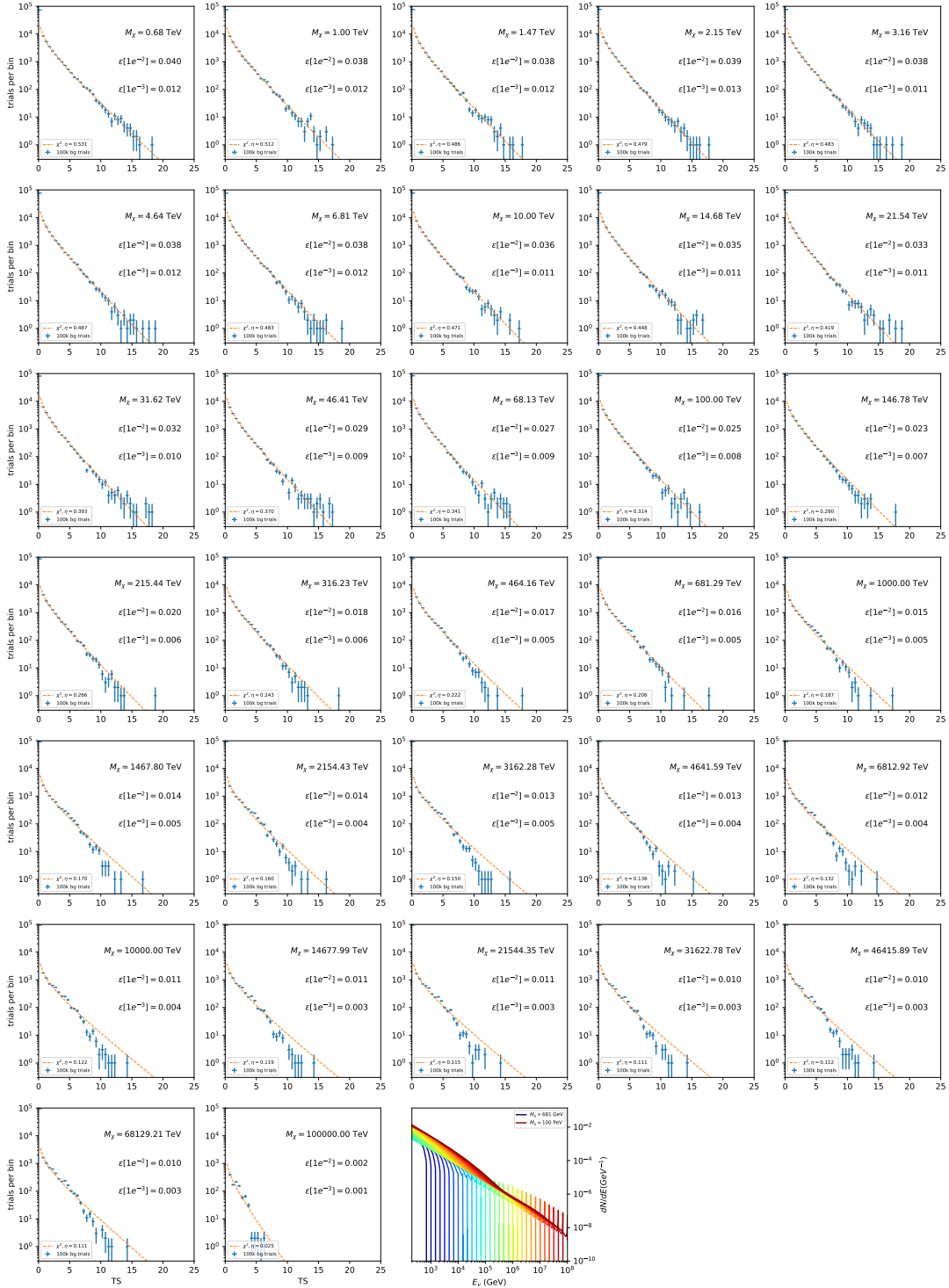


Figure 7.18 Same as Fig. 7.6 for 15,  $\mathcal{GS}$   $J$ -factor, stacked sources and  $\chi\chi \rightarrow \tau\bar{\tau}$ .

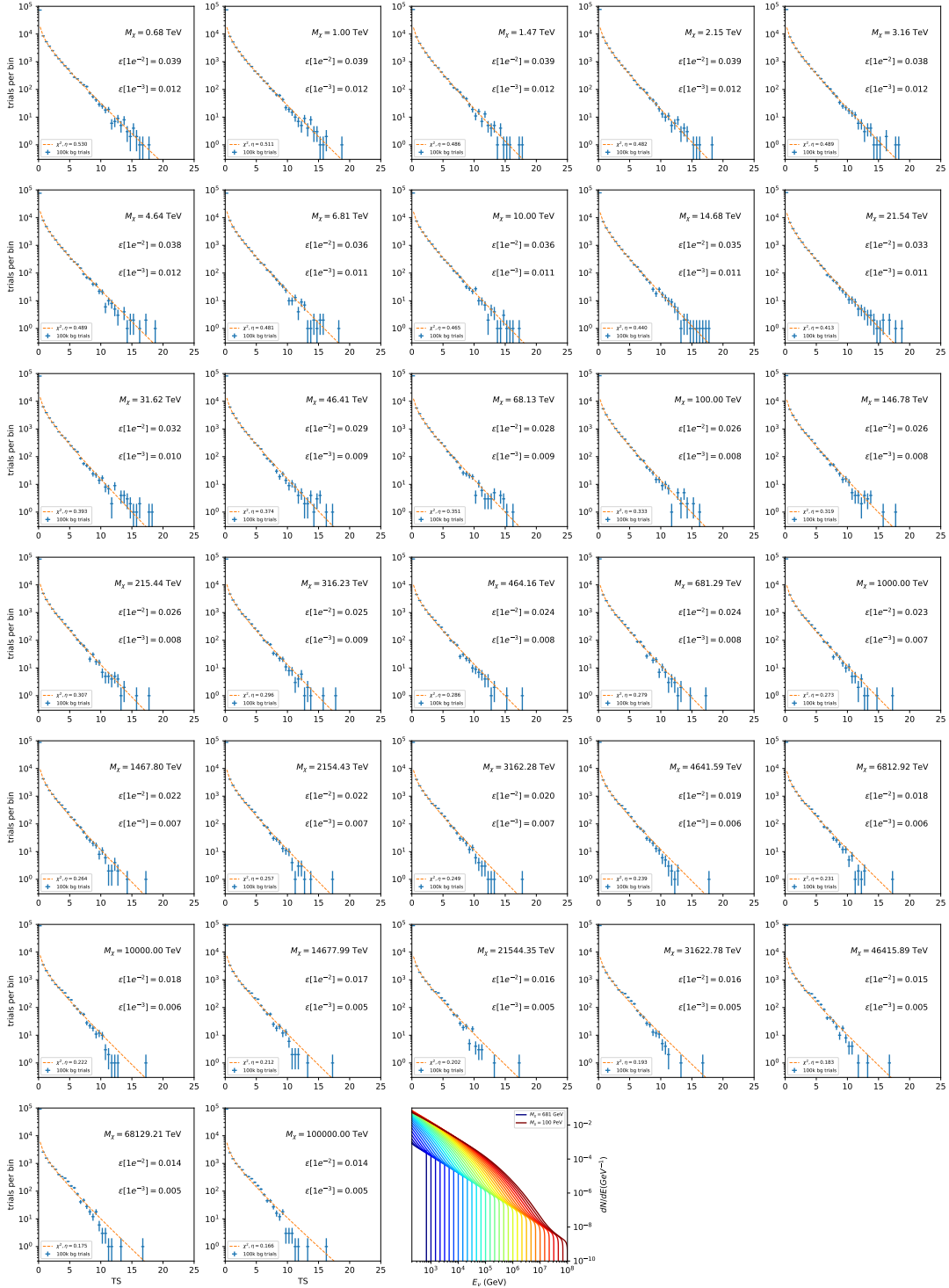


Figure 7.19 Same as Fig. 7.6 for 15,  $\mathcal{GS}$  J-factor, stacked sources and  $\chi\chi \rightarrow W^+W^-$ .

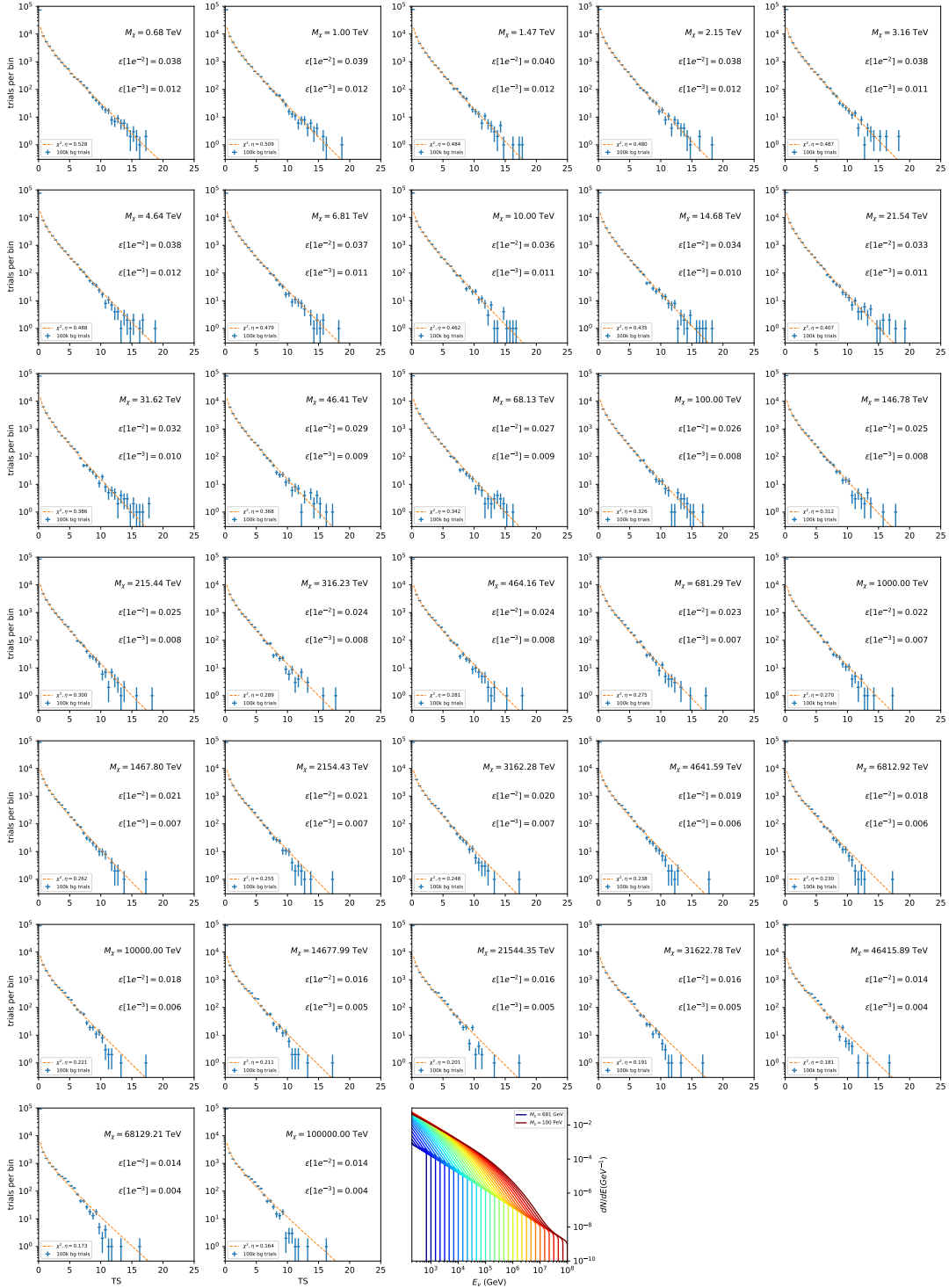


Figure 7.20 Same as Fig. 7.6 for 15,  $\mathcal{GS}$   $J$ -factor, stacked sources and  $\chi\chi \rightarrow ZZ$ .

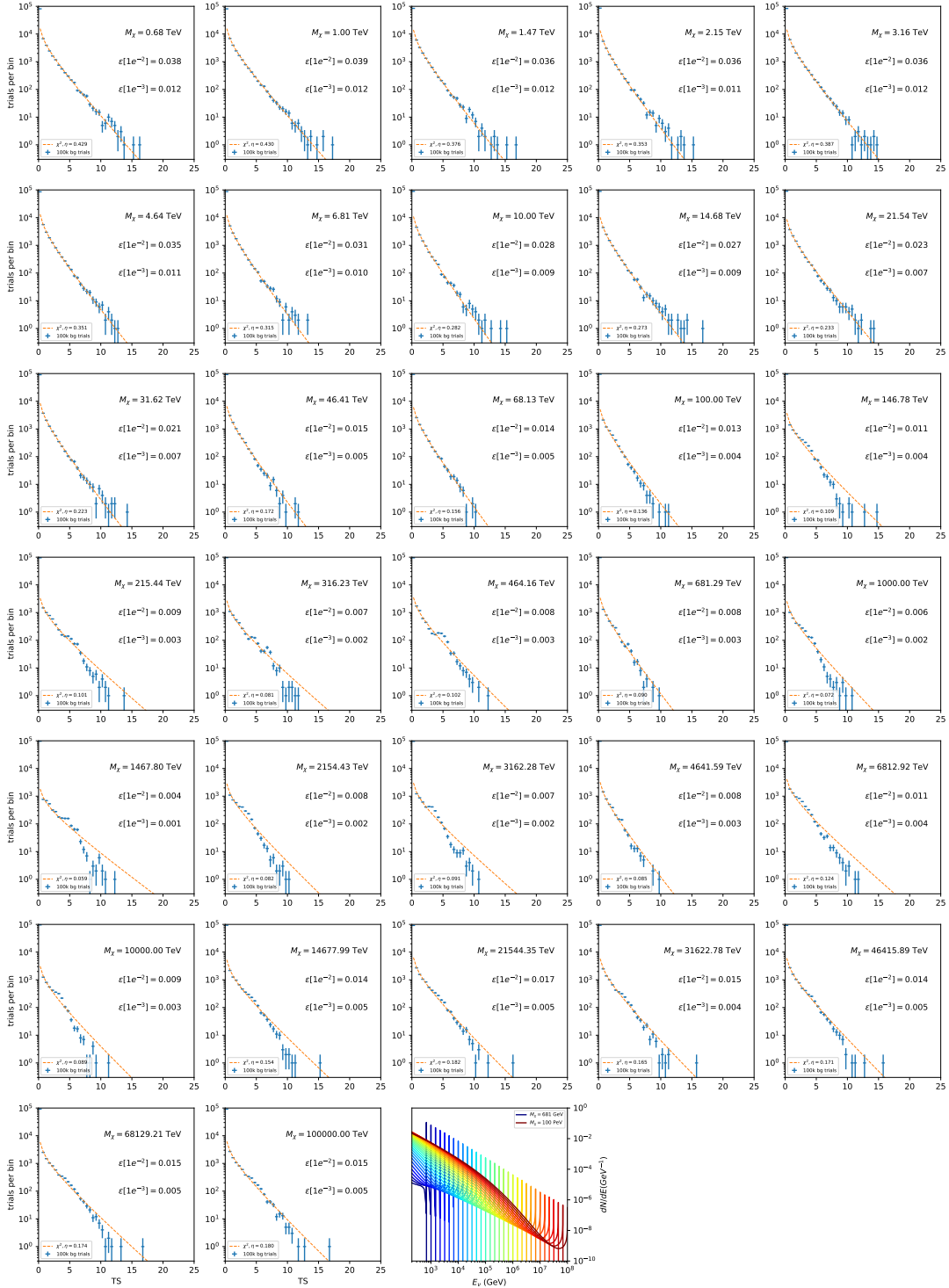


Figure 7.21 Same as Fig. 7.6 for 15,  $\mathcal{GS}$  J-factor, stacked sources and  $\chi\chi \rightarrow \nu_e \bar{\nu}_e$ .

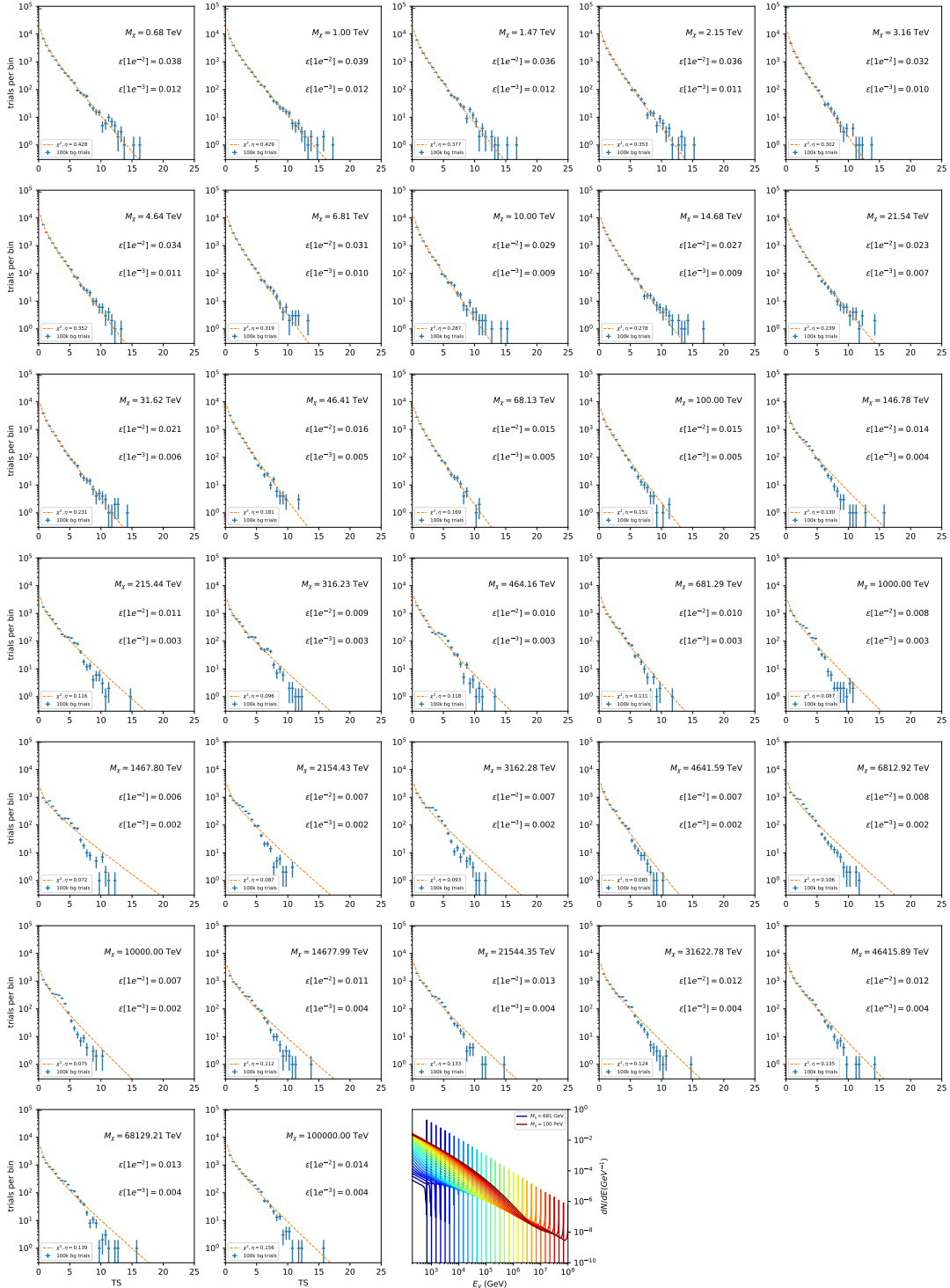


Figure 7.22 Same as Fig. 7.6 for 15,  $\mathcal{GS}$  J-factor, stacked sources and  $\chi\chi \rightarrow \nu_\mu \bar{\nu}_\mu$ .

1957 **7.5.1 TS per Source**

1958 Figure 7.6 to Figure 7.11 present the TS distributions for Segue 1 and Ursa Major II for 100,000  
1959 trials. More studies for all annihilation channels and remaining 13 sources were also performed  
1960 and are documented in IceCube’s internal wiki.

1961 Almost every distribution produced follows a  $\chi^2$  distribution with 1 degree of freedom. This is  
1962 more true for low  $m_\chi$  than high  $m_\chi$  models. These observations are important for future assumptions  
1963 made in Sec. 8 and may justify statistical calculations assuming our test statistics follow a  $\chi^2$  with  
1964 1 degree of freedom.

1965 **7.5.2 Stacked TS**

1966 Figure 7.12 to Figure 7.22 present the TS distributions for a stacked study of 15 sources with  
1967  $\mathcal{GS}$   $J$ -factors on 100,000 trials. The presentation of these plots are identical to the single source  
1968 distributions in Section 7.5.1. We see similar behaviour in the stacked TS distributions compared  
1969 to the single source studies.

1970 **7.6 Signal Recovery**

1971 We also wish to understand how well the analysis is able to reconstruct signal neutrinos. In  
1972 order to test this, we inject neutrinos from our spectral models randomly then attempt to discern  
1973 the number of signal neutrinos in the simulated data. Figure 7.23 and Figure 7.24 show this study  
1974 for  $\chi\chi \rightarrow b\bar{b}$ ,  $t\bar{t}$ , and  $\nu_\mu\bar{\nu}_\mu$  for a stacked analysis of 15 sources. Figure C.3 to Figure C.8 show  
1975 identical studies for Segue 1 and Ursa Major II. We see that the analysis is conservative at smaller  
1976  $m_\chi$ , yet improves at larger  $m_\chi$ . We also see that the uncertainty is small for the neutrino annihilation  
1977 spectra, and the uncertainty is larger for softer channels like  $b\bar{b}$ .

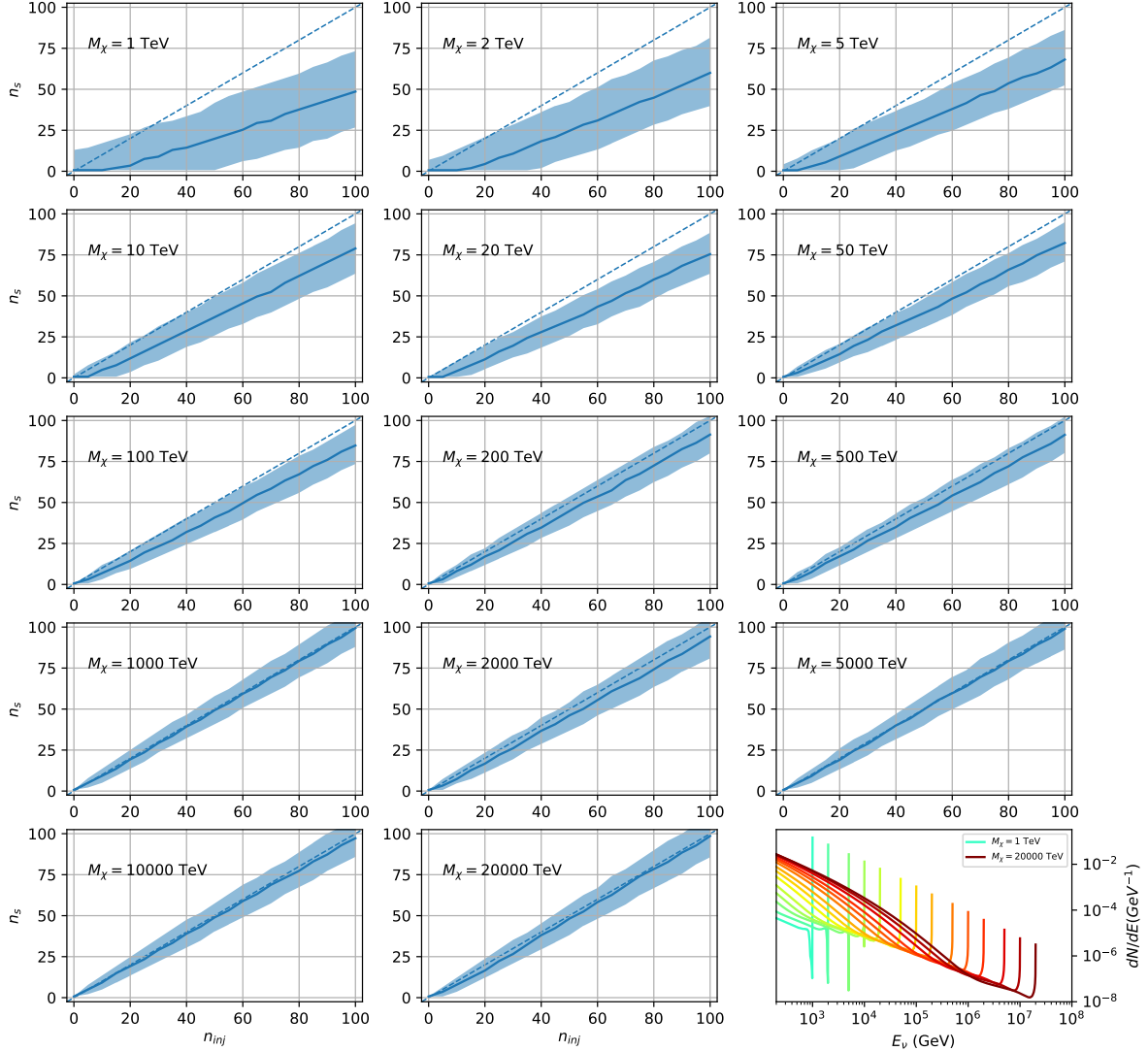


Figure 7.23 Signal Recovery study for an analysis with 15 stacked sources using the  $\mathcal{GS}$   $J$ -factors [59]. Above shows 14 studies for DM mass ranging between 1 TeV and 20 PeV for  $\chi\chi \rightarrow \mu_\mu\bar{\mu}_\mu$ . The bottom right subplot features every spectral model used as input for the remaining subplots. The remaining subplots show  $n_{inj}$  as the number of signal events injected into background simulation. Whereas,  $n_s$  is the number of signal events recovered from analyzing the injected simulation. Blue line represents the median values of 100 simulations. Light blue bands show the  $1\sigma$  statistical uncertainty around the median.

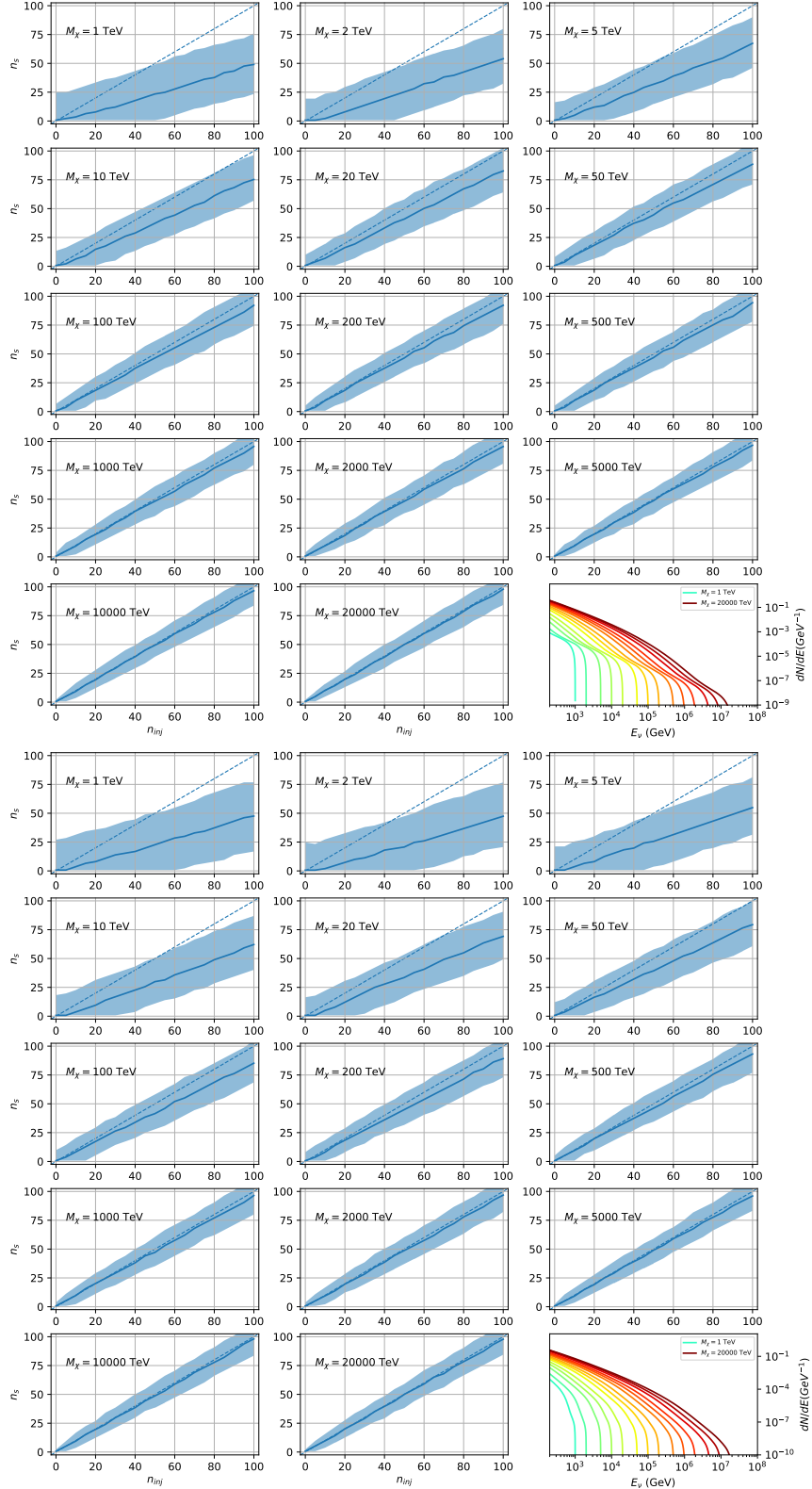


Figure 7.24 Same as Fig. 7.23 but for  $\chi\chi \rightarrow t\bar{t}$  (top) and  $b\bar{b}$  (bottom).

1978 **7.6.1 Sensitivities**

1979 In IceCube, we usually define the 90% confidence level (CL), as the minimum number of signal  
1980 events ( $n_s$ ) required to have a Type I error rate smaller than 0.5 and Type II error rate of 0.1. We  
1981 compute  $n_s$  from the following equation

$$n_s = T_{\text{live}} \int_0^{\Delta\Omega} d\Omega \int_{E_{\min}}^{E_{\max}} dE_\nu A_{\text{eff}}(\hat{n}, E_\nu) \frac{d\Phi_\nu}{d\Omega dE_\nu}(\hat{n}, E_\nu), \quad (7.8)$$

1982 to extract the sensitivity on the dark matter velocity-weighted annihilation cross-section,  $\langle\sigma v\rangle$ .  $T_{\text{live}}$   
1983 is the detector live time,  $A_{\text{eff}}$  is the effective area of the detector, and  $E_{\min}$ ,  $E_{\max}$  are the minimum,  
1984 maximum energies of the expected neutrinos, respectively.

1985 Sensitivities are calculated for each source individually as if they were the only source and as a  
1986 stack over 1000 trials. From Eq. (7.8) and Eq. (7.1) we can compute the  $\langle\sigma v\rangle$  at a 90% confidence  
1987 level. Figure 7.26 and Fig. 7.25 show the sensitivities for some DM annihilation channels. Not  
1988 all channels computed successfully in time for the writing of this dissertation. Among channels  
1989 missing include the charged leptons:  $e$  and  $\tau$ .

1990 **7.7 Systematics**

1991 The current analysis plan is to compare these sensitivities to another  $J$ -factor catalog such as  
1992  $\mathcal{LS}$  [80] although this was not completed in time for this dissertation. Additionally, we set out to  
1993 perform a standard suite of IceCube systematic studies which include: DOM efficiency, Hole ice,  
1994 ice absorption, and photon scattering. We do study Earth attenuation, and Section 7.7.1 enumerates  
1995 the impact of the Earth on our hardest neutrino spectra.

1996 **7.7.1 Earth Effects**

1997 We look to quantify the impact of the Earth on our sensitivity to  $\chi\chi \rightarrow \nu_\mu \bar{\nu}_\mu$ . This channel is  
1998 expected to be among the significantly impacted annihilation channels because it has a significant  
1999 contribution at PeV energies for  $m_\chi \geq 1\text{PeV}$ . The Earth is expected to attenuate these higher energy  
2000 neutrinos. However, these neutrino spectra have significant low energy contributions, so we do not  
2001 expect to entirely lose our sensitivity. This motivated a study examining our  $\langle\sigma v\rangle$  sensitivity over  
2002 all DM masses sampled for a selection of declinations.

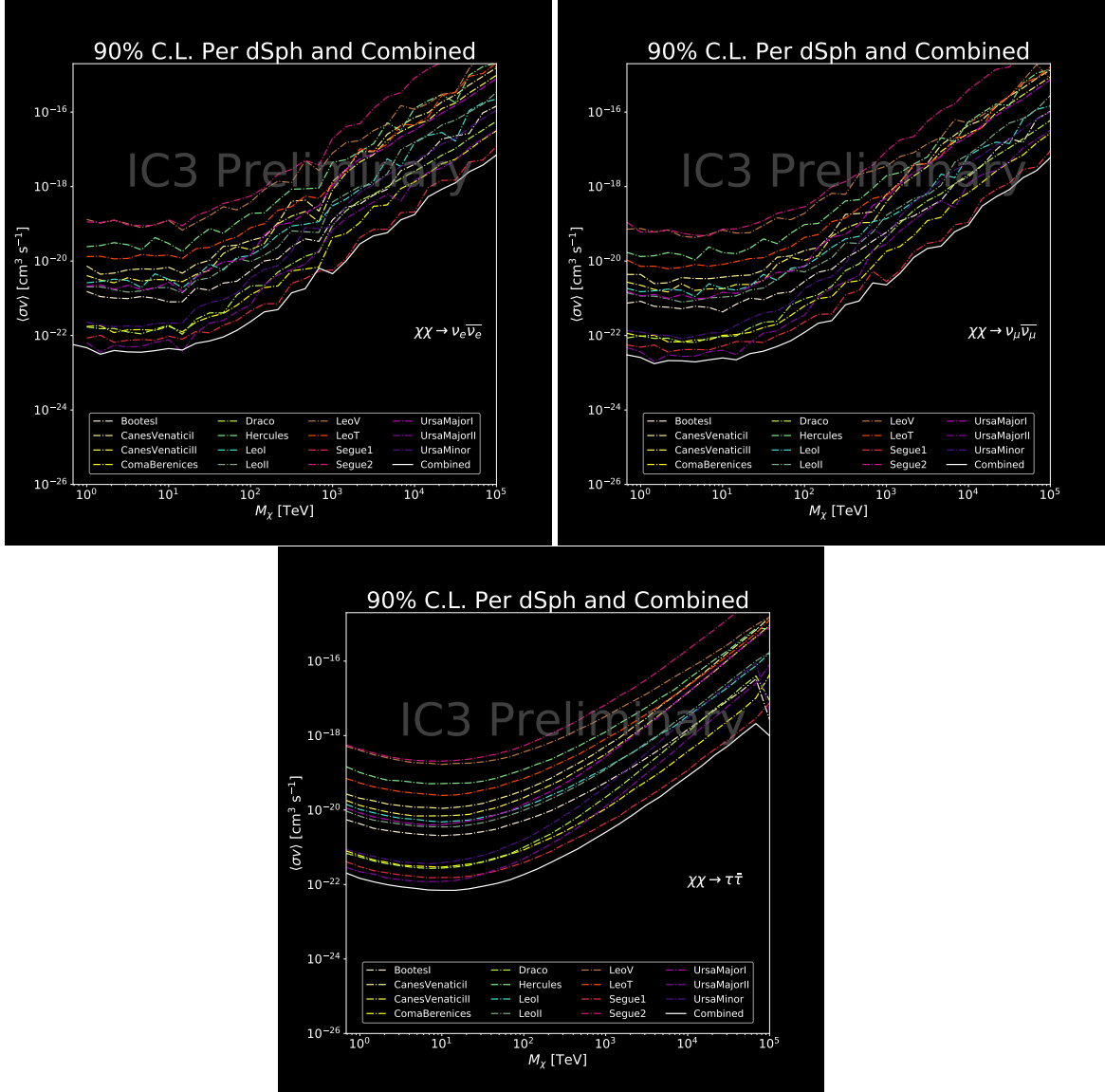


Figure 7.25 IceCube North Sky Track Sensitivities. Each panel shows sensitivity curves for various DM annihilation channels. Sensitivities are for the velocity-weighted cross-section  $\langle\sigma v\rangle$  versus  $m_\chi$ . Dotted, colored lines are sensitivities for individual sources. Solid white lines are for the combined sensitivity of all 15  $\mathcal{GS}$  sources used in this study.

2003 For this systematic study, I sample 6 DM masses per decade from 681 GeV to 100 PeV. I select  
 2004 declinations that are shared with sources in the  $\mathcal{GS}$  catalog: Boötes I, Canes Venatici II, Leo V,  
 2005 Ursa Major I, and Ursa Minor. I study a fake source who's  $J$ -factor is shared with Ursa Major II,  
 2006 but who's coordinates belong to the aforementioned list. The sensitivity studies performed for each  
 2007 source (Fig. 7.25 and Section C.5) provided  $n_s$  for 1000 trials which we extracted from Eq. (7.8).  
 2008 We derive  $\langle\sigma v\rangle$  using  $\log_{10} J = 19.42 \log_{10}(\text{GeV}^2 \text{cm}^{-5})$ . Figure 7.28 shows the results.

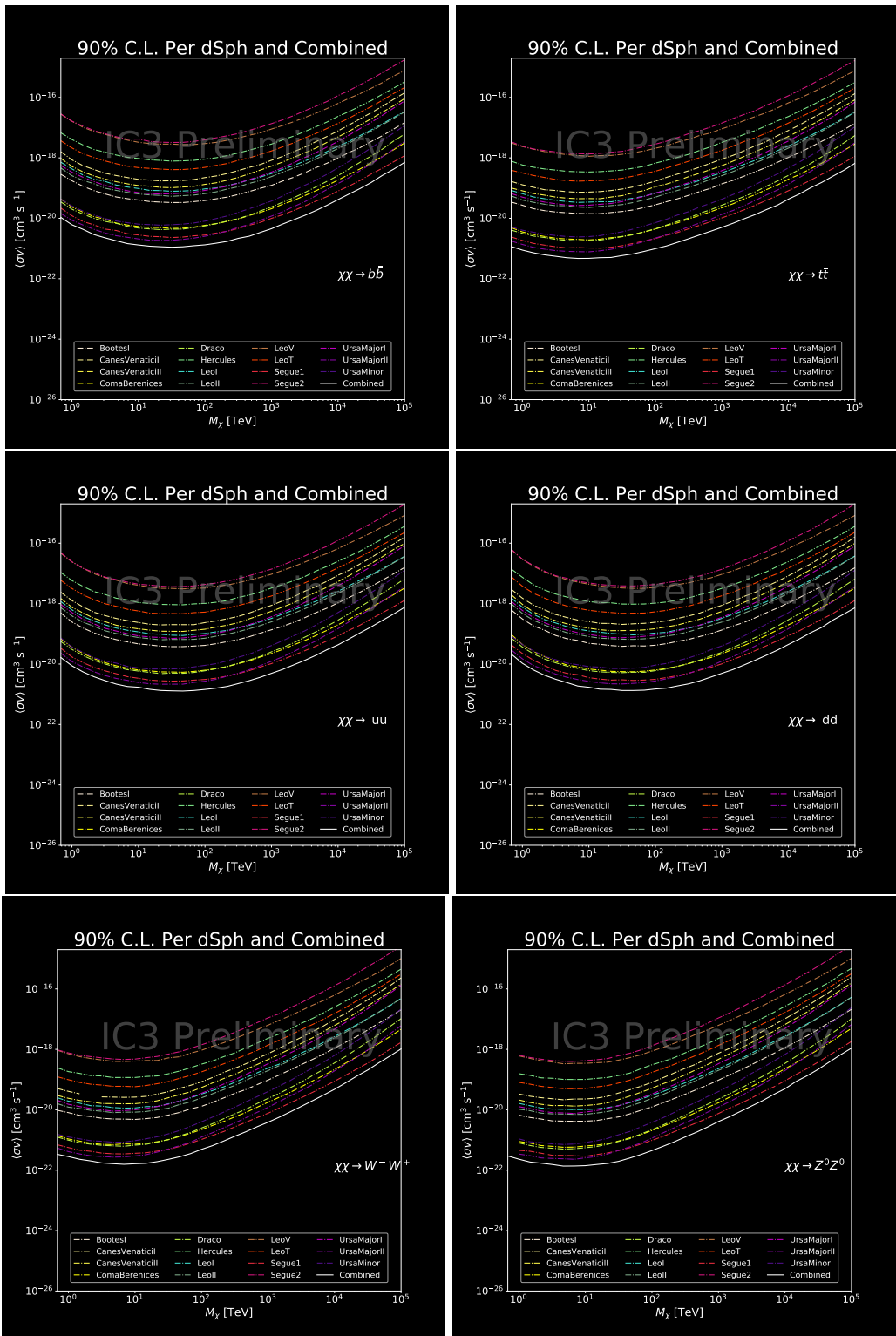


Figure 7.26 Same as Fig. 7.25 for three additional DM annihilation channels.

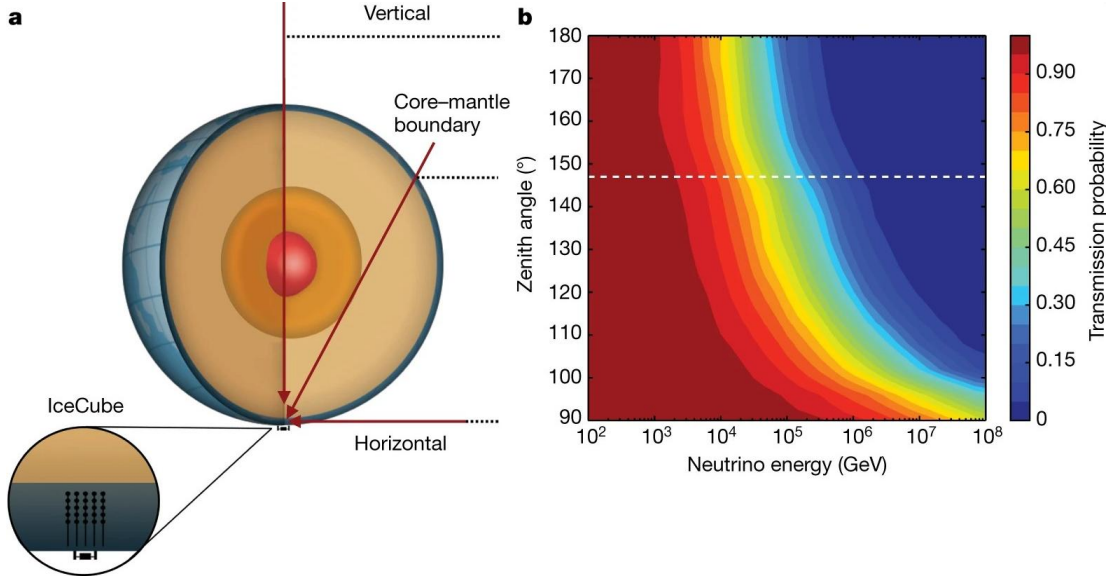


Figure 7.27 Panel A: Neutrino's from the Northern sky and incident on the IceCube detector will travel through the Earth. How much of the Earth these neutrinos travels is a function of zenith from the vertical axis. Panel B: SM prediction of neutrino transmission probabilities for neutrinos arriving at  $90^\circ - 180^\circ$  zenith and with 100 GeV to 100 PeV energies. High-energy neutrinos traversing the whole Earth are completely absorbed, whereas low-energy neutrinos pass through unimpeded. Neutrinos coming from above the horizon will arrive unimpeded for all neutrino energies. Figure pulled from [92].

2009     Figure 7.28 shows that we have significant but diminishing sensitivity to sources at high  
 2010    declination. We see in the worse case, the sensitivity at high declination is up to an order of  
 2011    magnitude worse than at low declination. However, for  $m_\chi < 1$  PeV, the sensitivities are very  
 2012    similar. The comparable sensitivities imply that a stacking analysis with IceCube is most powerful  
 2013    in the 500 GeV to 1 PeV region. Above 1 PeV, our limits and sensitivities are dominated by sources  
 2014    near the horizon. When we additionally consider the  $J$ -factors, we expect Segue 1 to dominate  
 2015    contributions to sensitivity and limits where  $m_\chi > 1$  PeV.

## 2016    7.8 Conclusions

2017     We utilized advanced computing techniques like parallel programming and spline fitting of  
 2018    particle physics Monte Carlo to greatly expand and refine IceCube's sensitivity to DM annihilation  
 2019    from dSphs. Furthermore, we imported updated astrophysical and particle physics models that  
 2020    better represent what we believe neutrino signals from DM annihilation should look like. We, for  
 2021    the first time, build an analysis that is sensitive to PeV DM annihilation.

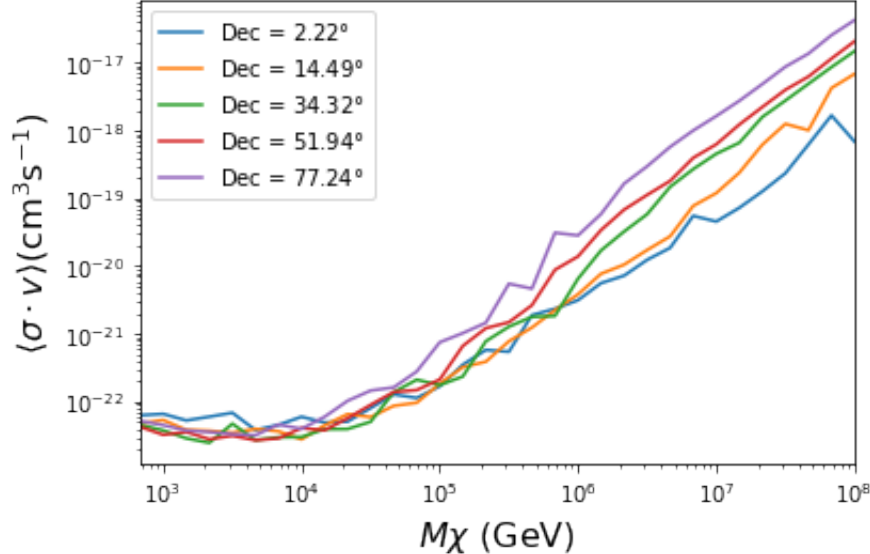


Figure 7.28  $\langle \sigma v \rangle$  sensitivities for 5 imaginary sources with  $\log_{10} J = 19.42$   $\log_{10}(\text{GeV}^2 \text{cm}^{-5})$ . Each imaginary source shares a declination with a source in Tab. 5.1

When we compare to previous IceCube publications of dSphs [83], we see an order of magnitude improvement to our sensitivity. This analysis has been working group approved within IceCube and is currently under collaboration review before unblinding. These processes did not complete in time for this dissertation. Therefore we do not show data for this thesis and is the clear next step.

The test statistic distributions in this analysis also demonstrate more characteristic behavior compared to previous DM analyses [87, 91]. With a 10-year dataset, we finally have enough statistics to almost trivially combine with other photon observatories, such as HAWC. The first groundwork for a multi-messenger DM search is provided with concluding remarks in chapter 8.

## CHAPTER 8

### 2030 NU DUCK: CONCLUSIONS AND FUTURE DIRECTIONS

#### 2031 8.1 Conclusions

2032 **TODO: Chat GPT the shit of everything below**In this work, three analyses were performed  
2033 with data from the HAWC and IceCube observatories in order to explore some of the fundamental  
2034 questions in particle astrophysics. The goal was to contribute to the understanding of the sources of  
2035 cosmic rays, their acceleration mechanisms, and the nature of dark matter. The detection techniques  
2036 and reconstruction methods for both observatories were described, along with the properties that  
2037 make them ideal instruments to perform such searches.

2038 This dissertation used data from the HAWC detector to probe cutting-edge physics beyond  
2039 the Standard Model. The techniques by which HAWC is able to detect cosmic gamma rays were  
2040 demonstrated and the many advantages of HAWC in probing ultra-high energy gamma-ray physics  
2041 were detailed. It was shown how HAWC data can be used to explore unanswered questions such as  
2042 the nature of dark matter and the limits of Lorentz invariance. In particular, a search for evidence of  
2043 WIMP dark matter in the Milky Way Galactic Halo was performed. To accomplish this, simulations  
2044 of the dark matter density profile were combined with estimates of the HAWC sensitivity to dark  
2045 matter-like energy spectra. This allowed strong constraints on dark matter annihilation and decay  
2046 from the Galactic Halo to be derived that are insensitive to the large uncertainties arising from  
2047 systematics in the dark matter spatial distribution. Multi-hundred TeV photon spectra were also  
2048 significantly detected from HAWC sources within the Galactic Plane. These results lead to the  
2049 strongest constraints on Lorentz invariance violation to be published at the time of writing.

2050 The work of this dissertation was made possible by the ongoing development of new algorithms  
2051 and reconstruction techniques within the HAWC collaboration. Probing the Galactic Halo required  
2052 the creation of a novel background estimation technique that relied on HAWC's wide field of view  
2053 and strong ability to discriminate between gamma rays and cosmic rays. Meanwhile, the constraints  
2054 on Lorentz invariance violation were enabled by the improved energy resolution from a machine  
2055 learning technique. HAWC has recently completed a reprocessing of all archival data using an

2056 updated set of algorithms that can lead to compelling follow-up work on these results. Combining  
 2057 the new background technique with the re-optimized energy estimators will allow for Galactic  
 2058 dark matter to be probed at even higher masses, as well as for analyses that require precise energy  
 2059 resolution such as gamma-ray line searches.

2060 **8.2 Future Directions: Multi-Messenger Dark Matter Search**

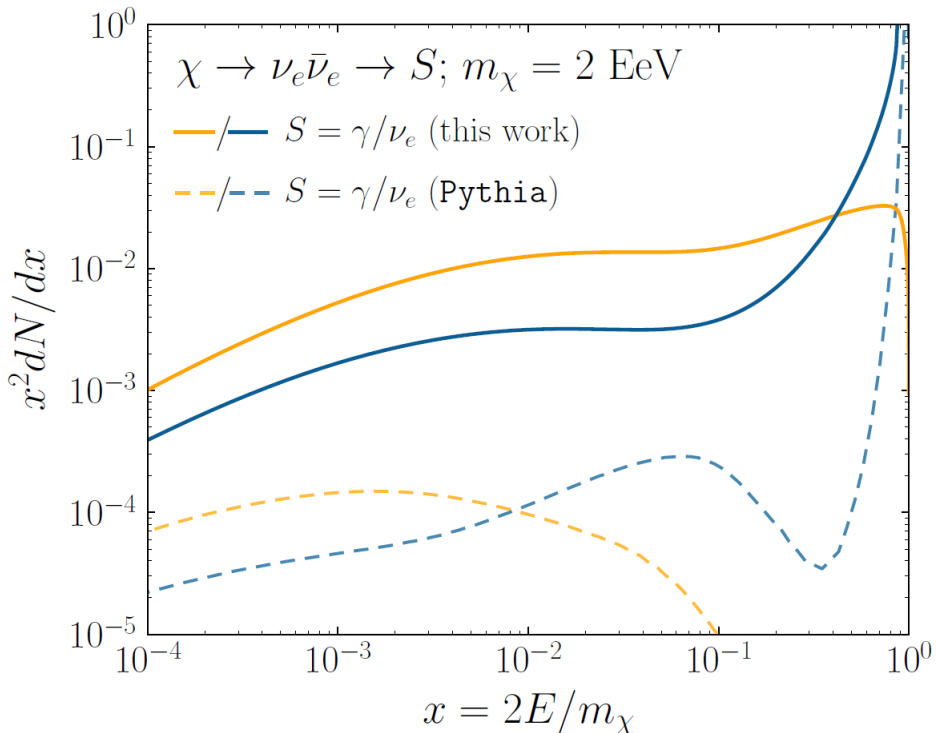


Figure 8.1 The prompt electron neutrino and photon spectrum resulting from the decay of a 2EeV DM particle to  $\nu_e \bar{\nu}_e$ , as currently being searched for at IceCube [5]. Solid curves represent the results of this work, and predict orders of magnitude more flux at certain energies than the dashed results of Pythia 8.2, one of the only existing methods to generate spectra at these masses. In both cases energy conservation is satisfied: there is a considerable contribution to a  $\delta$ -function at  $x = 1$ , associated with events where an initial W or Z was never emitted and thus no subsequent shower developed. Large disagreements are generically observed at these masses for electroweak dominated channels, while the agreement is better for colored initial SM states.

2061 As I have shown previously in Sec. 5 and Sec. 6, we can build a fast and robust analysis  
 2062 that shares tools with the field. The hope being that IceCube can eventually combine data with  
 2063 gamma-ray observatories.



Figure 8.2 TODO: neutrino and bb plot with nu Sensitivities[NEEDS A SOURCE][FACT CHECK THIS]

## MULTI-EXPERIMENT SUPPLEMENTARY FIGURES

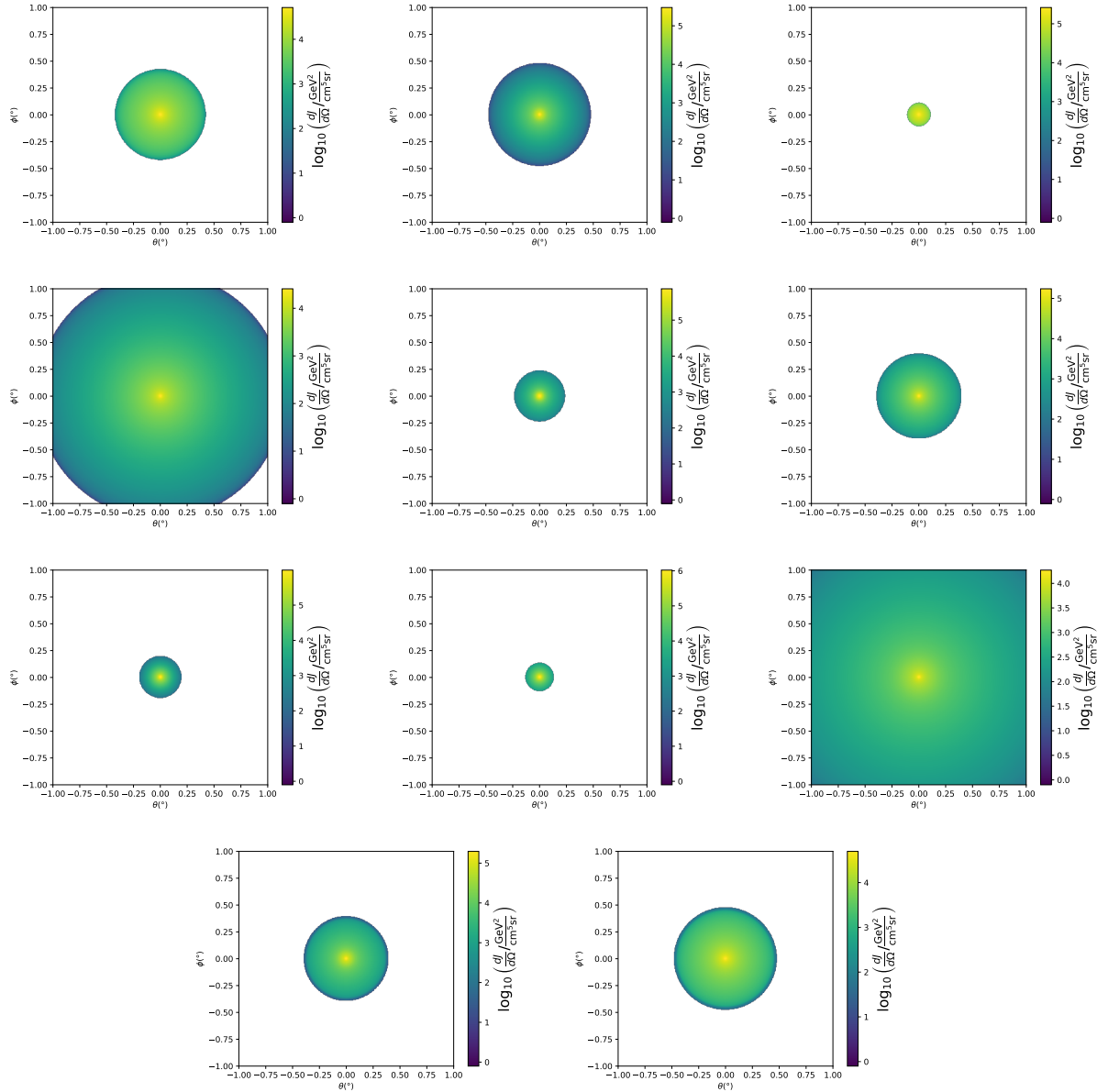


Figure A.1 Sister figure to Figure 5.3. Sources in the first row from left to right: Bootes I, Canes Venatici I, II. In second row: Draco, Hercules, Leo I. In the first row: Leo II, Leo IV, Sextans. In the final row: Ursa Major I, Ursa Major II.

## APPENDIX B

### 2065 MULTITHREADING DARK MATTER ANALYSES SUPPLEMENTARY MATERIAL

#### 2066 B.1 Remaining Spectral Models

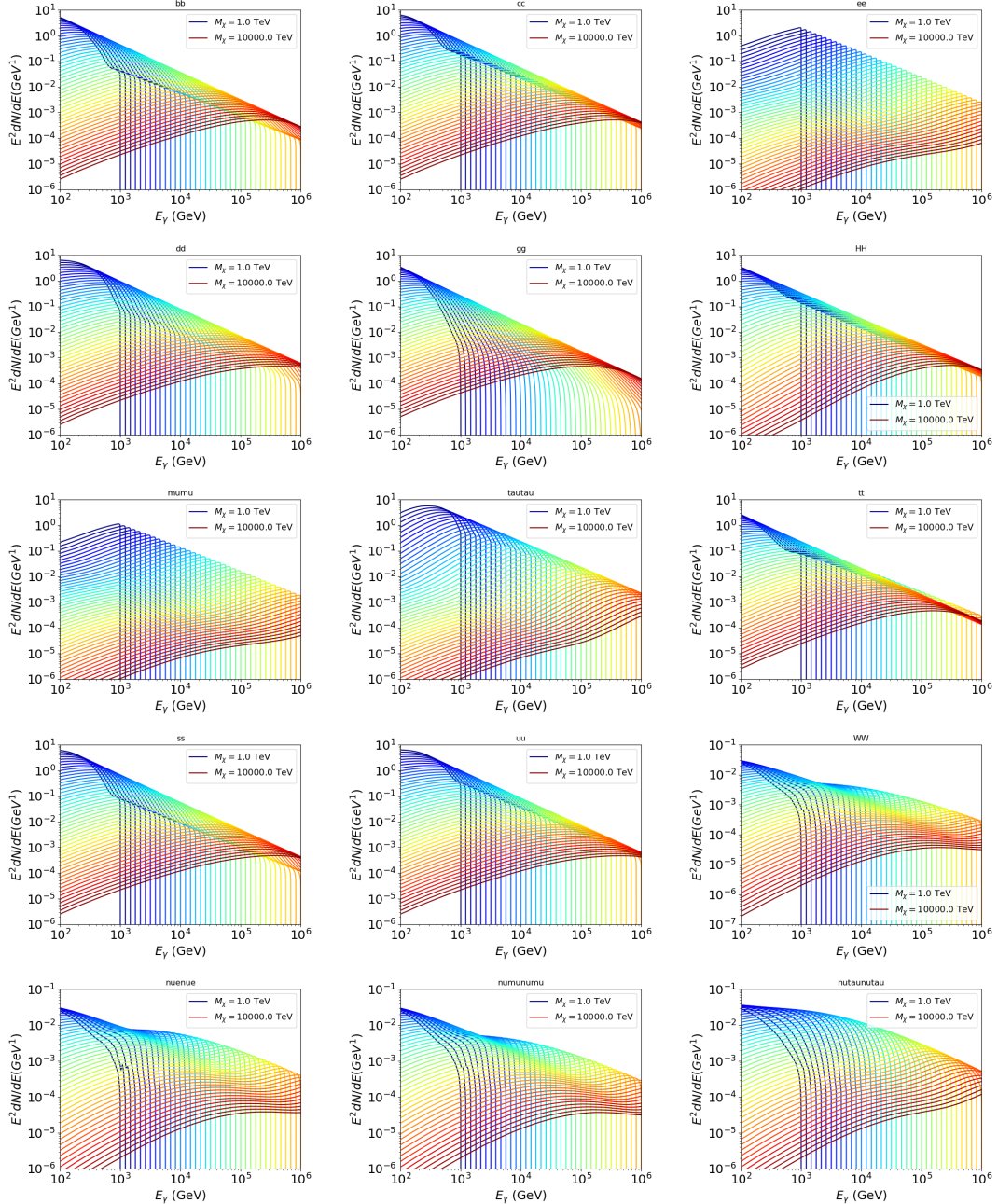


Figure B.1 Sister figure to Figure 6.2 for remaining SM primary annihilation channels studied for this thesis. These did not require any post generation smoothing and so are directly pulled from [79] with a binning scheme most helpful for a HAWC analysis.

2067 **B.2 mpu\_analysis.py**

```
20681 import warnings
20692 with warnings.catch_warnings():
20703     warnings.simplefilter("ignore")
20714 # Python base libraries
20725 import os
20736 import sys
20747 import time
20758 # Import general libraries with namespace
20769 import matplotlib
20770 # Necessary for computing on cluster
20781 matplotlib.use("agg")
20792 import numpy as np
20803 import multiprocessing as mp
20814 # Import HAWC software
20825 sys.path.insert(1, os.path.join(os.environ['HOME'], 'hawc_software', 'threeML-
2083     analysis-scripts', 'fitModel'))
20846 from analysis_modules import *
20857 from threeML import *
20868 from hawc_hal import HAL, HealpixConeROI
20879 from threeML.minimizer.minimization import FitFailed
20880 # Import Dark Matter HAWC Libraries
20891 import analysis_utils as au
20902 import spectra as spec
20913 import sources as srcs
20924
20935 #* READ ONLY PATHS This block will change eventually
20946 MASS_LIST = './plotting/studies/nd/masses.txt'
20957 CHAN_LIST = './plotting/studies/nd/chans.txt'
20968
20979 #* WRITE PATHS, default location is to scratch
20980 OUT_PATH = os.path.join(os.environ["SCRATCH"], os.environ["USER"], 'New_duck')
```

```

20991 print('Our out path is going to be {}'.format(OUT_PATH))
21002
21013 # Define parallel Function. Can also be run serially
21024 def some_mass_fit(sigVs, datalist, shape, dSph, jfactor, mass_chan,
21035                 progress=None, log_file='', queue=None, i_job=0):
21046
21057     if progress is None:
21068         progress = [0]
21079     else: # Create log files for each thread
21080         log_file = log_file.replace('.log', '_ThreadNo_')
21091         log_file = log_file + str(i_job) + ".log"
21102         sys.stdout = open(log_file, "w")
21113
21124     fits = []
21135
21146     try:
21157         for m_c in mass_chan:
21168             print(f'Mass chan tuple: {m_c}')
21179             mass = int(m_c[0])
21180             ch = m_c[1]
21191             # Build path to output files
21202             outPath = os.path.join(OUT_PATH, ch, dSph)
21213             au.ut.ensure_dir(outPath)
21224
21235             if progress[i_job] < 0:
21246                 # If the master gets a Keyboard interrupt, commit suicide.
21257                 break
21268
21279                 ### Start Model Building for DM mass and SM channel #####
21280                 spectrum = spec.DM_models.HDMSpectra()
21291                 spectrum.set_channel(ch)
21302
21313                 myDwarf = ExtendedSource(dSph, spatial_shape=shape,

```

```

21324                     spectral_shape=spectrum)
21335
21346             spectrum.J = jfactor * u.GeV**2 / u.cm**5
21357             spectrum.sigmav = 1e-24 * u.cm**3 / u.s
21368             spectrum.set_dm_mass(mass * u.GeV)
21379
21380             spectrum.sigmav.bounds = (1e-30, 1e-12)
21391             model = Model(myDwarf)
21402             ##### End model Building #####
21413
21424             jl = JointLikelihood(model, datalist, verbose=False)
21435
21446             try:
21457                 result, lhdf = jl.fit(compute_covariance=False)
21468                 ts = -2.* (jl.minus_log_like_profile(1e-30) - jl.
2147 _current_minimum)
21489                 # Also profile the LLH vs sv
21490                 ll = jl.get_contours(spectrum.sigmav, sigVs[0],
21501                                     sigVs[-1], len(sigVs),
21512                                     progress=False, log=['False'])
21523
21534                 sigv_ll = au.ut.calc_95_from_profile(ll[0], ll[2])
21545                 # Write results to file
21556                 outFileLL = outPath+f"/LL_{dSph}_{ch}_mass{int(mass)}_GD.txt"
21567                 np.savetxt(outFileLL, (sigVs, ll[2]),
21578                               delimiter='\t', header='sigV\tLL\n')
21589
21590                 with open(outPath+f"/results_{dSph}_{ch}_mass{int(mass)}_GD.
2160 txt", "w") as results_file:
21611                     results_file.write("mDM [GeV]\tsigV_95\tsigV_B.F.\n")
21622
21633                     results_file.write("%i\t%.5E\t%.5E\t%.5E"%(mass, sigv_ll,
21644                                         ts, result.value[0]))

```

```

21655         # End write to file
21656
21657     except FitFailed: # Don't kill all threads if a fit fails
21658         print("Fit failed. Go back and calculate this spectral model
21659             later")
21660
21661         fits.append((ch, mass, -1, -1))
21662
21663         with open(log_file+'.fail', 'w') as f_file:
21664             f_file.write(f'{ch}, {mass}\n')
21665
21666
21667         progress[i_job] += 1
21668
21669         matplotlib.pyplot.close() # Prevent leaky memory
21670
21671
21672         fits.append((ch, mass, result.value[0], ts))
21673         progress[i_job] += 1
21674
21675         matplotlib.pyplot.close()
21676
21677     except KeyboardInterrupt:
21678         progress[i_job] = -1
21679
21680
21681         fits = np.array(fits)
21682
21683     if queue is None:
21684         return fits
21685
21686     else:
21687         queue.put((i_job, fits))
21688
21689
21690 def main(args):
21691
21692     masses = np.loadtxt(MASS_LIST, dtype=int)
21693
21694     chans = np.loadtxt(CHAN_LIST, delimiter=',', dtype=str)
21695
21696     mass_chan = au.ut.permute_lists(chans, masses)
21697
21698
21699     print(f"DM masses for this study are: {masses}")
21700
21701     print(f"SM Channels for this study are XX -> {chans}")
21702
21703     print(mass_chan)
21704
21705
21706     # extract information from input argument

```

```

21987 dSph = args.dSph
21998 data_mngr = au.ut.Data_Selector('P5_NN_2D')
22009 dm_profile = srcts.Spatial_DM(args.catalog, dSph, args.sigma, args.decay)
22010
22021 ##### Extract Source Information #####
22032 if dm_profile.get_dec() < -22.0 or dm_profile.get_dec() > 62.0:
22043     raise ValueError("HAWC can't see this source D: Exitting now...")
22054
22065 print(f'{dSph} information')
22076 print(f'jfac: {dm_profile.get_factor()}\tRA: {dm_profile.get_ra()}\tDec: {dm_profile.get_dec()}\n')
2208
22097
22108 shape = SpatialTemplate_2D(fits_file=dm_profile.get_src_fits())
22119 ##### Finish Extract Source Information #####
22120
22131 ##### LOAD HAWC DATA #####
22142 roi = HealpixConeROI(data_radius=2.0, model_radius=8.0,
22153                         ra=dm_profile.get_ra(), dec=dm_profile.get_dec())
22164 bins = choose_bins.analysis_bins(args, dec=dm_profile.get_dec())
22175
22186 hawc = HAL(dSph, data_mngr.get_datmap(), data_mngr.get_detres(), roi)
22197 hawc.set_active_measurements(bin_list=bins)
22208 datalist = DataList(hawc)
22219 ##### FINISH LOAD HAWC DATA #####
22220
22231 # set up SigV sampling. This sample is somewhat standardized
22242 sigVs = np.logspace(-28,-18, 1001, endpoint=True) # NOTE This will change
2225 with HDM
22263
22274 if args.n_threads == 1:
22285     # No need to start || programming just iterate over the masses
22296     kw_arg = dict(sigVs=sigVs, datalist=datalist, shape=shape, dSph=dSph,
22307                     jfactor=dm_profile.get_factor(), mass_chan=mass_chan,

```

```

22318                 log_file=args.log)
22319         some_mass_fit(**kw_arg)
22320     else:
22321         # I Really want to suppress TQMD output
22322         from tqdm import tqdm
22323         from functools import partialmethod
22324         tqdm.__init__ = partialmethod(tqdm.__init__, disable=True)
22325
22326
22327         x = np.array_split(mass_chan, args.n_threads)
22328         n_jobs = len(x)
22329
22330
22331         print("Thread jobs summary by mass and SM channel")
22332         for xi in x:
22333             print(f'{xi}')
22334
22335         queue = mp.Queue()
22336         progress = mp.Array('i', np.zeros(n_jobs, dtype=int))
22337
22338
22339         # Define task pool that will be split amongsts threads
22340         kw_args = [dict(sigVs=sigVs, datalist=datalist, shape=shape,
22341                         dSph=dSph, jfactor=dm_profile.get_factor(),
22342                         mass_chan=mass_chan, progress=progress,
22343                         queue=queue, i_job=i, log_file=args.log)
22344             for i, mass_chan in enumerate(x)]
22345
22346
22347         # Define each process
22348         procs = [mp.Process(target=some_mass_fit, kwargs=kw_args[i]) \
22349             for i in range(n_jobs)]
22350
22351
22352         ### Start MASTER Thread only code block ###
22353         # Begin running all child threads
22354         for proc in procs: proc.start()
22355

```

```

22641     try:
22652         # In this case, the master does nothing except monitor progress of
2266         the threads
22673         # In an ideal world, the master thread also does some computation.
22684         n_complete = np.sum(progress)
22695         while_count = 0
22706
22717         while n_complete < len(mass_chan):
22728
22739             if np.any(np.asarray(progress) < 0):
22740                 # This was no threads are stranded when killing the script
22751                 raise KeyboardInterrupt()
22762             if while_count%1000 == 0:
22773                 print(f"{np.sum(progress)} of {len(mass_chan)} finished")
22784
22795             n_complete = np.sum(progress)
22806             time.sleep(.25)
22817             while_count += 1
22828
22839         except KeyboardInterrupt:
22840             # signal to jobs that it's time to stop
22851                 for i in range(n_jobs):
22862                     progress[i] = -2
22873                     print('\nKeyboardInterrupt: terminating early.')
22884             ### End MASTER Thread only code block ###
22895
22906             fitss = [queue.get() for proc in procs]
22917             print(fitss)
22928             print(f'Thread statuses: {progress[:]}')
22939
22940             # putting results in a file
22951
22962             print("QUACK! All Done!")

```

```

22973
22984
22995 if __name__ == '__main__':
23006     import argparse
23017
23028     p = argparse.ArgumentParser(description="Run a DM annihilation analysis on
2303         a dwarf spheroidal for a specific SM channel for DM masses [1 TeV to 10
2304         PeV]")
23059
23060     # Dwarf spatial modeling arguements
23071     p.add_argument("-ds", "--dSph", type=str,
23082                     help="dwarf spheroidal galaxy to be studied", required=
2309     True)
23103     p.add_argument("-cat", "--catalog", type=str, choices=['GS15', 'LS20'],
23114                     default='LS20', help="source catalog used")
23125     p.add_argument("-sig", "--sigma", type=int, choices=[-1, 0, 1], default=0,
23136                     help="Spatial model uncertainty. 0 corresponds to the
2314 median. +/-1 correspond to the +/-1sigma uncertainty respectively.")
23157
23168     # Arguements for the energy estimators
23179     p.add_argument("-e", "--estimator", type=str,
23180                     choices=['P5_NHIT', 'P5_NN_2D'],
23191                     default="P5_NN_2D", required=False,
23202                     help="The energy estimator choice. Options are: P5_NHIT,
2321 P5_NN_2D. GP not supported (yet).")
23223     p.add_argument("--use-bins", default=None, nargs="*",
23234                     help="Bins to use for the analysis", dest="use_bins")
23245     p.add_argument('--select_bins_by_energy', default=None, nargs="*",
23256                     help="Does nothing. May fill in later once better
2326 understood")
23277     p.add_argument('--select_bins_by_fhit', default=None, nargs="*",
23288                     help="Also does nothing see above")
23299     p.add_argument( '-ex', "--exclude", default=None, nargs="*",

```

```

23300         help="Exclude Bins", dest="exclude")
2331
23322     # Computing and logging arguements.
23333     p.add_argument('-nt', '--n_threads', type=int, default=1,
23344                         help='Maximum number of threads spawned by script. Default
23355                         is 4')
23365     p.add_argument('-log', '--log', type=str, required=True,
23376                         help='Name for log files. Especially needed for threads')
23387
23398     p.add_argument('--decay', action="store_true",
23409                         help='Set spectral DM hypothesis to decay')
23410
23421     args = p.parse_args()
23432     print(args.decay)
23443     if args.exclude is None: # default exclude bins 0 and 1
23454         args.exclude = ['B0C0Ea', 'B0C0Eb', 'B0C0Ec', 'B0C0Ed', 'B0C0Ee']
23465
23476     if args.decay: OUT_PATH += '_dec'
23487     else: OUT_PATH += '_ann'
23498
23509     OUT_PATH = OUT_PATH + '_' + args.catalog
23510     if args.sigma != 0: OUT_PATH += f'_{args.sigma}sig'
23521
23532     main(args)

```

2354 B.3 Comparison with Glory Duck

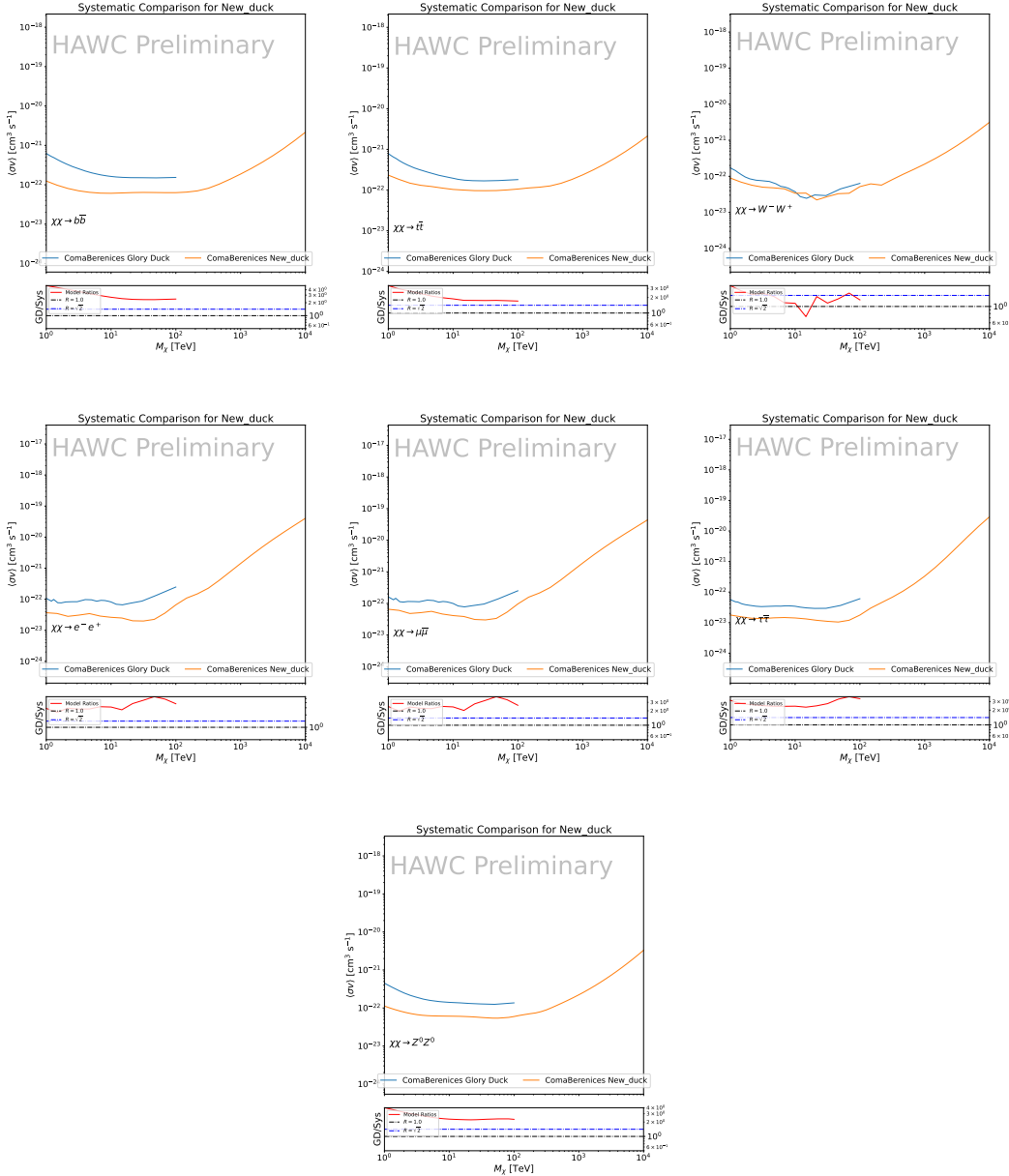


Figure B.2 Comparison of HAWC limits from this analysis to Glory Duck (Fig. 5.5) for Coma Berenices and 7 DM annihilation channels.

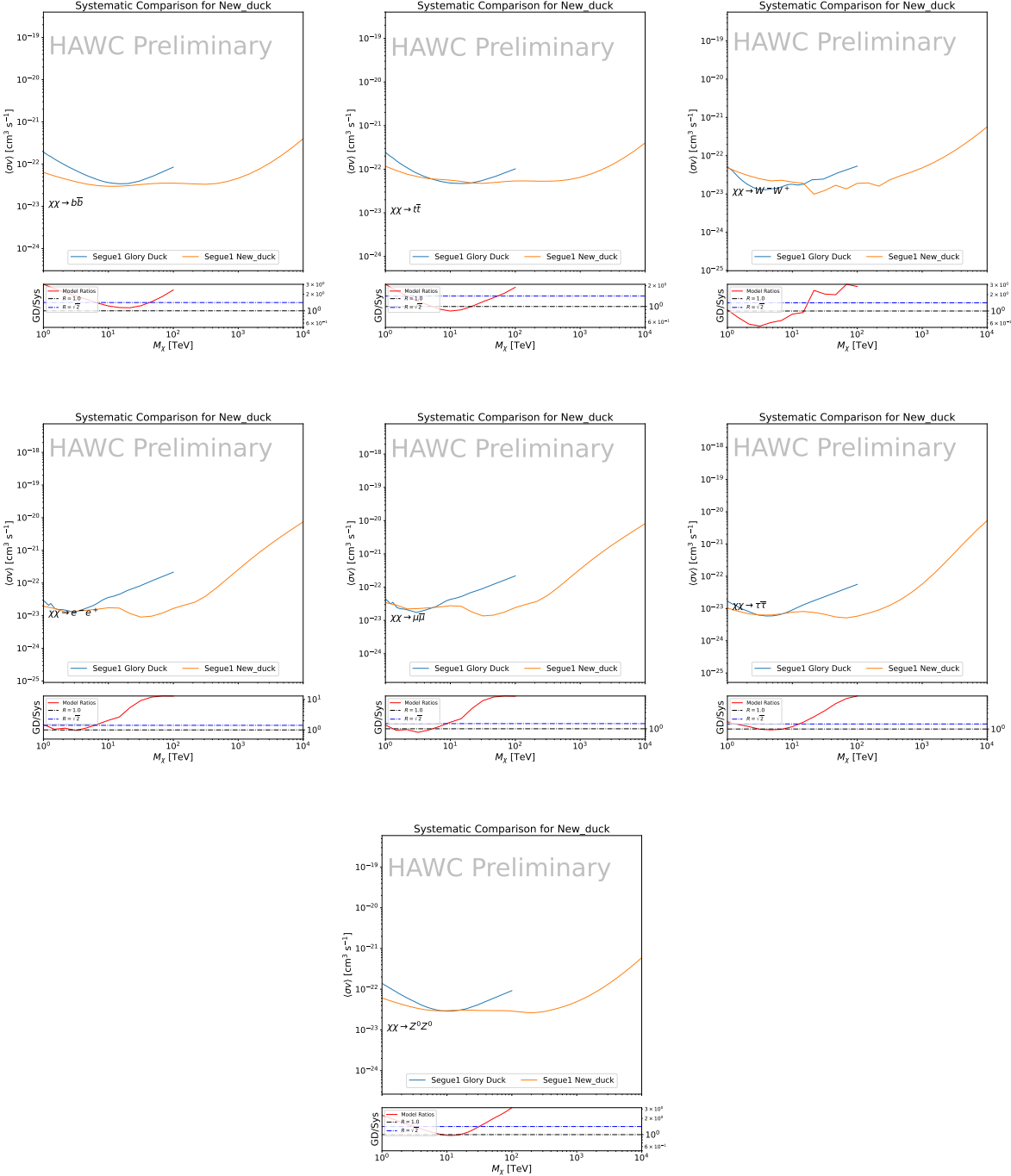


Figure B.3 Same as Fig. B.2 but for Segue 1.

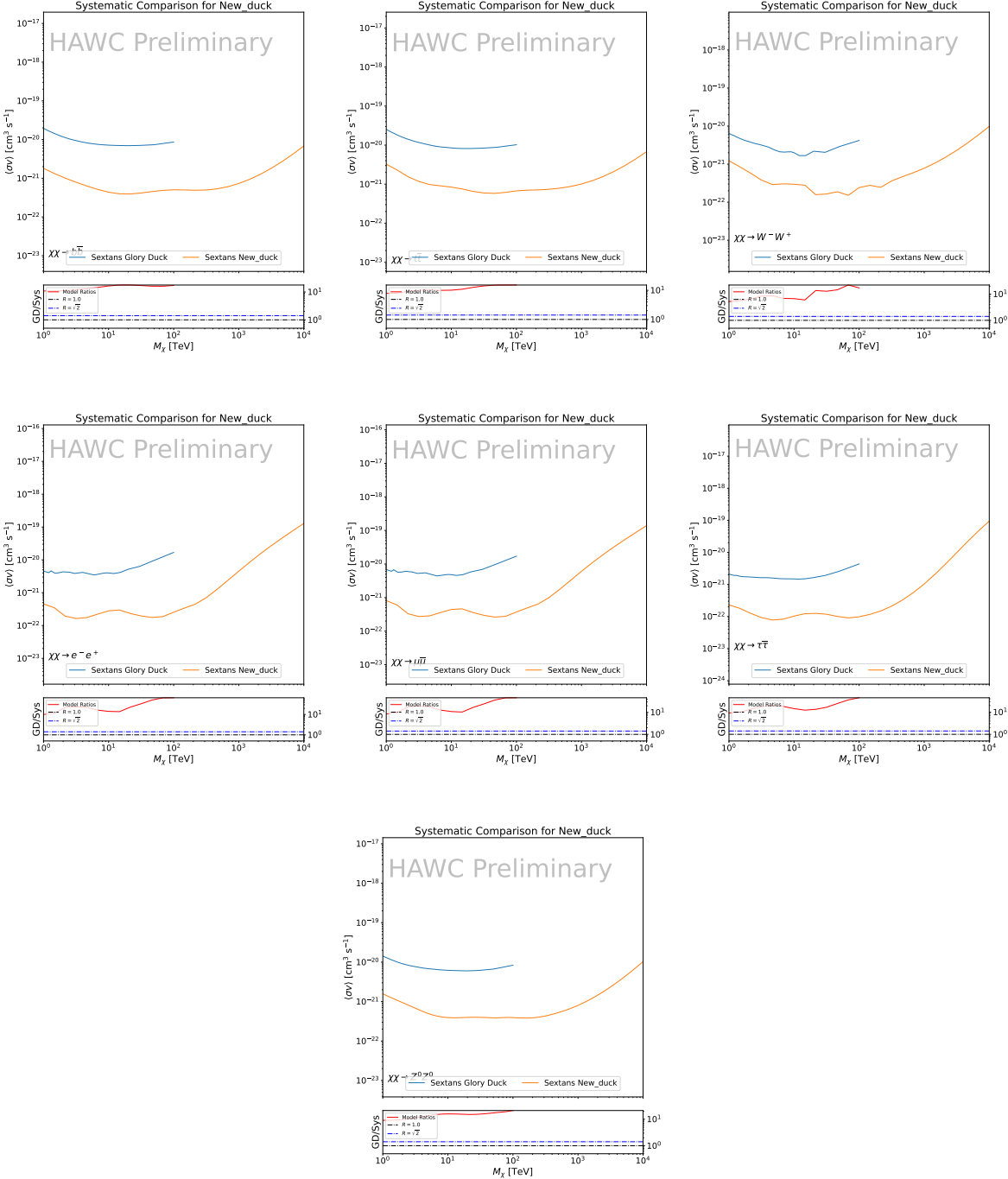


Figure B.4 Same as Fig. B.2 but for Sextans.

## APPENDIX C

### ICECUBE HEAVY DARK MATTER ANALYSIS SUPPLEMENTARY MATERIAL

#### C.1 Docker Image for Oscillating Neutrino Spectra

```
2355
2356 FROM ubuntu:18.04
2357
2358
2359 # Execute commands to install software packages
2360 RUN apt -y update
2361
2362     # Install utility programs
2363 RUN apt -y install vim wget git cmake
2364
2365 ARG DEBIAN_FRONTEND=noninteractive
2366
2367     # Install python
2368 RUN apt -y install python python-dev python-pip libjpeg-dev zlib1g-dev
2369
2370     # We need Python2 for installing Charon.
2371 RUN apt -y install python-numpy python-sympy python-matplotlib \
2372             python-sympy python-h5py python-astropy python-ipython
2373
2374     # Install dependencies of Charon : SQuIDS, NuSQuIDS
2375 RUN apt -y install libgsl-dev libgslcblas0 libgsl23 gsl-bin pkg-config
2376     # Install SQuIDS
2377 RUN mkdir /home/SQuIDS /home/SQuIDS_install
2378 WORKDIR /home/SQuIDS
2379 RUN git clone https://github.com/jsalvado/SQuIDS.git
2380 WORKDIR /home/SQuIDS/SQuIDS
2381 RUN git checkout 7ad9ba7c6ad06d1f0fa8418f937ebf1a403fef90
2382     # Before executing "make install" an environmental variable has to be set.
2383 ENV PKG_CONFIG_PATH=/home/SQuIDS/SQuIDS/lib
2384 RUN ./configure --prefix=../SQuIDS_install \
```

```

23859     && make
23860 RUN make install
23871
23882     # Set up an environmental variable that is required to install nuSQuIDS..
23893 ENV SQuIDS=/home/SQuIDS/SQuIDS
23904 ENV LD_LIBRARY_PATH=$SQuIDS/lib:$LD_LIBRARY_PATH
23915
23926     # Install NuSQuIDS
23937 RUN mkdir /home/nuSQuIDS
23948 WORKDIR /home/nuSQuIDS
23959 RUN git clone https://github.com/qrliu/nuSQuIDS.git
23960 WORKDIR /home/nuSQuIDS/nuSQuIDS
23971 RUN git checkout 072d8ef740e2fc7330f1fabaea94f0f4540c46f9
23982 RUN apt -y install libhdf5-dev hdf5-tools
23993 RUN apt -y install libboost1.65-all-dev
24004 RUN ./configure --with-squids=$SQuIDS --with-python-bindings --prefix=../
2401     nuSQuIDS_install \
24025     && make \
24036     && make install
24047
24058     # Set up an environmental variable for nuSQuIDS.
24069 ENV nuSQuIDS=/home/nuSQuIDS/nuSQuIDS
24070 ENV LD_LIBRARY_PATH=$nuSQuIDS/lib:$LD_LIBRARY_PATH
24081
24092     # Build the python bindings
24103 WORKDIR /home/nuSQuIDS/nuSQuIDS/resources/python/src
24114 RUN make
24125
24136     # Set up an environmental variable for the python bindings.
24147 ENV PYTHONPATH=$nuSQuIDS/resources/python/bindings/:$PYTHONPATH
24158
24169     # Install Charon in the /home/Charon/charon directory.
24170 RUN mkdir /home/Charon

```

```
24181 WORKDIR /home/Charon
24192 RUN git clone https://github.com/icecube/charon.git \
24203     && apt -y install unzip python-scipy
24214 WORKDIR charon
24225 RUN git checkout c531efe4e01dc364a60d1c83f950f04526ccd771
24236 RUN unzip ./charon/xsec/xsec.zip -d charon/xsec/ \
24247
24258 # Download neutrino spectra tables in the /home/Charon/charon/data directory
2426 .
24279 && mkdir ./charon/data
24280 WORKDIR ./charon/data
24291 RUN wget --no-check-certificate https://icecube.wisc.edu/~qliu/charon/
2430     SpectraEW.hdf5 \
24312 && wget --no-check-certificate https://icecube.wisc.edu/~qliu/charon/
2432     Spectra_PYTHIA.hdf5 \
24333 && wget --no-check-certificate https://icecube.wisc.edu/~qliu/charon/
2434     Spectra_noEW.hdf5
24354
24365 WORKDIR ../..
24376 RUN python setup.py install
24387 WORKDIR /home
```

2439 C.2 Spline Fitting Statuses

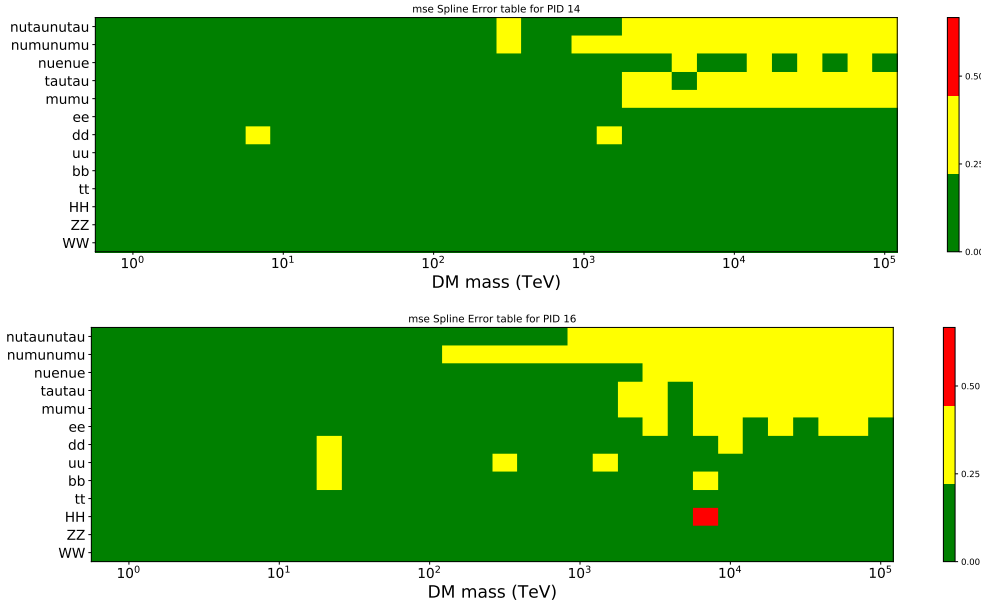


Figure C.1 Current status of spline tables according to constraints defined by Tab. 7.1. Green splines are splines that passed under the GOOD tolerance. Yellow are splines that are OK. Red are splines that FAIL. All yellow splines were inspected individually before running the analysis. Splines were made for the  $\mu$  (PID 14; top panel) flavor and  $\tau$  (PID 16; bottom panel) neutrino flavors.

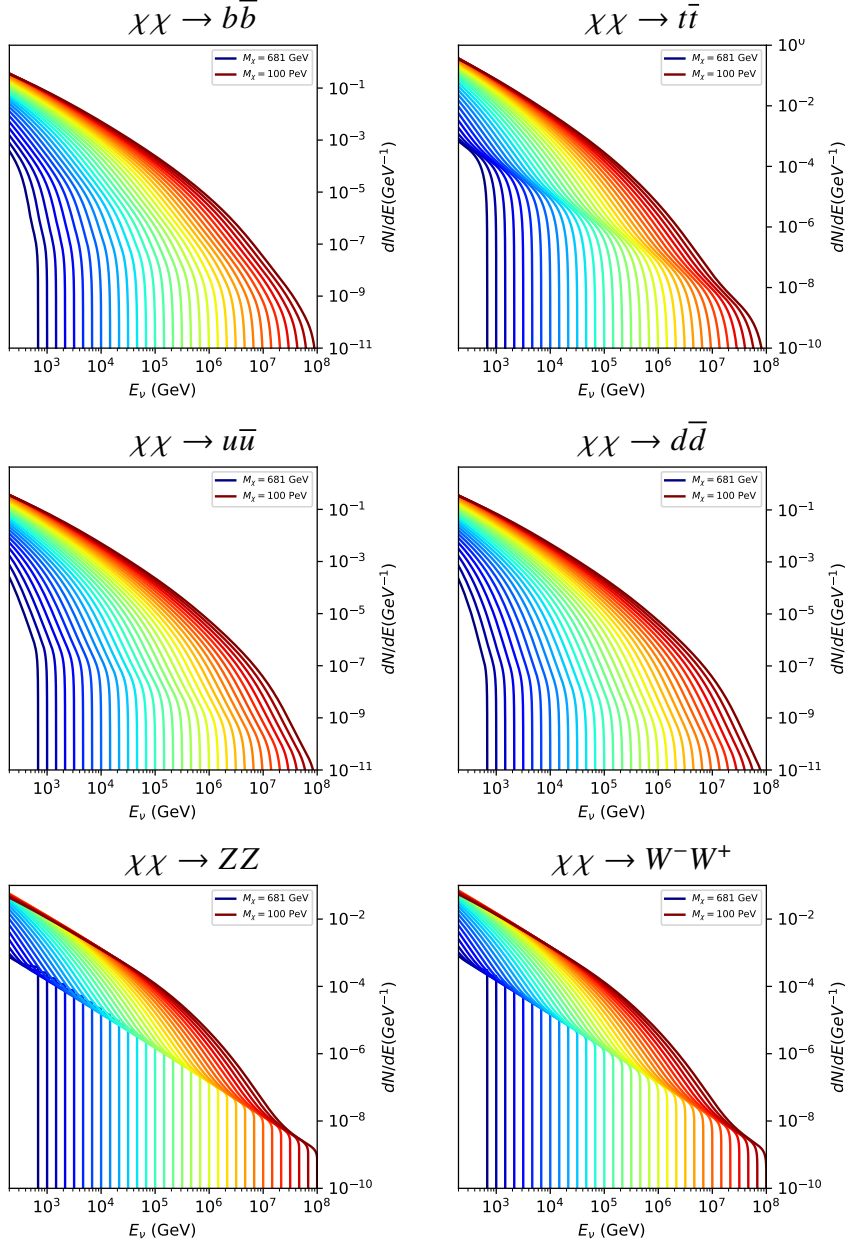


Figure C.2 Sister figure to Fig. 7.5 for annihilation channels that did not require kernel smoothing. These spectra are the composite ( $\nu_\mu + \nu_\tau$ ) of neutrino flavors. Every spectral model used for this analysis is featured as a colored solid line. Bluer lines are for lower DM mass spectral models. DM masses range from 681 GeV to 100 PeV.

2441 C.4 Segue 1 And Ursa Major II Signal Recovery

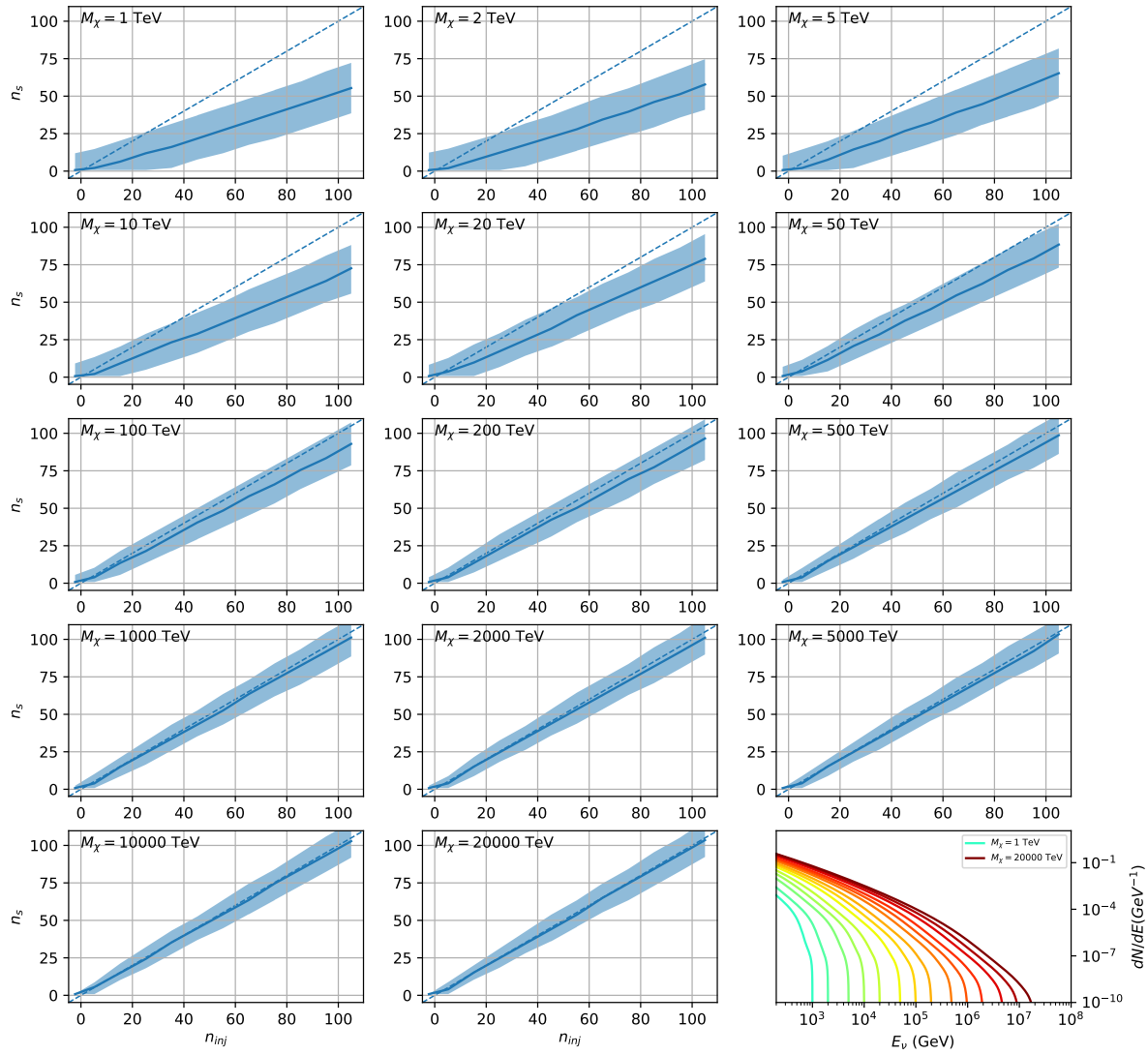


Figure C.3 Same as Fig. 7.23 but for Segue 1 and  $\chi\chi \rightarrow b\bar{b}$ .

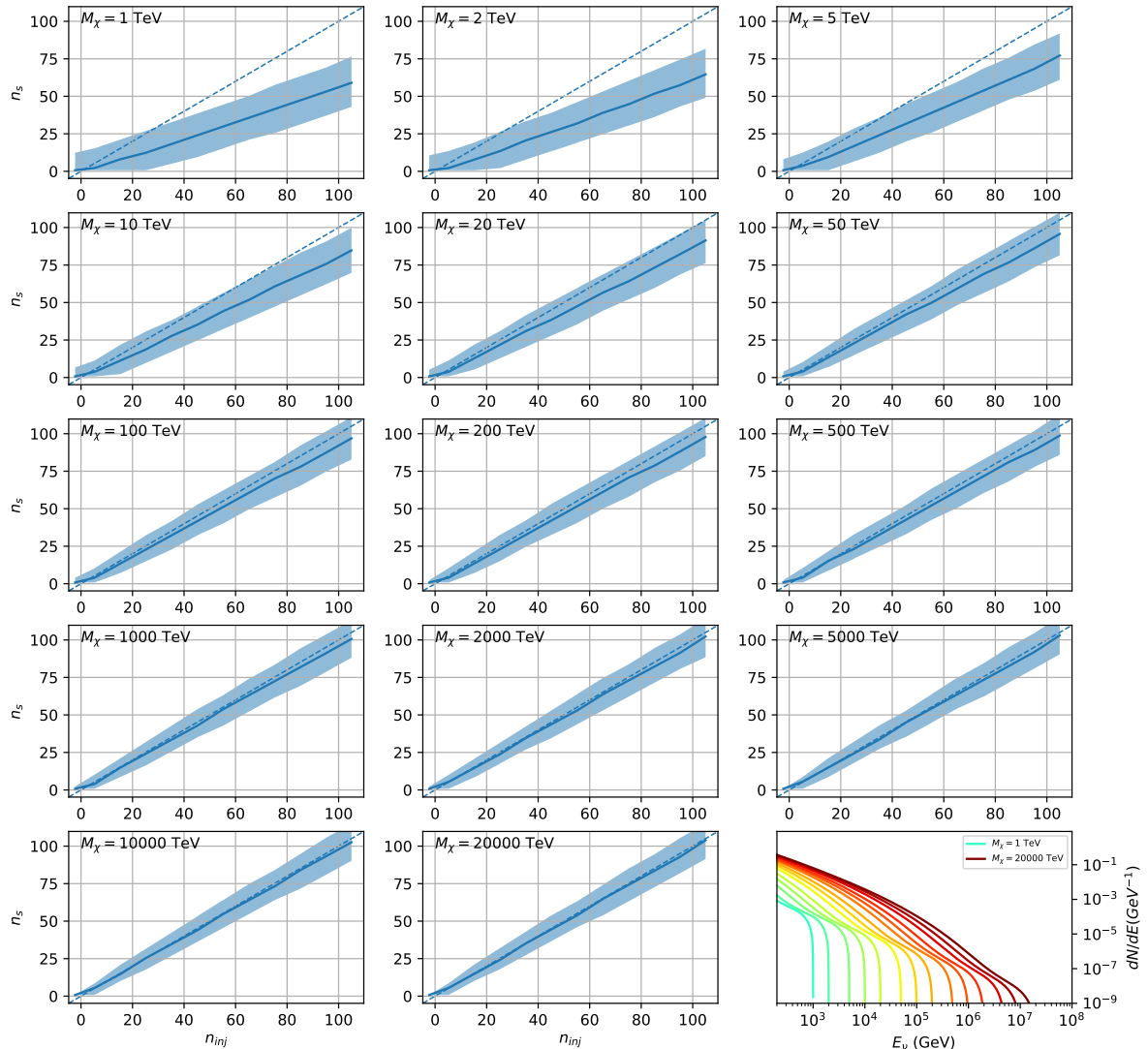


Figure C.4 Same as Fig. 7.23 but for Segue 1 and  $\chi\chi \rightarrow t\bar{t}$ .

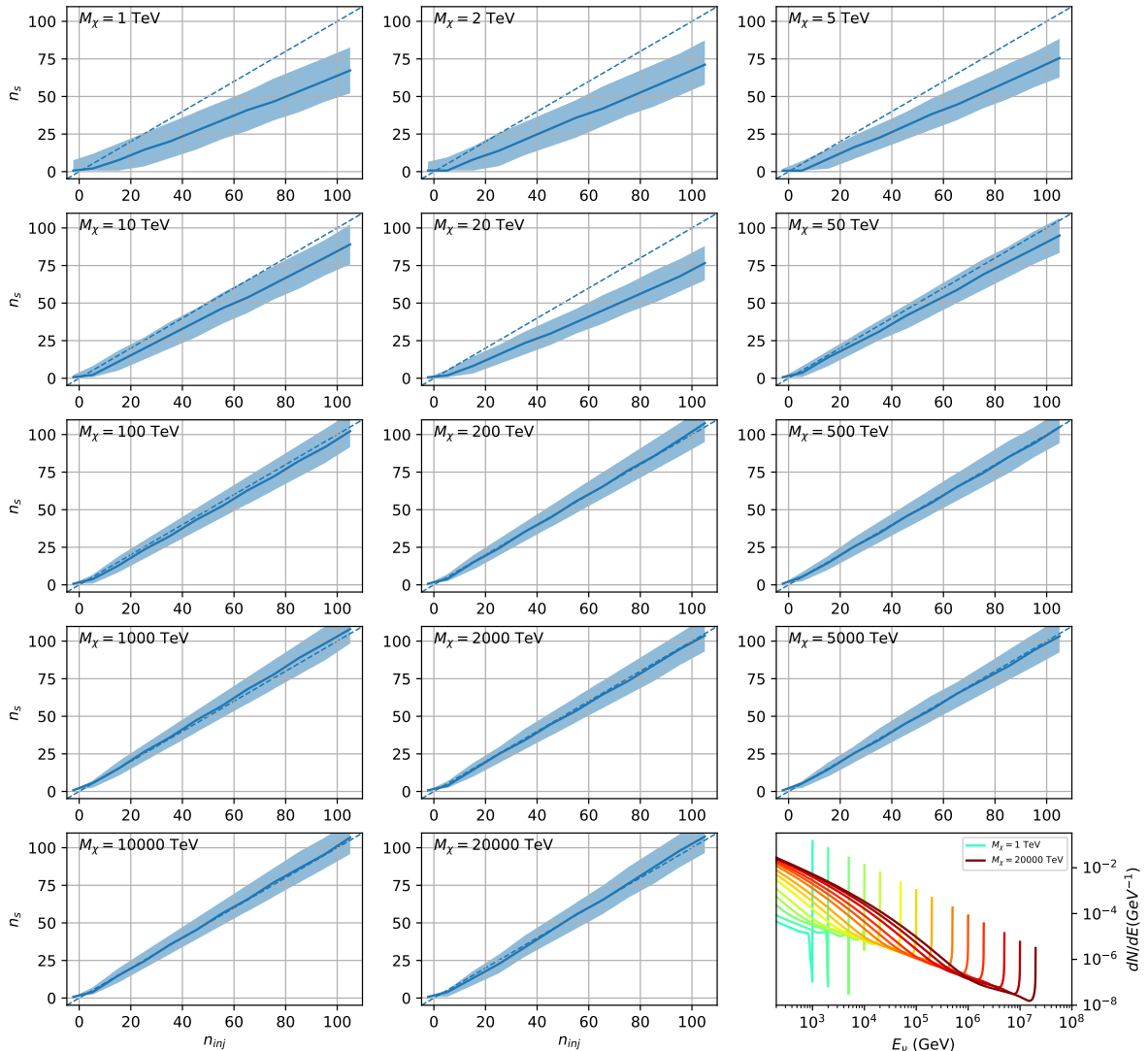


Figure C.5 Same as Fig. 7.23 but for Segue 1 and  $\chi\chi \rightarrow \nu_\mu \bar{\nu}_\mu$ .

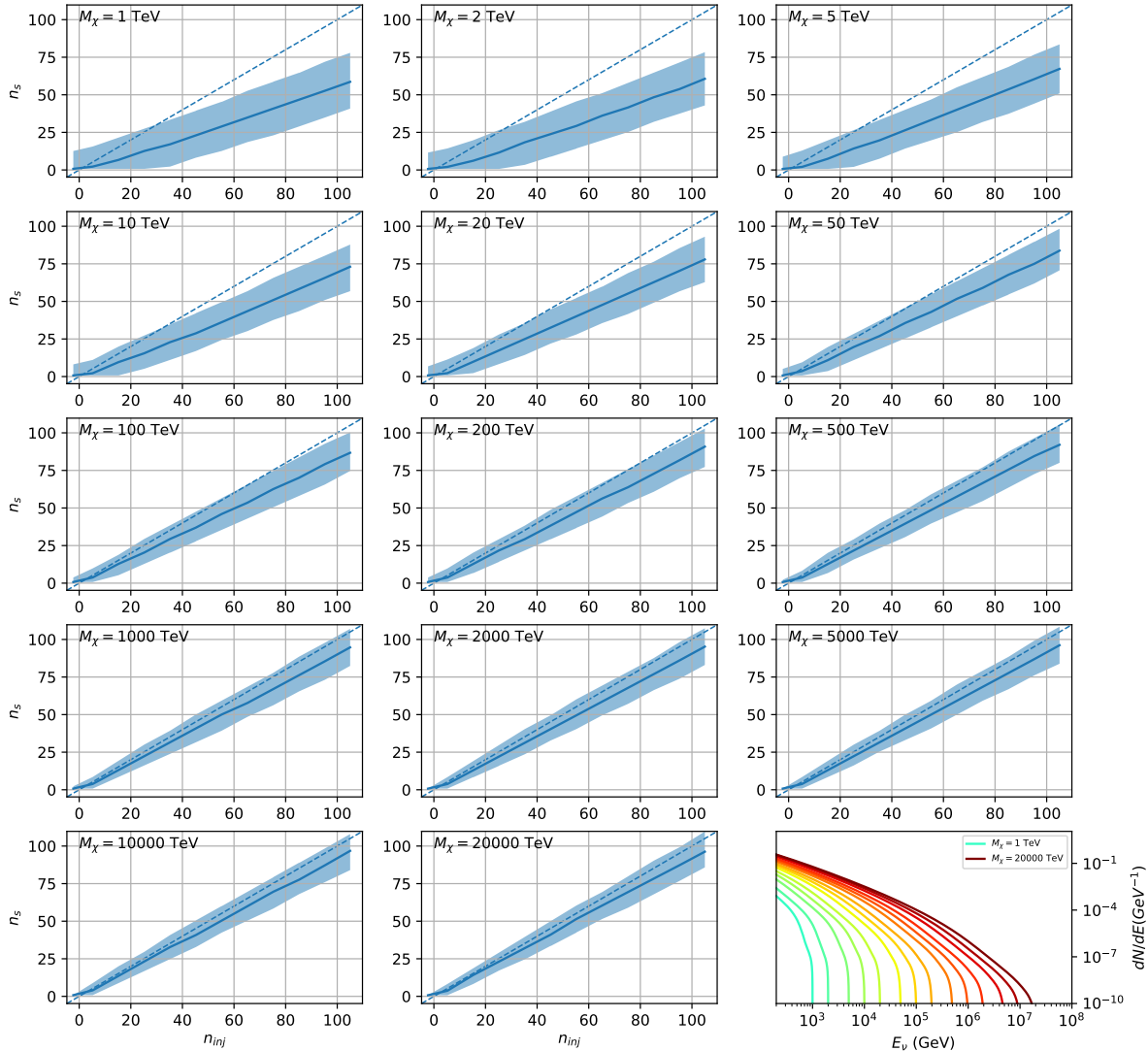


Figure C.6 Same as Fig. 7.23 but for Ursa Major II and  $\chi\chi \rightarrow b\bar{b}$ .

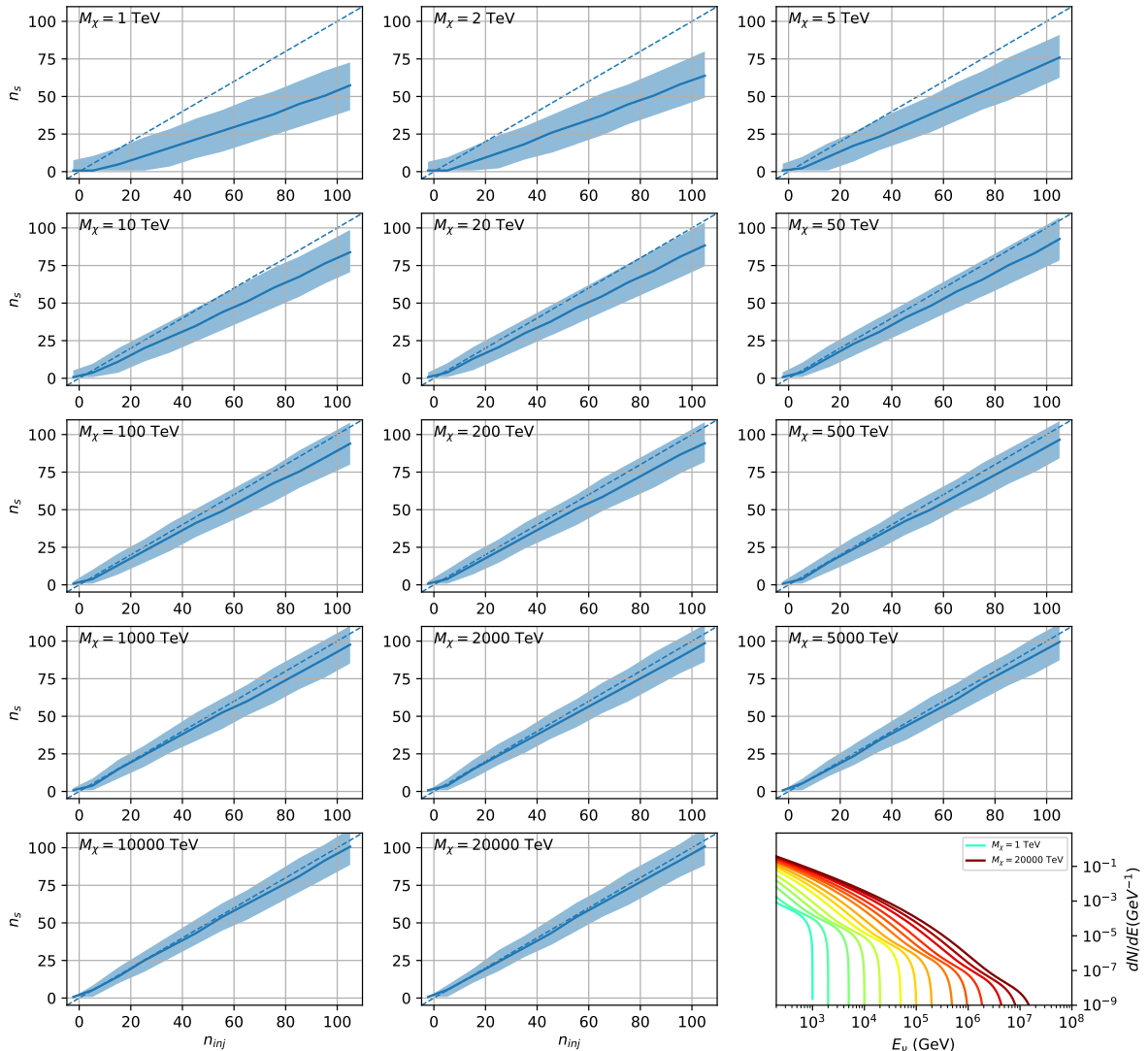


Figure C.7 Same as Fig. 7.23 but for Ursa Major II and  $\chi\chi \rightarrow t\bar{t}$ .

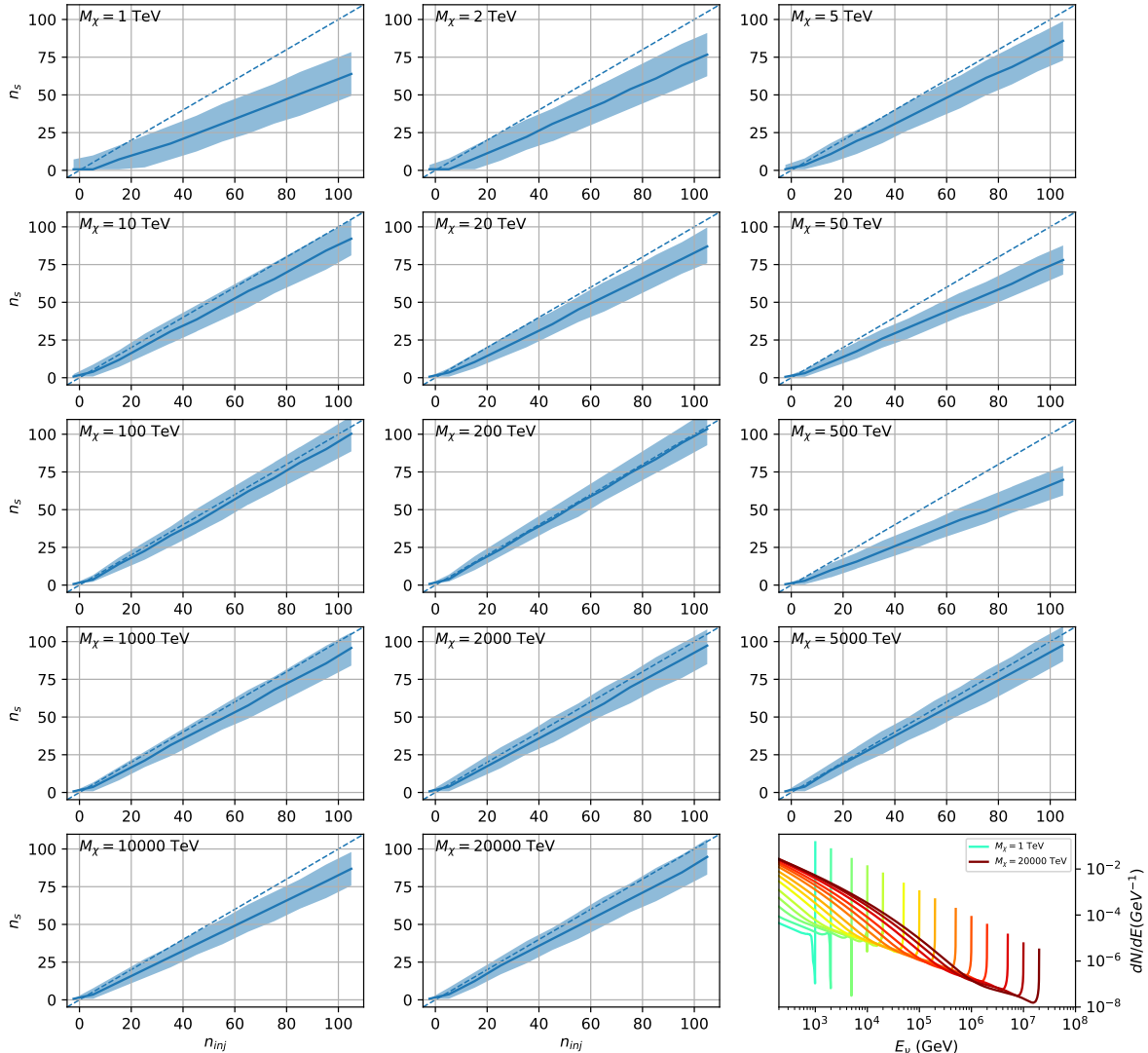


Figure C.8 Same as Fig. 7.23 but for Ursa Major II and  $\chi\chi \rightarrow \nu_\mu \bar{\nu}_\mu$ .

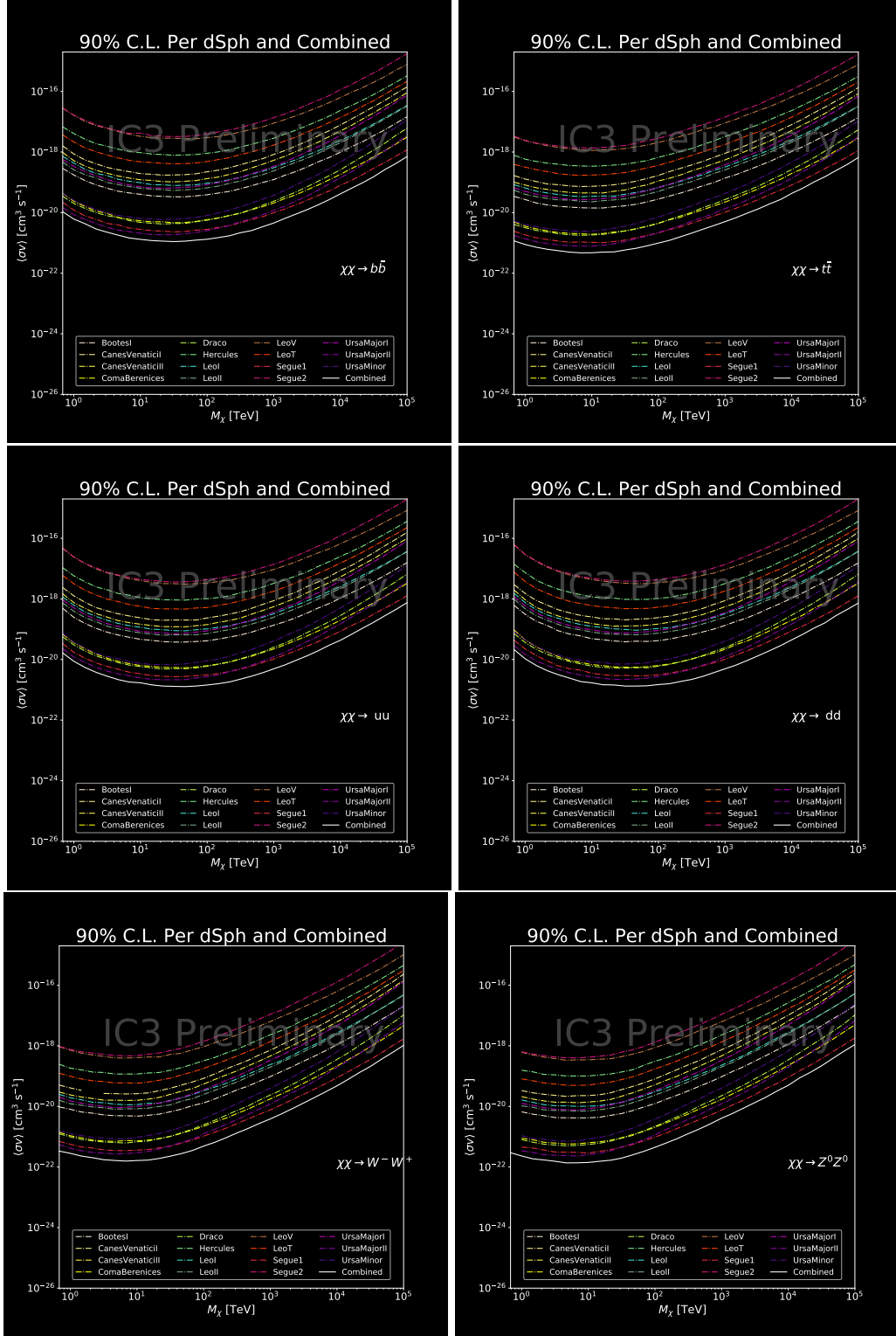


Figure C.9 IceCube North Sky Track Sensitivities for  $n_s/\langle N \rangle$ .  $n_s$  values are the counts fed into Eq. (7.8) to produce Fig. 7.26 and Fig. 7.25.

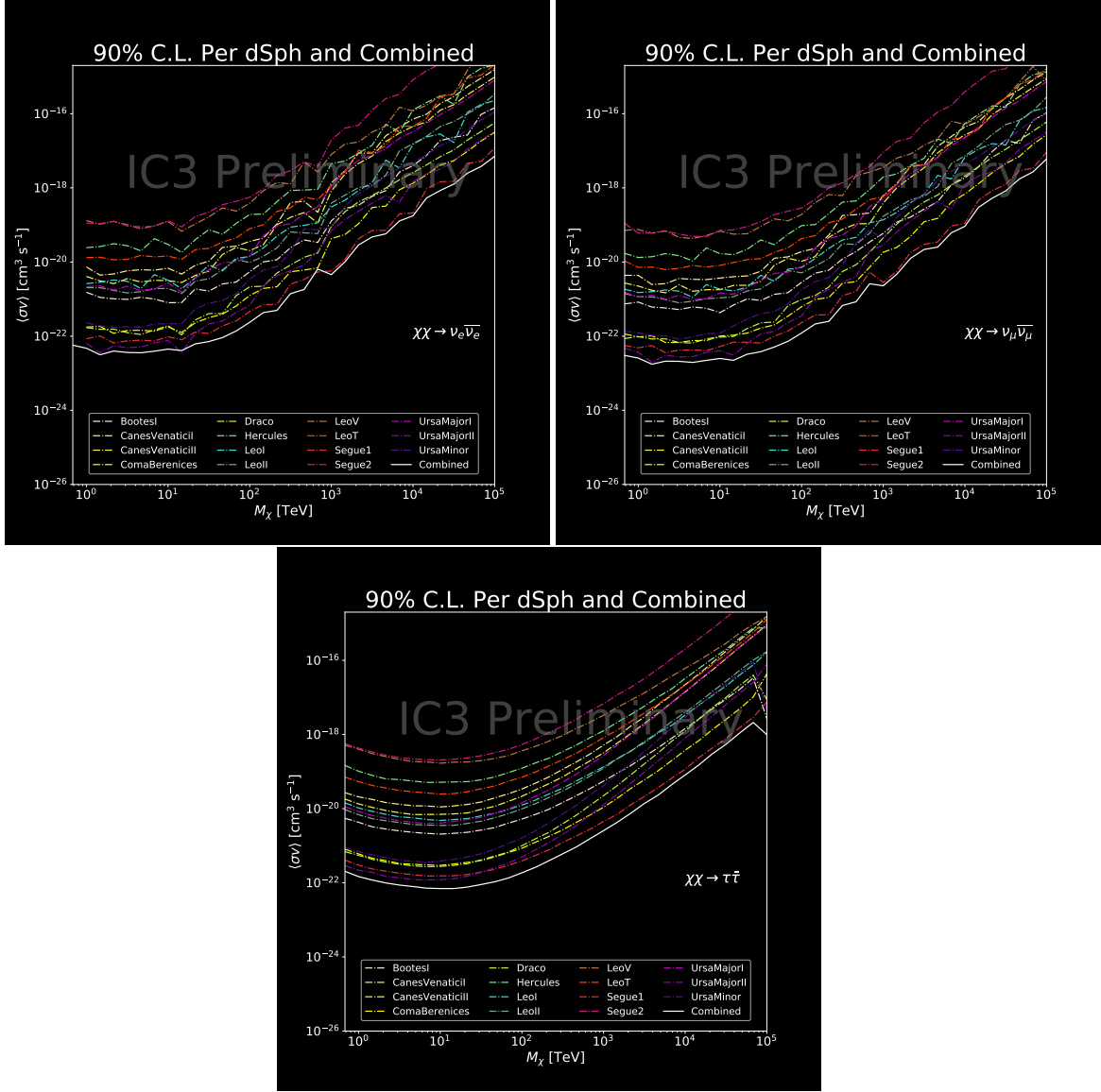


Figure C.10 Same as Fig. C.9 for three additional DM annihilation channels.

## BIBLIOGRAPHY

- 2444 [1] Anne M. Green. “Dark matter in astrophysics/cosmology”. In: *SciPost Phys. Lect.*  
 2445 *Notes* (2022), p. 37. doi: [10.21468/SciPostPhysLectNotes.37](https://doi.org/10.21468/SciPostPhysLectNotes.37). URL: <https://scipost.org/10.21468/SciPostPhysLectNotes.37>.
- 2447 [2] Bing-Lin Young. “A survey of dark matter and related topics in cosmology”. In: *Frontiers*  
 2448 *of Physics* 12 (Oct. 2016). doi: <https://doi.org/10.1007/s11467-016-0583-4>.  
 2449 URL: <https://doi.org/10.1007/s11467-016-0583-4>.
- 2450 [3] Gianfranco Bertone, Dan Hooper, and Joseph Silk. “Particle dark matter: evidence,  
 2451 candidates and constraints”. In: *Physics Reports* 405.5 (2005), pp. 279–390. ISSN:  
 2452 0370-1573. doi: <https://doi.org/10.1016/j.physrep.2004.08.031>. URL:  
 2453 <https://www.sciencedirect.com/science/article/pii/S0370157304003515>.
- 2454 [4] Gianfranco Bertone and Dan Hooper. “History of dark matter”. In: *Rev. Mod. Phys.*  
 2455 90 (4 Aug. 2018), p. 045002. doi: [10.1103/RevModPhys.90.045002](https://doi.org/10.1103/RevModPhys.90.045002). URL: <https://link.aps.org/doi/10.1103/RevModPhys.90.045002>.
- 2457 [5] Fritz Zwicky. “The Redshift of Extragalactic Nebulae”. In: *Helvetica Physica Acta* 6.  
 2458 (1933), pp. 110–127. doi: [10.5169/seals-110267](https://doi.org/10.5169/seals-110267).
- 2459 [6] Vera C. Rubin and Jr. Ford W. Kent. “Rotation of the Andromeda Nebula from a  
 2460 Spectroscopic Survey of Emission Regions”. In: *ApJ* 159 (Feb. 1970), p. 379. doi:  
 2461 [10.1086/150317](https://doi.org/10.1086/150317).
- 2462 [7] K. G. Begeman, A. H. Broeils, and R. H. Sanders. “Extended rotation curves of spiral galax-  
 2463 ies: dark haloes and modified dynamics”. In: *Monthly Notices of the Royal Astronomical So-*  
 2464 *ciety* 249.3 (Apr. 1991), pp. 523–537. ISSN: 0035-8711. doi: [10.1093/mnras/249.3.523](https://doi.org/10.1093/mnras/249.3.523).  
 2465 eprint: <https://academic.oup.com/mnras/article-pdf/249/3/523/18160929/mnras249-0523.pdf>. URL: <https://doi.org/10.1093/mnras/249.3.523>.
- 2467 [8] *Different types of gravitational lenses*. website. Feb. 2004. URL: <https://esahubble.org/images/heic0404b/>.
- 2469 [9] Douglas Clowe et al. “A Direct Empirical Proof of the Existence of Dark Matter”. In: *apjl*  
 2470 648.2 (Sept. 2006), pp. L109–L113. doi: [10.1086/508162](https://doi.org/10.1086/508162). arXiv: [astro-ph/0608407](https://arxiv.org/abs/astro-ph/0608407)  
 2471 [*astro-ph*].
- 2472 [10] Planck Collaboration and N. et. al. Aghanim. “Planck 2018 results I. Overview and the  
 2473 cosmological legacy of Planck”. In: *A&A* 641 (2020). doi: [10.1051/0004-6361/201833880](https://doi.org/10.1051/0004-6361/201833880). URL: <https://doi.org/10.1051/0004-6361/201833880>.
- 2475 [11] Wayne Hu. *Matter Density Animation*. web. 2024. URL: <http://background.uchicago.edu/~whu/animbut/anim2.html>.

- 2477 [12] Wenlong Yuan et al. “A First Look at Cepheids in a Type Ia Supernova Host with JWST”. in:  
2478     *The Astrophysical Journal Letters* 940.1 (Nov. 2022). doi: [10.3847/2041-8213/ac9b27](https://doi.org/10.3847/2041-8213/ac9b27).  
2479     URL: <https://dx.doi.org/10.3847/2041-8213/ac9b27>.
- 2480 [13] Wendy L. Freedman. “Measurements of the Hubble Constant: Tensions in Perspective”. In:  
2481     *The Astrophysical Journal* 919.1 (Sept. 2021), p. 16. doi: [10.3847/1538-4357/ac0e95](https://doi.org/10.3847/1538-4357/ac0e95).  
2482     URL: <https://dx.doi.org/10.3847/1538-4357/ac0e95>.
- 2483 [14] Jodi Cooley. “Dark Matter direct detection of classical WIMPs”. In: *SciPost Phys. Lect.*  
2484     *Notes* (2022), p. 55. doi: [10.21468/SciPostPhysLectNotes.55](https://doi.org/10.21468/SciPostPhysLectNotes.55). URL: <https://scipost.org/10.21468/SciPostPhysLectNotes.55>.
- 2486 [15] “Search for new phenomena in events with an energetic jet and missing transverse momentum  
2487     in  $pp$  collisions at  $\sqrt{s} = 13$  TeV with the ATLAS detector”. In: *Phys. Rev. D* 103  
2488     (11 July 2021), p. 112006. doi: [10.1103/PhysRevD.103.112006](https://doi.org/10.1103/PhysRevD.103.112006). URL: <https://link.aps.org/doi/10.1103/PhysRevD.103.112006>.
- 2490 [16] *Jetting into the dark side: a precision search for dark matter*. website. July 2020. URL:  
2491     <https://atlas.cern/updates/briefing/precision-search-dark-matter>.
- 2492 [17] Celine Armand et. al. “Combined dark matter searches towards dwarf spheroidal galaxies  
2493     with Fermi-LAT, HAWC, H.E.S.S., MAGIC, and VERITAS”. in: *Proceedings of Science*.  
2494     Vol. 395. Mar. 2022. doi: <https://doi.org/10.22323/1.395.0528>.
- 2495 [18] Tracy R. Slatyer. “Les Houches Lectures on Indirect Detection of Dark Matter”. In: *SciPost*  
2496     *Phys. Lect. Notes* (2022), p. 53. doi: [10.21468/SciPostPhysLectNotes.53](https://doi.org/10.21468/SciPostPhysLectNotes.53). URL:  
2497     <https://scipost.org/10.21468/SciPostPhysLectNotes.53>.
- 2498 [19] Christian W Bauer, Nicholas L. Rodd, and Bryan R. Webber. “Dark matter spectra from  
2499     the electroweak to the Planck scale”. In: *Journal of High Energy Physics* 2021.1029-8479  
2500     (June 2021). doi: [https://doi.org/10.1007/JHEP06\(2021\)121](https://doi.org/10.1007/JHEP06(2021)121).
- 2501 [20] Riccardo Catena and Piero Ullio. “A novel determination of the local dark matter density”.  
2502     In: *Journal of Cosmology and Astroparticle Physics* 2010.08 (Aug. 2010), p. 004. doi:  
2503     [10.1088/1475-7516/2010/08/004](https://doi.org/10.1088/1475-7516/2010/08/004). URL: <https://dx.doi.org/10.1088/1475-7516/2010/08/004>.
- 2505 [21] B. P. Abbott et al. “Observation of Gravitational Waves from a Binary Black Hole Merger”.  
2506     In: *Phys. Rev. Lett.* 116 (6 Feb. 2016), p. 061102. doi: [10.1103/PhysRevLett.116.061102](https://doi.org/10.1103/PhysRevLett.116.061102). URL: <https://link.aps.org/doi/10.1103/PhysRevLett.116.061102>.
- 2508 [22] R. Abbasi et. al. “Observation of high-energy neutrinos from the Galactic plane”. In: *Science*  
2509     380.6652 (June 2023), pp. 1338–1343.
- 2510 [23] NASA Goddard Space Flight Center. *Fermi’s 12-year view of the gamma-ray sky*. website.

- 2511 2022. URL: <https://svs.gsfc.nasa.gov/14090>.
- 2512 [24] Marco Cirelli et al. “PPPC 4 DM ID: a poor particle physicist cookbook for dark matter  
2513 indirect detection”. In: *Journal of Cosmology and Astroparticle Physics* 2011.03 (Mar.  
2514 2011), p. 051. doi: [10.1088/1475-7516/2011/03/051](https://doi.org/10.1088/1475-7516/2011/03/051). URL: <https://dx.doi.org/10.1088/1475-7516/2011/03/051>.
- 2516 [25] The HAWC Collaboration. “The High-Altitude Water Cherenkov (HAWC) observatory in  
2517 México: The primary detector”. In: *Nuclear Instruments and Methods in Physics Research*  
2518 *Section A: Accelerators, Spectrometers, Detectors and Associated Equipment* 1052 (2023),  
2519 p. 168253. ISSN: 0168-9002. doi: <https://doi.org/10.1016/j.nima.2023.168253>.  
2520 URL: <https://www.sciencedirect.com/science/article/pii/S0168900223002437>.
- 2522 [26] Alicia Lopez Oramas. “Multi-year Campaign of the Gamma-Ray Binary LS I +61° 303  
2523 and Search for VHE Emission from Gamma-Ray Binary Candidates with the MAGIC  
2524 Telescopes”. PhD thesis. Instituto de Astrofísica de Canarias, 2014. doi: <http://dx.doi.org/10.13140/RG.2.1.4140.4969>.
- 2526 [27] A.U. Abeysekara et. al. “The High-Altitude Water Cherenkov (HAWC) observatory in Méx-  
2527 ico: The primary detector”. In: *Nuclear Instruments and Methods in Physics Research*  
2528 *Section A: Accelerators, Spectrometers, Detectors and Associated Equipment* 1052 (2023),  
2529 p. 168253. ISSN: 0168-9002. doi: <https://doi.org/10.1016/j.nima.2023.168253>.  
2530 URL: <https://www.sciencedirect.com/science/article/pii/S0168900223002437>.
- 2532 [28] Hamamatsu Photonics KK. *Large Photocathode Area Photomultiplier Tubes*. 2019. URL:  
2533 [https://www.hamamatsu.com/content/dam/hamamatsu-photonics/sites/documents/99\\_SALES\\_LIBRARY/etd/LARGE\\_AREA\\_PMT TPMH1376E.pdf](https://www.hamamatsu.com/content/dam/hamamatsu-photonics/sites/documents/99_SALES_LIBRARY/etd/LARGE_AREA_PMT TPMH1376E.pdf).
- 2535 [29] The HAWC Collaboration. “Data acquisition architecture and online processing system  
2536 for the HAWC gamma-ray observatory”. In: *Nuclear Instruments and Methods in Physics*  
2537 *Research Section A: Accelerators, Spectrometers, Detectors and Associated Equipment* 888  
2538 (2018), pp. 138–146. ISSN: 0168-9002. doi: <https://doi.org/10.1016/j.nima.2018.01.051>. URL: <https://www.sciencedirect.com/science/article/pii/S0168900218300688>.
- 2541 [30] The Milagro Collaboratio. “Milagrito, a TeV air-shower array”. In: *Nuclear Instruments*  
2542 *and Methods in Physics Research Section A: Accelerators, Spectrometers, Detectors and*  
2543 *Associated Equipment* 449.3 (2000), pp. 478–499. ISSN: 0168-9002. doi: [https://doi.org/10.1016/S0168-9002\(00\)00146-7](https://doi.org/10.1016/S0168-9002(00)00146-7). URL: <https://www.sciencedirect.com/science/article/pii/S0168900200001467>.
- 2546 [31] Ian Gabriel Wisher. “Real-time Transient Monitoring With the HAWC Detector: Design  
2547 and Performance”. PhD thesis. The University of Wisconsin - Madison, 2016.

- 2548 [32] The ZeroMQ authors. “ZeroMQ An open-source universal messaging library”. In: (2021).  
2549 URL: <https://zeromq.org>.
- 2550 [33] Zigfried Hampel-Archisman. “Cosmic Ray Observations at the TeV Scale with the HAWC  
2551 Observatory”. PhD thesis. University of Wisconsin-Madison, 2017.
- 2552 [34] A. U. Abeysekara et al. “Observation of the Crab Nebula with the HAWC Gamma-Ray  
2553 Observatory”. In: *The Astrophysical Journal* 843.1 (June 2017), p. 39. doi: [10.3847/1538-4357/aa7555](https://doi.org/10.3847/1538-4357/aa7555). URL: <https://doi.org/10.3847/1538-4357/aa7555>.
- 2555 [35] Kenneth Greisen. “Cosmic Ray Showers”. In: *ANNUAL REVIEW OF NUCLEAR AND  
2556 PARTICLE SCIENCE* 10 (1960), pp. 63–108.
- 2557 [36] The HAWC Collabortion. “Sensitivity of the high altitude water Cherenkov detector to  
2558 sources of multi-TeV gamma rays”. In: *Astroparticle Physics* 50-52 (2013), pp. 26–32. ISSN:  
2559 0927-6505. doi: <https://doi.org/10.1016/j.astropartphys.2013.08.002>. URL:  
2560 <https://www.sciencedirect.com/science/article/pii/S0927650513001230>.
- 2561 [37] The HAWC Collaboration. “Measurement of the Crab Nebula Spectrum Past 100 TeV with  
2562 HAWC”. in: *The Astrophysical Journal* 881.2 (Aug. 2019), p. 134. doi: [10.3847/1538-4357/ab2f7d](https://doi.org/10.3847/1538-4357/ab2f7d). URL: <https://dx.doi.org/10.3847/1538-4357/ab2f7d>.
- 2564 [38] Samuel Miranelli. “CONSTRAINTS ON LORENTZ-INVARIANCE VIOLATION WITH  
2565 THE HAWC OBSERVATORY”. PhD thesis. Michigan State University, 2019.
- 2566 [39] A. A. Abdo et al. “OBSERVATION AND SPECTRAL MEASUREMENTS OF THE  
2567 CRAB NEBULA WITH MILAGRO”. in: *The Astrophysical Journal* 750.1 (Apr. 2012),  
2568 p. 63. doi: [10.1088/0004-637X/750/1/63](https://doi.org/10.1088/0004-637X/750/1/63). URL: <https://dx.doi.org/10.1088/0004-637X/750/1/63>.
- 2570 [40] Javier Rico. “Gamma-Ray Dark Matter Searches in Milky Way Satellites—A Comparative  
2571 Review of Data Analysis Methods and Current Results”. In: *Galaxies* 8.1 (Mar. 2020), p. 25.  
2572 doi: [10.3390/galaxies8010025](https://doi.org/10.3390/galaxies8010025). arXiv: [2003.13482 \[astro-ph.HE\]](https://arxiv.org/abs/2003.13482).
- 2573 [41] W. B. Atwood et al. “The Large Area Telescope on the Fermi Gamma-Ray Space Telescope  
2574 Mission”. In: *apj* 697.2 (June 2009), pp. 1071–1102. doi: [10.1088/0004-637X/697/2/1071](https://doi.org/10.1088/0004-637X/697/2/1071). arXiv: [0902.1089 \[astro-ph.IM\]](https://arxiv.org/abs/0902.1089).
- 2576 [42] M. Ackermann et al. “Searching for Dark Matter Annihilation from Milky Way Dwarf  
2577 Spheroidal Galaxies with Six Years of Fermi Large Area Telescope Data”. In: *prl* 115.23,  
2578 231301 (Dec. 2015), p. 231301. doi: [10.1103/PhysRevLett.115.231301](https://doi.org/10.1103/PhysRevLett.115.231301). arXiv:  
2579 [1503.02641 \[astro-ph.HE\]](https://arxiv.org/abs/1503.02641).
- 2580 [43] Mattia Di Mauro, Martin Stref, and Francesca Calore. “Investigating the effect of Milky  
2581 Way dwarf spheroidal galaxies extension on dark matter searches with Fermi-LAT data”.

- 2582 In: *Phys. Rev. D* 106 (12 Dec. 2022), p. 123032. doi: [10.1103/PhysRevD.106.123032](https://doi.org/10.1103/PhysRevD.106.123032).  
2583 URL: <https://link.aps.org/doi/10.1103/PhysRevD.106.123032>.
- 2584 [44] F. et al. Aharonian. “Observations of the Crab Nebula with H.E.S.S.”. In: *Astron. Astrophys.*  
2585 457 (2006), pp. 899–915. doi: [10.1051/0004-6361:20065351](https://doi.org/10.1051/0004-6361:20065351). arXiv: [astro-ph/0607333](https://arxiv.org/abs/astro-ph/0607333).
- 2587 [45] J. Albert et al. “VHE  $\gamma$ -Ray Observation of the Crab Nebula and its Pulsar with the MAGIC  
2588 Telescope”. In: *The Astrophysical Journal* 674.2 (Feb. 2008), p. 1037. doi: [10.1086/525270](https://doi.org/10.1086/525270). URL: <https://dx.doi.org/10.1086/525270>.
- 2590 [46] N. Park. “Performance of the VERITAS experiment”. In: *Proceedings, 34th International  
2591 Cosmic Ray Conference (ICRC2015): The Hague, The Netherlands, July, 30th July - 6th  
2592 August*. Vol. 34. 2015, p. 771. arXiv: [1508.07070](https://arxiv.org/abs/1508.07070) [astro-ph.IM].
- 2593 [47] A. Abramowski et al. “H.E.S.S. constraints on Dark Matter annihilations towards the Sculptor  
2594 and Carina Dwarf Galaxies”. In: *Astropart. Phys.* 34 (2011), pp. 608–616. doi: [10.1016/j.astropartphys.2010.12.006](https://doi.org/10.1016/j.astropartphys.2010.12.006). arXiv: [1012.5602](https://arxiv.org/abs/1012.5602) [astro-ph.HE].
- 2596 [48] A. Abramowski et al. “Search for dark matter annihilation signatures in H.E.S.S. observations  
2597 of Dwarf Spheroidal Galaxies”. In: *Phys. Rev. D* 90 (2014), p. 112012. doi: [10.1103/PhysRevD.90.112012](https://doi.org/10.1103/PhysRevD.90.112012). arXiv: [1410.2589](https://arxiv.org/abs/1410.2589) [astro-ph.HE].
- 2599 [49] H. Abdalla et al. “Searches for gamma-ray lines and ‘pure WIMP’ spectra from Dark  
2600 Matter annihilations in dwarf galaxies with H.E.S.S”. in: *JCAP* 11 (2018), p. 037. doi:  
2601 [10.1088/1475-7516/2018/11/037](https://doi.org/10.1088/1475-7516/2018/11/037). arXiv: [1810.00995](https://arxiv.org/abs/1810.00995) [astro-ph.HE].
- 2602 [50] J. Aleksić et al. “Optimized dark matter searches in deep observations of Segue 1 with  
2603 MAGIC”. in: *JCAP* 1402 (2014), p. 008. doi: [10.1088/1475-7516/2014/02/008](https://doi.org/10.1088/1475-7516/2014/02/008).  
2604 arXiv: [1312.1535](https://arxiv.org/abs/1312.1535) [hep-ph].
- 2605 [51] V.A. Acciari et al. “Combined searches for dark matter in dwarf spheroidal galaxies observed  
2606 with the MAGIC telescopes, including new data from Coma Berenices and Draco”. In: *Physics of the Dark Universe* (2021), p. 100912. ISSN: 2212-6864. doi: <https://doi.org/10.1016/j.dark.2021.100912>. URL: <https://www.sciencedirect.com/science/article/pii/S2212686421001370>.
- 2610 [52] M. L. Ahnen et al. “Indirect dark matter searches in the dwarf satellite galaxy Ursa Major II  
2611 with the MAGIC Telescopes”. In: *JCAP* 1803.03 (2018), p. 009. doi: [10.1088/1475-7516/2018/03/009](https://doi.org/10.1088/1475-7516/2018/03/009). arXiv: [1712.03095](https://arxiv.org/abs/1712.03095) [astro-ph.HE].
- 2613 [53] S. et al. Archambault. “Dark matter constraints from a joint analysis of dwarf Spheroidal  
2614 galaxy observations with VERITAS”. in: *prd* 95.8 (Apr. 2017). doi: [10.1103/PhysRevD.95.082001](https://doi.org/10.1103/PhysRevD.95.082001). arXiv: [1703.04937](https://arxiv.org/abs/1703.04937) [astro-ph.HE].

- 2616 [54] Louise Oakes et al. “Combined Dark Matter searches towards dwarf spheroidal galaxies with  
2617 Fermi-LAT, HAWC, HESS, MAGIC and VERITAS”. in: *Proceedings of Science*. 2019.
- 2618 [55] Celine Armand et al. on behalf of the Fermi-LAT, HAWC, HESS, MAGIC, VERITAS.  
2619 “Combined Dark Matter searches towards dwarf spheroidal galaxies with Fermi-LAT,  
2620 HAWC, HESS, MAGIC and VERITAS”. in: *Proceedings of Science*. 2021.
- 2621 [56] Daniel Kerszberg et al. on behalf of the Fermi-LAT, HAWC, HESS, MAGIC, and VER-  
2622 TIAS collaborations. “Search for dark matter annihilation with a combined analysis of  
2623 dwarf spheroidal galaxies from Fermi-LAT, HAWC, H.E.S.S., MAGIC and VERITAS”. in:  
2624 *Proceedings of Science*. 2023.
- 2625 [57] Giacomo Vianello et al. *The Multi-Mission Maximum Likelihood framework (3ML)*. 2015.  
2626 arXiv: [1507.08343 \[astro-ph.HE\]](https://arxiv.org/abs/1507.08343).
- 2627 [58] Marco Cirelli et al. “PPPC 4 DM ID: a poor particle physicist cookbook for dark matter  
2628 indirect detection”. In: *Journal of Cosmology and Astroparticle Physics* 2011.03 (Mar.  
2629 2011). ISSN: 1475-7516. doi: [10.1088/1475-7516/2011/03/051](https://doi.org/10.1088/1475-7516/2011/03/051). URL: <http://dx.doi.org/10.1088/1475-7516/2011/03/051>.
- 2631 [59] Alex Geringer-Sameth, Savvas M. Koushiappas, and Matthew Walker. “DWARF GALAXY  
2632 ANNIHILATION AND DECAY EMISSION PROFILES FOR DARK MATTER EXPERI-  
2633 MENTS”. in: *The Astrophysical Journal* 801.2 (Mar. 2015), p. 74. ISSN: 1538-4357. doi:  
2634 [10.1088/0004-637x/801/2/74](https://doi.org/10.1088/0004-637x/801/2/74). URL: <http://dx.doi.org/10.1088/0004-637X/801/2/74>.
- 2636 [60] A. Albert et al. “Dark Matter Limits from Dwarf Spheroidal Galaxies with the HAWC  
2637 Gamma-Ray Observatory”. In: *The Astrophysical Journal* 853.2 (Feb. 2018), p. 154. ISSN:  
2638 1538-4357. doi: [10.3847/1538-4357/aaa6d8](https://doi.org/10.3847/1538-4357/aaa6d8). URL: <http://dx.doi.org/10.3847/1538-4357/aaa6d8>.
- 2640 [61] HongSheng Zhao. “Analytical models for galactic nuclei”. In: *Mon. Not. Roy. Astron. Soc.*  
2641 278 (1996), pp. 488–496. doi: [10.1093/mnras/278.2.488](https://doi.org/10.1093/mnras/278.2.488). arXiv: [astro-ph/9509122](https://arxiv.org/abs/astro-ph/9509122)  
2642 [[astro-ph](https://arxiv.org/abs/astro-ph/9509122)].
- 2643 [62] Julio F. Navarro, Carlos S. Frenk, and Simon D. M. White. “The Structure of Cold Dark  
2644 Matter Halos”. In: *ApJ* 462 (May 1996), p. 563. doi: [10.1086/177173](https://doi.org/10.1086/177173). eprint:  
2645 [astro-ph/9508025](https://arxiv.org/abs/astro-ph/9508025) (astro-ph).
- 2646 [63] V. Bonnivard et al. “Spherical Jeans analysis for dark matter indirect detection in dwarf  
2647 spheroidal galaxies - Impact of physical parameters and triaxiality”. In: *Mon. Not. Roy.  
2648 Astron. Soc.* 446 (2015), pp. 3002–3021. doi: [10.1093/mnras/stu2296](https://doi.org/10.1093/mnras/stu2296). arXiv:  
2649 [1407.7822 \[astro-ph.HE\]](https://arxiv.org/abs/1407.7822).
- 2650 [64] M. Ackermann et al. “Searching for Dark Matter Annihilation from Milky Way Dwarf

- 2651 Spheroidal Galaxies with Six Years of Fermi Large Area Telescope Data”. In: *prl* 115.23,  
2652 231301 (Dec. 2015), p. 231301. doi: [10.1103/PhysRevLett.115.231301](https://doi.org/10.1103/PhysRevLett.115.231301). arXiv:  
2653 [1503.02641 \[astro-ph.HE\]](https://arxiv.org/abs/1503.02641).
- 2654 [65] M. L. Ahnen et al. “Limits to Dark Matter Annihilation Cross-Section from a Combined  
2655 Analysis of MAGIC and Fermi-LAT Observations of Dwarf Satellite Galaxies”. In: *JCAP*  
2656 1602.02 (2016), p. 039. doi: [10.1088/1475-7516/2016/02/039](https://doi.org/10.1088/1475-7516/2016/02/039). arXiv: [1601.06590](https://arxiv.org/abs/1601.06590)  
2657 [astro-ph.HE].
- 2658 [66] Javier Rico et al. *gLike: numerical maximization of heterogeneous joint  
2659 likelihood functions of a common free parameter plus nuisance parameters.*  
2660 <https://doi.org/10.5281/zenodo.4601451>. Version v0.09.03. Mar. 2021. doi: [10.5281/zenodo.4601451](https://doi.org/10.5281/zenodo.4601451). URL: <https://doi.org/10.5281/zenodo.4601451>.
- 2662 [67] Tjark Miener and Daniel Nieto. *LklCom: Combining likelihoods from different experiments.*  
2663 <https://doi.org/10.5281/zenodo.4597500>. Version v0.5.3. Mar. 2021. doi: [10.5281/zenodo.4597500](https://doi.org/10.5281/zenodo.4597500). URL: <https://doi.org/10.5281/zenodo.4597500>.
- 2665 [68] T. Miener et al. “Open-source Analysis Tools for Multi-instrument Dark Matter Searches”.  
2666 In: *arXiv e-prints*, arXiv:2112.01818 (Dec. 2021), arXiv:2112.01818. arXiv: [2112.01818](https://arxiv.org/abs/2112.01818)  
2667 [astro-ph.IM].
- 2668 [69] Alex Geringer-Sameth and Matthew Koushiappas Savvas M. and Walker. “Dwarf galaxy  
2669 annihilation and decay emission profiles for dark matter experiments”. In: *Astrophys.  
2670 J.* 801.2 (2015), p. 74. doi: [10.1088/0004-637X/801/2/74](https://doi.org/10.1088/0004-637X/801/2/74). arXiv: [1408.0002](https://arxiv.org/abs/1408.0002)  
2671 [astro-ph.CO].
- 2672 [70] Gianfranco Bertone, Dan Hooper, and Joseph Silk. “Particle dark matter: evidence, can-  
2673 didates and constraints”. In: *Physics Reports* 405.5-6 (Jan. 2005), pp. 279–390. ISSN:  
2674 0370-1573. doi: [10.1016/j.physrep.2004.08.031](https://doi.org/10.1016/j.physrep.2004.08.031). URL: <http://dx.doi.org/10.1016/j.physrep.2004.08.031>.
- 2676 [71] V. Bonnivard et al. “Dark matter annihilation and decay in dwarf spheroidal galaxies: The  
2677 classical and ultrafaint dSphs”. In: *Mon. Not. Roy. Astron. Soc.* 453.1 (2015), pp. 849–867.  
2678 doi: [10.1093/mnras/stv1601](https://doi.org/10.1093/mnras/stv1601). arXiv: [1504.02048 \[astro-ph.HE\]](https://arxiv.org/abs/1504.02048).
- 2679 [72] A. et al. Albert. “Searching for Dark Matter Annihilation in Recently Discovered Milky Way  
2680 Satellites with Fermi-LAT”. in: *Astrophys. J.* 834.2 (2017), p. 110. doi: [10.3847/1538-4357/834/2/110](https://doi.org/10.3847/1538-4357/834/2/110). arXiv: [1611.03184 \[astro-ph.HE\]](https://arxiv.org/abs/1611.03184).
- 2682 [73] Mattia Di Mauro and Martin Wolfgang Winkler. “Multimessenger constraints on the dark  
2683 matter interpretation of the Fermi-LAT Galactic Center excess”. In: *prd* 103.12, 123005  
2684 (June 2021), p. 123005. doi: [10.1103/PhysRevD.103.123005](https://doi.org/10.1103/PhysRevD.103.123005). arXiv: [2101.11027](https://arxiv.org/abs/2101.11027)  
2685 [astro-ph.HE].

- 2686 [74] H. C. Plummer. “On the Problem of Distribution in Globular Star Clusters: (Plate 8.)”  
 2687 In: *Monthly Notices of the Royal Astronomical Society* 71.5 (Mar. 1911), pp. 460–470.  
 2688 ISSN: 0035-8711. doi: [10.1093/mnras/71.5.460](https://doi.org/10.1093/mnras/71.5.460). eprint: <https://academic.oup.com/mnras/article-pdf/71/5/460/2937497/mnras71-0460.pdf>. URL:  
 2689 <https://doi.org/10.1093/mnras/71.5.460>.
- 2691 [75] Daniel R. Hunter. “Derivation of the anisotropy profile, constraints on the local velocity  
 2692 dispersion, and implications for direct detection”. In: *JCAP* 02 (2014), p. 023. doi:  
 2693 [10.1088/1475-7516/2014/02/023](https://doi.org/10.1088/1475-7516/2014/02/023). arXiv: [1311.0256 \[astro-ph.CO\]](https://arxiv.org/abs/1311.0256).
- 2694 [76] Barun Kumar Dhar and Liliya L. R. Williams. “Surface mass density of the Einasto family  
 2695 of dark matter haloes: are they Sersic-like?” In: *Mon. Not. Roy. Astron. Soc.* (2010). doi:  
 2696 [10.1111/j.1365-2966.2010.16446.x](https://doi.org/10.1111/j.1365-2966.2010.16446.x).
- 2697 [77] M. Baes and E. Van Hese. “Dynamical models with a general anisotropy profile”. In: *Astron. Astrophys.* 471 (2007), p. 419. doi: [10.1051/0004-6361:20077672](https://doi.org/10.1051/0004-6361:20077672). arXiv:  
 2698 [0705.4109 \[astro-ph\]](https://arxiv.org/abs/0705.4109).
- 2700 [78] Matthew G. Walker, Edward W. Olszewski, and Mario Mateo. “Bayesian analysis of re-  
 2701 solved stellar spectra: application to MMT/Hectochelle observations of the Draco dwarf  
 2702 spheroidal”. In: *mnras* 448.3 (Apr. 2015), pp. 2717–2732. doi: [10.1093/mnras/stv099](https://doi.org/10.1093/mnras/stv099).  
 2703 arXiv: [1503.02589 \[astro-ph.GA\]](https://arxiv.org/abs/1503.02589).
- 2704 [79] Nicholas L. Rodd et al. “Dark matter spectra from the electroweak to the Planck scale”. In:  
 2705 *J. High Energy Physics* 121.10.1007 (June 2021).
- 2706 [80] Pace, Andrew B and Strigari, Louis E. “Scaling relations for dark matter annihilation and  
 2707 decay profiles in dwarf spheroidal galaxies”. In: *Monthly Notices of the Royal Astronomical  
 2708 Society* 482.3 (Oct. 2018), pp. 3480–3496. ISSN: 0035-8711. doi: [10.1093/mnras/sty2839](https://doi.org/10.1093/mnras/sty2839).
- 2710 [81] Albert, A. et al. “Search for gamma-ray spectral lines from dark matter annihilation in  
 2711 dwarf galaxies with the High-Altitude Water Cherenkov observatory”. In: *Phys. Rev. D* 101 (10 May 2020), p. 103001. doi: [10.1103/PhysRevD.101.103001](https://doi.org/10.1103/PhysRevD.101.103001). URL:  
 2712 <https://link.aps.org/doi/10.1103/PhysRevD.101.103001>.
- 2714 [82] Victor Eijkhout and Edmund Show and Robert van de Geijn. *The Science of Computing. The Art of High Performance Computing*. Vol. 3. Open Copy published under CC-BY 4.0  
 2715 license, 2023, pp. 63–66.
- 2717 [83] Aartsen, M. et al. “IceCube search for dark matter annihilation in nearby galaxies and galaxy  
 2718 clusters”. In: *Phys. Rev. D* 88 (12 Dec. 2013), p. 122001. doi: [10.1103/PhysRevD.88.122001](https://doi.org/10.1103/PhysRevD.88.122001). URL: <https://link.aps.org/doi/10.1103/PhysRevD.88.122001>.
- 2720 [84] Pearl Sandick et al. “Sensitivity of the IceCube neutrino detector to dark matter annihilating

- 2721 in dwarf galaxies”. In: *Phys. Rev. D* 81 (8 Apr. 2010), p. 083506. doi: [10.1103/PhysRevD.81.083506](https://doi.org/10.1103/PhysRevD.81.083506). URL: <https://link.aps.org/doi/10.1103/PhysRevD.81.083506>.
- 2722
- 2723 [85] Qinrui Liu and Jeffrey Lazar and Carlos A. Argüelles and Ali Kheirandish. “ $\chi$ aro: a tool  
2724 for neutrino flux generation from WIMPs”. In: *Journal of Cosmology and Astroparticle  
2725 Physics* 2020.10 (Oct. 2020), p. 043. doi: [10.1088/1475-7516/2020/10/043](https://doi.org/10.1088/1475-7516/2020/10/043). URL:  
2726 <https://dx.doi.org/10.1088/1475-7516/2020/10/043>.
- 2727 [86] Tessa Cerver. “Time Integrated searches for Astrophysical Neutrino Sources using the  
2728 IceCube Detector and Gender in Physics studies for the Genera Project”. PhD thesis.  
2729 UNIVERSITE DE GEN ´ EVE, 2019, pp. 57–64.
- 2730 [87] Minjin Jeong on behalf of the IceCube Collaboration. “Search for Dark Matter Decay in  
2731 Nearby Galaxy Clusters and Galaxies with IceCube”. In: *Proceedings of Science* 444.38  
2732 (2023).
- 2733 [88] IceCube Collaboration. “Evidence for neutrino emission from the nearby active galaxy NGC  
2734 1068”. In: *Science* 378.6619 (2022).
- 2735 [89] Nathan Whitehorn and Jakob van Santen. *Photospline*. IceCube: GitHub.
- 2736 [90] Paul H. C. Eilers and Brian D. Marx. “Flexible smoothing with B-splines and penalties”.  
2737 In: *Statistical Science* 11.2 (1996), pp. 89–121. doi: [10.1214/ss/1038425655](https://doi.org/10.1214/ss/1038425655). URL:  
2738 <https://doi.org/10.1214/ss/1038425655>.
- 2739 [91] The IceCube Collaboration. *Search for neutrino lines from dark matter annihilation and  
2740 decay with IceCube*. 2023. arXiv: [2303.13663 \[astro-ph.HE\]](https://arxiv.org/abs/2303.13663).
- 2741 [92] The IceCube Collaboration. “Measurement of the multi-TeV neutrino interaction cross-  
2742 section with IceCube using Earth absorption”. In: *Nature* 551 (2017).